

**THE GEOLOGY OF THE ARCHAEOAN GRANTOID - GREENSTONE
TERRANE IN THE VICINITY OF THREE SISTERS,
BARBERTON GREENSTONE BELT**

Ernst Alfred Kohler

*A thesis submitted to the Faculty of Science,
University of the Witwatersrand, Johannesburg, for
the degree of Doctor of Philosophy*

Johannesburg, 1994

ABSTRACT

This thesis provides a comprehensive account of the geology of the Archaean granitoid-greenstone terrane centred around Three Sisters in the northeastern sector of the Barberton Mountain Land.

The supracrustal succession in the region comprises a diverse variety of altered volcanic and sedimentary rock types that have been correlated with the principal lithostratigraphic units of the Barberton greenstone belt (BGB) as follows:

- 1) schistose basic and ultrabasic lithologies correlated with the Theespruit Formation of the Onverwacht Group are mainly developed in a narrow unit fringing the northern margin of the BGB;
- 2) ferruginous shale greywacke - banded iron-formation assemblages correlated with the Jheba and Belvue Road Formations constitute the dominant Fig Tree Group rocks in the region. A sequence of silicic metavolcanic rocks, now altered to a variety of micaceous schists, occurs west, north and northeast of Three Sisters. Viljoen and Viljoen (1970) correlated these schists with the Theespruit Formation. In this study, the schists have been assigned to a new lithostratigraphic unit, referred to as the Bien Venue Formation, which forms the uppermost formation of the Fig Tree Group in the northeastern part of the BGB. Isotopic studies on zircons indicate that the schists have an age of 3256 ± Ma, which is some 200 Ma younger than the most recent age estimates for the lower portions of the Onverwacht Group. Chemically, the silicic schists resemble calc-alkaline rocks found in modern arcs, suggesting that the Bien Venue Formation represents a period of arc-like volcanism; and
- 3) conglomeratic and quartzitic rocks constitute the dominant lithologies within the Moodies Group, which unconformably or paraconformably overlies lithologies of the Fig Tree and Onverwacht Groups.

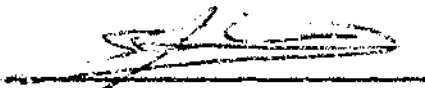
North of the BGB is a complex suite of granitoid rocks, previously investigated by Robb *et al.* (1983) who defined a large (~60 km long and ~6 km wide), elongate plutonic body of tonalitic-to-trondhjemitic composition known as the Stentor pluton. It was suggested that this pluton is correlatable with the trondhjemite gneiss plutons that intrude the southwestern parts of the BGB. Field evidence indicates, however, that the Stentor pluton

forms a much smaller (~ 14 km long and ~4 km wide) ovoid body located immediately north of the village of Louw's Creek. Furthermore, the pluton consists of equigranular-textured granodiorite-adamellite, totally unlike any of the trondhjemite gneisses. In terms of texture, mineralogy and chemical composition, the Stentor pluton closely resembles the Hebron and Berlin plutons which constitute a phase of the Nelspruit batholith. Thus, it is concluded that the Stentor pluton also forms an integral part of the batholith.

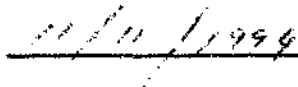
Three deformation phases have been identified. The regional event affected all stratigraphic units in response to a northerly oriented compressional stress and gave rise to east-northeasterly trending, tight to isoclinal, upright and north-verging folds that are bounded by southward-dipping longitudinal reverse faults. The regional deformation occurred both prior and subsequent to the emplacement of the Stentor pluton at *circa* 3100 Ma. Deformation associated with the diapiric intrusion of the Stentor pluton into the greenstone assemblage during the regional deformation phase, led to the formation of large-scale folds that have modified earlier formed structures. The final deformation episode is manifested by the presence of northwest- to northeast-striking, oblique-slip normal faults that exhibit both left- and right-lateral strike-slip components.

DECLARATION

I, the undersigned, declare that this thesis is my own, unaided work. It is being submitted for the degree of Doctor of Philosophy in the University of the Witwatersrand, Johannesburg. It has not been submitted to any other University for the purpose of obtaining a degree.



E.A. KOHLER



22/11/1994

*To Jennifer,
for reasons beyond listing*

Omne ignotum pro magnifico.

- Tacitus

*The most incomprehensible thing about the world
is that it is comprehensible.*

- Einstein

c
c

ACKNOWLEDGEMENTS

The writer is indebted to the following persons and organizations:

Firstly, the writer would like to thank Dr. C. Frick, Director of the Council for Geoscience, Geological Survey of South Africa, and Prof. C.R. Anhaeusser, Director of the Economic Geology Research Unit, University of the Witwatersrand, for the opportunity to undertake this project.

A. Schoeman, J. Eisenbroek, H. Cloete and J. Trojak of the Geological Survey of South Africa, and V. Govender of the University of the Witwatersrand, carried out the XRF geochemical analyses. The assistance of the staff of the Schonland Research Centre for Nuclear Science, especially Dr. R.J. Hart, in the analysis of samples by INAA is gratefully acknowledged. Dr. F.M. Meyer of the University of the Witwatersrand is thanked for his invaluable assistance with respect to the analytical aspects of this thesis.

Dr. E.A. Retief is thanked for his advice and guidance while the writer was working in the laboratories of the Department of Earth, Marine and Atmospheric Sciences and Technology (EMATEK) of the Council for Science and Industrial Research. The writer is indebted to Prof. S.A. Bowring and Dr. C. Isachsen of the Department of Earth, Atmospheric and Planetary Sciences, Massachusetts Institute of Technology, for carrying out the U-Pb isotopic analyses.

The thesis benefitted from discussions with, and technical assistance from, the following: Profs. D.R. Lowe, K. Suwa, L.J. Robb and J.R. McIver; Drs. T. Wallmach, T.O. Reimer, B.M. Eglington, T.J. Molyneux, F. Walraven, R.L. Gibson, M. Cloete, C. Heubeck, A.F.M. Kisters and G. De Kock; Messrs. P.D. Harris, P. Harrison, J.H.W. Ward, R. Le Roux, C. Meyer, V.J. King and N. Niemand.

The writer also wishes to express his gratitude to Prof. R. Crewe of the Department of Zoology at the University of the Witwatersrand for permission to use the Pullen Farm house during the initial period of fieldwork, and the owners of the various farms mapped, in particular Messers. D. Van Graan and L. Von Johnstone, for access to their properties and hospitality.

My field assistant, Mr. W. Mhlongo, is thanked for his help during the period of fieldwork. The thin sections were prepared by Messers. A. Mathebula, J. Molotsi and M.M. Lekotcko. Thanks are also due to Mr. M.D. Kohler for providing photographic services.

Anglo American Prospecting Services (Pty.) Ltd., General Mining, Metals and Minerals Ltd. (GENMIN) and Phelps Dodge Mining Ltd. provided borehole core and unpublished company information on various aspects of the geology in the region. Mr. J.H.R. Raubenheimer of GENMIN is thanked for permission to conduct an underground visit to the Three Sisters Gold Mine.

Finally, special thanks are due to my fiancée, Jennifer Rodel, for moral support during the course of this project.

CONTENTS

VIII

	Page
ABSTRACT	I
DECLARATION	III
DEDICATION	IV
ACKNOWLEDGEMENTS	VI
CONTENTS	VIII
LIST OF TABLES	XIV
LIST OF FIGURES	XVI
1. INTRODUCTION	1
1.1 General statement and location of the study area	1
1.2 Objectives of the study	1
1.3 Topography and vegetation	3
1.4 Summary of previous work	6
1.5 Methods of investigation	7
1.5.1 Fieldwork	7
1.5.2 Petrography and X-ray diffraction analysis	8
1.5.3 X-ray fluorescence spectrometry and instrumental neutron activation analysis	8
1.5.4 Isotopic studies	10
2. GEOLOGICAL REVIEW	11
2.1 Introduction	11
2.2 Nature of the earliest crust	11
2.3 Supracrustal rocks: the Barberton Supergroup	11
2.4 Granitoid rocks	15
2.5 Geochronology	16
2.5.1 Barberton Supergroup	16
2.5.2 Granitoid rocks	20

	Page	
2.6	Tectonic evolution	21
2.7	Alteration	22
3. ONVERWACHT GROUP		24
3.1	Introduction	24
3.2	Basic and ultrabasic schists	25
3.3	Amphibolites	27
3.4	Serpentinities	28
3.5	Silicic schists	28
3.6	Metagabbros	29
3.7	Metapyroxenites	30
3.8	Geochemistry	30
3.9	Metamorphism - metasomatism	35
4. FIG TREE GROUP		38
4.1	Introduction	38
4.2	Sheba and Belvue Road Formations	39
4.2.1	Shales and slates	39
4.2.2	Metagreywackes	43
4.2.3	Banded iron-formations and cherts	45
4.2.4	Silicic and intermediate metavolcanic-volcaniclastic rocks	48
4.2.5	Depositional setting	51
4.3	Bien Venue Formation	52
4.3.1	Quartz-muscovite schists	54
4.3.2	Biotite-oligoclase schists	60
4.3.3	Chlorite schists, talc schists and serpentinites	62
4.3.4	Cherts and cherty dolomites	63
4.3.5	Phyllites and slates	66

	Page	
4.3.6	Stentor barite deposit	66
4.3.7	Bien Venue massive sulphide deposit	68
4.3.8	Quartz \pm tourmaline veins	69
4.3.9	Depositional setting	70
5.	GEOCHEMISTRY AND GEOCHRONOLOGY OF THE BIEN VENUE FORMATION	76
5.1	Introduction	76
5.2	Quartz-muscovite schists	77
5.2.1	Metamorphism - metasomatism	81
5.2.1.1	Prograde effects	83
5.2.1.2	Retrograde effects	89
5.2.2	Element distribution patterns	89
5.2.2.1	Low field-strength elements	90
5.2.2.2	High field-strength elements	95
5.2.3	Comparison with rocks of the Theespruit Formation	106
5.3	Biotite-oligoclase schists	111
5.3.1	Comparison with rocks of the Schoongezicht Formation	113
5.4	Chlorite schists	114
5.5	Palaeotectonic setting	118
5.5.1	The role of plate tectonics in the evolution of the Earth's early crust	118
5.5.2	Geotectonic setting of modern silicic magmatism	121
5.5.3	Discrimination and interpretation	122
5.6	Geochronology	129
5.6.1	Analytical method	129
5.6.2	Zircon description	132
5.6.3	Results and interpretation	133

	Page
6. ASSESSMENT OF THE BASE-METAL ORE POTENTIAL OF THE BIEN VENUE FORMATION AND OTHER SILICIC UNITS OF THE BARBERTON SUPERGROUP	137
6.1 Introduction	137
6.2 Classification and interpretation	138
6.3 Discussion	144
7. MOODIES GROUP	146
7.1 Introduction	146
7.2 Conglomerates	147
7.3 Quartzites and siltstones	150
7.4 Depositional setting	152
8. GRANITOID ROCKS AND LATE-STAGE INTRUSIVES	154
8.1 Introduction	154
8.2 Description of the Nelspruit batholith	154
8.3 Stentor pluton	157
8.3.1 Field characteristics	157
8.3.2 Petrography	163
8.3.3 Chemistry	166
8.3.3.1 Major elements	169
8.3.3.2 Trace elements	176
8.3.3.3 Modelling	179
8.3.4 Comparison with the Hebron and Berlin plutons	186
8.4 Nelspruit Migmatite and Gneiss Terrane	189
8.4.1 Field characteristics	189
8.4.2 Petrography	191
8.4.3 Chemistry	192
8.4.3.1 Major elements	192

	Page
8.4.3.2	Trace elements 198
8.5	Late-stage intrusive rocks 200
9. STRUCTURAL GEOLOGY	202
9.1	Introduction 202
9.2	Description of structural elements 204
9.2.1	D_{main} 204
9.2.1.1	F_{main} 204
9.2.1.1.1	Big Buffalo Syncline 204
9.2.1.1.2	Hlambanyathi Syncline 206
9.2.1.1.3	Amo Syncline 208
9.2.1.1.4	Igwalagwala Syncline 208
9.2.1.1.5	Lily West and Lily East Synclines 209
9.2.1.1.6	Three Sisters Syncline 212
9.2.1.1.7	American Syncline 213
9.2.1.1.8	Louieville Antiform 214
9.2.1.1.9	Strathmore Anticline 214
9.2.1.1.10	Koedoe Anticline 215
9.2.1.1.11	Koedoe and Scotsman Blocks 216
9.2.1.2	B_{main} 218
9.2.1.2.1	American Fault 218
9.2.1.2.2	Barite Fault 220
9.2.1.2.3	Southern Fault 220
9.2.1.2.4	Koedoe Fault 221
9.2.1.2.5	Igwalagwala Fault 223
9.2.1.2.6	Mac Mac Fault 224
9.2.1.2.7	Barbrook Fault 226
9.2.1.2.8	Inyoka Fault 227
9.2.1.2.9	Overton Fault 228

		Page
9.2.1.2.10	Stentor Fault	230
9.2.1.2.11	Revolver Fault	233
9.2.1.2.12	Scotsman Fault	238
9.2.1.2.13	Adananda Fault	242
9.2.1.2.14	Ardonachi Fault	244
9.2.1.3	Other D_{main} structures	246
9.2.1.3.1	Structure of the Eldorado Mine area	246
9.2.1.3.2	Structure of the Spago and Sussex Mines areas	247
9.2.2	D_{disipic}	251
9.2.2.1	Stentor Antiform	251
9.2.2.2	Bien Venue Synform	254
9.2.2.3	Strain analysis	258
9.2.3	D_{final}	261
9.3	Discussion and interpretation	261
9.3.1	D_{main}	261
9.3.2	D_{disipic}	267
9.3.3	D_{final}	271
10. SUMMARY AND CONCLUSIONS		272
10.1	Onverwacht Group	272
10.2	Fig Tree Group	273
10.3	Moodies Group	275
10.4	Granitoid rocks and late-stage intrusives	275
10.5	Structure	276
10.6	Economic geology	277
11. REFERENCES		278

LIST OF TABLES

	Page
2.1 Selected isotopic ages for units of the Barberton Supergroup	17
2.2 Selected isotopic ages for granitoid rocks surrounding the BGB	18
3.1 Major and trace element compositions of some rock types correlated with the Onverwacht Group in the study area	31
4.1 Chemical analyses of shales and slates from the Sheba and Belvue Road Formations	41
4.2 Chemical analyses of metagreywackes from the Sheba Formation	46
4.3 Chemical analyses of silicic and intermediate metavolcanic-volcaniclastic rocks from the Belvue Road Formation	50
5.1 Chemical data for quartz-muscovite schists from the Bien Venue Formation	78
5.2 Calculated mass and volume changes for the quartz-muscovite schists	104
5.3 Chemical data for silicic metavolcanic-volcaniclastic rocks from the Theespruit Formation	107
5.4 Chemical data for biotite-oligoclase schists from the Bien Venue Formation	112
5.5 Chemical data for metavolcanic-volcaniclastic rocks from the Schoongezicht Formation	115
5.6 Chemical data for chlorite schists from the Bien Venue Formation	117
5.7 U-Pb isotope data for sample BVR4	130
6.1 Comparison of the geochemistry of silicic metavolcanic rocks of the Barberton and Murchison greenstone belts with mineralized and barren successions in the Superior Province, Canada	139
8.1 Major and trace element data obtained from XRF analysis of samples from the Stentor pluton	167
8.2 Trace element data obtained from INAA of selected samples from the Stentor pluton	169
8.3 Mineral - liquid partition coefficients used in model calculations	183
8.4 Results of crystallization modelling for the Stentor pluton	184

	Page
8.5 Averaged major element compositions and compositional ranges of the Stentor, Hebron and Berlin plutons	187
8.6 Major and trace element data obtained from XRF analysis of gneisses from the Nelspruit Migmatite and Gneiss Terrane	193
8.7 Trace element data obtained from INAA of selected samples of gneiss from the Nelspruit Migmatite and Gneiss Terrane	195
9.1 Summary of structural elements encountered in the study area	204
9.2 Trace element analysis of an enigmatic chert \pm carbonate lithology outcropping along the Mac Mac Fault on Scotsman 258 JU	225
9.3 Strain data for deformed clasts within the Stentor Antiform - Bien Venue Synform pair	259

LIST OF FIGURES

	Page
1.1 Geological sketch map showing the locality and extent of the region investigated.	2
1.2 SPOT image of the northeastern sector of the BML.	4
1.3 Scenic views of the study area.	5
1.4 Geological map of the granitoid-greenstone terrane in the vicinity of Three Sisters.	Back Cover
2.1 Simplified geological map of the BML.	12
2.2 Generalized stratigraphic column of the Barberton Supergroup.	13
3.1 Features of some lithologies correlated with the Onverwacht Group.	26
3.2 Ternary $Al_2O_3 - (FeO + Fe_2O_3 + TiO_2) - MgO$ plot of Onverwacht Group basic and ultrabasic metavolcanic rocks in the study area, and comparison with fields for least-altered Onverwacht rocks from the southwestern parts of the BGB.	34
4.1 Plots of Cr and Ni versus Zr for shales and slates of the Fig Tree Group in the study area and comparison with Moodies Group shales.	42
4.2 Structures and textural characteristics observed in metasediments of the Sheba and Belvue Road Formations.	44
4.3 Distribution of the Bien Venue Formation and location of the type area.	53
4.4 Mesoscopic and microscopic features of quartz-muscovite schists.	56
4.5 Microscopic and mesoscopic features of biotite-oligoclase schists.	61
4.6 Breccia unit in grey and white banded chert.	64
4.7 Dolomite - chert lithology.	66
4.8 Crudely banded quartz-tourmaline veins in quartz-muscovite schist.	69
5.1 $Zr/TiO_2 - Nb/Y$ discrimination diagram for metavolcanic- volcaniclastic rocks of the Bien Venue Formation.	80
5.2 Envelope of chondrite-normalised REE data for the quartz-muscovite schists.	81

	Page
5.3 A'FK plot for quartz-muscovite schists.	82
5.4 Schematic phase diagrams of $\log a\text{Na}^+ / a\text{H}^+$ versus $\log a\text{K}^+ / a\text{H}^+$ and $\log a\text{Fe}^{2+} / a(\text{H}^+)^2$ versus $\log a\text{K}^+ / a\text{H}^+$ showing the relative stability fields of the main metasomatic transformations that are inferred to have occurred during prograde alteration of the quartz-muscovite schists.	84
5.5 P-T grid showing the various equilibria that have been used to constrain the conditions of prograde alteration of quartz-muscovite schists in the Three Sisters area.	87
5.6 Plots of Na_2O and CaO versus K_2O for quartz-muscovite schists.	91
5.7 LFSE plots for the quartz-muscovite schists showing the extent to which muscovite controls Rb, Cs, Ba and Sr distributions.	92
5.8 Schematic diagrams illustrating the effect of allochemical / allovolumetric alteration on immobile element abundances in chemically homogeneous and heterogeneous precursor systems.	96
5.9 Selected HFSE variation diagrams for the quartz-muscovite schists.	98
5.10 Schematic diagram showing the relationship between alteration arrays and primary igneous trends.	101
5.11 Plot of Al_2O_3 against Zr for the samples of quartz-muscovite schist, and comparison with the igneous fractionation curve defined by Cenozoic calc-alkaline volcanic rocks.	102
5.12 Ternary Ba - Rb - Sr, Ti - Cr - V and Y - Nb - Zr plots illustrating some compositional differences between quartz-muscovite schists from the Bien Venue Formation and silicic metavolcanic-volcaniclastic rocks from the Theespruit Formation.	109
5.13 Chondrite-normalized REE patterns for silicic metavolcanic rocks from the Theespruit Formation and comparison with the compositional envelope of quartz-muscovite schists from the Bien Venue Formation.	110
5.14 Chondrite-normalized REE profiles for biotite-oligoclase schists.	113
5.15 Chondrite-normalised REE abundance patterns of Schoongezicht Formation metavolcaniclastic rocks and comparison with the compositional envelope of biotite-oligoclase schists from the Bien Venue Formation.	116

	Page
5.16 Chondrite-normalised REE patterns for chlorite schists.	119
5.17 Chemical discriminant diagrams showing the geotectonic affinities of rocks from the Bien Venue Formation.	124
5.18 Primordial-mantle-normalized trace element diagrams for schists of the Bien Venue Formation.	126
5.19 Photomicrographs of zircons from sample BVR4.	132
5.20 Concordia diagram showing U-Pb data for all zircon fractions analysed.	134
7.1 Features preserved in rocks of the Moodies Group.	148
8.1 Simplified revised map of the north western sector of the BML showing the distribution of the three main phases of the Nelspruit batholith.	155
8.2 Geological map of the granitoid terrane north of the BGB.	158
8.3 Mesoscopic features observed in rocks of the Stentor pluton.	159
8.4 Lower hemisphere equal area projection of poles to S_4 foliation in the Stentor pluton.	161
8.5 K-feldspar - quartz - plagioclase classification plot for samples from the Stentor pluton.	164
8.6 Plot of mol fraction $Al_2O_3 / (Na_2O + K_2O)$ against $Al_2O_3 / (CaO + Na_2O + K_2O)$ for samples from the Stentor pluton.	170
8.7 $K_2O - Na_2O$ plot for samples from the Stentor pluton.	171
8.8 CIPW normative albite - anorthite - orthoclase plot for samples from the Stentor pluton.	172
8.9 Classification of samples from the Stentor pluton based on the R_1R_2 plot.	172
8.10 CIPW normative compositions of samples from the Stentor pluton projected onto the anhydrous base of the albite - quartz - orthoclase - H_2O tetrahedron.	173
8.11 Harker variation diagrams for selected major elements in samples from the Stentor pluton.	174
8.12 Ternary Ba - Rb - Sr plot for samples from the Stentor pluton.	176

	Page
8.13 Harker variation diagrams for Ba, Rb, Sr and Zr in samples from the Stentor pluton.	177
8.14 Chondrite-normalized distribution of the REE's in samples from the Stentor pluton.	178
8.15 Plots of Ba/Rb and Sr/Rb against Zr for samples from the Stentor pluton.	181
8.16 Distribution of Ba, Rb and Sr in samples from the Stentor pluton and comparison with solid phase and residual liquid compositions predicted by the fractional and equilibrium crystallization models for 1 - 90 % crystallization.	185
8.17 Comparison of the averaged trace element compositions of samples from the Stentor, Hebron and Berlin plutons, normalized against the average composition of the Nelspruit batholith and chondrite.	188
8.18 Features observed in rocks of the Nelspruit Migmatite and Gneiss Terrane.	190
8.19 Plot of K_2O against Na_2O for gneissic samples from the Nelspruit Migmatite and Gneiss Terrane.	196
8.20 Plot of mol fraction $Al_2O_3 / (Na_2O + K_2O)$ versus $Al_2O_3 / (CaO + Na_2O + K_2O)$ for gneissic samples from the Nelspruit Migmatite and Gneiss Terrane.	197
8.21 Normative albite - anorthite - orthoclase classification plot for samples from the Nelspruit Migmatite and Gneiss Terrane.	197
8.22 R_1R_2 plot for gneisses of the Nelspruit Migmatite and Gneiss Terrane.	198
8.23 Chondrite-normalized REE distribution profiles for gneisses of the Nelspruit Migmatite and Gneiss Terrane.	199
8.24 Diabase dyke intruding homogeneous gneiss of the Nelspruit Migmatite and Gneiss Terrane.	200
9.1 Sketch map showing the distribution of folds and faults in the study area.	203
9.2 Lower hemisphere equal area projections summarizing structural data for F_m folds.	205

	Page
9.3 View of the Hlambanyathi Syncline looking west to east across the Amo Fault.	207
9.4 Structural features of the Lily East Syncline.	211
9.5 Lower hemisphere equal area projections summarizing structural data for the Koedoe and Scotsman Blocks.	217
9.6 Structural features of rocks outcropping along the Koedoe Fault.	222
9.7 Strongly sheared and banded appearance of quartz-carbonate rock outcropping along the Mac Mac Fault.	224
9.8 Structural features of rocks within the Overton Fault zone.	229
9.9 Structural features of rocks within the Revolver Fault zone.	235
9.10 View, looking north-northeast from the Holnekt trigonometrical beacon showing the principal structures within the Revolver Creek Valley.	239
9.11 Structural features of rocks along the Scotsman Fault.	241
9.12 View, looking east from the middle of the Three Sisters peaks, showing the position of the Adamanda Fault along the northwestern slope of the easternmost of the Three Sisters peaks.	243
9.13 Polished slab showing strongly flattened and brecciated pebbles in sheared conglomerate along the Ardonachi Fault.	244
9.14 Structural features of rocks outcropping in the vicinity of the Spago and Sussex Mines.	248
9.15 Schematic three-dimensional representation of the Stentor Antiform - Bien Venue Synform pair, with sketch maps of S_d foliation, and L_d stretching lineation trajectories.	252
9.16 Lower hemisphere equal area projections of poles to S_d and L_d stretching lineations in the Stentor Antiform.	253
9.17 Structural features in rocks of the Bien Venue Synform.	255
9.18 Results of strain analyses on deformed clasts within the Stentor Antiform - Bien Venue Synform pair.	260
9.19 Schematic diagram illustrating a possible mechanism for late-stage inflation of a diapir.	270

1. INTRODUCTION

1.1 General statement and location of the study area

The Barberton Mountain Land (BML) - embracing the supracrustal successions of the Barberton greenstone belt (BGB) and surrounding silicic plutonites in the Eastern Transvaal and Swaziland - comprises an internationally renowned Archaean granitoid-greenstone terrane that has provided important insights into the evolution of such sequences world-wide (e.g. Viljoen and Viljoen 1969c; Anhaeusser *et al.*, 1969; Anhaeusser, 1973; Anhaeusser and Robb, 1981; De Wit *et al.*, 1987b; De Wit and Hart, 1993). However, despite considerable scientific research during the past 30 years, large portions of the BML, especially in its eastern and northeastern regions, remain poorly mapped, and not well understood. This study was thus initiated with a view to investigating the stratigraphy and structure of the granitoid-greenstone terrane centred around Three Sisters in the northeastern sector of the BML (Figure 1.1) .

1.2 Objectives of the study

Four principal objectives were defined at the outset of this project: (1) to produce a detailed geological map of the study area; (2) to give a comprehensive account of the various rock types encountered in the area and to classify these lithologies according to the stratigraphic nomenclature of the Barberton Supergroup¹, as defined by the South African Committee for Stratigraphy (SACS, 1980); (3) to investigate the geochemical characteristics of selected lithologies; and (4) to undertake a structural analysis of the region.

¹ The South African Committee for Stratigraphy recently decided that the term "sequence", as defined in the 1980 SACS publication, should be replaced by "supergroup".

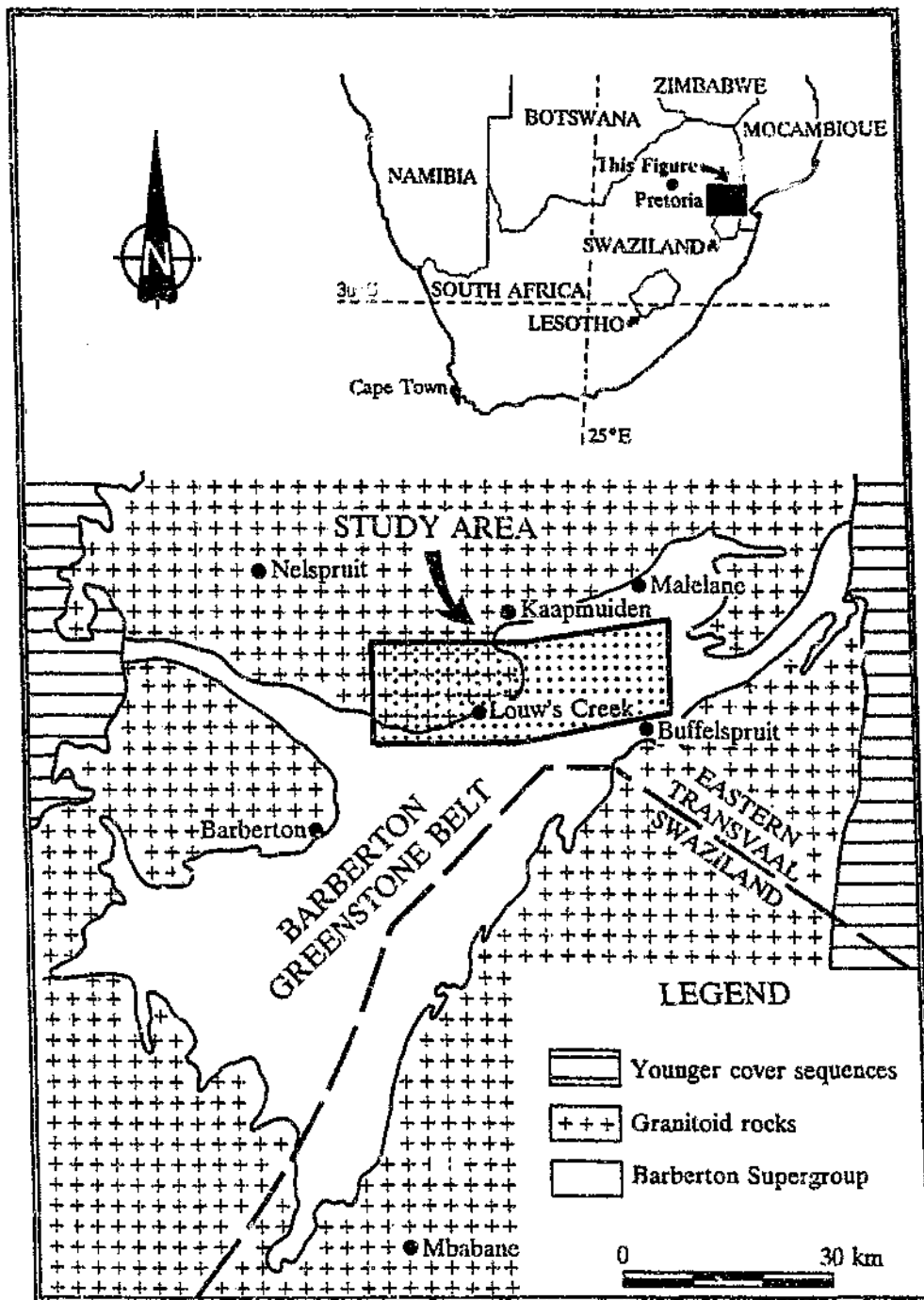


Figure 1.1 Geological sketch map showing the locality and extent of the region investigated.

1.3 Topography and vegetation

Topography in the mapped area is dominated by a series of rugged, northeast-trending mountain ranges, the most prominent of which is known as the Three Sisters Range (Figure 1.2). This range derives its name from three peaks situated ~7 km east of the village of Louw's Creek, and attains a maximum elevation of ~1200 m above sea-level (Figure 1.3A). The region north and northeast of the Three Sisters Range is characterised by numerous steep-sided hills and ridges, and is drained by non-perennial streams that flow northwards into the Crocodile River. The area west and northwest of Three Sisters exhibits more subdued topography, descending gradually into a broad, extensively cultivated valley drained by the Kaap River. The confluence of the Kaap and Crocodile Rivers lies ~2 km west of the village of Kaapmuiden. Whale-back granitoid domes build the Krokodilpoort Range to the west of the Kaap River. The Lily Ridge, situated to the south of Three Sisters, is separated from the latter by the deeply incised valley of the Revolver Creek which forms a major tributary of the Kaap River (Figure 1.3B).

Relief in the eastern and southeastern parts of the area is dominated by Kaalrug Ridge and the Makhonjwa and Big Buffalo Ranges (Figure 1.3C). The Mhlambanyathi River, which drains the valley between the Makhonjwa Range and the eastern parts of the Three Sisters Range, flows eastward for much of its course, but to the northeast of the Buffelspruit township, the river flows southwards, finally merging with the Mlomathi River (Figure 1.3D).

The indigenous vegetation consists mainly of grass, scrub and dense bush which becomes impenetrable near watercourses. Agricultural activities are centred around the cultivation of subtropical fruits, most of which are grown on extensive alluvial terraces flanking the Kaap, Crocodile and Mlomathi Rivers. The rugged central and southeastern portions of the region are generally unsuitable for cultivation or stock farming and have

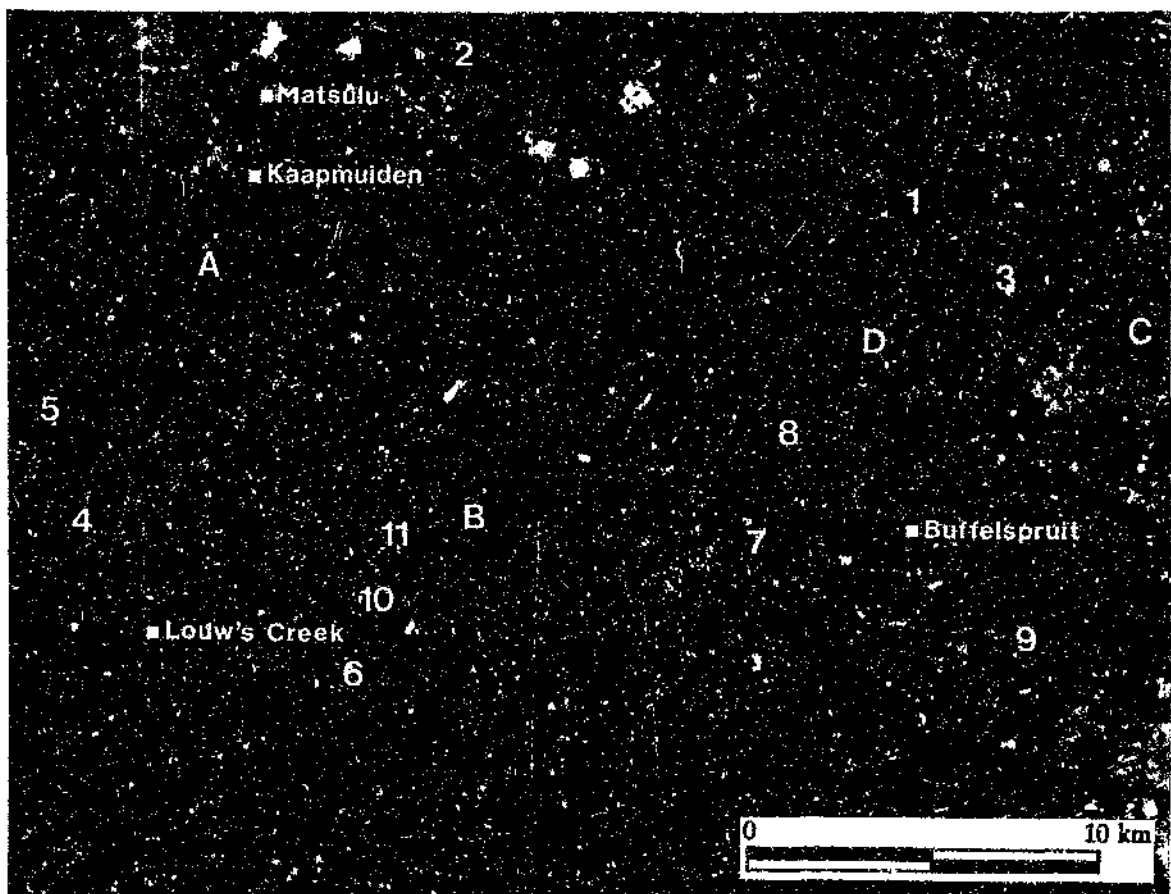
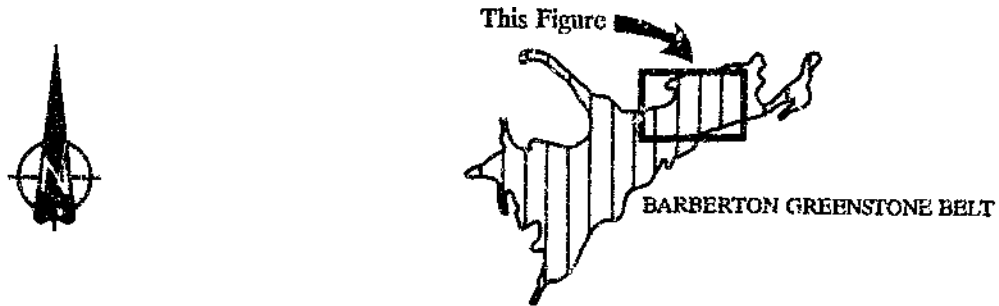


Figure 1.2 SPOT image (29 May 1992; band 321) of the northeastern sector of the BML showing the principal topographic features in the study area (reproduced with permission of the Satellite Applications Centre, MIKOMtek, Council for Science and Industrial Research). Explanation: 1 - Big Buffalo Range; 2 - Crocodile River; 3 - Kaalrug Ridge; 4 - Kaap River; 5 - Krokodilpoort Range; 6 - Lily Ridge; 7 - Makhonjwa Range; 8 - Mhlambanyathi River; 9 - Mlomathi River; 10 - Revolver Creek; 11 - Three Sisters Range. The letters A - D mark the viewpoints of photographs shown in Figure 1.3.

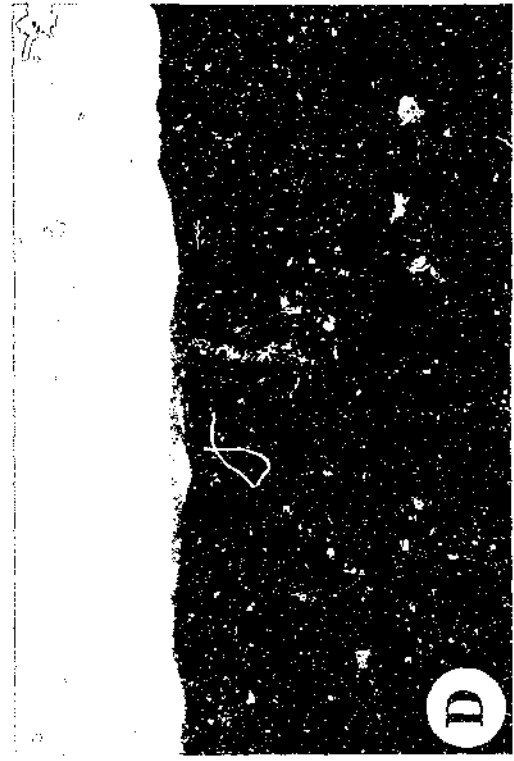
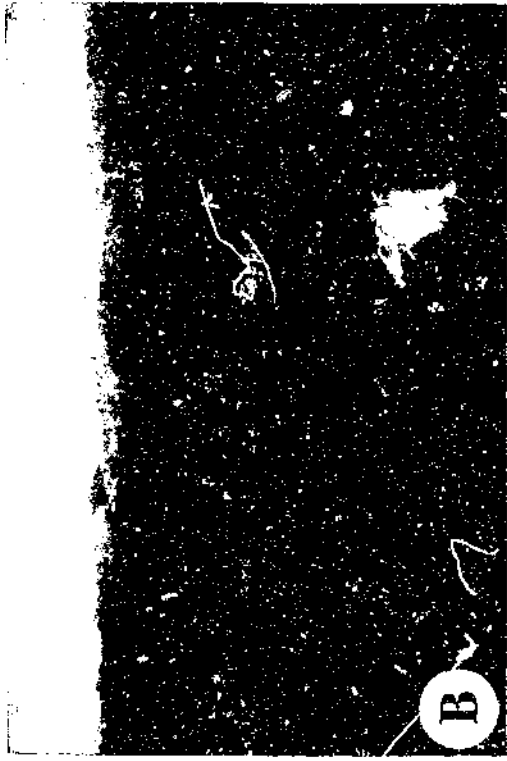


Figure 1.3 Scenic views of the study area (see Figure 1.2 for viewpoints):

(A) General view across the granitoid-greenstone terrane in the northeastern sector of the BML looking south from Pettygrew's Nek along the Kaapmuiden - Louw's Creek - Barberton road. The prominent mountain in the centre of the photograph is the westernmost of the Three Sisters peaks, on which resistant silicic metavolcanic and rhyolitic rocks of the Fig Tree and Moodies Groups crop out. The gently undulating terrane in the foreground is underlain by basic and ultrabasic assemblages of the Onverwacht Group and granitoids of the Stentor pluton.

(B) View of the Lily Ridge and the Revolver Creek Valley looking west from Three Sisters Radio Station. The slimes dump marks the position of the Three Sisters Gold Mine, the most important, and until recently the only active, gold producer in the region.

(C) View, looking west-northwest from the Richershoek turn-off along the Malelane - Jeppes Reef road, showing the precipitous slopes of Kaalrug Ridge. The hills in the middleground constitute the eastern extension of the Makhonjwa Range. Both mountains consist of Moodies Group quartzites and conglomerates, and are separated by highly decomposed argillites of the Fig Tree Group which crop out on the bush-clad spurs at the foot of Kaalrug. The flat, cultivated country in the foreground forms part of the Mlomathi River Valley, and is underlain by lithologies of the Onverwacht Group.

(D) Valley of the Mhlambanyathi River as seen looking west from Kaalrug, part of which occupies the foreground. Three Sisters Range to the north, Makhonjwa Range to the south.

either been left in their natural state or are utilized for game farming. Bluegum plantations cover the southern slopes of the Three Sisters Range and the western parts of the Makhonjwa Range.

Geological exposures throughout the region are generally fairly good, but deteriorate in valleys which contain extensive veneers of unconsolidated Quaternary alluvium and colluvium. Nevertheless, river gullies in these areas usually provide adequate exposure of the underlying Archaean formations for regional mapping purposes.

1.4 Summary of previous work

The first comprehensive investigation dealing with the geology of the region under review was carried out by A.L. Hall of the Geological Survey of South Africa, who mapped the area on a scale of ~1:150 000 as part of a regional study encompassing the entire BGB (Hall, 1918). The region was subsequently remapped on a scale of 1:50 000 by other officers of the Geological Survey during the period 1938 - 1940, the results of which are presented in Visser *et al.* (1956). Further regional-scale mapping of the extreme eastern part of the study area was also carried by the Geological Survey during 1953 and 1960, but was never published. Reconnaissance mapping along the northern boundary of the area led Viljoen and Viljoen (1970) to correlate the silicic schists that crop out to the north of Three Sisters with the Theespruit Formation of the Onverwacht Group. The geology of the region west of Louw's Creek is described by Anhaeusser (1963).

Fripp *et al.* (1980) conducted a regional structural investigation along the north-central flank of the BGB. Gravity and DC resistivity work covering the entire BML has been carried out by Darracott (1975) and De Beer *et al.* (1988).

Brief accounts of the granitoid terrane immediately north of the BGB are provided by Hall (1918), Visser *et al.* (1956), Viljoen (1963) and Anhaeusser (1963, 1969, 1972). A more detailed mapping and geochemical study of the rocks in this region was carried out by Robb *et al.* (1983), who defined a large body of trondhjemitic composition known as the Stentor pluton. Geochronological studies of the Stentor pluton have been undertaken by Barton *et al.* (1983), Tegtmeyer and Kröner (1987) and Kamo and Davis (1994).

Comprehensive accounts of the geological setting and mining history of the various mineral deposits in the area are provided by Viljoen and Viljoen (1969g), Groeneveld (1973), Widenbar (1976), Reimer (1980), Viljoen *et al.* (1986), Harwood and Murphy (1988) and Murphy (1990). Mineralogical, metallurgical and fluid inclusion studies of the auriferous ores at the Three Sisters Mine have been carried out by De Villiers (1957), Gay (1964), Schweigart and Liebenberg (1966), Liebenberg (1972) and De Ronde *et al.* (1991b, 1992). Exploration for, and re-evaluation of, mineral deposits has been conducted by several companies, including General Mining, Metals and Minerals Ltd., Phelps Dodge Mining Ltd. and Anglo American Prospecting Services (Pty.) Ltd.

Preliminary conclusions which have emerged from the research described in this thesis are presented by Kohler *et al.* (1992, 1993).

1.5 Methods of investigation

1.5.1 Fieldwork

Detailed surface mapping of the study area on a scale of 1:10 000 was carried out by the writer with the aid of aerial photographs over a total of 15 months from March to December 1990 and again from March to August 1993. Initially it was decided to restrict the mapping programme to that portion of the BGB north and east of Louw's

Creek. However, as fieldwork progressed, it became apparent that the granitoid terrane immediately west and northwest of Louw's Creek also required remapping, and this region was included in the study. The total area investigated covers ~575 km², of which roughly half forms part of the BGB. Copies of two maps produced during the period of fieldwork are shown in Figures 1.4 (foldout in back cover) and 8.2 (page 158) .

In addition, the writer also undertook several trips to examine the geology of the western and southwestern parts of the BGB, as well as portions of the Nelspruit batholith to the north of Nelspruit. Several representative samples of Theespruit and Schoongezicht Formation lithologies were collected to facilitate geochemical comparison with rocks in the study area.

1.5.2 Petrography and X-ray diffraction analysis

Reflected and transmitted light microscopy was used to examine ~420 thin sections in order to document the mineralogical and textural characteristics of all lithologies in the region. Plagioclase compositions were determined through the Michel-Lévy method (Michel-Lévy, 1877) or with the aid of a universal stage. X-ray diffraction (XRD) identification techniques were applied to ~60 samples in order to confirm the presence of minerals which could not be positively identified under the microscope.

1.5.3 X-ray fluorescence spectrometry and instrumental neutron activation analysis

Major element concentrations in ~110 samples have been determined by means of standard X-ray fluorescence (XRF) techniques on fused glass discs (Norrish and Hutton, 1969) in the laboratories of the Council for Geoscience, Geological Survey of South Africa, and at the Department of Geology, University of the Witwatersrand, using Phillips PW-1480 and PW-1400 sequential X-ray spectrometers. Pressed powder briquettes were used for the Na₂O analyses carried out at the Geological Survey. H₂O

and H_2O^+ were determined by infrared adsorption on LECO RMC-100 and LECO RC-412 moisture analysers at the Geological Survey. A LECO CS-244 Infrared Absorbtion Spectrometer was used to determine CO_2 content. International standards were used for all calibrations. Routine precision of the major element analyses is better than 1 - 5 % at reasonable concentration levels. The sample localities are shown in Figures 1.4 and 8.2.

Ba, Rb, Sr, Y, Nb, Zr, Ga, Zn, Cu, Ni, Pb, V and Cr concentrations were also determined by standard XRF procedures on pressed powder briquettes at the Geological Survey using a Phillips PW-1400 spectrometer. Detection limits are ~5 - 10 ppm for Ba, ~2 - 5 ppm for Rb, Sr, Pb, Y, Nb, Zr, V, Cr and Cu, and ~1 ppm for Ga, Zn and Ni. Analytical uncertainty is estimated at less than 10 - 15% for Nb and Cr, and less than 5 - 10% for all other trace elements.

Data for the rare-earth elements (REE) and nine other trace elements (Cs, U, Th, Hf, Ta, Co, Sc, As and Au) have been obtained by the writer using instrumental neutron activation analysis (INAA) techniques, following Fesq *et al.* (1973) and Erasmus *et al.* (1977). Na_2O abundances quartz-muscovite schists of the Bien Venue Formation were also determined by INAA. Following weighing into silica vials and sealing, the samples and five standards were packed into cadmium cans and irradiated for 48 hours in the poolside rack of the SAFARI 1 Oak Ridge-type research reactor at Pelindaba. A multichannel analyzer equipped with Ge and Ge-(Li) detectors, housed at the Schonland Research Centre for Nuclear Science, University of the Witwatersrand, was used to measure the γ -activity of the samples and standards. The REE data have been presented graphically in the form of chondrite-normalized plots using the preferred values of Evensen *et al.* (1978). Eu/Eu^* was calculated by linear interpolation between the normalized Sm and Tb values (i.e. $Eu/Eu^* = 2Eu_N/[Sm_N + Tb_N]$).

1.5.4 Isotopic studies

Conventional U-Pb isotopic studies on zircons extracted from a single sample of quartz-muscovite schist from the Bien Venue Formation have been undertaken by Prof. S.A. Bowring and Dr. C. Fachsen of the Massachusetts Institute of Technology (MIT). Further details are given in Section 5.6.1.

2. GEOLOGICAL REVIEW

2.1 Introduction

The geology of the BML has, for many years, been the subject of considerable debate. The purpose of this chapter is to provide a brief review of this ancient terrane, and to outline the various theories that have been proposed to account for early crustal evolution in the region.

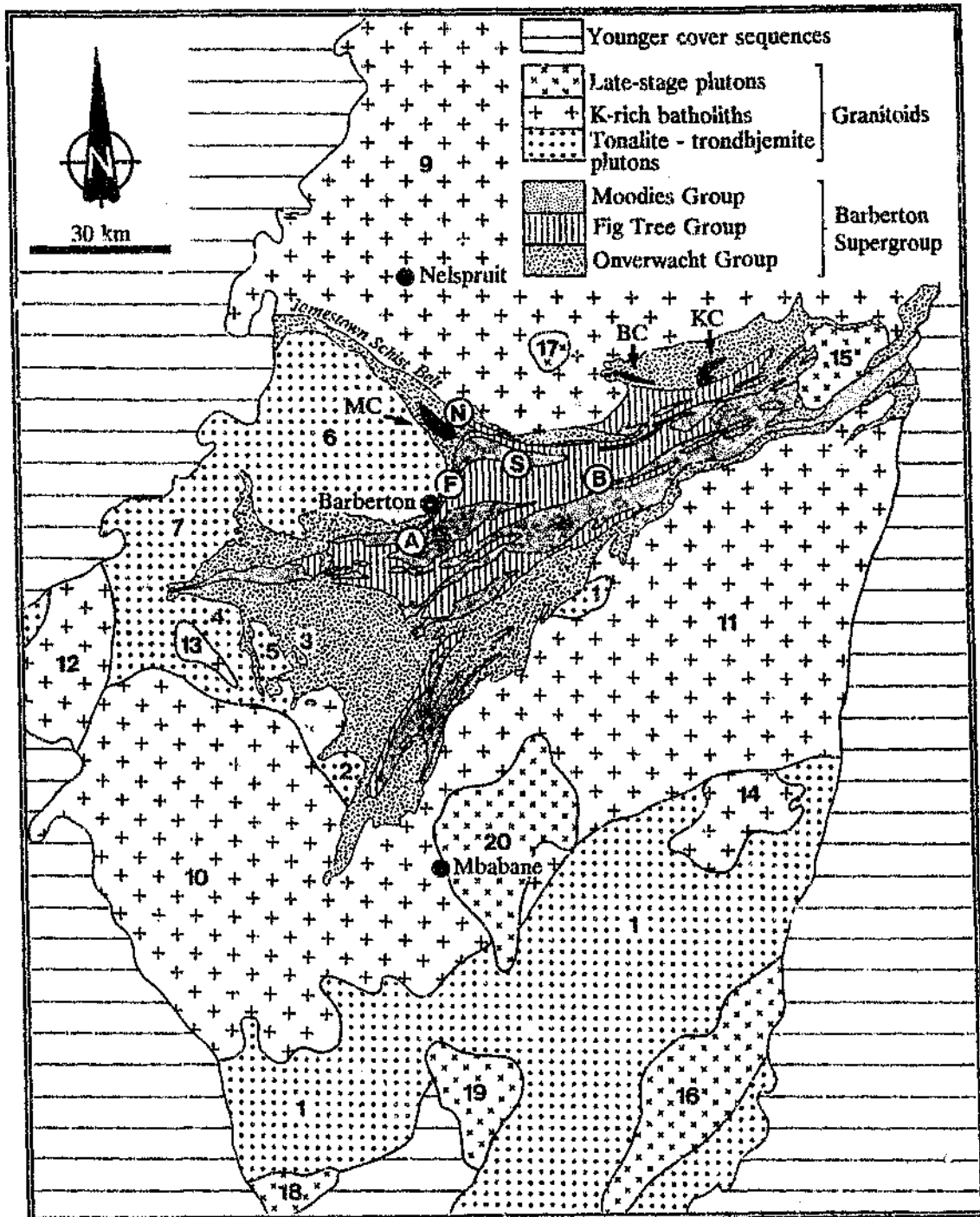
2.2 Nature of the earliest crust

Perhaps the greatest controversy surrounding the geology of the Barberton region concerns the nature of the oldest identifiable rocks. Hunter (1970, 1973, 1974, 1991) and Kröner *et al.* (1989, 1991b) suggested that portions of the Ancient Gneiss Complex (AGC)(Figure 2.1) pre-date the BGB, representing protocontinental crust on which the volcano-sedimentary successions were laid down in response to rifting. The opposing view was taken by Anhaeusser (1973, 1975, 1981a, b, 1984) and Anhaeusser and Robb (1981) who contended that the basal portions of the Barberton Supergroup represent the oldest rocks in the region. According to these workers, the early granitoids, including those of the AGC, were derived from the anatexis of basic and ultrabasic oceanic crust in a primitive tectonic regime.

2.3 Supracrustal rocks: the Barberton Supergroup

Three principal lithostratigraphic units are recognised within the BGB, viz., the Onverwacht, Fig Tree and Moodies Groups (SACS, 1980)(Figure 2.2)². The Onverwacht

² At present, there is no consensus as to the amount of structural repetition within the BGB and the validity of the stratigraphy of the Barberton Supergroup as defined by the South African Committee for Stratigraphy (compare Lowe *et al.*, 1985; Anhaeusser, 1986a; Lowe, 1991; De Wit, 1982; De Wit *et al.*, 1983, 1987b). For the purposes of the present investigation, the writer prefers to follow the original subdivisions and nomenclature recommended by SACS (1980).



30 km

C
G

Figure 2.1 Simplified geological map of the BML (modified after Anhaeusser et al., 1983). Numerals correspond to the following granitoids: 1 - Ancient Gneiss Complex; 2 - Steynsdorp pluton; 3 - Doornhoek pluton; 4 - Stolzburg pluton; 5 - Theespruit pluton; 6 - Kaap Valley pluton; 7 - Nelshoogte pluton; 8 - Dalmein pluton; 9 - Nelspruit batholith; 10 - Mpuluzi batholith; 11 - Piggs Peak batholith; 12 - Heerenveen batholith; 13 - Boesmanskop pluton; 14 - Mliba pluton; 15 - Salisbury Kop pluton; 16 - Sinceni pluton; 17 - Mpageni pluton; 18 - Sicunusa pluton; 19 - Ngwempisi pluton; 20 - Mbabane pluton. The black areas represent the Budd (BC), Koedoe (KC) and Mundt's Concession (MC) ultrabasic intrusive complexes. The circled letters mark the positions of major gold deposits: A - Agnes Mine; F - Fairview Mine; N - New Consort Mine; S - Sheba Mine; B - Barbrook group of mines.

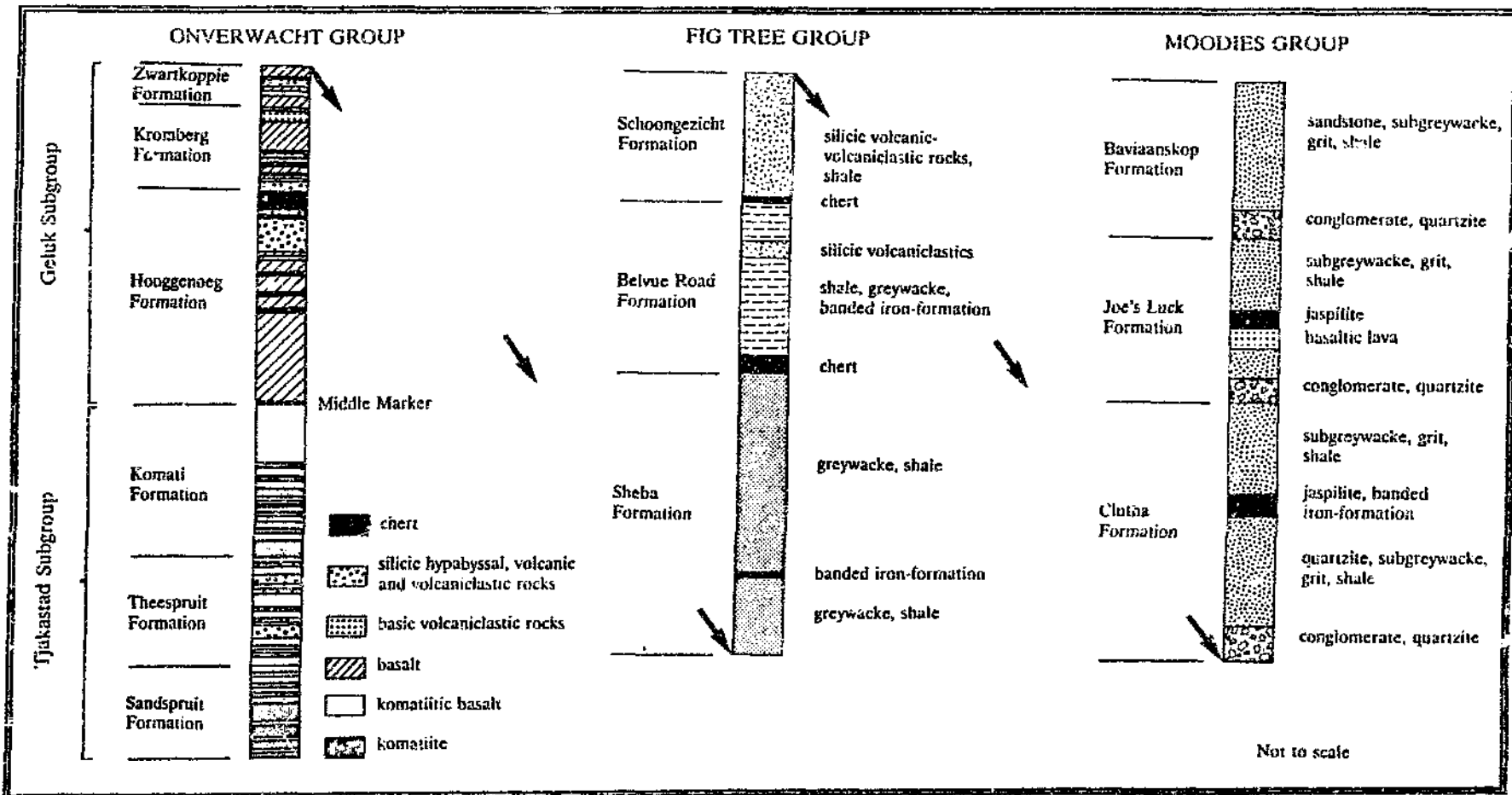


Figure 2.2 Generalized stratigraphic column of the Barberton Supergroup (modified after Anhaeusser, 1973).

Group, at the base, attains an estimated maximum thickness of ~15 km and comprises a grossly inhomogeneous sequence of variably deformed and altered volcanic rocks (Viljoen and Viljoen, 1969a, d, f; Anhaeusser *et al.*, 1983; Lowe, 1991). It is made up of two distinctive subgroups that are separated by a thin chertified sedimentary horizon known as the Middle Marker. The oldest, the Tjakastad Subgroup, is further subdivided into the following units: (1) the Sandspruit Formation, which is dominated by komatiite; (2) the Theespruit Formation, consisting chiefly of basalts and komatiitic basalts with subordinate intercalated silicic pyroclastic and epiclastic rocks; and (3) the Komati Formation, which includes komatiite and komatiitic basalt as well as a number of layered ultrabasic sills. The Geluk Subgroup conformably overlies the Tjakastad Subgroup, but is only well-developed in the southwestern part of the BGB where it consists of (1) the Hooggenoeg Formation, a sequence of massive and pillowed tholeiitic basalts, interbedded cherts and, near the top, dacitic intrusive / extrusive rocks; (2) the Kromberg Formation, which is dominated by tholeiitic basalt lavas and pyroclastic rocks, together with minor chert; and (3) the Zwartkoppie Formation, which consists of a variety of ultrabasic, basic and silicic schists, as well as banded cherty sedimentary rocks.

The overlying Fig Tree Group attains a maximum thickness of about 2100 m and comprises: (1) the Sheba Formation, which contains interbedded, fine- to medium-grained greywacke turbidite, siltstone and banded iron-formation (BIF); (2) the Belvue Road Formation, which includes shales and siltstones with minor greywacke, tuff and BIF; and (3) the Schoongezicht Formation³, which is represented by a succession of silicic volcanoclastic rocks (Condie *et al.*, 1970; Lowe, 1991).

The youngest principal lithostratigraphic unit of the Barberton Supergroup is the Moodies Group. Where best-developed in the north-central parts of the BGB, this group attains a maximum thickness of ~3000 m and comprises three cyclically repetitive clastic

³ Formation name not yet approved by the South African Committee for Stratigraphy.

sedimentary sequences, known in ascending stratigraphic order as the Clutha, Joe's Luck and Bavianskop Formations (Anhaeusser, 1976b). Each formation has a basal unit consisting of conglomerate, grit and sandstone, succeeded upwards by subgreywacke, siltstone, jaspilitic chert and BIF.

2.4 Granitoid rocks

Surrounding and intruding the BGB is a diverse suite of granitoid rocks (Figure 2.1). The oldest (see later) granitoids crop out to the west and southwest of the belt and predominantly comprise tonalite-trondhjemite gneisses (Viljoen and Viljoen, 1969b; Anhaeusser and Robb, 1981; Robb and Anhaeusser, 1983). These gneisses typically occur as discrete plutons that are rounded or elliptical in map-view, and are interpreted to have been emplaced into the supracrustal assemblage as magmatic or solid-state diapirs (Anhaeusser, 1984; Kisters and Anhaeusser, 1993). Chemical studies suggest that the tonalites and trondhjemites were derived from the partial melting of basic and ultrabasic protoliths (Robb and Anhaeusser, 1983; Glikson and Jahn, 1985; Robb *et al.*, 1986), and that they resemble coeval silicic metavolcanics / high-level intrusives within the Onverwacht and Fig Tree Groups (De Wit *et al.*, 1987a; De Ronde *et al.*, 1991a).

Underlying vast areas to the north and south of the BGB are multi-component K-rich batholithic complexes. These batholiths consist dominantly of coarse- to very coarse-grained, often porphyritic granodiorite-adamellite, and are considered to have formed by high degrees of fusion of tonalite-trondhjemite precursors (Anhaeusser and Robb, 1983; Robb *et al.*, 1983). Structural investigations suggest that the batholiths were forcibly emplaced into the greenstone assemblage at relatively high crustal levels (Jackson and Robertson, 1983). Migmatites occur along the margins and in the basal portions of the batholiths, and are considered to have formed by the injection of the K-rich magmas into pre-existing granitoids (Robb *et al.*, 1983; Anhaeusser and Robb, 1983).

Late-stage magmatism in the region is manifest as numerous massive, coarse-textured granodiorite and granite (*sensu stricto*) plutons. Work by Robb and Meyer (1990), Meyer *et al.* (1992) and Robb *et al.* (1993) indicated that these plutons can be subdivided into metaluminous high-Ca and peraluminous low-Ca suites. According to these workers, high-Ca plutons such as the Mpageni and Mbabane plutons display I-type characteristics and were probably produced by partial melting and restite unmixing of a quartz-diorite source. The low-Ca plutons, exemplified by the Sinceni pluton, are considered by Robb and Meyer (1990), Meyer *et al.* (1992) and Robb *et al.* (1993) to have S-type characteristics and to have been derived from a siliceous metagreywacke parent.

2.5 Geochronology

Recent advances in the isotope geosciences, particularly with regard to the advent of rapid high-precision dating techniques on single zircons, have led to a wealth of good quality geochronological data for the BML. A summary of the most recent published ages is presented in Tables 2.1 and 2.2.

2.5.1 Barberton Supergroup

The best currently available age estimates of the Tjakastad Subgroup indicate that this unit formed between ~3490 - 3450 Ma ago (Table 2.1). These estimates supersede the > 3500 Ma Sm-Nd whole-rock ages reported by Hamilton *et al.* (1979, 1983) and Jahn *et al.* (1982) which are now known to have no geological significance (Gruau *et al.*, 1990).

The oldest precise age yet measured on rocks from within the BGB comes from a ~3540 Ma lens of tonalite gneiss in tectonic contact with volcanoclastic sedimentary rocks of the Theespruit Formation (Armstrong *et al.*, 1990; Kamo and Davis, 1994). Zircons from the adjacent sedimentary rocks yielded ages of between 3531 - 3453 Ma

Table 2.1 Selected isotopic ages for units of the Barberton Supergroup

STRATIGRAPHIC UNIT	LITHOLOGY DATED	AGE (Ma) [§]	TECHNIQUE	REFERENCE
MOGDIES GROUP				
	Granitoid clasts	3474 +35/-31 - 3306 ± 65 3570 ± 12 - 3518 ± 36	U-Pb zircon conventional U-Pb zircon ion-microprobe	Tegtmeier and Kröner (1987) Kröner and Compston (1988)
FIG TREE GROUP				
Schoongezicht Formation	Dacitic volcanoclastic conglomerate Ignimbrite and feldspar porphyry	3225 ± 3 3275 ± 1 - 3222 +10/-4	Pb-Pb zircon evaporation U-Pb zircon conventional	Kröner <i>et al.</i> (1991a) Kamo and Davis (1994)
Sheba Formation	Greywacke	< 3453 ± 18	U-Pb zircon ion-microprobe	Kröner and Compston (1988)
ONVEKWACHT GROUP				
Kromberg Formation	Dacite dyke	> 3241 ± 6	Pb-Pb zircon evaporation	Kröner <i>et al.</i> (1991a)
Hoogenoeg Formation	Silicic volcanic	3438 ± 22	Pb-Pb zircon evaporation	Kröner and Todt (1988)
	Dacite	3445 ± 3 - 3416 ± 5	Pb-Pb zircon evaporation	Kröner <i>et al.</i> (1991a)
	Dacite	3445 ± 8	U-Pb zircon ion-microprobe	Armstrong <i>et al.</i> (1990)
	(Middle Marker) Volcaniclastic sediment	3472 ± 5	U-Pb zircon ion-microprobe	Armstrong <i>et al.</i> (1990)
Komati Formation (Mundt's Concession)	Gabbro, pyroxenite, dunite	3244 ± 140	Pb-Pb whole-rock	Dupré and Arndt (1990)
	Metagabbro	> 3352 +6/-5	U-Pb zircon conventional	Kamo and Davis (1994)
	Komatiitic basalt, basalt	3460 ± 70	Pb-Pb whole-rock	Brévar <i>et al.</i> (1986)
	Quartz-feldspar porphyry dyke	> 3470 +39/-9	U-Pb zircon conventional	Kamo and Davis (1994)
	Komatiite, komatiitic basalt	3488 ± 13 - 3425 ± 20	Ar-Ar whole-rock step-heating	López-Martínez <i>et al.</i> (1992)
Theespruit Formation	Volcaniclastic sediment	< 3453 ± 6	U-Pb zircon ion-microprobe	Armstrong <i>et al.</i> (1990)
	(tectonic lens) Tonalite gneiss	3538 +4/-2 3538 ± 6	U-Pb zircon conventional U-Pb zircon ion-microprobe	Kamo and Davis (1994) Armstrong <i>et al.</i> (1990)

§ - ages quoted with 2σ errors

Table 2.2 Selected isotopic ages for granitoid rocks surrounding the BGB

GEOLOGICAL UNIT	AGE (Ma) [§]	TECHNIQUE	REFERENCE
Mbabane pluton	2691 ± 4	Pb-Pb zircon evaporation	Layer <i>et al.</i> (1989)
	2687 ± 6	Ar-Ar hornblende step-heating	Layer <i>et al.</i> (1989)
Ngwempisi pluton	2720 ± 4	Pb-Pb zircon evaporation	Maphalala and Kröner (1993)
Sicunusa pluton	2723 ± 7	Pb-Pb zircon evaporation	Maphalala and Kröner (1993)
Mpageni pluton	2740 ± 15	U-Pb zircon conventional	Kamo and Davis (1994)
Sinceni pluton	3074 ± 4	Pb-Pb zircon evaporation	Wendt <i>et al.</i> (1993)
Salisbury Kop pluton	3079 ± 39	U-Pb zircon vapour digestion	Heubeck <i>et al.</i> (1993)
	3079 ± 6	Pb-Pb zircon evaporation	Heubeck <i>et al.</i> (1993)
	3109 +10/-8	U-Pb zircon conventional	Kamo and Davis (1994)
Mliba pluton	3105 ± 10	Pb-Pb zircon evaporation	Wendt <i>et al.</i> (1993)
	3100 ± 11	U-Pb zircon vapour digestion	Wendt <i>et al.</i> (1993)
Boesmanskop pluton	3107 ± 3	U-Pb zircon conventional	Kamo and Davis (1994)
Nelspruit batholith	3106 ± 3	U-Pb zircon conventional	Kamo and Davis (1994)
Mpuluzi batholith	3107 +4/-2	U-Pb zircon conventional	Kamo and Davis (1994)
Dalmein pluton	3216 +2/-1	U-Pb zircon conventional	Kamo and Davis (1994)
Neishoogte pluton	3212 ± 2	Pb-Pb zircon evaporation	York <i>et al.</i> (1989)
Kaat Valley pluton	3226 ± 14	U-Pb zircon ion-microprobe	Armstrong <i>et al.</i> (1990)
	3229 ± 5	U-Pb zircon conventional	Tegtmeyer and Kröner (1987)
	3228 +2/-1	U-Pb zircon conventional	Kamo and Davis (1994)
	3212 ± 12	Ar-Ar hornblende step-heating	Layer (1991)
Theespruit pluton	3437 ± 6	U-Pb zircon ion-microprobe	Armstrong <i>et al.</i> (1990)
	3440 ± 5	Pb-Pb zircon evaporation	Kröner <i>et al.</i> (1991a)
	3443 +4/-3	U-Pb zircon conventional	Kamo and Davis (1994)
Stolzberg pluton	3445 ± 4	Pb-Pb zircon evaporation	Kröner <i>et al.</i> (1991a)
	3460 +5/-4	U-Pb zircon conventional	Kamo and Davis (1994)
Doornhoek pluton	3448 ± 4	U-Pb zircon conventional	Kamo and Davis (1994)
Steynsdorp pluton	3490 ± 4	Pb-Pb zircon evaporation	Kröner <i>et al.</i> (1991a)
	3509 +8/-7	U-Pb zircon conventional	Kamo and Davis (1994)
	3510 ± 4	Pb-Pb zircon evaporation	Kröner (1993)
Ancient Gneiss Complex			
Usutu Suite	3306 ± 4 - 3220 ± 8	Pb-Pb zircon evaporation	Kröner <i>et al.</i> (1991b)
Tsawela Gneiss	3458 ± 6 - 3362 ± 22	Pb-Pb zircon evaporation and U-Pb zircon vapour digestion	Kröner <i>et al.</i> (1989, 1991b)
Ngwane Gneiss	3644 ± 4 - 2981 ± 30	Pb-Pb zircon evaporation, U-Pb zircon ion-microprobe, conventional and vapour digestion	Compston and Kröner (1988), Kröner <i>et al.</i> (1989, 1991b)

§ - ages quoted with 2σ errors

(Armstrong *et al.*, 1990), suggesting that rocks assigned to the Theespruit Formation are younger than the latter age. Brévart *et al.* (1986) reported an imprecise Pb-Pb whole-rock age of 3460 ± 70 Ma for the overlying Komati Formation. Minimum ages of 3470 and 3352 Ma for this unit may also be inferred from the emplacement ages of a quartz-feldspar porphyry dyke and a cross-cutting metagabbro (Kamo and Davis, 1994). Low-grade hydrothermal alteration of the Komati Formation has been dated at between 3488 - 3425 Ma (López-Martínez *et al.*, 1992).

The only geochronological data currently available for rocks of the Tjakastad Subgroup along the northern flank of the BGB is the imprecise Pb-Pb whole-rock age of 3244 ± 140 Ma reported by Dupré and Arndt (1990) for the Mundt's Concession Layered Ultrabasic Complex in the eastern extremity of the Jamestown Schist Belt (Figure 2.1). Anhaeusser (1969, 1972) suggested that this complex forms part of the Komati Formation, and the ~220 Ma discrepancy between the age obtained by Dupré and Arndt (1990) and the age of the Komati Formation in the southwestern part of the belt remains unexplained, but probably reflects metamorphic resetting by the Kaap Valley pluton (see later).

Volcaniclastic sedimentary rocks of the Middle Marker at the base of the Hooggenoeg Formation have an age of 3472 Ma (Armstrong *et al.*, 1990). Silicic rocks near the top of the formation range in age from 3445 - 3416 Ma (Kröner and Todt, 1988; Kröner *et al.*, 1991a; Armstrong *et al.*, 1990). A minimum age of 3241 Ma for the overlying Kromberg Formation may be inferred from the age of a cross-cutting dacite dyke (Kröner *et al.*, 1991a).

Detrital zircons from a sample of greywacke collected from the basal portions of the Fig Tree Group yielded an age of 3453 Ma suggesting that they were derived from the erosion of upper Onverwacht rocks (Kröner and Compston, 1988). Dacitic metavolcanic-volcaniclastic rocks of the Schoongezicht Formation have been dated at

between 3226 - 3222 Ma (Kröner *et al.*, 1991a; Kamo and Davis, 1994). These ages also provide a maximum constraint on the age of deposition of the overlying Moodies Group.

Granitoid clasts in Moodies conglomerates and xenocrystic zircons within Onverwacht and Fig Tree silicic metavolcanics have yielded ages in excess of 3500 Ma, possibly indicating the presence of continental crust older than the basal successions of the BGB (Kröner and Compston, 1988; Kröner *et al.*, 1991a; Armstrong *et al.*, 1990).

2.5.2 Granitoid rocks

Granitoid rocks surrounding the BGB range in age from older than 3600 Ma to younger than 2700 Ma (Table 2.2). The oldest age which has been reported to date comes from an inlier of strongly deformed Ngwane Gneiss in tectonic contact with rocks of the BGB in northwest Swaziland. Zircons from this unit contain cores with a mean age of 3644 Ma (Compston and Kröner, 1988). Other samples from the Ngwane Gneiss elsewhere in Swaziland have occasionally also yielded ages in excess of 3500 Ma, indicating that portions of the AGC pre-date the Barberton Supergroup (Kröner *et al.*, 1989, 1991b).

The Doornhoek, Stolzburg and Theespruit trondhjemite plutons are dated at between 3460 - 3437 Ma, indicating that they are coeval with silicic magmatism at the top of the Hooggenoeg Formation (Section 2.5.1)(Armstrong *et al.*, 1990; Kröner *et al.*, 1991a; Kamo and Davis, 1994). Anomalously old ages of *circa* 3500 Ma have, however, been reported for the geochemically and texturally similar Steynsdorp pluton (Kröner *et al.*, 1991a; Kröner, 1993; Kamo and Davis, 1994). The tonalitic Kaap Valley pluton is dated at ~3230 Ma (Tegtmeyer and Kröner, 1987; Armstrong *et al.*, 1990; Kamo and Davis, 1994) and appears to be broadly coeval with the trondhjemitic Nelshoogte (3212 Ma; York *et al.*, 1989) and granodioritic Dalmein (3216 Ma; Kamo and Davis, 1994) plutons, as well as dacitic volcanism within the Schoongezicht Formation (Section 2.5.1).

Granodioritic-to-adamellitic rocks of the Mpuluzi and Nelspruit batholiths (3107 and 3106 Ma; Kamo and Davis, 1994) are temporally associated with syenogranites and granodiorites of the Boesmanskop (3107 Ma; Kamo and Davis, 1994), Mliba (3105 - 3100 Ma; Wendt *et al.*, 1993) and Salisbury Kop (3109 - 3079 Ma; Heubeck *et al.*, 1993; Kamo and Davis, 1994) plutons. Late-stage plutonic activity in the region ended with the intrusion of the Mpageni, Sicunusa, Ngwempisi and Mbabane plutons at *circa* 2700 Ma ago (Leyer *et al.*, 1989; Maphalala and Kröner, 1993; Kamo and Davis, 1994).

2.6 Tectonic evolution

As with most Archaean granitoid-greenstone terranes, the BML is characterised by a complex, polyphase tectonic history. The various models that have been proposed to account for the structural evolution of the region can be divided into two groups, one of which emphasizes vertical tectonics, the other horizontal. Early studies by Anhaeusser *et al.* (1969) and Anhaeusser (1975, 1981a, 1984) suggested that much of the deformation can be related to gravity-driven processes, involving the slumping of unstable supracrustal assemblages and the preferential development of regional-scale longitudinal slides and tight-to-isoclinal synclinoria. This was followed by deformation of a more localized nature, associated with the emplacement of granitoid diapirs.

Other workers (e.g. De Wit, 1982; De Wit *et al.*, 1983; Williams and Furnell, 1979; Lamb, 1984; Paris, 1984; Lamb and Paris, 1988; Tomkinson and King, 1991) have taken the opposite view, arguing that extensive thrust faulting and associated nappe formation and recumbent folding have led to the development of a complex tectonostratigraphic assemblage from an originally much thinner supracrustal sequence. De Wit *et al.* (1987b, 1992), De Wit and Tredoux (1988), De Wit and Hart (1993) and De Ronde and De Wit (in press) have also suggested that some basic-ultrabasic assemblages within the Onverwacht Group are analogous to those found in modern mid-ocean ridge crust. This interpretation has, however, been questioned by Bertrand *et al.* (1993) and Cloete (1994), who pointed out significant volcanological differences between the Onverwacht rocks in

question and mid-ocean ridge crust, the most important of which relates to the absence of any compelling evidence for a sheeted dyke complex. De Wit *et al.* (1987b, 1992), De Wit and Hart (1993) and De Ronde and De Wit (in press) also speculated that the Onverwacht rocks form part of an ophiolite, referred to as the Jamestown Ophiolite Complex, which was thrust onto an early arc-like terrane. Later, northwest-directed thrusting is interpreted to have juxtaposed this arc against a similar, but younger greenstone succession to the north.

2.7 Alteration

Rocks of the BGB have undergone varying degrees of very low- to medium-grade alteration. Three styles are recognised, viz., synvolcanic / seafloor alteration, burial metamorphism and contact metamorphism, each of which will be briefly discussed in turn.

Synvolcanic and seafloor alteration: this style of alteration is inferred to have occurred in both submarine as well as subaerial settings and is held responsible for the pervasive hydration, silicification and carbonatization of rocks within the Onverwacht and Fig Tree Groups (e.g. De Wit *et al.*, 1982; Paris *et al.*, 1985; Lowe *et al.*, 1985; Lowe and Byerly, 1986; Ducháč and Hanor, 1987; Hanor and Ducháč, 1990; Byerly and Palmer, 1991; amongst others). The alteration has been attributed to the widespread, but shallow-seated convection of low- to moderate-temperature hydrothermal fluids, mainly of modified seawater origin, either contemporaneously with the volcanism and sedimentation, or soon afterwards.

Burial metamorphism: investigations by Cloete (1990, 1991, 1994) into the metamorphism of the Komati Formation where it is best preserved in the southwestern part of the BGB have shown that metamorphic grade within this unit increases with

stratigraphic depth. Pressure estimates at the base of the formation correspond to the calculated pressures exerted by the overlying strata, implicating burial metamorphism.

Contact metamorphism: the studies of Viljoen and Viljoen (1969e), Anhaeusser *et al.* (1969) and Anhaeusser (1969, 1984) indicated that those supracrustal rocks in close proximity with the intrusive granitoids have commonly been subjected to at least one episode of dynamothermal contact metamorphism. This alteration reached the amphibolite facies and was usually characterised by an initial period of prograde metamorphism, followed by post-tectonic recrystallization and, in the waning stages, partial retrogression.

3. ONVERWACHT GROUP

3.1 Introduction

Lithologies of the Onverwacht Group are best exposed along the southwestern border of the study area, where they form a laterally persistent unit fringing the northern margin of the BGB. Investigations within and to the east of the Jamestown Schist Belt (Figure 2.1) by Anhaeusser (1972, 1976b, 1986b) and Harris *et al.* (1993) led these workers to conclude that this unit, which consists principally of amphibolites, serpentinites and basic-to-ultrabasic schists, but which also contains distinctive horizons of aluminous silicic schist, constitutes part of the Theespruit Formation. No isotopic age data are, however, currently available to corroborate this interpretation. East of Louw's Creek, the Theespruit rocks are confined to a narrow, east-northeast-trending block bounded by the Revolver, Scotsman and Adamanda Faults (Figure 1.4; Sections 9.2.1.2.11, 9.2.1.2.12 and 9.2.1.2.13).

Rocks of the Onverwacht Group also crop out to the north of the Stentor Fault (Section 9.2.1.2.10), in the core zones of the Strathmore and Koedoe Anticlines (Sections 9.2.1.1.9 and 9.2.1.1.10), and at the Buffelspruit Talc Mine on Sherlock 461 JU (Figure 1.4, D13; Section 9.2.1.2.14). The succession north of the Stentor Fault contains assemblages characteristic of the Komati Formation (Viljoen and Viljoen, 1970). Additional exposures of Onverwacht rocks occur in numerous, elongate greenstone remnants preserved within gneisses of the Nelspruit Migmatite and Gneiss Terrane (Section 8.4) to the north of the BGB (Figure 8.2). Field relationships suggest that these remnants, some of which extend for several kilometres, represent xenoliths prized from the BGB, but the possibility cannot be discounted that some of the larger remnants represent tectonically interleaved or infolded portions of the greenstone belt. The precise stratigraphic position of the lithologies comprising the xenoliths, as well as those within the Strathmore and Koedoe Anticlines, could not be resolved, although it seems likely that they also form part of the Tjakastad Subgroup.

In order to preclude repetition, the field, petrological and geochemical characteristics of the various rock types correlated with the Onverwacht Group throughout the study area are described together.

3.2 Basic and ultrabasic schists

Most Onverwacht basic and ultrabasic rocks have been extensively deformed, occurring as a variety of densely foliated, amphibole-, chlorite-, and talc-bearing schists. Primary textures are rarely preserved, and are limited to ellipsoidal millimetre-scale amygdales filled with quartz and/or carbonate. Minor bands of weathered phyllite, probably representing argillaceous metasediments, occur interlayered with the schists in places.

Basic schists, which constitute the dominant schist variety, range from dark-green to greyish-green and typically form jagged, lenticular outcrops that are oriented subparallel to the foliation trend. They consist of preferentially oriented chlorite laths, along with xenoblastic carbonate (mainly calcite) and quartz grains, the latter often showing pronounced strain extinction. Acicular crystals of actinolite-tremolite, showing varying degrees of alteration to chlorite and talc, were recorded in some samples. Minor constituents include sodic plagioclase, epidote - clinozoisite, biotite, sphene, sericite, tourmaline and Fe-oxides. Quartz and quartz + carbonate veining is fairly common in outcrops in the Revolver Creek Valley, as are ribbon aggregates composed of sutured carbonate and quartz (Figure 3.1A).

Narrow bands and lenses of grey-green ultrabasic schist occur locally as sporadic interlayers within the basic schists, but can usually only be observed in old mine workings or in road-cutting exposures. These rocks exhibit a satin-like sheen when fresh, and consist mainly of colourless or pale-green talc and chlorite, together with accessory

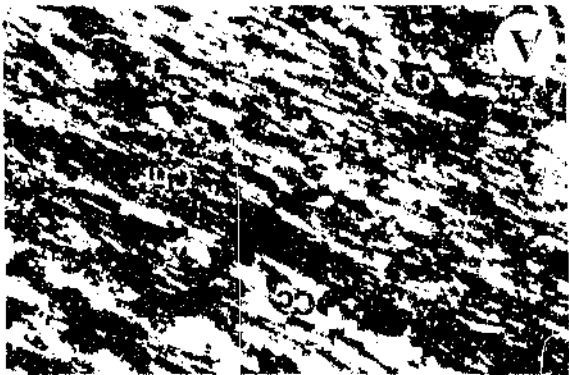
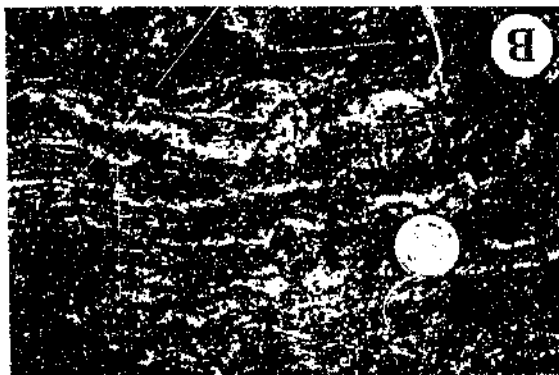
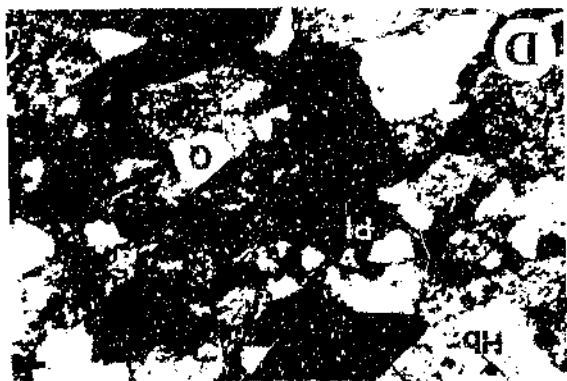


Figure 3.1 Features of some lithologies correlated with the Onverwacht Group:

(A) Photomicrograph (cross-polarised light; length of field of view = 1.8 mm) showing quartz (Q) and calcite (Cc) ribbon structures in quartz-chlorite (Chl)-carbonate schist.

(B) Carbonate veinlets (arrows) in crenulated talc-magnesite schist (Buffelspruit Talc Mine, Sherlock 461 JU). Coin is 2.4 cm across.

(C) Enclave of hornblende amphibolite (Am) in gneiss (Gn) (Mara 233 JU). Hammer is 30 cm long.

(D) Photomicrograph (cross-polarised light; length of field of view = 1.8 mm) showing the mineral assemblage: hornblende (Hb) + plagioclase (Pl) + quartz (Q) in amphibolite.

(E) Polished rock slab showing what have been interpreted as reworked amygdaloids or silicified accretionary lapilli in quartz-muscovite schist (sample collected on the farm Louieville 325 JU).

(F) Photomicrograph (cross-polarised light; length of field of view is 4.3 mm) showing the typical appearance of metagabbro. Felted masses of actinolite (Ac), probably representing uranitized clinopyroxenes, are accompanied by stubby, relic plagioclase crystals (Pl) and xenoblastic grains of secondary quartz (Q).

(G) Photomicrograph (cross-polarised light; length of field of view = 4.3 mm) of metapyroxenite showing aggregates of chlorite (Chl) and talc (Tc), interpreted as multiphase pseudomorphs after orthopyroxene.

carbonate, tremolite and opaques. Magnesite is a major constituent of talcose schists at the Buffelspruit Talc Mine, which also frequently contain numerous carbonate veinlets (Figure 3.1B; Section 9.2.1.2.14). Fuchsitic ultrabasic schists characteristically display a bright-green coloration.

3.3 Amphibolites

Amphibolites occur in two areas: (1) along the BGB - Nelspruit batholith contact; and (2) in the previously described greenstone remnants (Figure 3.1C). In the field, the rocks build low, homogeneous, dark-green or grey outcrops that characteristically display a pervasive schistosity produced by the preferred alignment of the amphibole crystals. This fabric is locally accentuated by thin (~1 - 5 mm wide) anastomosing quartz veinlets. No primary textures are preserved. In some outcrops, the amphibolites, particularly those comprising the xenoliths, are seen to be intruded by leuco pegmatite veins and fine-grained granitoid dykes. Amphibolites in the smaller (< 0.5 m long) enclaves occasionally display partial assimilation by the intruding granitoids. In some exposures, they are also seen to contain abundant biotite, or more rarely, large (up to ~1 cm long), generally randomly oriented, idiomorphic microcline megacrysts. The formation of these minerals probably reflects the introduction of K-rich metasomatic fluids from the enveloping gneisses.

Mineralogically, the amphibolites consist dominantly of large (~0.2 - 2 mm long), subidioblastic-to-idioblastic, dark-green hornblende crystals, with lesser quartz and plagioclase (Figure 3.1D). Actinolite and tremolite occur sporadically, but are most common in amphibolites away from the immediate granitoid contact. Plagioclase compositions range from oligoclase to andesine. Accessory constituents include biotite, sphene, apatite, ilmenite and magnetite. Retrograded amphibolites contain accessory chlorite, epidote, carbonate and sodic plagioclase, the former typically rimming the amphiboles and biotite.

3.4 Serpentinities

Serpentinities are uncommon in the study area. The best exposures occur on a small hill situated ~0.5 km southeast of Louw's Creek (Figure 1.4, H2). This hill consists almost entirely of massive, dense, greyish-green serpentinite. Minor outcrops of variably sheared, bluish-grey serpentinite were also recorded in the upper reaches of the Revolver Creek Valley, as well as in some of the larger greenstone remnants, but are too limited in extent to be plotted in Figures 1.4 and 8.2.

Seen in thin section, the serpentinites consist principally of antigorite, which typically forms massive mesh-like intergrowths, with lesser talc, chlorite, carbonate and opaques. In some specimens, however, antigorite pseudomorphs after olivine have been recognized; the margins and fractures of the original olivine grains are outlined by minute granules of secondary magnetite. Locally the serpentinites contain narrow cross-fibre chrysotile veinlets ranging up to ~4 mm in width.

3.5 Silicic schists

Two bands of strongly silicified quartz-muscovite schist occur interlayered with basic schists to the south of Louw's Creek, giving rise to prominent east-trending ridges that outline the limbs of the Louieville Antiform (Figure 1.4, I2; Section 9.2.1.1.8). Petrologically, the schists consist almost entirely of fine-grained quartz and muscovite, with minor chlorite, andalusite, chloritoid, sericitized feldspar, epidote, tourmaline and opaques. In some outcrops, the schists are seen to contain thin (a few centimetres wide) lenses of fine-grained tuffaceous sedimentary rock. Finely laminated argillaceous rocks and a thin (~2 m wide) unit of grey and white banded chert crop out sporadically along the southern contact of the northern schist band.

Distinctive, poorly sorted, spherule-bearing horizons up to ~20 cm wide were recorded at a locality ~2 km due west of the Eldorado Gold Mine (Figure 1.4, I3)(Figure 3.1E). The spherules range from ~1 - 5 mm across, often display weak concentric zonation, and occur in association with angular-to-rounded clasts of recrystallized chert. Thin section investigations indicate that they consist mainly of fine-grained, polygonal-textured quartz with accessory muscovite and chlorite. Preserved textural evidence suggests that the spherule beds represent reworked amygdale or silicified accretionary lapilli deposits.

Additional exposures of Onverwacht silicic schist were recorded in the core of the Koedoe Anticline along the boundary between Stentor 219 JU and Koedoe 218 JU (Figure 1.4, D9).

3.6 Metagabbros

A prominent, ~1.7 km long and ~300 m wide, body of massive, homogeneous, medium- to coarse-grained metagabbro is exposed in the western part of the Strathmore Anticline (Figure 1.4, D6 and D7). Contact relationships between this unit and the schistose metavolcanic rocks to the east could not be ascertained due to inadequate exposures, although it seems likely that the former is intrusive into the latter. In the south, the metagabbros abut against banded grey and white chert at the base of the Bien Venue Formation (Section 4.3). A second, much smaller (~150 m long and ~50 m wide) body of metagabbroic rocks, texturally identical to those comprising the main occurrence, straddles the boundary between Strathmore 214 JU and Stentor 219 JU (Figure 1.4, D7).

Petrographically, the metagabbros are seen to consist dominantly of actinolite and plagioclase (Figure 3.1F). The amphiboles display marked blue-green pleochroism and typically form felted masses up to ~3 mm long which probably represent uranitized clinopyroxenes. Plagioclase occurs as stubby crystals, ~0.5 - 3 mm long, which frequently show extensive alteration to saussurite. The feldspars are mainly albites, but more calcic

varieties (oligoclase - andesine) were also recorded; it is assumed that most of the feldspars were originally more calcic than An_{50} . Quartz, chlorite, calcite, epidote - clinozoisite, biotite, muscovite, apatite and opaques occur in minor amounts throughout the rock.

3.7 Metapyroxenites

Two small (~300 - 500 m long and ~100 - 300 m wide) bodies of what is believed to be altered pyroxenite crop out immediately north of the Scotsman Fault in the western part of Three Sisters 256 JU (Figure 1.4, H4). Both bodies have undergone deformation along their margins; consequently their original relationship to the enclosing basic-ultrabasic schists could not be determined. Where best exposed, the metapyroxenites have a massive, coarse-textured appearance, and are dark-green or bluish-green on fresh surfaces. Seen in thin section, they contain large (~2 - 4 mm long), idioblastic, aggregates of chlorite, talc and, in rare cases, anthophyllite (Figure 3.1G). These aggregates probably represent multiphase pseudomorphs after orthopyroxene. Surrounding the aggregates is a fine-grained groundmass consisting of intergrown chlorite, talc and amphibole, with minor disseminated opaques. A few small remnant grains of strongly birefringent clinopyroxene, showing alteration to amphibole and chlorite, were also recorded.

3.8 Geochemistry

Representative chemical analyses of some rock types correlate with the Onverwacht Group are compiled in Table 3.1. Although the analyses listed represent least-altered specimens, examination of the geochemical data, coupled with petrographic observations, suggests that the abundances of most, if not all, elements have been

Table 3.1 Major and trace element compositions of some rock types correlated with the Onverwacht Group in the study area

Column	1	2	3	4	5	6	7
Sample	K2	SC2	SC3	M1	S4	M4	M5
SiO ₂ (wt %)	79.99	54.02	51.56	48.32	46.34	50.50	49.05
TiO ₂	0.42	1.17	1.07	1.68	1.14	1.18	0.69
Al ₂ O ₃	12.46	11.40	10.36	12.85	12.26	12.66	4.42
Fe ₂ O ₃ ^{total}	0.62	14.51	14.70	13.96	11.21	11.58	12.85
MnO	bdl	0.17	0.29	0.15	0.14	0.16	0.20
MgO	0.48	2.25	3.19	3.51	6.13	6.93	19.66
CaO	0.12	5.57	6.39	5.79	8.55	3.52	9.87
Na ₂ O	0.33	2.44	2.14	2.55	2.34	2.73	0.12
K ₂ O	3.08	0.37	0.38	0.03	0.02	0.03	0.02
P ₂ O ₅	0.13	0.14	0.12	0.20	0.15	0.16	0.07
H ₂ O ⁻	0.02	0.13	0.02	0.09	0.07	0.26	0.21
H ₂ O ⁺	1.21	2.21	2.12	2.78	4.49	3.49	3.72
CO ₂	0.02	6.23	8.57	7.94	6.50	1.58	0.02
Total	98.83	100.61	100.82	99.85	98.95	99.78	100.90
Ba (ppm)	199	232	132	17	bdl	bdl	bdl
Rb	64	13	18	bdl	bdl	bdl	bdl
Sr	29	143	110	90	78	122	6
Y	32	26	25	26	21	21	9
Nb	10	7	6	8	6	5	bdl
Zr	175	105	92	101	63	36	bdl
V	12	254	269	337	295	279	144
Cr	bdl	43	41	51	225	249	2843
Zn	17	125	127	109	85	85	85
Cu	33	191	235	277	93	115	6
Ni	16	8	21	76	91	117	641

bdl - below detection level

Columns: 1. Quartz-muscovite schist (Louieville 325 JU)
 2 - 5. Quartz-chlorite-carbonate schist (Three Sisters 254 JU, Three Sisters 256 JU and Stentor 219 JU)
 6. Quartz-chlorite-actinolite schist (Louieville 325 JU)
 7. Talc-chlorite schist (Three Sisters 256 JU)

Table 3.1 (continued)

Column	8	9	10	11	12	13	14	15
Sample	L2	L3	REN1	WEL1	M3	ON2	ON3	ON1
SiO ₂ (wt %)	57.27	50.91	54.28	52.26	38.43	49.08	49.53	48.11
TiO ₂	0.96	1.83	0.96	0.90	0.09	1.49	1.51	0.19
Al ₂ O ₃	16.24	13.73	8.46	6.69	2.29	13.78	14.39	10.17
Fe ₂ O ₃ ^{total}	7.65	12.79	12.32	14.04	7.95	17.90	17.40	9.19
MnO	0.14	0.25	0.20	0.26	0.10	0.21	0.21	0.15
MgO	5.88	3.50	9.84	10.60	36.08	4.91	4.71	20.39
CaO	8.04	10.98	10.98	12.42	1.02	8.78	8.65	5.75
Na ₂ O	3.36	1.30	1.68	1.18	bdl	2.82	2.90	1.15
K ₂ O	0.52	0.55	0.83	0.43	bdl	0.25	0.12	0.07
P ₂ O ₅	0.26	0.56	0.11	0.10	bdl	0.05	0.06	0.05
H ₂ O ⁻	0.03	0.09	0.08	0.05	0.07	0.02	0.09	0.07
H ₂ O ⁺	0.71	0.81	0.28	0.32	11.44	0.54	0.63	3.96
CO ₂	0.38	2.47	0.09	0.39	1.46	0.26	0.22	0.16
Total	101.44	99.78	100.11	99.64	98.93	100.09	100.42	99.41
Ba (ppm)	bdl	67	47	bdl	bdl	73	43	102
Rb	36	21	14	13	bdl	30	13	bdl
Sr	215	50	177	137	bdl	257	392	39
Y	17	56	19	15	bdl	8	13	11
Nb	8	16	7	5	bdl	bdl	bdl	bdl
Zr	109	206	78	45	bdl	25	40	bdl
V	183	264	177	186	58	620	547	125
Cr	53	bdl	870	818	3675	bdl	bdl	2723
Zn	66	147	98	147	52	101	89	50
Cu	6	15	82	153	10	17	84	25
Ni	48	33	246	228	1716	19	27	945

bdl - below detection level

Columns: 8 and 9. Amphibolite (BGB) (Louws Creek 271 JU)
 10 and 11. Amphibolite (greenstone remnant) (Rensberg 273 JU and Weltevreden 229 JU)
 12. Serpentinite (Louws Creek 271 JU)
 13 and 14. Metagabbro (Strathmore 214 JU)
 15. Metapyroxenite (Three Sisters 256 JU)

modified to a greater or lesser degree from primary values - e.g. note the high CO_2 and low K_2O abundances of the quartz-chlorite-carbonate schists (Table 3.1, columns 2 - 5), and the high H_2O^+ and low K_2O and Na_2O contents of the serpentinite (Column 12). However, despite this, evaluation of the most likely protoliths of the rocks is still possible.

According to the Zr/TiO_2 - Nb/Y criterion of Winchester and Floyd (1977), the quartz-muscovite schist listed in Table 3.1, column 1, may be classified as dacite or rhyodacite. The high SiO_2 content of 80 wt % recorded for this sample is suggestive of a rhyolitic precursor, but more likely reflects post-eruptive silicification. The quartz-chlorite-carbonate and quartz-chlorite-actinolite schists (Columns 2 - 6) chemically resemble, and were probably derived from, basalts (Figure 3.2), although three of the samples (SC2, SC3, M1) exhibit low MgO values of between 2.3 - 3.5 wt %. Major and trace (Cr, Ni) element abundances in the sample of talc-chlorite schist (Column 7) indicate a probable komatiitic precursor. Amphibolites in the vicinity of Louw's Creek (Columns 8 and 9) are likely metamorphosed basalts, but amphibolites in greenstone remnants north of the BGB (Columns 10 and 11) are characterised by higher MgO, Cr and Ni contents, showing affinities with komatiitic basalts. The serpentinite (Column 12) is markedly enriched in MgO relative to $(\text{FeO} + \text{Fe}_2\text{O}_3 + \text{TiO}_2)$ and Al_2O_3 , suggesting that it represents an altered komatiite (Figure 3.2). The samples of metagabbro (Columns 13 and 14) and metapyroxenite (Column 15) display an overall chemical resemblance to basalts and komatiites, respectively.

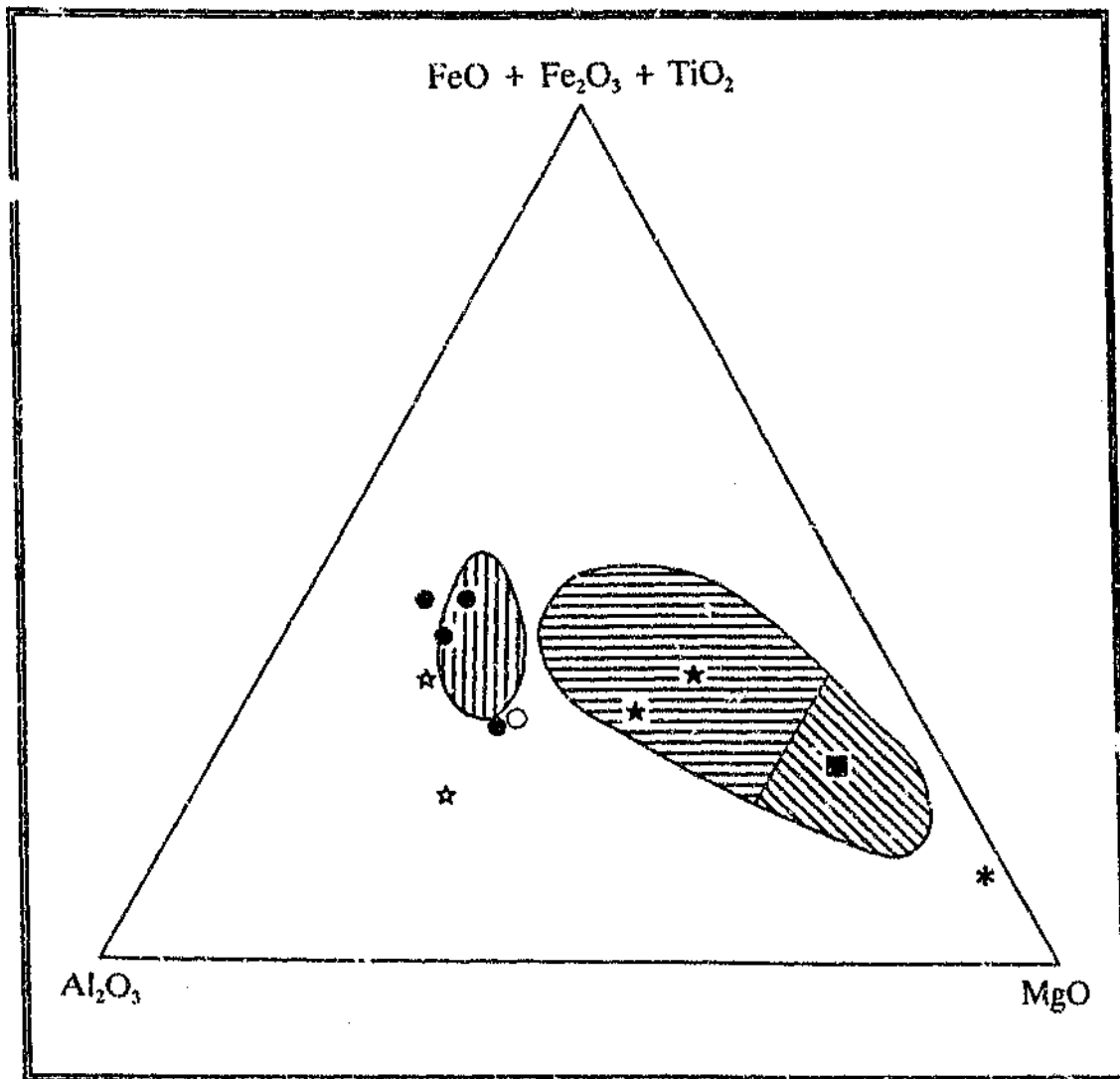


Figure 3.2 Ternary Al_2O_3 - $(\text{FeO} + \text{Fe}_2\text{O}_3 + \text{TiO}_2)$ - MgO (cation %) plot of Onverwacht Group basic and ultrabasic metavolcanic rocks in the study area (data from Table 3.1), and comparison with fields for least-altered Onverwacht rocks from the southwestern parts of the BGB (after Viljoen et al., 1982). FeO contents were calculated according to the formula: $\text{FeO (wt\%)} = [\text{Fe}_2\text{O}_3^{\text{total}} (\text{wt\%}) - \text{TiO}_2 (\text{wt\%}) - 1.5] \times 0.8998$, following Jensen (1976). Fields: vertical hatch - basalt; horizontal hatch - komatiitic basalt; diagonal hatch - komatiite. Symbols: closed circles - quartz-chlorite-carbonate schist; open circle - quartz-chlorite-actinolite schist; square - talc-chlorite schist; open stars - amphibolite (BGB); closed stars - amphibolite (greenstone remnants); asterisk - serpentinite.

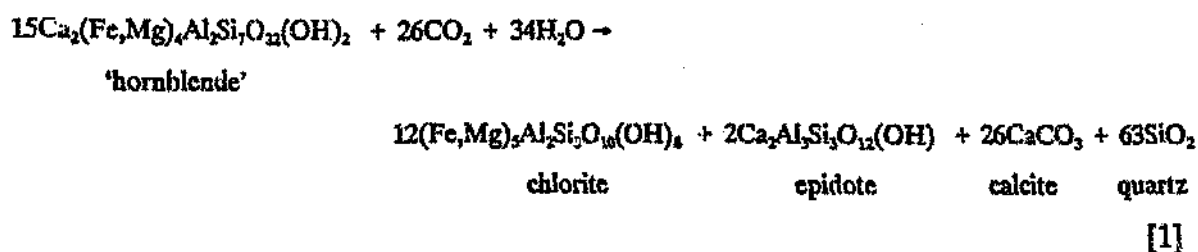
3.9 Metamorphism - metasomatism

Studies dealing with the metamorphism of Onverwacht Group rocks along the northern flank of the BGB have previously been undertaken by Anhaeusser (1963, 1969, 1972) and Viljoen (1963) so that only a few general points will be made here. Peak metamorphic conditions accompanied intrusion of the Nelspruit batholith and attained medium-grade, as indicated by the prograde assemblage: hornblende + quartz + oligoclase - andesine + ilmenite \pm sphene \pm biotite in the contact amphibolites (Section 3.3) (Winkler, 1979; Spear, 1981). Temperatures of 520 - 590°C during metamorphism may be inferred from coexisting arsenopyrite - pyrrhotite - tellurite geothermometry of synmetamorphic mineralized zones hosted by amphibolites at the New Consort Gold Mine, ~2 km to the south of the granitoid contact in the Jamestown Schist Belt (Figure 2.1) (Tomkinson and Lombard, 1990). Andalusite stability in the silicic schists (Section 3.5) constrains the pressure to less than 4.5 kb (Pattison 1992). Away from the immediate granitoid contact, the basic rocks are characterised by the assemblage: chlorite + quartz + sodic plagioclase + Fe-oxides \pm actinolite - tremolite \pm carbonate \pm talc \pm epidote - clinozoisite \pm sphene \pm mica (Sections 3.2 and 3.6) which is characteristic of low-grade metamorphism (Winkler, 1979; Laird, 1980; Laird and Albee, 1981).

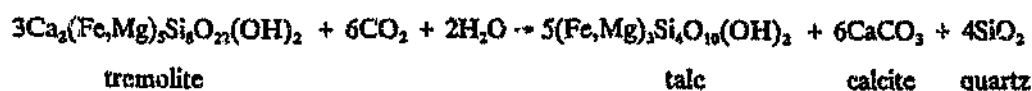
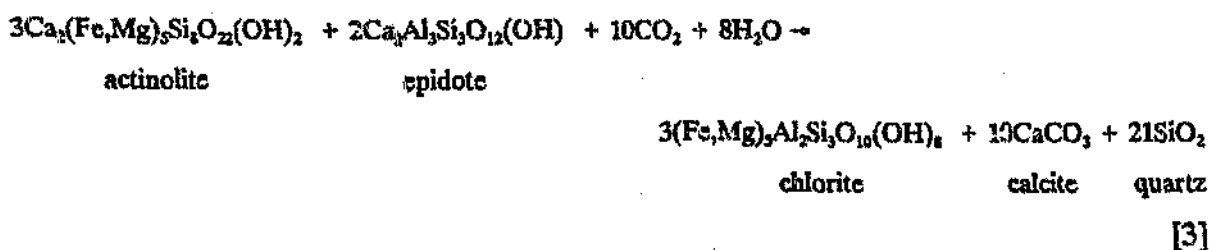
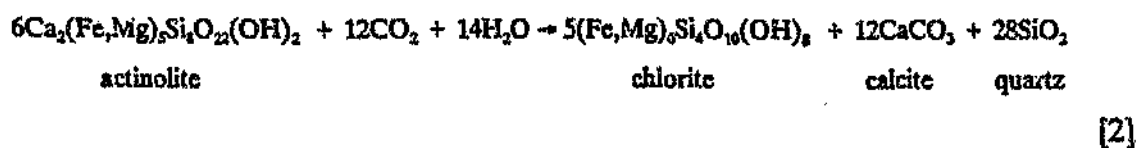
Rocks of the Onverwacht Group in the study area frequently show evidence of retrogression, manifested mainly in the breakdown of amphiboles (Sections 3.2 and 3.3). Field and petrographic observations indicate that these retrograde effects can be ascribed to the introduction of a CO₂-bearing fluid, either during the waning stages of contact metamorphism or associated with subsequent deformation of the greenstone succession. The presence of such a fluid is clearly indicated by the ubiquitous presence of carbonate minerals (mainly calcite) in most lithologies showing evidence of retrogression, particularly those within the Revolver Creek Valley which have been affected by late-stage shearing (Sections 9.2.1.2.12 and 9.2.1.2.13). The addition of CO₂ during downgrading of rocks in this general area is also evident when the analysis of an amphibolite showing no significant retrogression (Table 3.1, column 8) is compared with

a partly retrograded amphibolite (Column 9), and when the quartz-chlorite-actinolite schist (Column 6) is compared with the essentially amphibole-free quartz-chlorite-carbonate schists (Columns 2 - 5).

The breakdown of hornblende in the contact amphibolites can be expressed as follows (Harte and Graham, 1975):



Similarly, the decomposition of actinolite and tremolite is described by the following reactions (Harte and Graham, 1975; Nishiyama, 1990):



The source of the CO₂-rich fluids influencing the retrograde reactions is uncertain, but possibilities include: (1) derivation from granitoids (e.g. De Ronde *et al.*, 1991b, 1992; Burrows *et al.*, 1986); (2) decarbonatization reactions in the basal zone of the greenstone pile, the CO₂ originally having been introduced during volcanism or early seafloor alteration (e.g. Anhaeusser, 1969; Viljoen *et al.*, 1969; Phillips *et al.*, 1987); and/or (3) deep crustal or mantle sources (e.g. Cameron, 1988; Groves *et al.*, 1988; Van Schalkwyk and Van Reenen, 1992).

4. FIG TREE GROUP

4.1 Introduction

The Fig Tree Group comprises a monotonous succession of shale-slate, metagreywacke and argillaceous BIF, stratigraphically overlain by a succession of silicic schists (Figure 1.4). Correlation of the lower, predominantly argillaceous, portions of the Group with either the Sheba or Belvue Road Formations as outlined in Section 2.3 is hampered by structural complexities and, locally, inadequate exposure. Nonetheless, investigations by the author indicate that metagreywacke assemblages are particularly well-developed in the southern parts of the study area, and the rocks in this region have been correlated tentatively with the Sheba Formation. Assemblages in the northern sector of the region under review, on the other hand, contain a greater proportion of shale and, in places, also units of silicic and intermediate metavolcaniclastic rock, and have accordingly been assigned to the Belvue Road Formation.

Detailed lithostratigraphic and structural mapping by the writer has also led to the recorrelation of the silicic schists that crop out west, north and northeast of Three Sisters (Kohler *et al.*, 1992, 1993). Field relationships outlined in Sections 9.2.1.1.6 and 9.2.1.1.7 indicate that parts of this succession, previously correlated by Viljoen and Viljoen (1970) with the Theespruit Formation, overlie argillaceous assemblages of the Belvue Road Formation and are, in turn, overlain by arenaceous metasediments of the Moodies Group. The silicic rocks therefore appear to occupy the same *apparent* stratigraphic position in the Barberton Supergroup as the Schoongezicht Formation (Section 2.3), and have accordingly been correlated with the Fig Tree Group (Kohler *et al.*, 1992). However, despite similarities in *apparent* stratigraphic position, significant age differences (Section 5.6) and the nature of the dominant lithology preclude correlation with the

Schoongezicht Formation (Kohler *et al.*, 1993). Hence, the silicic schists have been assigned to a new lithostratigraphic unit, referred to as the Bien Venue Formation⁴.

The purpose of this chapter is to document the field and petrographic characteristics of the various lithologies making up the Fig Tree Group in the study area, and to describe their most likely depositional palaeoenvironment. Aspects of the geochemistry of the main rock types within the Sheba and Belvue Road Formations is also dealt with briefly. The chemistry of the rocks of the Bien Venue Formation is discussed separately in Chapter 5.

4.2 Sheba and Belvue Road Formations

To simplify documentation, lithologies of these two formations are described together.

4.2.1 Shales and slates

Shales and their metamorphosed equivalents constitute the principal rock types within the Sheba and Belvue Road Formations in most parts of the study area. The rocks are generally well-laminated and micaceous, and range from reddish-brown in ferruginous varieties to dark purplish-grey in carbonaceous varieties. Thickness of the laminae typically varies between 0.1 - 2 mm. Locally, the rocks contain thin beds of porcellaneous chert up to ~1 cm wide.

XRD and petrographic investigations indicate that the shales and slates consist of angular, clay- or silt-sized quartz grains in a matrix composed dominantly of chlorite and muscovite-illite, with accessory sodic plagioclase, biotite, carbonate, opaque phases

⁴ Not yet approved by the South African Committee for Stratigraphy.

and carbonaceous material. Cleavage in the slates is produced mainly by aligned mica and chlorite laths, and is usually subparallel to bedding, except in the hinges of minor and major folds where it clearly transects bedding. In some areas, the fabric is only imperfectly developed, and the rocks should, more correctly, be termed phyllites.

Chemically, the shales and slates are generally characterised by high $\text{Fe}_2\text{O}_3^{\text{total}}$ (8.7 - 17.8 wt %) and low CaO (< 0.2 wt %) and Na_2O (≤ 1 wt %) contents (Table 4.1). MgO abundances in five of the samples analysed (FT2, FT4, FT9, FT14 and FT15) exceed 5 wt %. The rocks are remarkable for their high Cr (821 - 1482 ppm) and Ni (288 - 552 ppm) contents, which are 6 - 12 and 5 - 10 times enriched over concentrations in the "North American shale composite" (NASC; Gromet *et al.*, 1984), respectively. These data imply that the source region of the Fig Tree Group contained an appreciable proportion of ultrabasic material (see also Danchin, 1967; Condie *et al.*, 1970; McLennan *et al.*, 1983). In contrast, Zr concentrations (41 - 117 ppm), which reflect the detrital zircon content of the shales and, hence, the contribution of silicic igneous material in the provenance of the rocks (Wronkiewicz and Condie, 1987; Meyer *et al.*, 1990), are low (0.2 - 0.6 x NASC), leading to high Cr/Zr (8 - 35) and Ni/Zr (3 - 14) ratios.

In Figure 4.1, Cr, Ni and Zr distributions in shales analysed during the present study are compared with data for Moodies Group shales. It is evident that the Fig Tree Group shales are generally enriched in Cr, but depleted in Zr relative to the latter which are characterised by lower Cr/Zr (4 - 6) and Ni/Zr (2 - 3) ratios. These differences imply an increase in the proportion of silicic source components in the provenance of the Moodies Group sediments relative to the Fig Tree Group sediments. The observed chemical trends are consistent with the interpretations of Anhaeusser (1973), Eriksson (1980b), McLennan *et al.* (1983) and Jackson *et al.* (1987) indicating a progressive increase in granitoid detritus from Fig Tree to Moodies times (see also Section 7.4).

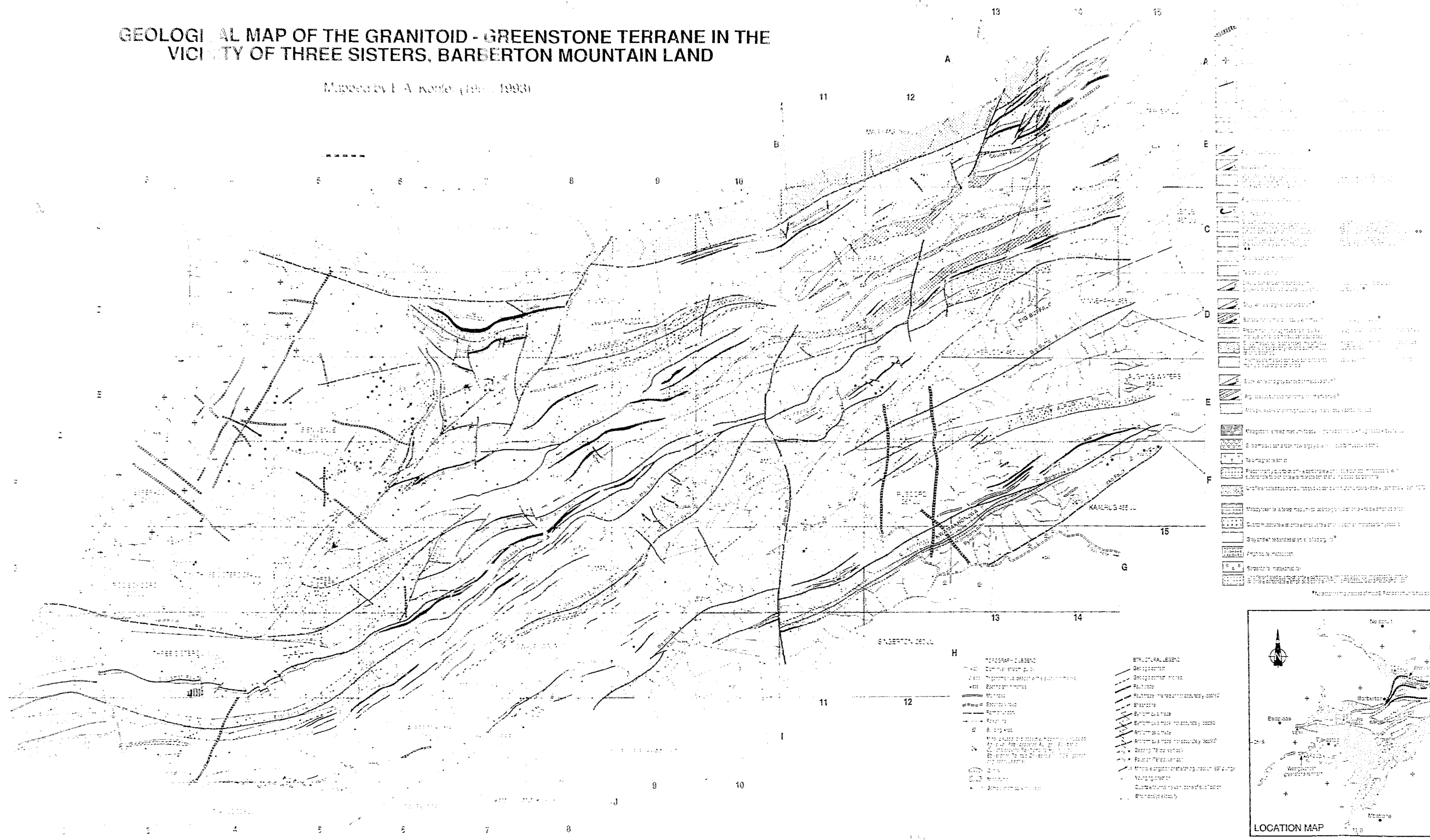
Table 4.1 Chemical analyses of shales and slates from the Sheba and Beivue Road Formations

Sample	FT1	FT2	FT4	FT5	FT9	FT10	FT13	FT14	FT15
SiO ₂ (wt %)	55.43	52.66	63.25	55.49	54.99	53.50	62.14	54.10	60.71
TiO ₂	0.57	0.54	0.64	0.64	0.81	0.65	0.65	0.38	0.43
Al ₂ O ₃	14.24	16.94	13.26	16.68	13.87	13.76	12.94	12.30	11.11
Fe ₂ O ₃ <i>total</i>	14.02	11.88	9.83	8.71	11.26	17.83	10.21	13.55	12.80
MnO	0.10	0.05	0.10	0.02	0.07	0.13	0.04	0.10	0.10
MgO	2.34	7.09	5.43	4.46	6.30	2.14	3.98	9.58	6.47
CaO	9.01	bdl	0.12	0.01	0.14	0.02	0.16	0.01	0.01
Na ₂ O	0.10	bdl	1.36	bdl	1.35	0.05	0.99	0.06	0.02
K ₂ O	3.35	1.94	1.38	2.27	1.80	2.68	2.40	2.10	0.37
P ₂ O ₅	0.15	0.07	0.09	0.05	0.10	0.12	0.15	0.03	0.05
H ₂ O ⁻	1.07	1.47	0.08	3.78	0.75	2.08	0.96	1.64	1.55
H ₂ O ⁺	5.04	6.26	3.85	5.66	5.33	5.60	4.27	6.44	4.76
CO ₂	2.53	0.94	0.29	2.08	2.18	1.13	0.68	0.46	1.19
Total	98.96	99.84	99.68	99.78	98.95	99.69	99.47	100.75	99.57
Ba (ppm)	1535	347	248	387	310	1055	578	1254	479
Rb	160	81	50	120	82	163	90	84	25
Sr	24	18	41	12	28	10	44	5	bdl
Pb	8	9	9	10	bdl	10	14	5	bdl
Y	18	19	18	25	22	19	18	10	10
Nb	9	9	8	9	10	8	9	6	5
Zr	75	47	66	65	102	85	117	52	41
Ga	26	28	24	28	19	18	18	11	11
V	131	150	136	171	178	149	129	151	164
Cr	932	1109	821	955	1129	1482	941	902	1415
Zn	384	124	102	167	153	157	106	120	123
Cu	111	35	54	91	86	47	56	11	17
Ni	330	418	306	417	306	374	288	358	552

bdl - below detection limit

GEOLOGICAL MAP OF THE GRANITOID - GREENSTONE TERRANE IN THE VICINITY OF THREE SISTERS, BARBERTON MOUNTAIN LAND

Mapped by F. A. Kohler (1961 - 1993)



Legend

A - Archean granitoid gneiss (horizontal lines)

B - Archean mafic gneiss (vertical lines)

C - Archean quartzite (dots)

D - Archean metabasites (diagonal lines)

E - Archean schists (alternating horizontal and vertical lines)

F - Archean amphibolites (dotted pattern)

G - Archean mafic schists (diagonal lines, different orientation)

H - Archean mafic gneiss (horizontal lines, different orientation)

I - Archean mafic schist (vertical lines, different orientation)

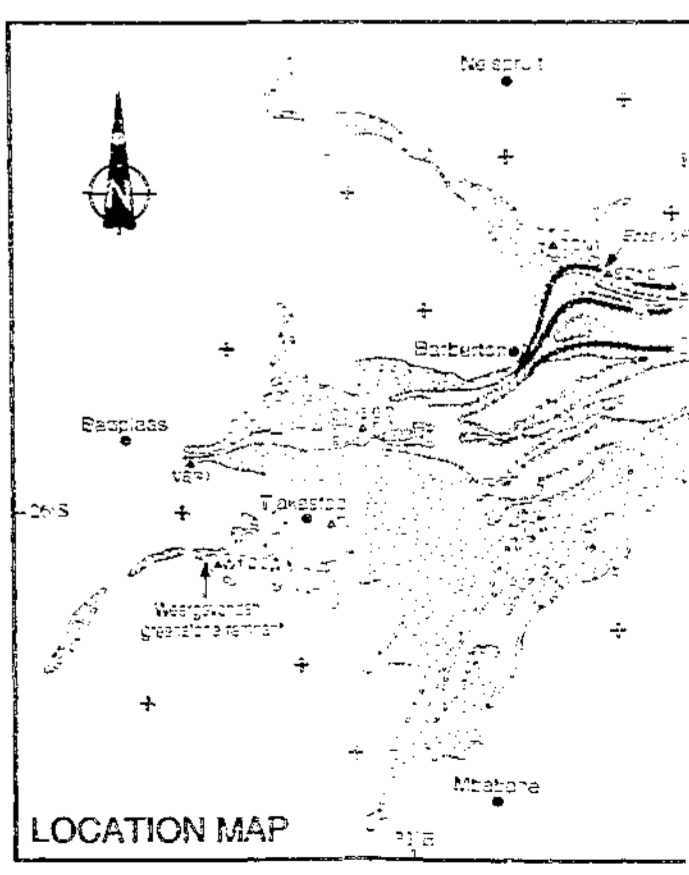
J - Archean mafic gneiss (diagonal lines, different orientation)

TOPOGRAPHIC LEGEND

- Contour interval 20m
- Stream bed
- Drainage basin boundary
- Stream head
- Stream mouth
- Stream confluence
- Stream bifurcation
- Stream intersection
- Stream junction
- Stream fork
- Stream split
- Stream divide
- Stream barrier
- Stream dam
- Stream weir
- Stream culvert
- Stream bridge
- Stream tunnel
- Stream dam structure
- Stream weir structure
- Stream culvert structure
- Stream bridge structure
- Stream tunnel structure
- Stream dam structure
- Stream weir structure
- Stream culvert structure
- Stream bridge structure
- Stream tunnel structure

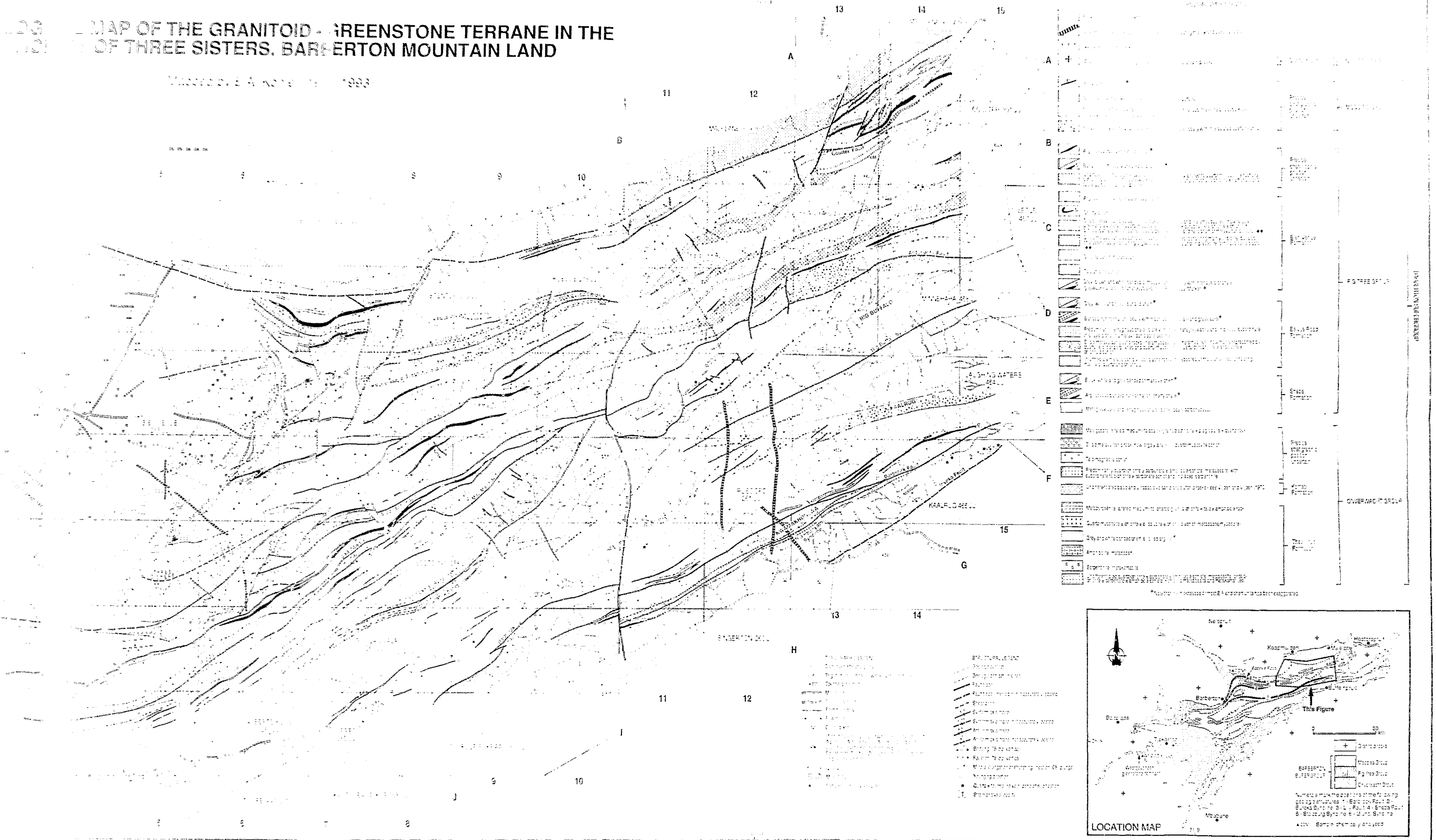
STRUCTURAL LEGEND

- Shear zone
- Shear fault
- Normal fault
- Reverse fault
- Thrust fault
- Strike-slip fault
- Normal fault
- Reverse fault
- Thrust fault
- Strike-slip fault
- Normal fault
- Reverse fault
- Thrust fault
- Strike-slip fault
- Normal fault
- Reverse fault
- Thrust fault
- Strike-slip fault
- Normal fault
- Reverse fault
- Thrust fault
- Strike-slip fault
- Normal fault
- Reverse fault
- Thrust fault
- Strike-slip fault



LOG MAP OF THE GRANITOID - GREENSTONE TERRANE IN THE
 OF THREE SISTERS, BARBERTON MOUNTAIN LAND

WILLIAMS, E. A. 1983



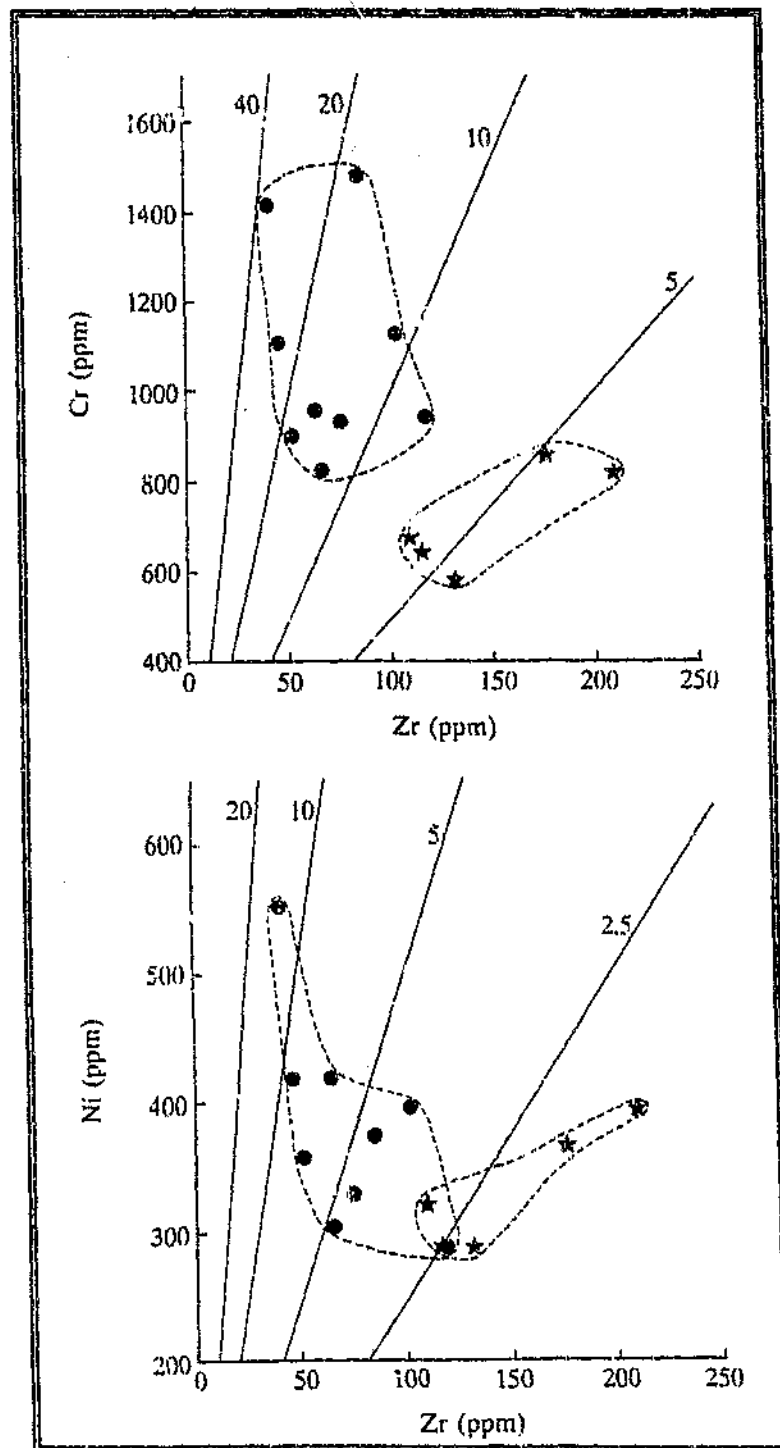


Figure 4.1 Plots of Cr and Ni versus Zr for shales and slates of the Fig Tree Group in the study area (circles) and comparison with Moodies Group shales (stars; data from McLennan et al., 1983). Also shown are reference lines of constant Cr/Zr and Ni/Zr values.

4.2.2 Metagreywackes

Metagreywackes occur as thin, grey- to brown-weathering units interbedded with the shales and slates. The rocks range from poor to moderately sorted and, as seen in outcrop, contain angular sand- and grit-sized clastic fragments set in a fine-grained, often conspicuously foliated matrix. Thickness of individual metagreywacke units, which are often capped by bands of finely laminated shale, varies from a few centimetres to over a metre. Primary structures other than bedding and crude grain-size grading are seldom visible due to shearing and weathering; small-scale cross-laminations and shale rip-up clasts were recorded in road-cutting exposures in the vicinity of the Eldorado Gold Mine on Louieville 325 JU (Figure 1.4, I3). At another locality on Amo 259 JU (near to sample site FT16 in Figure 1.4, G11), water-worn pavements in the Mhlambanyathi River show units of poorly sorted greywacke conglomerate up to several metres wide. The conglomerate contain a variety of poorly sorted, angular-to-subrounded chert and greenish-grey metavolcanic clasts in a fine-grained metagreywacke matrix (Figure 4.2A). The clasts typically vary between ~1 - 8 cm in size, but chert boulders having diameters in excess of 10 cm also occur.

Fragments of quartz and feldspar dominate all metagreywackes studied microscopically (Figure 4.2B). Quartz is most common and occurs both as monocrystalline and polycrystalline (mainly recrystallised chert) grains. Some of the monocrystalline grains resemble, and probably represent, embayed quartz phenocrysts derived from silicic volcanic-volcaniclastic rocks. Feldspar is dominantly microcline, with lesser plagioclase and untwinned orthoclase, and is usually extensively sericitized. Fragments of chlorite, amphibole, serpentine, mica and opaque phases are common, as are chloritized and epidotized basic and silicic volcanic grains, some of which exhibit a pre-incorporation schistosity. Lithic grains of argillaceous material are also fairly common, but granitoid fragments (i.e. coarse-grained quartz + feldspar aggregates) are comparatively rare. Matrix constituents, which usually comprise over 30 % of the total volume of the rocks, include quartz, chlo. muscovite-illite, carbonate, biotite, epidote

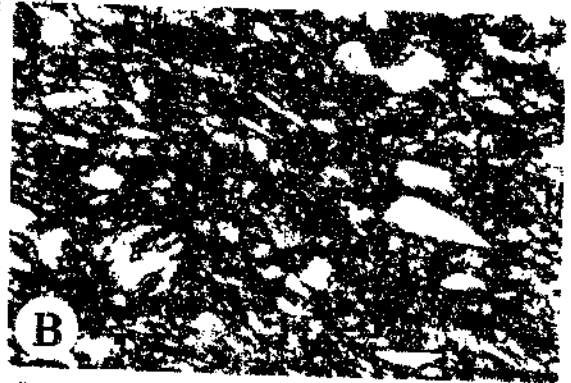
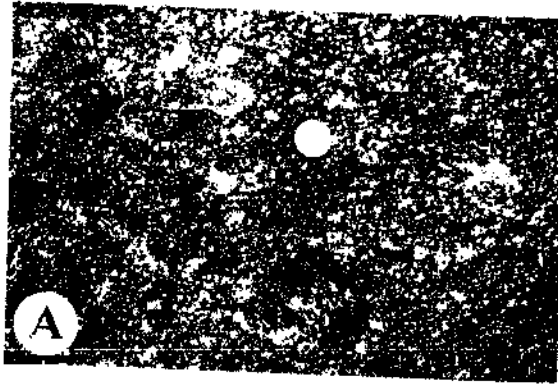


Figure 4.2 Structures and textural characteristics observed in metasediments of the Sheba and Belvue Road Formations:

(A) Angular chert and metavolcanic (arrows) clasts in metagreywacke conglomerate (Arno 259 JU). Coin has a diameter of 2.4 cm.

(B) Photomicrograph (plane-polarised light; length of field of view = 1.8 mm) showing the typical appearance of metagreywacke. Specimen contains angular sand- and silt-sized clastic fragments composed mainly of quartz and altered feldspar in a fine-grained, foliated matrix consisting of chlorite, carbonate, quartz, mica and opaques.

(C) Thin BIF lens in shale (Kaalrug 465 JU). Units such as the one shown are fairly common throughout the study area, but generally cannot be traced laterally for more than ~10 - 20 m at any one locality. Hammer is 30 cm long.

(D) Intraformational breccia in BIF (Stentor 219 JU). Note how several of the larger fragments (arrow) can be fit together, suggesting in situ brecciation. Lens cap is 4.9 cm across.

(E) Boudinage structures in argillaceous BIF (Koedoe 218 JU).

(F) "Snuff-box" weathering structures in BIF (Stentor 219 JU).

and opaque phases. Cleavage is defined by the preferred dimensional arrangement of chlorite and mica laths, and is accentuated by aligned lensoidal clastic fragments.

Whole-rock major and trace element analyses of five specimens of metagreywacke are listed in Table 4.2. Compared with the shales (Table 4.1), the metagreywackes are characterised by appreciably higher Na_2O (1.7 - 3.6 wt %), CaO (1.3 - 5.1 wt %) and Sr (88 - 406 ppm), reflecting the greater modal abundance of carbonates and detrital feldspar fragments in these rocks. SiO_2 (61 - 71 wt %) concentrations are marginally higher, but $\text{Fe}_2\text{O}_3^{\text{total}}$ (5.3 - 7.2 wt %), V (76 - 100 ppm) and Zn (58 - 79 ppm) contents are markedly lower. Cr and Ni abundances are also lower than in associated shales, ranging from 432 - 788 ppm and 87 - 314 ppm, but are markedly enriched relative to concentrations in Palaeozoic greywackes which have average Cr and Ni contents of 42 ppm and 11 ppm, respectively (Bhatia and Crook, 1986).

4.2.3 Banded iron-formations and cherts

Lenticular units of BIF occur prominently intercalated within the shale-greywacke assemblages described above. Present-day thicknesses range from a few centimetres to over 300 m, but are usually less than ~25 m, so that the width of most units shown in Figure 1.4 has had to be exaggerated (Figure 4.2C). Although the majority of BIF's are only traceable along strike for several tens of metres to a few kilometres, some of the thicker occurrences are traceable for over 10 km. The latter typically also give rise to prominent ridges, and thus form useful marker horizons within the otherwise poorly exposed Fig Tree successions.

The BIF's consist of subparallel quartz- and iron-oxide-rich mesobands (terminology after Morris, 1993), ranging from a fraction of a millimetre to ~5 cm in width. The former are composed of fine-grained mosaics of microquartz (recrystallized chert), together with accessory muscovite, and are usually light-grey or dull-white; fine

Table 4.2 Chemical analyses of metagreywackes from the Shebr Formation

Sample	FT3	FT6	FT8	FT12	FT16
SiO ₂ (wt %)	64.65	64.25	70.63	61.03	60.86
TiO ₂	0.57	0.49	0.61	0.59	0.62
Al ₂ O ₃	10.90	11.23	9.93	13.07	13.22
Fe ₂ O ₃ ^{total}	5.25	7.19	5.64	6.27	6.17
MnO	0.16	0.14	0.10	0.09	0.11
MgO	2.19	5.51	3.31	5.07	5.04
CaO	5.08	2.23	1.29	2.01	2.56
Na ₂ O	2.32	1.67	1.79	2.14	3.58
K ₂ O	1.17	1.00	1.58	1.88	1.40
P ₂ O ₅	0.13	0.07	0.08	0.10	0.18
H ₂ O ⁺	0.23	0.11	0.14	0.10	0.04
H ₂ O ⁻	2.53	2.88	2.26	2.62	2.37
CO ₂	4.34	2.95	1.73	4.13	3.63
Total	99.52	99.72	100.49	99.10	99.78
Ba (ppm)	1622	257	313	295	496
Rb	46	29	58	62	44
Sr	406	97	88	205	337
Pb	12	24	11	bdl	10
Y	9	15	19	14	17
Nb	2	6	10	10	9
Zr	57	60	138	136	131
Ga	21	21	12	16	15
V	76	96	83	82	100
Cr	514	696	788	664	432
Zn	58	69	72	78	79
Cu	34	48	63	29	13
Ni	87	226	314	222	109

bdl - below detection limit

disseminations of iron-oxide, however, locally impart a reddish coloration. Iron-oxide-rich mesobands consist of crystallized grains of hematite and magnetite, ranging from submicroscopic to ~1 mm across, with minor quartz and chert.

Thin, laterally impersistent lenses of intraformational breccia were recorded in some BIF horizons (Figure 4.2D). These units are up to ~30 cm wide and contain randomly oriented tabular chert (\pm iron oxide) fragments embedded in a magnetite- and hematite-rich matrix. They conformably overly, and are, in turn, conformably overlain by, undeformed mesobands. In places, the breccia fragments can be still be fit together, suggesting that the brecciation occurred more or less *in situ*.

The majority of BIF's mapped also contain macrobands of ferruginous shale and chert. Thicknesses of these units is usually in the decimetre to metre range. Where exposed, contacts of the shaly macrobands with the over- and underlying BIF macrobands are conformable, but gradational over an interval of several centimetres. Some of the BIF's also grade laterally into predominantly argillaceous units containing only relatively minor proportions of interbedded chert. Thin (typically a few centimetres wide) interbeds of metagreywacke and, less commonly, silicic tuffaceous sedimentary rock, now generally altered to micaceous phyllite or schist, were noted in places.

Features related to later tectonism include pinch-and-swell and boudinage structures (Figure 4.2E), and minor folds ranging from a few centimetres to a few metres across. The folds usually show fairly consistent orientations at any particular locality, and are often characterised by a distinct Z-, M- or S-type geometry which can be related to their position on larger structures. In some areas, the folds also have an associated axial planar cleavage, providing further evidence of a tectonic rather than synsedimentary or diagenetic origin. Field relationships suggest that great thickness of some of the BIF's mapped - notably those in the northern and northeastern parts of Figure 1.4 - is due to tectonic duplication by folding (e.g. Section 9.2.1.3.2). "Snuff-box" structures and botryoidal goethite are common in zones of severe weathering (Figure 4.2F).

Despite the widespread occurrence of BIF throughout the eastern part of the study area, only one iron deposit of note has been discovered to date, on Spago 460 JU (Figure 1.4, C12). According to Groeneveld (1973), the formation of this deposit can be related to secondary upgrading of the host BIF along the contacts of a cross-cutting basic dyke. Quarrying of the ore body during the period 1954 - 1962 yielded ~28 000 tons of high-grade hematite (Groeneveld, 1973).

Siliceous, grey, green and white banded cherty rocks crop out locally, particularly in the Belvue Road Formation, but are less common than the BIF's. The chert units are typically between 1 - 50 m thick and are seldom traceable laterally for more than a kilometre. A notable exception, which is discontinuously exposed over a strike length of ~10 km, occurs along the Scotsman Fault (Section 2.2.1.2.12) in the Revolver Creek Valley (Figure 1.4). The cherts have often undergone considerable ductile shearing and brecciation, but generally resemble cherts within the Bien Venue Formation which are described in detail in Section 4.3.4.

4.2.4 Silicic and intermediate metavolcanic-volcaniclastic rocks

Interlayered with the predominantly argillaceous assemblages of the Belvue Road Formation in some areas are silicic and intermediate volcanic-volcaniclastic rocks, now generally altered to a variety of fine-grained, white-to-grey schists. Thickness of these units is usually less than ~0.5 m and they are seldom traceable along strike for more than a few tens of metres at any one locality. However, on Coulter 391 JU, Koedoe 218 JU and Stentor 219 JU the rock types described above form large lens-like occurrences, with associated minor cherty and shaly intercalations (Figure 1.4, B14, C14, D10, D11, E7 and E10). In the absence of any field evidence to the contrary, these occurrences are also considered to form an integral part of the Belvue Road Formation, but the possibility that some represent Bien Venue Formation rocks coring synclinal folds cannot be ruled out entirely.

Three main varieties of metavolcaniclastic rock have been distinguished mineralogically, viz., muscovite-feldspar-rich, pyrophyllite-rich and chloritoid-rich varieties. The former, which constitute the dominant variety, generally resemble quartz-muscovite schists found within the Bien Venue Formation (Section 4.3.1), but where least deformed are best described as quartz-feldspar porphyries. The porphyries contain millimetre-scale, subhedral-to-anhedral feldspar (albite, microcline, perthite) and quartz porphyroclasts in a fine-grained, homogeneous matrix consisting of quartz, muscovite and feldspar, with minor chlorite, carbonate, epidote and opaques. The feldspars typically show signs of extensive sericitization. In terms of major element chemistry, the quartz-feldspar porphyries are characterised by high SiO_2 , moderate K_2O and Na_2O , and low $\text{Fe}_2\text{O}_3^{\text{total}}$ and MgO abundances, which suggests that they were derived from rhyolitic or rhyodacitic precursors (Table 4.3, columns 1 and 2). TiO_2 concentrations are unusually low and clearly distinguish these rocks from similar lithologies within the Bien Venue Formation (Section 5.2).

Fine-grained quartz-pyrophyllite schists crop out in the vicinity of sample localities BR1 and BR2 in the central part of Coulter 391 JU (Figure 1.4, C14). These rocks closely resemble quartz-muscovite schists, but can be distinguished from the latter in the field by their distinct talcy feel. Where best developed, the schists consist of ~50 - 60 % quartz and ~30 - 40 % pyrophyllite with minor chloritoid and andalusite, the latter showing extensive replacement by pyrophyllite. Accessory minerals include illite-muscovite, chlorite, feldspar, epidote and opaques. Chemically the quartz-pyrophyllite schists are distinguishable from the quartz-feldspar porphyries by their much lower Na_2O , K_2O , Ba, Rb and Sr contents (Table 4.3, columns 3 and 4), reflecting the paucity of feldspar and mica. In places, the rocks grade into quartzose schists containing only traces of pyrophyllite, feldspar, chlorite and mica.

Greyish-green resistant rocks with a fine-grained, massive- to weakly foliated texture occur in the vicinity of sample locality BR6 in the southwestern segment of Koedoe 218 JU (Figure 1.4, E10). These rocks consist predominantly of quartz and

Table 4.3 Chemical analyses of silicic and intermediate metavolcanic-volcaniclastic rocks from the Belvue Road Formation

Column	1	2	3	4	5
Sample	BR4	BR5	BR1	BR2	BR6
SiO ₂ (wt %)	75.25	74.05	80.95	77.95	62.81
TiO ₂	0.08	0.10	0.15	0.15	0.65
Al ₂ O ₃	14.75	16.23	16.09	16.55	17.91
Fe ₂ O ₃ total	0.77	0.84	0.13	2.29	12.39
MnO	0.01	0.01	bdl	0.06	0.21
MgO	0.12	0.57	0.02	0.31	1.55
CaO	1.00	0.06	0.20	0.04	0.22
Na ₂ O	4.87	3.95	0.06	0.12	0.10
K ₂ O	3.40	3.77	0.02	0.03	0.12
P ₂ O ₅	0.02	0.01	0.05	0.03	0.10
H ₂ O ⁻	0.03	0.24	0.01	0.01	0.03
H ₂ O ⁺	0.32	0.67	2.16	2.42	3.70
CO ₂	0.84	5.15	0.02	0.13	0.04
Total	101.46	100.65	99.86	100.09	99.83
Ba (ppm)	290	179	bdl	bdl	57
Rb	69	77	4	4	5
Sr	199	78	10	32	24
Pb	97	5	bdl	2	8
Y	bdl	12	bdl	bdl	17
Nb	6	6	5	5	8
Zr	64	71	74	81	57
Ga	14	15	13	13	24
V	9	8	14	28	241
Cr	bdl	bdl	bdl	bdl	197
Zn	8	9	bdl	6	53
Cu	bdl	8	7	11	24
Ni	7	6	4	23	89

bdl - below detection limit

Columns:
 1 and 2. Quartz-feldspar porphyry (Coulter 391 JU)
 3. Quartz-pyrophyllite-andalusite schist (Coulter 391 JU)
 4. Quartz-pyrophyllite-chloritoid schist (Coulter 391 JU)
 5. Massive quartz-chloritoid-chlorite rock (Koedoe 218 JU)

chloritoid with minor chlorite, the latter two minerals often forming fan-shaped monomineralic clusters. Judging from the analysis listed in Table 4.3, column 5, the rocks represent altered dacite or andesite, although high $\text{Fe}_2\text{O}_3^{\text{total}}$, Cr and V abundances are suggestive of a basaltic precursor.

4.2.5 Depositional setting

Rocks of the Sheba and Belvue Road Formations in the northern part of the BGB have previously been described as representing deep-water slope, fan and basin plain deposits (Eriksson, 1980a, b; Lowe, 1980, 1991; Jackson *et al.*, 1987). Although the origin of the metagreywackes in the study area could not be determined conclusively due to a paucity of diagnostic sedimentary textures (Section 4.2.2), studies elsewhere in the BGB indicate that the rocks are often structured by partial to complete Bouma sequences (Bouma, 1962), implying deposition from low concentration turbidity currents (Eriksson, 1980a, b). The origin of the greywacke conglomerates exposed in the Mhlambanyathi River on Amo 259 JU is uncertain, although absence of bedding, poor sorting and the heterogeneous, variably rounded, clast population suggest that the rocks were deposited as (submarine) debris flows. The shales (Section 4.2.1) represent suspended load material deposited via settling under low-energy conditions; shaly rocks intercalated with the metagreywackes were either deposited during the waning stages of turbidity currents or between successive turbidity flows (Eriksson, 1980a). Petrographic and geochemical data suggest derivation of the sediments from a source composed of cherts, granitoids, and ultrabasic, basic and silicic metavolcanics, the latter probably akin to those found within the Onverwacht Group. Concomitant volcanism during sedimentation is indicated by the localized occurrence of silicic and intermediate metavolcanic-volcaniclastic rocks within the Belvue Road Formation (Section 4.2.4). The BIF's (Section 4.2.3) are likely the product of chemical sedimentation during periods of low clastic sediment input (Beukes, 1973; Eriksson, 1980a; De Ronde *et al.*, 1994); some contemporaneous clastic sedimentation is, however, indicated by the shaly macrobands. Scattered occurrences of intraformational breccia give evidence of the localized reworking of BIF.

4.3 Bien Venue Formation

Rocks of the Bien Venue Formation, named after the type area on the farm Bien Venue 255 JU, are largely restricted to the Stentor Antiform and the Bien Venue Synform (Sections 9.2.2.1 and 9.2.2.2), although exposures also occur in the Strathmore Anticline (Section 9.2.1.1.9) and in the extreme northeastern part of the study area (Figures 1.4 and 4.3). The Formation is made up principally of mica schists, including quartz-muscovite and biotite-oligoclase varieties, derived from silicic volcanic-volcaniclastic precursors. These schists overlie a prominent grey and white banded chert, informally named the Basal Marker, which conformably rests on metasediments of the Belvue Road Formation; locally, however, the basal contact is sheared and appears to be faulted (Section 9.2.1.2.1). Outcrops of chlorite schist, talc schist, serpentinite, phyllite, chert and cherty dolomite occur in places, but are volumetrically of minor importance. Nevertheless, these rocks constitute the only easily recognisable units within the generally highly sheared succession, although their discontinuous nature precludes their use as marker beds on a regional-scale. On Stentor 219 JU and Bien Venue 255 JU, lithologies of the Bien Venue Formation host subeconomic barite and massive sulphide mineralization.

The amount of deformation and alteration which has affected the rocks of the Bien Venue Formation varies considerably, both on a regional- as well as local-scale. Least deformed lithologies occur immediately north of the dam and old iron mine on Spago 460 JU (Figure 1.4, C12 and C13); exposures in this area are, however, very poor, precluding detailed work. Elsewhere, the rocks are pervasively, but heterogeneously, deformed, showing few preserved primary textures. Strain heterogeneity on outcrop scale is locally indicated by the presence of small (5 - 20 cm long), tectonically formed, lozenge-shaped pods of comparatively less deformed schist embedded in a strongly sheared matrix. Distribution of strain in the area north of Three Sisters can be related to proximity to the Stentor pluton which intrudes the Bien Venue Formation in the west

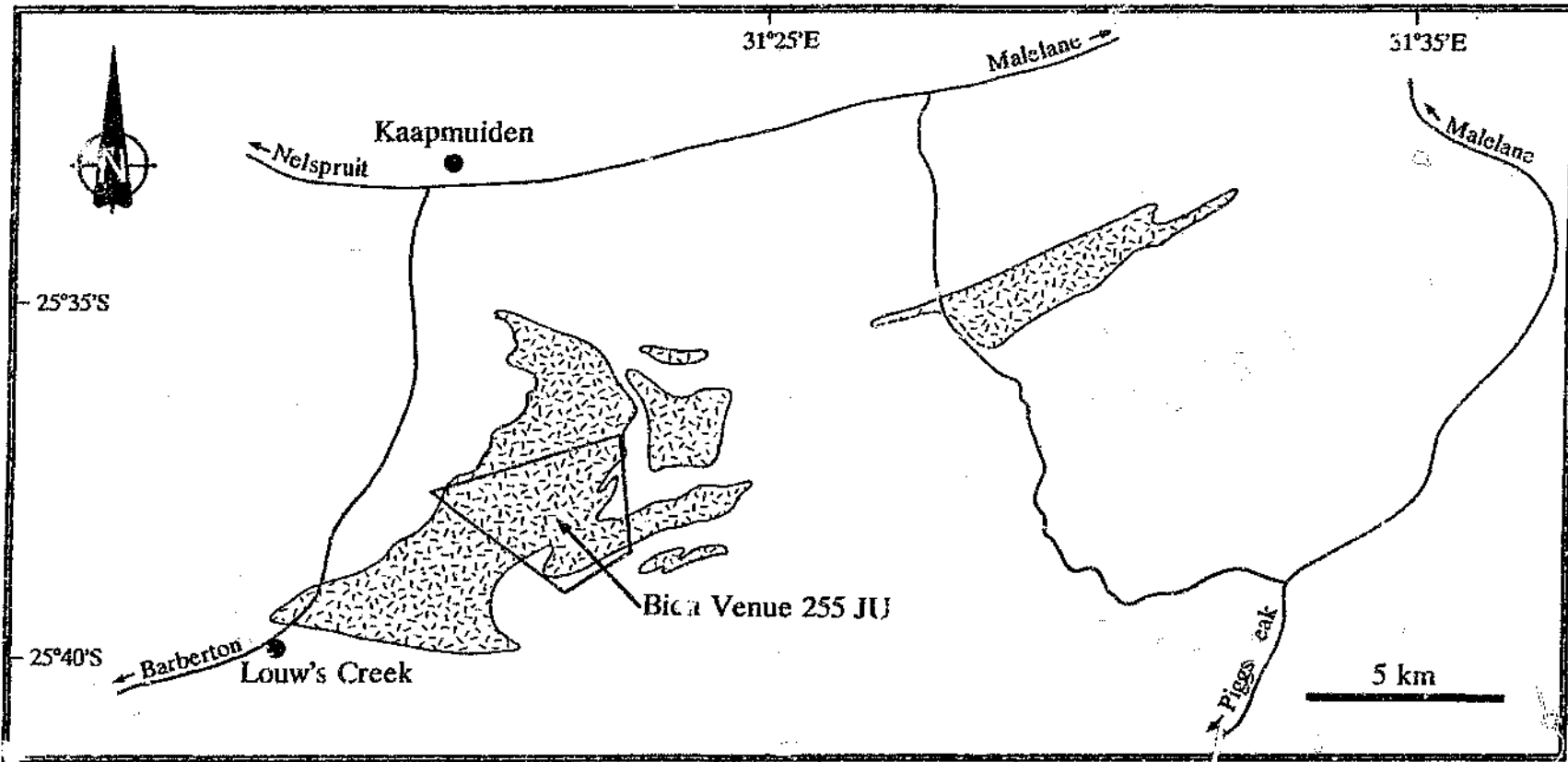


Figure 4.3 Distribution of the Bien Venue Formation and location of the type area (Bien Venue 255 JU).

(Section 8.3.1); foliations (S_4 ; Section 9.2.2.1) are best developed in schists along the granitoid contact and progressively diminish in intensity eastwards.

Owing to structural complications, as well as pronounced lateral and vertical variations, no type section representative of the entire formation can be defined, and the thickness of the original volcanic-volcaniclastic pile cannot readily be determined.

4.3.1 Quartz-muscovite schists

Quartz-muscovite schists constitute the dominant lithology encountered in the Bien Venue Formation. On Bien Venue 255 JU, Stentor 219 JU, Driehoek 221 JU and Strathmore 214 JU these rocks build an arcuate belt of hills overlooking the Kaap River Valley to the west. The schists vary from fine- to medium-grained and, in general, form prominent, jagged, lenticular outcrops. Fresh surfaces are buff or greyish-green, but weathered surfaces are often pale rusty brown due to iron staining. Fuchsite-bearing varieties are characterised by a bright-green coloration. Silicification of the schists is common, particularly close to the granitoid contact and in the core of the Bien Venue Synform. Pseudomorphs of limonite after sulphides occur as fine disseminations in outcrops close to the Bien Venue massive sulphide deposit (Section 4.3.7), as well as along the western boundary of Stentor 219 JU and in the north-central parts of Driehoek 221 JU. Rocks in these areas also in places contain thin limonite encrustations coating fractures and joints.

Despite intense tectono-hydrothermal alteration, relic textures attesting to a volcanic or volcaniclastic protolith are occasionally recognizable in the field. By far the most common primary structures encountered in the rocks are stubby insets of colourless or, less commonly, light-blue quartz ('quartz eyes'). These crystals, which are undoubtedly prekinematic (see later), and probably represent relic β -quartz phenocrysts or pyrogenic grains (Section 4.3.9), impart a weak- to well-developed porphyroclastic texture to the schists. They are most prominent in a broad arcuate band, concave to the west, extending

from the central part of Bien Venue 255 JU to the southeastern apex of Driehoek 221 JU. The insets generally range from ~1 - 5 mm in size, and locally comprise an estimated 30 % or more of the total volume of the schists.

In some areas, the schists contain clasts of recrystallized, granular-textured chert or, more rarely, fine-textured silicic metavolcanic (quartz-muscovite) rock (Figures 4.4A and B). These schists, which typically either contain chert clasts or metavolcanic clasts, occur sporadically throughout the succession, but are best preserved on the ridge overlooking the homestead on Bien Venue 255 JU (Figure 1.4, F5). Here, chert-clast-bearing schists form a discontinuous, northeast-striking unit that is traceable laterally for a few hundred metres. The clasts are generally poorly sorted, range from subangular to rounded, but are typically highly deformed; long axes of ellipsoidal clasts tectonically flattened in the plane of the foliation typically define a prominent L_4 down-dip stretching lineation (Section 3.2.2.3). Clast sizes range between ~0.5 - 15 cm, although highly elongated metavolcanic clasts having long axis dimensions in excess of 50 cm were recorded in a river gully ~700 m southeast of Manders Dam on Three Sisters 254 JU (Figure 1.4, G4). Locally, both the chert-clast- as well as the metavolcanic-clast-bearing schists are affected by extensive silicification. In some exposures, however, variably silicified metavolcanic clasts show evidence of pre-incorporation alteration, occurring in a non-silicified matrix.

Petrographic investigations focused on schists in the immediate vicinity of Three Sisters, which often contain aluminium and ferromagnesian aluminium silicate minerals in addition to quartz and muscovite. Schists adjacent to the Stentor pluton consist essentially of quartz + muscovite \pm andalusite \pm pyrophyllite \pm biotite and are coarser-textured than schists away from the pluton, which consist of quartz + muscovite \pm chlorite \pm chloritoid \pm andalusite \pm pyrophyllite \pm biotite. Minor calcite, plagioclase and microcline have been identified in some samples. Zircon, apatite, tourmaline, epidote and opaques occur as accessory constituents.

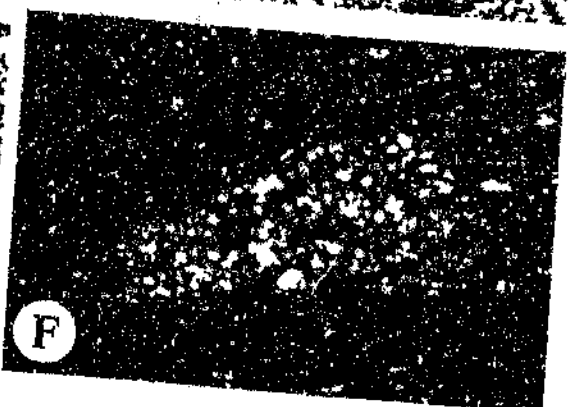
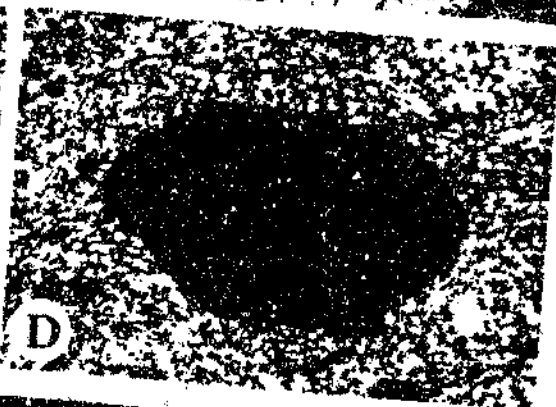
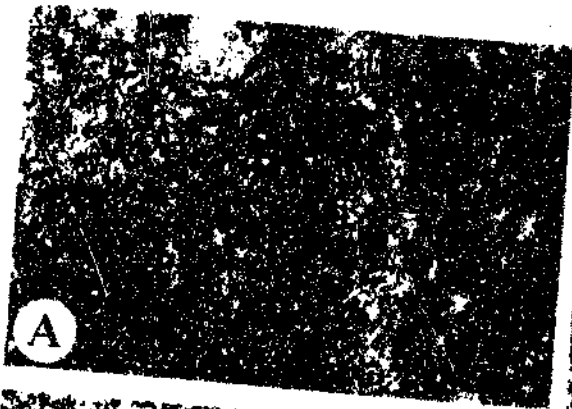


Figure 4.4 Mesoscopic and microscopic features of quartz-muscovite schists:

(A) Chert clasts in quartz-muscovite schist (Bien Venue 255 JU). The clasts are tectonically flattened in the plane of the matrix foliation (S_4) which is parallel to the plane of the photograph; long axes of the clasts define a prominent down-dip stretching lineation (L_4). Lens cap has a diameter of 4.9 cm.

(B) Rounded clasts of silicic metavolcanic rock in quartz-muscovite schist (Bien Venue 255 JU).

(C) Photomicrograph (cross-polarised light; length of field of view = 4.3 mm) showing unstrained, embayed quartz inset.

(D) Photomicrograph (cross-polarised light; length of field of view = 4.3 mm) of quartz inset showing well-developed β -quartz habit.

(E) Photomicrograph (cross-polarised light; length of field of view = 1.8 mm) showing subgrain formation in the necked zones of a boudinaged quartz porphyroclast.

(F) Photomicrograph (cross-polarised light; length of field of view = 4.3 mm) of lensoid mosaic-textured quartz aggregate interpreted as a recrystallized quartz porphyroclast.

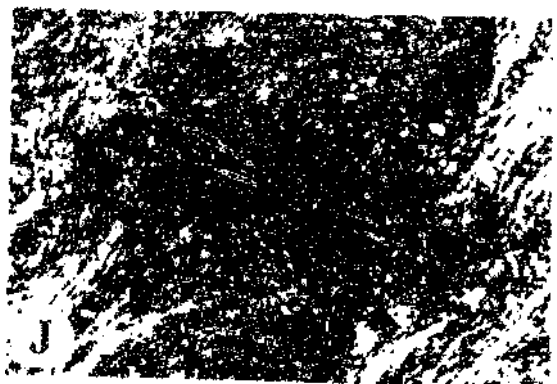
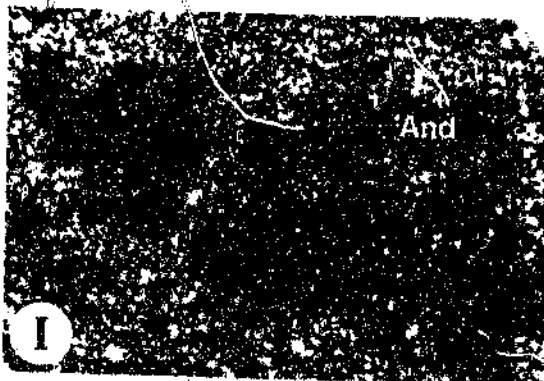
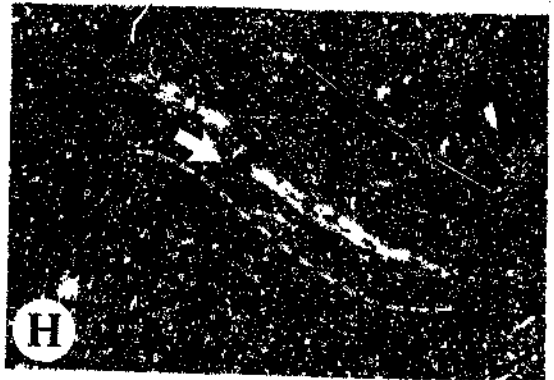
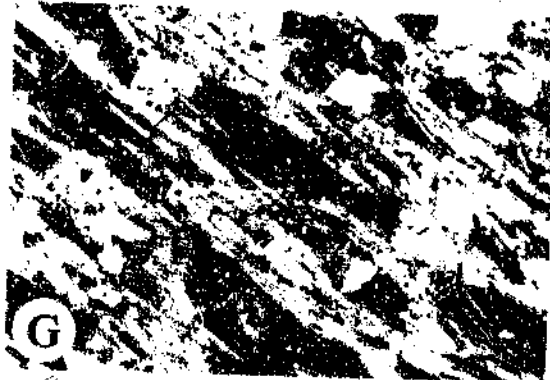


Figure 4.4 (continued):

(G) Photomicrograph (cross-polarised light; length of field of view = 1.8 mm) showing the typical appearance of quartz-muscovite schists close to the Stentor pluton contact.

(H) Photomicrograph (cross-polarised light; length of field of view = 1.8 mm) of andalusite poikiloblast with S-shaped inclusion trails (dashed line). Note the twinned chloritoid crystal (arrow) transgressing the fabric in the andalusite.

(I) Photomicrograph (cross-polarised light; length of field of view = 1.8 mm) of andalusite (And) porphyroblast partly altered to pyrophyllite (Py).

(J) Photomicrograph (cross-polarised light; length of field of view = 1.8 mm) of radial chloritoid aggregate. Note how the matrix foliation (S_d) intensifies close to, and is deflected around, the porphyroblast terminations, suggesting some post-chloritoid flattening.

(K) Photomicrograph (cross-polarised light; length of field of view = 1.8 mm) showing the alteration of fractured plagioclase (Pl) porphyroclast by fine-grained aggregates of muscovite (Ms).

Quartz is the most abundant constituent of the schists, commonly accounting for between ~50 - 65 % of the total volume. The bulk of the quartz occurs as xenoblastic microcrystalline grains. The remainder forms the previously described insets. Under the microscope, the insets display angular-to-rounded, commonly deeply embayed shapes (Figure 4.4C). Hexagonal insets (e.g. Figure 4.4D) are comparatively rare. Most insets are also characterised by strain phenomena; as a general rule, intensity of strain can be related to the intensity of the schistosity in the groundmass, but marked variations are apparent even within individual thin sections. Weakly strained porphyroclasts are typically characterised by slight undulose extinction and occasionally also quartz-infilled pressure shadows in peripheral zones. Porphyroclasts in moderately strained specimens are flattened in the plane of the foliation and exhibit pronounced undulose extinction. Pressure shadows, deformation lamellae, boudinage structures and partial recrystallization are fairly common (Figure 4.4E). Intensely strained and recrystallized porphyroclasts in schists close to the granitoid contact typically occur as lensoid aggregates of mosaic-textured quartz (Figure 4.4F).

Muscovite occurs as finely disseminated, aligned laths or in sheaf-like aggregates defining the matrix foliation (S_0), and generally accounts for ~25 - 40 % of the volume of most specimens examined (Figure 4.4G).

Andalusite may constitute up to ~15% of the total volume of the specimen in which it occurs. The mineral forms xenoblastic porphyroblasts and poikiloblasts ranging up to ~4 mm in size. The poikiloblasts contain straight or weakly sigmoidal inclusion trails defined primarily by lensoid grains of quartz and opaques (Figure 4.4H). Microstructural relationships indicate that andalusite growth occurred both during and after formation of S_0 .

Pyrophyllite can usually only be positively identified by XRD, and is invariably restricted to those specimens which also contain andalusite. The mineral occurs as a fine-grained postkinematic replacement product of the latter along grain boundaries, cleavage planes and microfractures (Figure 4.4I).

Chlorite typically forms discrete, synkinematic xenoblastic flakes and wispy aggregates, intergrown with, and replacing, muscovite. Some chlorite is, however, also found as a postkinematic retrograde alteration product rimming chloritoid and biotite.

Chloritoid displays pronounced multiple twinning and typically occurs as small (~0.1 - 2 mm long), subidioblastic-to-idioblastic porphyroblasts which account for over 15 % of the volume of some specimens. Isolated crystals are most common, but radial and fan-shaped aggregates composed of several crystals were also noted (Figure 4.4J). Chloritoid growth was dominantly postkinematic with respect to S_0 , but as shown in Figure 4.4J, there is also evidence of synkinematic growth.

Biotite typically occurs as isolated ragged flakes intergrown and aligned with muscovite and chlorite, but is occasionally also found in monomineralic clusters. The mineral is usually only present in trace amounts, but one of the specimens analysed chemically (BVR16; Section 5.2.1) contains ~15% biotite.

Finely disseminated xenoblastic grains and granular aggregates of calcite were noted in some specimens, but generally the mineral is present only in trace abundances.

Relic grains of plagioclase (albite - oligoclase) and, less commonly, microcline, invariably showing evidence of deformation and extensive alteration to fine-grained aggregates of muscovite, were recorded in a few samples collected in areas away from the granitoid contact (Figure 4.4K).

Thin sections of least deformed, but commonly highly weathered, rocks on Spago 460 JU reveal abundant euhedral-to-subhedral plagioclase, microcline and perthite crystals, typically ~0.1 - 1 mm across, and showing variable degrees of alteration to muscovite. Large quartz inlets, identical in size and shape to least deformed inlets in schists to the north of Three Sisters, occur sporadically. Surrounding the crystals is a fine-grained, isogranular-to-lepidoblastic groundmass consisting of quartz, feldspar, calcite, muscovite, chlorite, with accessory apatite, epidote - clinozoisite, zircon and opaques. Relic ash- and lapilli-sized fragments of silicic volcanic material were noted in some thin sections. These range from angular to subrounded and are usually characterised by abundant, unoriented feldspar microphenocrysts. With increasing deformation and alteration, the fragments as well as the enveloping groundmass show progressive replacement by muscovite.

4.3.2 Biotite-oligoclase schists

Dark-grey or grey-green weathering micaceous schists consisting predominantly of biotite, but also characteristically containing abundant crystals of oligoclase up to ~7 mm long, were recorded at several localities. The principal exposures of these rocks lie immediately east of the homestead on Bien Venue 255 JU, forming a conspicuous, ~200 m wide and ~1.8 km long, northeast-striking lens-shaped unit, intercalated within, and in places containing intercalations of, quartz-muscovite schist (Figure 1.4, F5). Another notable, but less extensive, occurrence is developed along the western boundary of Stentor 219 JU (Figure 1.4, E7); elsewhere the schists only form thin, isolated outcrops seldom wider than a few metres. Rarely, the rocks are almost totally devoid of large plagioclase crystals, assuming a more homogeneous appearance not unlike that commonly associated with fine-grained amphibolites.

Seen in thin section, oligoclase occurs as discrete, euhedral-to-rounded, occasionally embayed, sericite-dusted porphyroclasts which commonly account for between 15 - 40 % of the volume of rocks (Figure 4.5A). Biotite constitutes the main

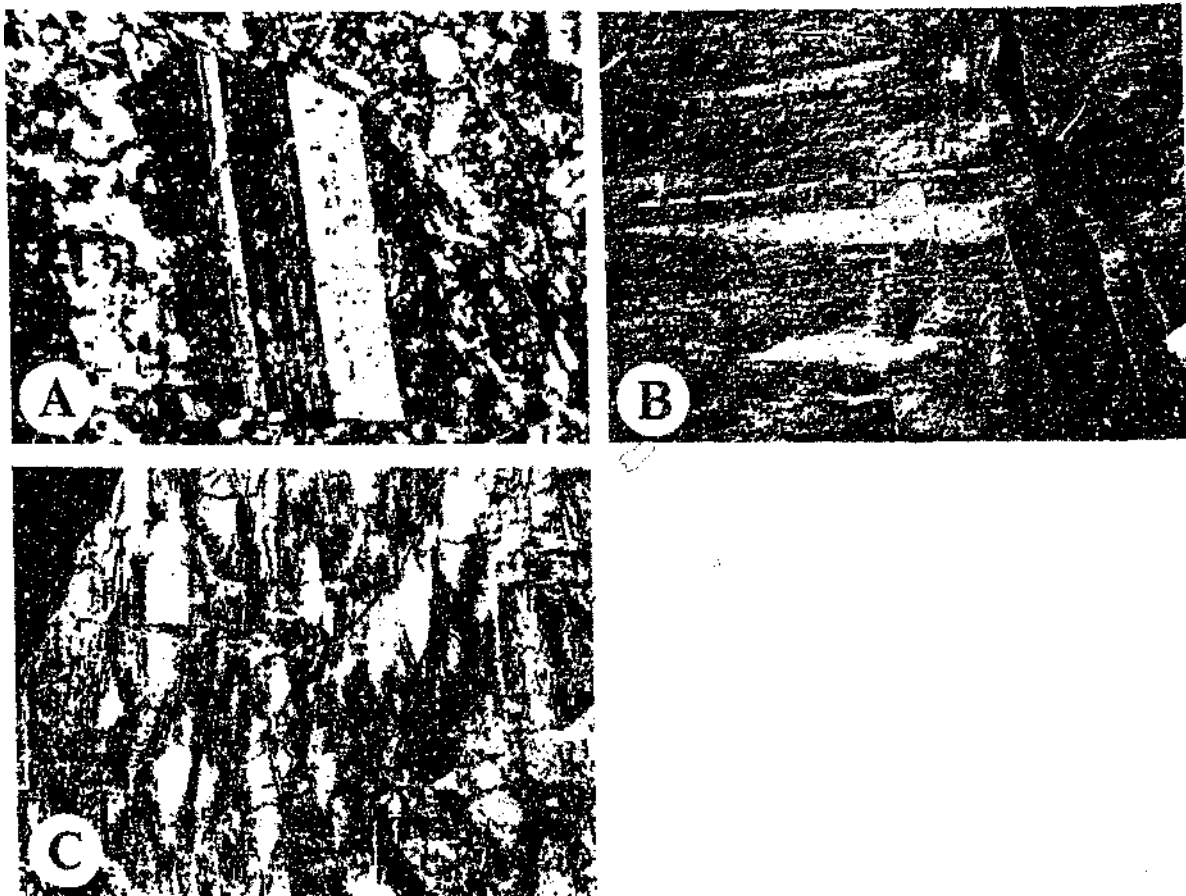


Figure 4.5 Microscopic and mesoscopic features of biotite-oligoclase schists:

(A) Photomicrograph (cross-polarised light; length of field of view = 4.3 mm) showing sericitized, euhedral oligoclase crystal surrounded by microcrystalline biotite-rich matrix.

(B) Lenticular structures interpreted as flattened volcanic clasts (Bien Venue 255 JU). Long axes of the clasts are aligned parallel to the schistosity in the rock (dashed line). Lens cap is 4.9 cm in diameter.

(C) Volcanic conglomerate of the Schoongezicht Formation exposed at Ezzey's Pass, ~15 km northeast of Barberton (see the location map in Figure 1.4).

groundmass mineral, occurring as aligned ragged flakes defining the S_1 schistosity which wraps around the feldspars. Chlorite, calcite, quartz, feldspar and epidote - clinozoisite occur as fine-grained xenoblastic grains intergrown with biotite. Chlorite also commonly occurs as a retrograde replacement product of the mica, while some quartz and calcite is found infilling pressure shadows against the plagioclase porphyroclasts. Accessory minerals include muscovite, sphene, apatite and zircon.

Conspicuous at several localities within the main occurrence of biotite-oligoclase schist are distinctive light-grey lenticular structures, some of which have long axis dimensions in excess of 40 cm (Figure 4.5B). These structures are invariably aligned parallel to the S_1 schistosity in the rocks, suggesting that their present-day morphology is due to tectonic flattening rather than a primary feature. They closely resemble structures found in rocks of the Schoongezicht Formation to the southeast of the New Consort Gold Mine and at Ezzey's Pass (Figure 4.5C), and are believed to represent altered relic clasts of volcanic origin (see also Visser *et al.*, 1956; Viljoen, 1963; Anhaeusser, 1963, 1969, 1976b; Eriksson, 1980b). Apart from the lighter colour, the material comprising the clasts is virtually identical in texture and mineralogy to the surrounding the matrix, and also characteristically contains abundant large oligoclase crystals set in a foliated biotite-rich groundmass. Strongly flattened clasts of recrystallized chert, or more rarely, medium-textured, quartz-feldspar porphyry, were also recorded in some outcrops.

4.3.3 Chlorite schists, talc schists and serpentinites

Basic schists, comprising mainly chlorite \pm amphibole varieties, are locally interlayered with quartz-muscovite schists in the basal parts of the Bien Venue Formation on Stentor 219 JU and Strathmore 214 JU. The principal exposures of these rocks occur along the southern limb of the Strathmore Anticline (Section 9.2.1.1.9). Here the schists form a ~150 - 250 m wide and ~1.5 km long, northwest-striking band which is capped by a 1 - 2 m thick horizon of recrystallized siliceous chert (Figure 1.4, D6, D7 and E7). The basic unit widens progressively eastwards, attaining its fullest development

in the vicinity of the Stentor Barite Mine (Figure 1.4, E7; Section 4.3.6) where it has been affected by W-type parasitic folding associated with the Bien Venue Synform (Section 9.2.2.2). Along the northern limb of the Strathmore Antiform, the basic schists are mainly restricted to a thin, lens-shaped unit that crops out discontinuously over a strike length of ~250 m (Figure 1.4, D7).

Seen in outcrop, the basic schists have a fine-grained, moderate- to well-foliated texture and are devoid of primary structures. Thin sections revealed preferentially oriented chlorite laths together with lesser amounts of quartz, tremolite - actinolite and carbonate. Euhedral-to-subhedral, but generally fractured, porphyroclasts of plagioclase are fairly common. Accessory constituents include sphene, biotite, epidote, stibnomelane and opaques.

Ankle-high outcrops of highly weathered, greyish-green ultrabasic schist were encountered at a few localities, but are far less common than the basic varieties. These rocks consist predominantly of talc with accessory chlorite, carbonate and opaques, and are best developed in a thin (~40 m wide), poorly exposed band underlying the main chlorite schist unit described above (Figure 1.4, D7).

A small (~80 m long and ~30 m wide) lens of weathered greyish-green serpentinite is exposed ~1 km to the northeast of the Bien Venue homestead, but is too limited in extent to plot at the scale of Figure 1.4. Thin outcrops of serpentinite, grading laterally into talc schist, were also sporadically encountered on the eastern slopes of the densely vegetated valley north of the Bien Venue massive sulphide deposit (Section 4.3.7).

4.3.4 Cherts and cherty dolomites

Siliceous cherty rocks occur as a minor component throughout the Bien Venue Formation, but as mentioned in Section 4.3, are best developed along the lower contact, forming the Basal Marker. This unit ranges in thickness from less than one metre to a

maximum of ~350 m, and consists of banded, grey, brown and white chert, grading in places into zones of massive- to finely laminated grey chert. Thicknesses of the mesobands, which are parallel and continuous on outcrop scale, generally varies between ~0.1 - 3 cm, but layers as thick as ~15 cm are not uncommon. The thicker grey chert layers often contain numerous light-to-undulating microlaminae of white chert and *visa versa*. Thin (generally < 30 cm wide) breccia lenses containing tabular fragments of white chert enclosed by a dark-grey cherty matrix occur in places (Figure 4.6). Microscopically, the chert consists of recrystallized, polygonal-textured microquartz, with minor to accessory amounts of sericite, feldspar, chlorite, carbonate, epidote and iron oxide. The darker coloration of the grey mesobands reflects the presence of carbonaceous material which is visible under the microscope as fine opaque disseminations between the quartz crystals. In some thin sections, ghost outlines of original angular-to-rounded, silt- and sand-sized detrital grains can be recognised.

Locally, the Basal Marker contains impersistent intercalations of finely laminated shale, greywacke and silicic tuffaceous metasedimentary rocks, the latter often extensively altered to quartz-muscovite schist. The thickness of these macrobands is usually in the centimetre to decimetre range, although tuffaceous units several metres wide were recorded on Sutherland 214 JU and Koedoe 218 JU. Replacement of the contained tuffaceous and argillaceous units by irregular cross-cutting veinlets and networks of chert is common.

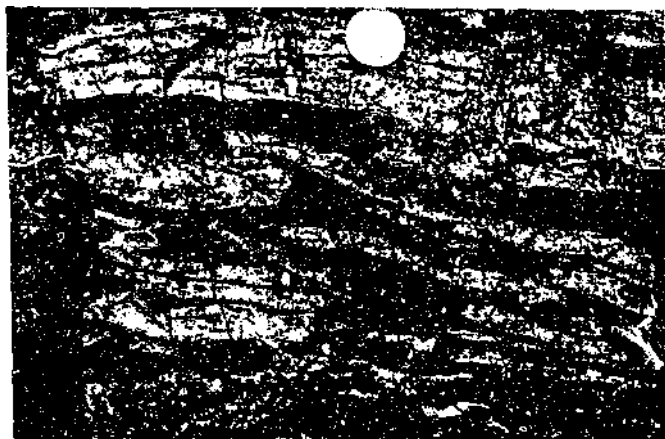


Figure 4.6 Breccia unit in grey and white banded chert (outcrop 219 JU). Coin is 2.4 cm across.

Cherty units higher up in the stratigraphy of the Bien Venue Formation generally resemble the Basal Marker texturally, but are rarely thicker than a few tens of metres, nor traceable along strike for more than a few hundred metres to a few kilometres. Cherts outcropping in the vicinity of the Stentor Mine (Figure 1.4, E7) also contain thin layers and lenses of barite which are described in greater detail in Section 4.3.6.

Tectonized cherts are characterised by a pervasive shear or fracture cleavage, oriented both parallel and oblique to bedding, and are often seen to contain conspicuous amounts of fuchsite, the latter imparting a bright-green coloration to the rocks. Small-scale fold structures, seldom more than a few tens of centimetres across, are also locally developed.

Less common than the siliceous cherts described above are dark coloured, dolomite-rich lithologies. Unlike the former, outcrops of these rocks are generally poor and discontinuous. The best exposures occur at a locality ~700 m to the west of the main workings of the Stentor Mine. Here, the carbonate rocks form a ~4 - 5 m wide and ~250 m long unit outlining the hinge and southern limb of a small isoclinal fold (Figure 1.4, E7). Outcrops show crude, but generally subparallel bands of recrystallized dark-brown dolomite and grey chert varying in thickness between ~5 - 50 cm (Figure 4.7). Contacts between individual dolomite and chert layers are typically highly irregular, with thin veinlets of the latter penetrating the former and *visa versa*, suggesting that the rocks either represent silicified dolomites or dolomitized cherts.

Thin (typically < 2 m wide) discontinuous outcrops of cherty dolomite were also sporadically encountered along the northern limb of the Strathmore Anticline. The rocks in this area have, however, undergone severe deformation and recrystallization, and consequently do not display the layering seen in outcrops west of the Stentor Mine.



Figure 4.7 Dolomite (D) - chert (C) lithology (Stentor 219 JU). Compass (circled) is 10 cm long.

4.3.5 Phyllites and slates

Discontinuous lenses of thinly bedded, brown- to grey-weathering argillaceous phyllite and slate occur interlayered with the quartz-muscovite and biotite-oligoclase schists in some areas. Thicknesses of these units is typically in the centimetre-to-decimetre range, but locally exceed several tens of metres; only the distribution of the main occurrences is shown in Figure 1.4. Interbeds of quartz-muscovite schist are found in some of the thicker units, while angular phyllite clasts occur within the enclosing schists. Mineralogically, the phyllites consist of angular, silt-sized quartz and rare feldspar grains set in a fine-grained, muscovite- and chlorite-rich matrix which is locally carbonaceous. In some outcrops, the phyllites are seen to contain scattered quartz insets, identical to those which occur in the porphyroclastic quartz-muscovite schists (Section 4.3.1), or less commonly, strongly flattened pebble-sized clasts of recrystallized chert.

4.3.6 Stentor barite deposit

Mention was made in Section 4.3.4 of the barite mineralization at the Stentor Mine, situated ~1.8 km west of the homestead on Stentor 219 JU (Figure 1.4, E7). The geology of this deposit, which was mined during the early 1940's, has been

comprehensively described by previous workers (Viljoen and Viljoen, 1969g; Groeneveld, 1973; Reimer, 1980) so that only a brief description need be included here. The barite occurs as thin (~1 - 15 cm wide), pale-green or grey-coloured interlayers and lenses within steep- to subvertically dipping cherty rocks, the latter hosted by quartz-muscovite schists to the south of the main chlorite schist unit outlined in Section 4.3.3. According to Reimer (1980), the mineralized zone extends over a stratigraphic height of ~70 m and is traceable along strike for about 700 m. Microscopic examination of several specimens of barite collected by the writer in the old mine workings revealed fine-grained, granular masses of turbid barite, along with minor amounts of quartz, pyrite and hematite/limonite, the latter two minerals probably representing oxidized sulphides. Disseminated carbonate and chalcopyrite occur in places. Reimer (1980) reported the presence of faint cross-laminations and rounded chert fragments in some of the barite layers.

Total barite production from Stentor Mine amounted to ~1350 tons (Groeneveld, 1973). A re-evaluation of the deposit by Anglo American Prospecting Services (Pty) Ltd. during the mid 1980's indicated further reserves of ~10 000 tons (SAMINDABA⁵).

Correlation of the Stentor barite deposit, which was originally thought to occur in rocks of the Onverwacht Group (Viljoen and Viljoen, 1969g; Groeneveld, 1973; Reimer, 1980), with the Fig Tree Group makes this occurrence somewhat unique in the BGB. In contrast to other barite deposits in the Fig Tree Group - notably those in the Barite Valley Syncline to the south of Barberton - which occur in clastic sedimentary rocks (Heinrichs and Reimer, 1977), the Stentor mineralization is hosted by sheared metavolcanic-volcaniclastic rocks. Such a host rock association is more typical of the barite occurrences within the Theespruit Formation, particularly those along the Londozi River in northern Swaziland and on the farms Vergelegen 728 JT, Witklip 188 IT and Houtbosch 189 IT to the south and southwest of Barberton (Viljoen and Viljoen, 1969g; Widenbar, 1976; Reimer, 1980; Barton, 1982).

⁵ South African Mineral Deposit Data Base, Council for Geoscience, Geological Survey of South Africa.

4.3.7 Bien Venue massive sulphide deposit

The Bien Venue massive sulphide deposit, situated in the southern sector of Bien Venue 255 JU (Figure 1.4, G5), was discovered in 1978 by Anglo American Prospecting Services (Pty) Ltd. during a regional-scale soil sampling geochemical survey (T. Molyneux, pers. comm., 1992). Evaluation work continued up to 1986, but no economic mineralization was located. Further work was carried out by General Mining, Metals and Minerals Ltd. who acquired the exploration rights for 1990 (P. Harrison, pers. comm., 1991). The results of both exploration programmes are confidential, so that the size and grade of the ore body are not known to the writer.

A detailed study of the Bien Venue deposit (Harwood and Murphy, 1988; Murphy, 1990) indicated that the mineralized zone, which has a width of ~50 - 70 m, is localized within quartz-muscovite schists, interpreted to represent deformed lapilli tuffs. The host rocks, as well as the contained sulphide zone, have been subjected to folding associated with the Bien Venue Synform (Section 9.2.2.2), so that on surface the mineralization is manifest as a poorly exposed, V-shaped zone of gossan and gossanous schist, traceable over a strike length of ~300 m.

The bulk of the sulphide mineralization occurs in steep- to subvertically dipping, massive and semi-massive lenses situated near the top of the host tuff unit (Murphy, 1990). The lenses consist of recrystallized fine-grained pyrite and sphalerite, together with variable, but lesser, amounts of galena, tennantite, chalcopyrite and covellite; sphalerite and galena are preferentially concentrated towards the stratigraphic hangingwall of the deposit. Native silver and copper-silver sulphides, including jalpaite and mackinstryite, occur interstitially. The sulphides often occur in stringers aligned parallel the host rock S_4 schistosity (confirmed in this study), which is axial planar to the Bien Venue Synform (Section 9.2.2.2), suggesting that the recrystallization accompanied D_4 deformation

(Section 9.3.2). Fine disseminations of pyrite and chalcopyrite are present in the immediate footwall, while thin (< 1 m wide) laterally impersistent barite, chert and dolomite layers characterise the uppermost portions of the ore body (Murphy, 1990).

4.3.8 Quartz \pm tourmaline veins

Quartz veins, some of which exceed ~70 m in length, are prolifically developed in schists to the north and west of Three Sisters. The veins are best developed along the Stentor pluton contact and generally lie within the S_4 foliation. The vein material is predominantly a grey quartz. Tourmaline occurs as an accessory constituent in most of the veins, typically forming discrete, acicular crystals ranging in length from ~0.5 - 2 cm. However, in some places the veins contain dense fibrous masses of greenish-black tourmaline. Locally, these veins exhibit a crude banding consisting of alternating quartz- and tourmaline-rich layers which are oriented subparallel to the long axis of the vein (Figure 4.8). The enclosing schists are typically extensively silicified and tourmalinized. There is little doubt that the veins resulted from silica and boron metasomatism accompanying the intrusion of the Stentor pluton.



Figure 4.8 Crudely banded quartz (Q) +tourmaline (T) veins in quartz-muscovite schist (S) (Bien Venue 255 JU). Width of main vein in view is ~1.5 m.

4.3.9 Depositional setting

Alteration and deformation have generally obliterated the primary textural and petrographic characteristics of the Bien Venue Formation lithologies and, hence, any discussion pertaining to the latter's depositional setting cannot be definitive. Moreover, volcanic terranes are known to be influenced by a wide range of syn- and post-eruptive processes that are difficult to unambiguously interpret even in weakly deformed ancient successions (Cas and Wright, 1987). However, despite these limitations, some broad interpretations concerning the most likely pre-alteration characteristics and palaeoenvironment of the Bien Venue Formation rocks can be made from the available relic textures, and more importantly, the nature of the associated mineralization.

Quartz inclusions similar to those in the study area (Section 4.3.1) have been widely documented in ancient silicic volcanic terranes around the world (e.g. Hopwood, 1976; Berge, 1981; Frater, 1983). Their origin and significance has, however, attracted some debate in the past. Hopwood (1976) suggested that the inclusions represent porphyroblasts formed by solid state growth during metamorphism and deformation, but subsequent work by Vernon and Flood (1977), Berge (1981), Frater (1983), Vernon (1986) and Williams and Burr (1994) indicated that they represent relic inverted β -quartz phenocrysts or pyrogenic crystals. Petrographic evidence obtained during the course of the present investigation (Section 4.3.1) favours the latter interpretation. Further evidence supporting a prekinematic origin for the quartz inclusions includes their occurrence in only weakly altered rocks in the northeastern parts of the study area (Section 4.3.1). The plagioclase porphyroclasts (Sections 4.3.1, 4.3.2 and 4.3.3) are similarly interpreted as relic phenocrysts or pyrogenic crystals. The irregular embayments that characterise the majority of quartz, and some of the plagioclase porphyroclasts probably reflect magmatic resorption prior to eruption (Vernon, 1986). The rounding of the corners and edges of the porphyroclasts may reflect epiclastic reworking, but may also have resulted from pre-eruptive reaction with magma (Cas and Wright, 1987).

Thus, the textural evidence suggests that the porphyroclastic quartz-muscovite and biotite-oligoclase schists were derived from crystal-rich protoliths. According to Cas and Wright (1987), the production of crystal-rich volcanoclastic rocks can be attributed to a variety of factors. These include the (explosive) eruption of highly crystallised magmas from high-level magma chambers and/or syn- to post-eruptive physical crystal fractionation mechanisms involving the destruction and elutriation of less resistant and fine-grained fragments, and the concomitant concentration of resistant crystals. Hence, the porphyroclastic schists either represent primary pyroclastic deposits (crystal tuffs) or crystal-rich epiclastic sediments. The possibility that *some* of the schists represent near-surface intrusive rocks also cannot be discounted. The significance of the quartz insets is discussed further in Section 6.2.

Those schists that contain relic clasts of volcanic material (Sections 4.3.1 and 4.3.2) superficially resemble coarse-textured pyroclastic, hyaloclastic and autobreccia deposits such as occur in the vicinity of some volcanic-hosted massive sulphide (VHMS) deposits (e.g. De Rosen-Spence *et al.*, 1980; Cas, 1992). However, the generally rounded nature of the clasts indicates that they were subjected to post-eruptive reworking and, hence, that the rocks represent volcanolithic sediments rather than primary breccias. This is supported by their overall resemblance to, and close spatial association with, the chert-clast conglomerates which are undoubtedly of sedimentary origin. Whether the clasts represent epiclasts derived from the erosion and weathering of volcanic rock (Fisher and Schmincke, 1984) or whether they represent reworked unconsolidated pyroclastic, hyaloclastic or autobrecciated debris is, however, not clear.

Cas and Wright (1987) demonstrated that conglomerates in volcanic terranes often record the reworking and redeposition of detritus in fluvial or near-shore settings, but may also be the product of debris flows and high concentration turbidity currents. Thus, it is evident that the rocks form in both subaerial as well as subaqueous settings, and that by themselves, they have little palaeoenvironmental significance. Nonetheless, rounding of some of the clasts, particularly the resistant chert varieties, is suggestive of vigorous

fluvial and/or wave-related abrasion. The occurrence of conglomeratic units as an integral part of the volcanic-volcaniclastic succession, coupled with the absence of extraneous clasts composed of ultrabasic, basic or granitoid material such as occur in the underlying Sheba and Belvue Road Formations (Section 4.2.2), indicates that the sediments were derived solely from the localized, penecontemporaneous reworking of the volcanic pile.

The phyllite and slate intercalations (Section 4.3.5) provide further evidence of the dominantly effusive nature of the succession. Thin bedding suggests that the rocks were mainly deposited under quite hydrodynamic conditions. The muscovite-rich mineralogy of the rocks, coupled with the localized presence of embayed quartz insets and the absence of extraneous basic-ultrabasic or granitoid fragments, once again suggests that the sediments were derived mainly from the localized reworking of the volcanic pile.

Available textural evidence suggests that the cherty horizons (Section 4.3.4) represent silicified argillaceous and tuffaceous sedimentary rocks. Studies on similar rocks elsewhere in the BGB (e.g. Louw and Knauth, 1977; Lanier and Lowe, 1982; Paris *et al.*, 1985; Paris, 1990) suggested that the chertification took place during or soon after deposition of the sediments as a consequence of surface or near-surface hydrothermal activity. The origin of the cherty dolomites (Section 4.3.4) is uncertain, although they probably represent silicified calcareous sediments.

From the foregoing it is clear that the preserved textures and rock types do not single out any particular palaeoenvironment for the Bien Venue Formation. More significant clues to the environment of deposition are, however, provided by the Stentor barite deposit (Section 4.3.6) and the Bien Venue massive sulphide deposit (Section 4.3.7). Field and stable-isotope studies of the former led Viljoen and Viljoen (1969g) and Reimer (1980; pers. comm., 1991) to conclude that the barite mineralisation formed in a low-energy submarine environment as a consequence of synvolcanic fumarolic

exhalations. Similarly, despite recrystallization, preserved textural evidence indicates that the Bien Venue sulphide ores also resulted from sea-floor exhalative activity coeval with the volcanism (Murphy, 1990; P. Harrison, pers. comm., 1991). Thus, the nature of the associated mineralization strongly suggests that the Bien Venue Formation lithologies were deposited in a subaqueous environment.

The probable exhalative origin of the Bien Venue sulphide ores also allows some speculation as to the palaeodepth (shallow or deep) of the volcanism, even though the depths at which VHMS ores form has proved to be controversial. To some extent, this controversy reflects the diversity of settings in which such deposits are known or inferred to occur (e.g. Hutchinson, 1980, 1990; Franklin, 1986; Sawkins, 1990). Osterberg *et al.* (1987) suggested that silicic volcanic units outcropping in the vicinity of the Headway-Coulee massive sulphide prospect in Canada are comparable to modern, shallow, subaqueous-to-subaerial hydroclastite deposits, providing evidence that the ores formed in a shallow-water environment. Apparent shallow-water settings are also indicated by primary ignimbritic units and shallow marine fossils within silicic volcanics and associated sedimentary rocks hosting the sulphide ores at the Mount Chalmers Mine in Australia (Sainty, 1992) and in the Lima region of Peru (Vidal, 1987).

Most of the recent literature dealing with VHMS deposits, however, emphasizes the deep-water setting of these ores (e.g. Rona, 1988; Barley, 1992; Cas, 1992; Waters and Wallace, 1992; Allen, 1992). Shallow depth estimates that have been proposed for some deposits may be incorrect due to: (1) the misinterpretation of fragmental rocks which formed by the autobrecciation and quench fragmentation of deep-water lavas as *in situ* pyroclastic rocks of shallow-water origin (Cas, 1992); (2) the formation of apparent subaerial or shallow-water pseudopyroclastic textures in lavas which have been subjected to the combined effects of devitrification, perlitic fracturing and hydrothermal alteration (Allen, 1988; Berry *et al.*, 1992); (3) the downslope transport of shallow-water or even subaerially deposited facies by mass-flow processes (Cas and Wright, 1987; Cas, 1992); and/or (4) the juxtaposition of shallow- and deep-water volcanic facies as a consequence

of synvolcanic extensional tectonics, which some workers maintain forms an integral part of the exhalative ore-forming environment (e.g. Sillitoe, 1982; Cathles *et al.*, 1983; Ohmoto and Takahashi, 1983; Swinden, 1991), or due to subsequent thrust imbrication.

Given the diversity of VHMS-type ores, it is prudent to limit the present discussion to comparison with the well-preserved and comprehensively studied Miocene polymetallic Kuroko deposits of Japan (Ohmoto and Skinner, 1983), which display most of the salient geologic and mineralization features of the Bien Venue deposit (Murphy, 1990), as well as Archaean massive sulphide deposits in general (Cathles *et al.*, 1983; Nisbet, 1987; Ujike and Goodwin, 1987; Poulsen *et al.*, 1992). Fluid inclusion (Pisutha-Arnond and Ohmoto, 1983) and foraminiferal studies (Guber and Merrill, 1983) have shown that the Kuroko ores formed at water depths of at least 1800 m. Modern Kuroko-type analogues, presently forming on the sea floor in the Okinawa Trough and in the Sumisu Rift, have not been recorded at depths shallower than ~1200 m (Kimura *et al.*, 1988; Halbach *et al.*, 1989; Urabe and Kusakabe, 1990). Theoretical constraints also indicate that Kuroko-type mineralization is unlikely to occur, or have occurred, in shallow-water environments. According to Ridge (1973), water depths of greater than ~900 m are necessary to prevent boiling (phase separation) of the ascending ore-forming hydrothermal fluids below the water - rock interface; shallower depths result in premature, subsurface boiling, producing vein- or replacement-type deposits rather than exhalative-type ores.

From the above, it seems likely that the Bien Venue massive sulphide ores and, hence, the associated volcanic-volcaniclastic rocks of the Bien Venue Formation were deposited in a deep-marine environment at depths of greater than ~1000 m. In making this statement, the writer does not preclude the possibility that some of the schists were derived from shallow-water or possibly even subaerial deposits. Indeed, it is possible, if not likely, that the volcanic terrane was characterised by considerable relief and/or marked subsidence. Furthermore, as mentioned previously, rounding of the clasts may indicate high-energy reworking of the sediments by fluvial or littoral processes in

emergent parts of the volcanic complex (no longer preserved?). However, given the presence of VHMS mineralization, it seems likely that these sediments were subsequently redeposited in a deep-water environment; such downslope resedimentation of subaerial and shallow-water deposits has been widely documented in modern and ancient volcanic terranes (e.g. Giles and Hallberg, 1982; Ricketts *et al.*, 1982; Cas and Wright, 1987; Dolozi and Ayres, 1991; Car and Ayres, 1991; Cas, 1992).

Although speculative, the deep-water setting favoured by the writer for the Bien Venue Formation conforms with the palaeoenvironmental setting of the underlying Sheba and Belvue Road Formations in the northern sector of the BGB (Section 4.2.5). Because of recrystallization, a fluid inclusion study of the Bien Venue sulphide ores would probably not yield any useful information about the depth of ore-formation to corroborate or refute the writers preferred interpretation.

5. GEOCHEMISTRY AND GEOCHRONOLOGY OF THE BIEN VENUE FORMATION

5.1 Introduction

A detailed geochemical investigation of the principal rock types within the Bien Venue Formation was undertaken in order to: (1) identify their likely protoliths; (2) characterise the chemical effects of the alteration process on the quartz-muscovite schists; (3) compare the quartz-muscovite and biotite-oligoclase schists with similar rocks elsewhere in the BGB; and (4) constrain their most likely tectonomagmatic setting.

Considerable care was taken to avoid sampling outcrops that showed severe deformation / alteration, so that the analyses reflect, as closely as possible, primary compositions. Nonetheless, interpretation of the chemical data is limited by the mobility of certain elements during alteration. Unfortunately, owing to a lack of any unaltered material as well as precursor heterogeneity (see later), evaluation of element mobility during alteration, using, for instance, the isocon method of Grant (1986), is not possible. Numerous chemical studies have, however, shown that Al, the high field-strength elements (HFSE - Ti, Y, Nb, Zr, Hf, Ta), the rare earth elements (REE) and, to a lesser extent Th and some transition metals (V, Cr, Sc, Ni), are immobile during low-grade alteration of basic and silicic rocks, while Si, Fe, Mg, Ca, Na and K, and the low field-strength elements (LFSE - Ba, Rb, Sr, Cs) are mobile (e.g. Wood *et al.*, 1979; Ludden *et al.*, 1982; Campbell *et al.*, 1984; MacLean and Kranidiotis, 1987; Whitford *et al.*, 1989; Blundy and Crocket, 1992; Cullers *et al.*, 1993). The writer has taken cognizance of these studies and has manipulated and interpreted the data accordingly. In particular, the use of traditional classification schemes based on major elements, such as those presented by Irvine and Baragar (1971), Jensen (1976) and Le Bas *et al.* (1986), has been avoided.

5.2 Quartz-muscovite schists

A total of eighteen samples of quartz-muscovite schist, ranging in mass from ~1 - 2 kg, were collected for analysis by XRF. Eleven of these have also been analysed by INAA. A list of the samples and their respective compositions is given in Table 5.1.

The major and trace element analyses exhibit a fair degree of variability reflecting differences in modal mineralogy. SiO_2 varies in the range 63 - 80 wt %, but in most cases exceeds 72 wt %; those samples containing abundant quartz porphyroclasts (e.g. X3, BVR10 and BVR18) characteristically exhibit the highest SiO_2 concentrations. Al_2O_3 contents are usually very high (> 16 wt %). Together, SiO_2 and Al_2O_3 typically account for ~90 wt % of the total major element composition of the schists. K_2O ranges from ~1.4 - 6.2 wt %. Na_2O abundances in the majority of samples analysed are extremely low and could not be detected by means of the standard XRF techniques employed at the University of the Witwatersrand; Na_2O concentrations in those samples that have been analysed by INAA typically range between 0.2 - 0.4 wt %; the higher Na_2O value of 3.8 wt % recorded for sample BVR15 reflects the presence of relic plagioclase. CaO concentrations are usually very low, rarely exceeding 0.3 wt %; the higher CaO contents of samples BVR15 (1.2 wt %) and BVR16 (3.6 wt %) can be attributed to the presence of plagioclase porphyroclasts in the former and minor amounts of secondary calcite in the latter. The schists are also poor in the ferromagnesian elements, with $\text{Fe}_2\text{O}_3^{\text{total}} + \text{MnO} + \text{MgO}$ generally < 5 wt %.

Rb, Ba and Cs abundances range, respectively, from 35 - 124 ppm (\bar{x} = 64 ppm), 96 - 299 ppm (\bar{x} = 156 ppm) and 1.9 - 6.7 ppm (\bar{x} = 4.2 ppm). Sr values seldom exceed 40 ppm; the much higher Sr content of 120 ppm recorded for BVR15 can, once again, be attributed to plagioclase. On the Zr/TiO₂ - Nb/Y discrimination diagram of Winchester and Floyd (1977), the schists plot in the field of rhyodacites and dacites, with a minor overlap into the andesite field (Figure 5.1).

Table 5.1 Chemical data for quartz-muscovite schists from the Bien Venue Formation

Sample	BVR1	BVR2	BVR3	BVR4	BVR5	BVR6	BVR7	BVR8	BVR9
SiO ₂ (wt %)	74.55	76.57	78.76	71.73	72.04	72.47	74.28	73.90	75.16
TiO ₂	0.5 [§]	0.36	0.36	0.58	0.47	0.59	0.47	0.51	0.56
Al ₂ O ₃	16.21	15.39	12.86	18.37	16.87	18.64	17.29	18.01	16.11
Fe ₂ O ₃ <i>total</i>	0.23	3.44	0.75	2.92	3.93	2.68	1.90	2.68	3.02
MnO	bdl	0.14	0.02	0.06	0.27	0.18	0.11	0.25	0.15
MgO	0.37	0.58	3.85	0.45	0.52	0.31	3.18	0.24	0.37
CaO	0.33	0.14	0.02	0.30	0.08	0.03	0.01	0.04	0.27
Na ₂ O [§]	-	0.26	-	0.19	-	0.26	-	0.25	-
K ₂ O	3.81	2.71	2.22	4.01	1.96	1.62	2.10	1.36	2.07
P ₂ O ₅	0.15	0.12	0.02	0.16	0.06	0.51	0.04	0.09	0.16
L.O.I.	1.98	1.86	2.23	1.96	2.34	2.85	2.63	2.80	2.21
Total	98.21	101.57	101.09	100.73	98.54	100.14	99.01	100.17	100.08
Ba (p.p.m.)	299	116	220	103	198	104	120	138	96
Rb	77	65	41	49	124	47	52	35	66
Sr	33	9	26	13	38	39	19	21	18
Cs	-	4.67	-	2.32	-	4.73	-	3.63	-
Pb	6	5	6	6	8	9	8	9	8
U	-	1.61	-	0.72	-	0.84	-	1.47	-
Th	-	5.35	-	3.52	-	4.27	-	4.70	-
Y	21	21	21	23	26	23	22	25	19
Nb	9	9	6	14	13	14	15	13	13
Zr	131	85	169	141	147	152	147	145	140
Hf	-	3.51	-	2.71	-	3.76	-	3.74	-
Ta	-	1.02	-	0.75	-	0.85	-	0.94	-
Ga	22	21	20	22	23	22	22	21	19
V	79	57	29	74	90	79	60	72	59
Cr	50	14	5	20	37	37	21	37	43
Se	-	8.18	-	6.13	-	10.4	-	8.37	-
Zn	18	23	44	18	18	17	13	17	15
Cu	18	15	13	9	9	14	12	8	10
Ni	20	24	12	23	28	56	17	13	28
Co	-	10.4	-	3.32	-	8.95	-	1.40	-
As	-	1.61	-	2.83	-	3.43	-	4.22	-
La	-	24.5	-	16.3	-	21.7	-	24.6	-
Ce	-	50.5	-	32.5	-	46.6	-	50.1	-
Nd	-	22.2	-	15.9	-	21.4	-	21.3	-
Sm	-	3.76	-	2.48	-	3.35	-	3.68	-
Eu	-	1.06	-	0.74	-	0.95	-	1.14	-
Tb	-	0.59	-	0.47	-	0.60	-	0.60	-
Yb	-	2.35	-	1.61	-	4.22	-	2.51	-
Lu	-	0.25	-	0.22	-	0.31	-	0.41	-
Au (ppb)	-	2.9	-	1.0	-	1.7	-	1.5	-

§ - Na₂O analysis by INAA; L.O.I. - loss on ignition; bdl - below detection level

Table 5.1 (continued)

Sample	BVR10	BVR11	BVR12	BVR13	BVR14	BVR15	BVR16	BVR17	BVR18
SiO ₂ (wt %)	76.26	72.57	73.51	72.01	69.25	66.88	63.36	73.06	79.71
TiO ₂	0.60	0.48	0.45	0.56	0.65	0.61	0.25	0.50	0.52
Al ₂ O ₃	16.05	17.15	17.04	16.62	18.56	19.46	16.48	18.95	13.53
Fe ₂ O ₃ ^{total}	0.87	4.08	2.81	3.35	3.38	2.03	2.92	1.60	0.93
MnO	bdl	0.32	0.17	0.20	0.14	0.01	0.10	0.13	0.02
MgO	0.11	0.41	0.38	0.88	0.61	2.17	2.24	0.26	0.34
CaO	0.25	0.12	0.08	0.30	0.12	1.15	3.62	0.07	0.09
Na ₂ O [§]	0.25	-	0.27	0.32	0.35	3.77	0.43	0.31	-
K ₂ O	2.03	1.72	2.32	3.30	3.96	1.64	6.24	2.35	2.14
P ₂ O ₅	0.16	0.11	0.11	0.17	0.17	0.28	0.08	0.10	0.10
L.O.I.	1.50	2.55	2.59	2.25	2.52	2.42	4.35	3.02	1.82
Total	100.08	99.51	99.73	99.96	99.71	100.42	100.07	100.35	99.20
Ba (ppm)	98	121	114	176	220	183	236	121	139
Rb	50	42	57	74	51	58	111	50	48
Sr	12	19	28	26	32	120	33	29	17
Cs	2.92	-	4.16	5.51	6.70	1.86	6.05	4.24	-
Pb	7	8	9	5	6	12	15	7	5
U	1.07	-	1.77	1.03	1.23	1.16	1.66	1.87	-
Th	2.84	-	5.81	3.36	4.13	4.51	6.92	5.98	-
Y	19	20	26	21	23	39	19	24	25
Nb	12	14	15	10	12	19	12	15	15
Zr	142	138	145	148	171	241	96	160	232
Hf	3.27	-	3.62	3.76	4.43	5.34	2.83	4.30	-
Ta	0.64	-	1.10	0.73	0.82	1.14	1.13	1.13	-
Ga	20	22	22	21	23	25	18	23	19
V	74	65	64	111	125	116	49	86	53
Cr	56	25	23	73	82	34	78	49	27
Sc	6.57	-	6.65	9.87	11.2	12.9	4.51	6.09	-
Zn	11	23	19	21	19	66	38	19	12
Cu	10	18	20	10	17	14	22	16	23
Ni	22	27	23	33	22	11	18	15	12
Co	1.78	-	3.74	7.77	4.69	6.28	7.32	1.73	-
As	3.15	-	4.06	2.69	13.4	0.57	0.31	5.95	-
La	19.6	-	26.5	25.5	25.8	33.6	26.1	31.6	-
Ce	42.0	-	55.0	51.7	55.9	76.7	55.3	61.4	-
Nd	20.7	-	22.5	20.7	25.7	33.9	20.1	27.4	-
Sm	3.28	-	3.78	3.79	4.20	6.19	3.27	4.47	-
Eu	0.90	-	0.99	1.15	1.31	1.83	0.72	1.12	-
Tb	0.53	-	0.60	0.59	0.65	0.96	0.52	0.62	-
Yb	1.20	-	2.51	2.49	2.49	3.51	2.32	2.46	-
Lu	0.22	-	0.31	0.32	0.51	0.45	0.33	0.32	-
Au (ppb)	4.7	-	2.2	2.5	5.0	4.7	4.9	5.9	-

§ - Na₂O analysis by INAA; L.O.I. - loss on ignition; bdl - below detection level

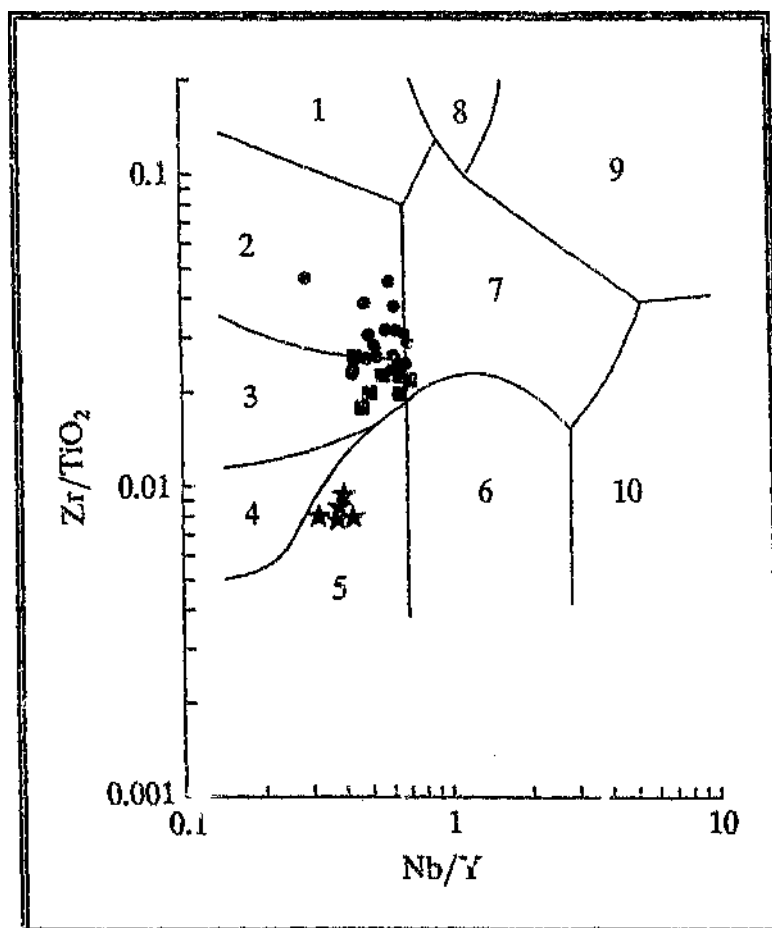


Figure 5.1 Zr/TiO_2 - Nb/Y discrimination diagram (after Winchester and Floyd, 1977) for metavolcanic-volcaniclastic rocks of the Bien Venue Formation. Symbols: circles - quartz-muscovite schists; squares - biotite-oligoclase schists; triangles - chlorite schists. Fields: 1 - rhyolite; 2 - rhyodacite / dacite; 3 - andesite; 4 - andesite / basalt; 5 - sub-alkaline basalt; 6 - alkali basalt; 7 - trachyandesite; 8 - comendite / pantellerite; 9 - trachyte; 10 - basanite / nephelinite.

Relative to chondrite, the schists have strongly fractionated REE patterns ($La_N/Yb_N = 6.4 - 11$), with no, or only weakly developed, negative Eu anomalies ($Eu/Eu^* = 0.71 - 1.01$) (Figure 5.2). These steep REE profiles suggest a primary alkaline or calc-alkaline affinity (e.g. Jakeš and Gill, 1970; Lesher *et al.*, 1986). Nb/Y ratios generally ≤ 0.65 (Figure 5.1) and Ce concentrations significantly < 100 ppm, however, preclude an alkalic affinity (see Winchester and Floyd, 1977).

In summary, the geochemical data suggest that the quartz-muscovite schists were derived from a suite of calc-alkaline dacites and rhyodacites.

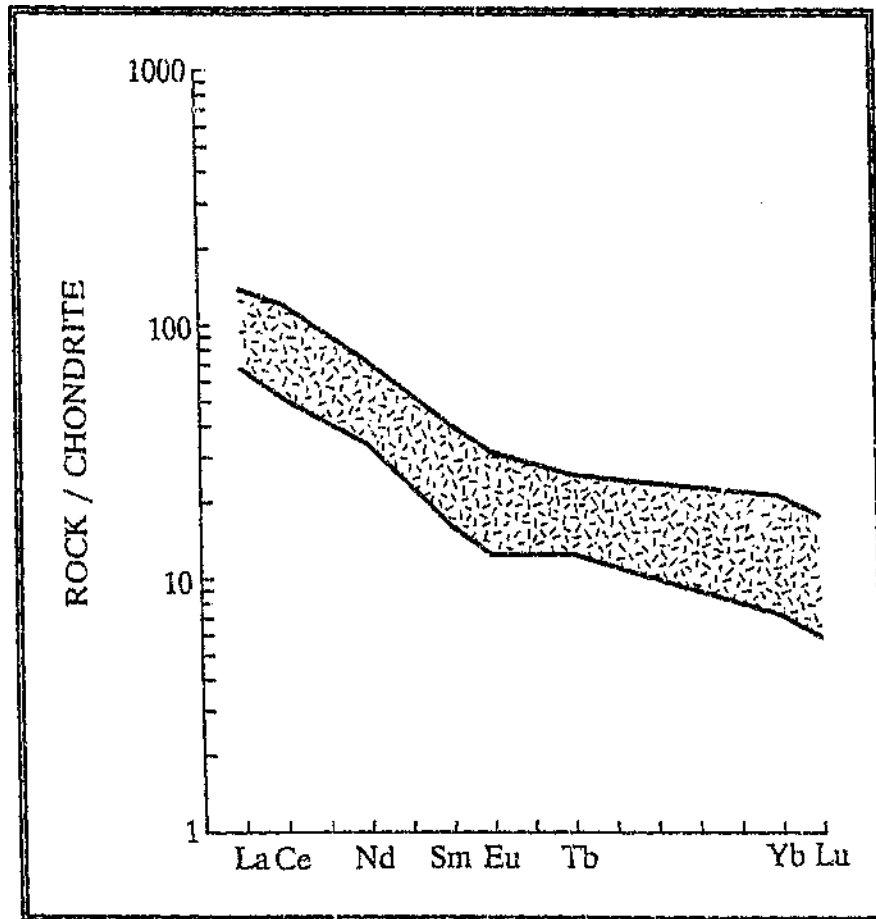


Figure 5.2 Envelope of chondrite-normalised REE data for the quartz-muscovite schists.

5.2.1 Metamorphism - metasomatism

Field and petrographic considerations outlined in Sections 4.3.1, 8.3.1 and 9.3.2 indicate that rocks of the Bien Venue Formation to the north and west of Three Sisters have been subjected to a single episode of dynamothermal contact metamorphism - metasomatism associated with the diapiric intrusion of the Stentor pluton. The purpose

of this section is to summarise the principal mineral transformations that occurred during the alteration of the quartz-muscovite schists, and to provide some quantitative pressure - temperature (P - T) constraints. Note that the various reactions discussed take into account chemical constraints outlined in Sections 5.1, 5.2.2.1 and 5.2.2.2.

On an A'FK diagram (Figure 5.3), the schist samples generally plot either within the muscovite - chloritoid - andalusite + pyrophyllite field or within the muscovite - chloritoid - chlorite field. However, sample BVR16, which contains conspicuous amounts of biotite (Section 4.3.1), plots along the muscovite - biotite tie-line.

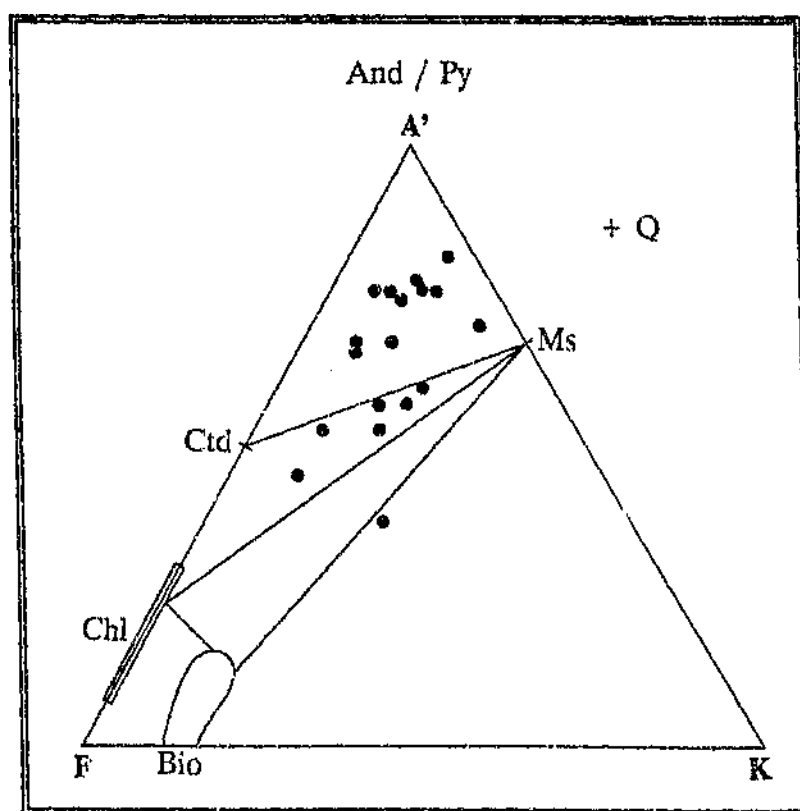
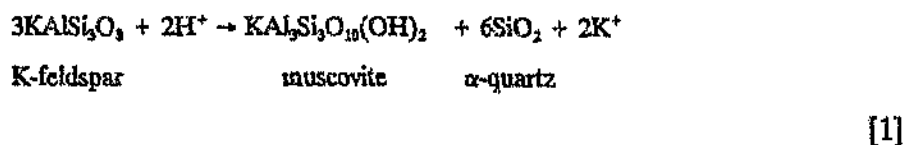


Figure 5.3 A'FK ($A' = Al_2O_3 + Fe_2O_3 - Na_2O + K_2O + CaO$; $F = FeO + MgO + MnO$; $K = K_2O$; all abundances expressed as molecular proportions of the oxides) plot for quartz-muscovite schist (after Winkler, 1979). Fe_2O_3 / FeO ratios were fixed at 0.1. Corrections were carried out for ilmenite, the paragonite component of muscovite, calcite (BVR16) and the albite component of plagioclase (BVR15). Mineral abbreviations: And - andalusite; Bio - biotite; Chl - chlorite; Ctd - chloritoid; Ms - muscovite; Py - pyrophyllite; Q - quartz.

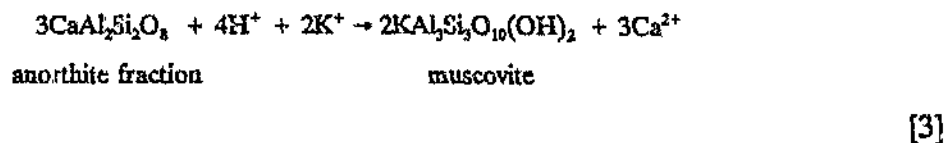
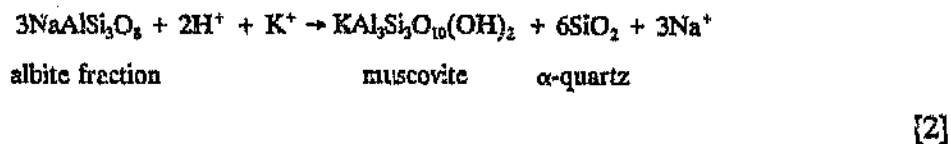
5.2.1.1 Prograde effects

The main mineralogical changes that took place during the prograde event, as deduced from microtextural evidence outlined in Section 4.3.1, involved: (1) the breakdown of primary feldspars to muscovite; and (2) the formation of andalusite, chlorite, biotite and chloritoid. The relative stabilities of the various reactions that are inferred to have occurred during prograde alteration have been summarized in two schematic phase diagrams utilizing the variables aK^+/aH^+ , aNa^+/aH^+ and $aFe^{2+}/a(H^+)^2$ (Figure 5.4). These variables are among the most important involved in the metasomatic transformations.

Ubiquitous white mica in the schists reflects the hydrolysis of feldspar. The breakdown of K-feldspar to muscovite is described by the reaction:



Similarly, the hydrolysis of plagioclase in the presence of K^+ , the latter possibly supplied by [1], can be accounted for by the reactions:



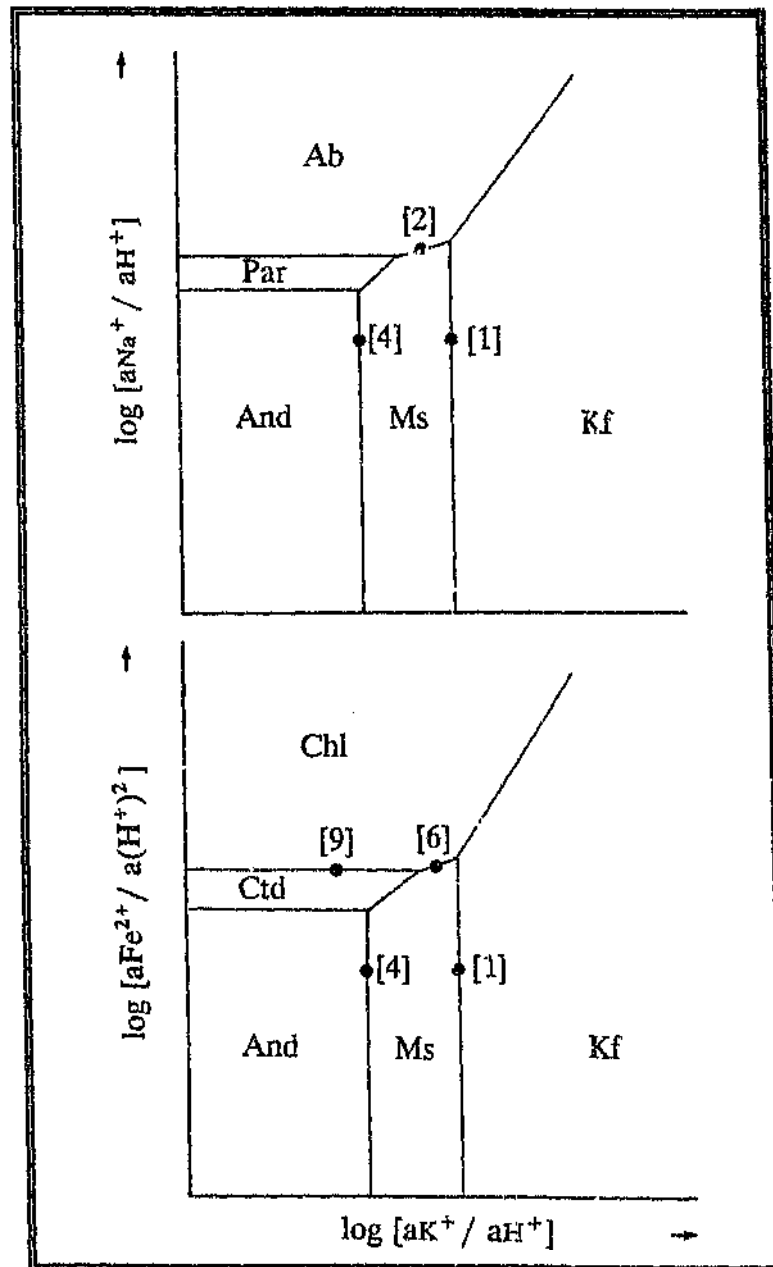
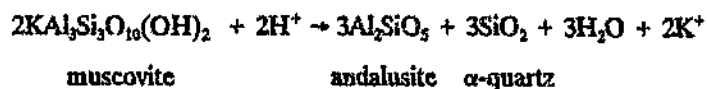


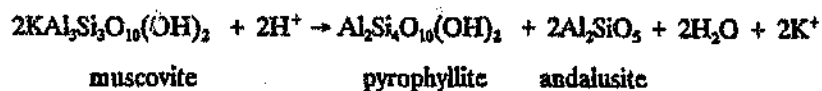
Figure 5.4 Schematic phase diagrams of $\log aNa^+/aH^+$ versus $\log aK^+/aH^+$ (after Bowers et al., 1984) and $\log aFe^{2+}/a(H^+)^2$ versus $\log aK^+/aH^+$ (modified after Phillips, 1988), showing the relative stability fields of the main metasomatic transformations (circles; numbers refer to equations listed in the text) that are inferred to have occurred during prograde alteration of the quartz-muscovite schists. All phases in equilibrium with quartz. Mineral abbreviations: Ab - albite; And - andalusite; Chl - chlorite; Ctd - chloritoid; Kf - K-feldspar; Ms - muscovite; Par - paragonite.

The formation of andalusite can be attributed to the hydrolysis of muscovite formed in [1], [2] and [3] (Montoya and Hemley, 1975):



[4]

Some andalusite may also have formed via the following reaction (Hemley, 1959):

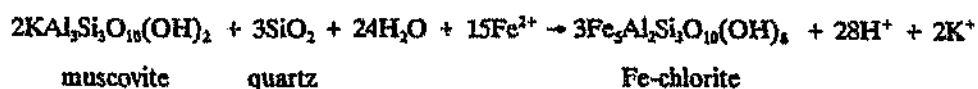


[5]

This reaction is, however, not favoured by the writer since pyrophyllite appears to occur as a retrograde alteration product of andalusite (see later) rather than as a stable co-product (Section 4.3.1). However, since fine-grained pyrophyllite is indistinguishable from fine-grained muscovite in thin section, the possible existence of prograde pyrophyllite cannot be disproved and, hence, reaction [5] has been included for completeness.

The hydrolysis of feldspar to muscovite and ultimately to andalusite resulted from a decrease in the $a\text{K}^+/a\text{H}^+$ and $a\text{Na}^+/a\text{H}^+$ values (and probably also the pH) of the fluid (Figure 5.4).

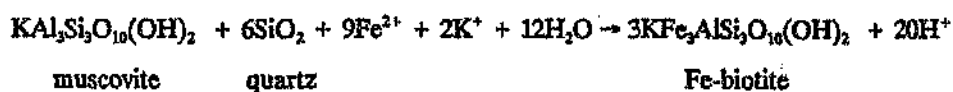
Chlorite in the prograde assemblage appears to have formed at the expense of muscovite according to the following reaction which assumes an iron end-member composition (Jasiński, 1988):



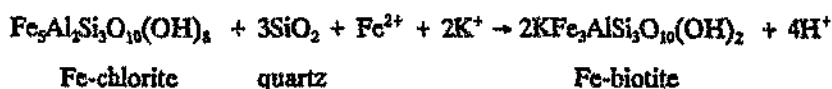
[6]

This reaction accompanied an increase in the $a\text{Fe}^{2+}/a(\text{H}^+)^2$ value of the fluid (Figure 5.4).

Biotite also appears to have formed from muscovite, but some may have been derived from chlorite. Assuming an iron end-member composition, the formation of biotite may be expressed as follows (Jasiński, 1988; Hemley and Hunt, 1992):

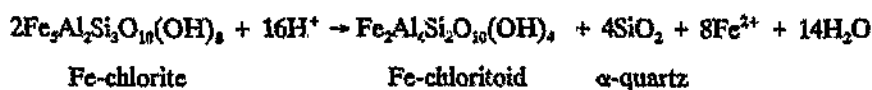


[7]



[8]

The nature of the chloritoid-forming reaction is not entirely clear, but probably involved the late-stage breakdown of chlorite as follows:



[9]

The various equilibria that have been used to constrain the P - T conditions during prograde alteration are shown in Figure 5.5. PH_2O is assumed to have equalled total pressure.

The occurrence of andalusite within the assemblage indicates that the pressure was less than 4.5 kb (Pattison, 1992). Maximum temperatures along the granitoid contact are constrained by the stability of quartz + muscovite. According to the experimental

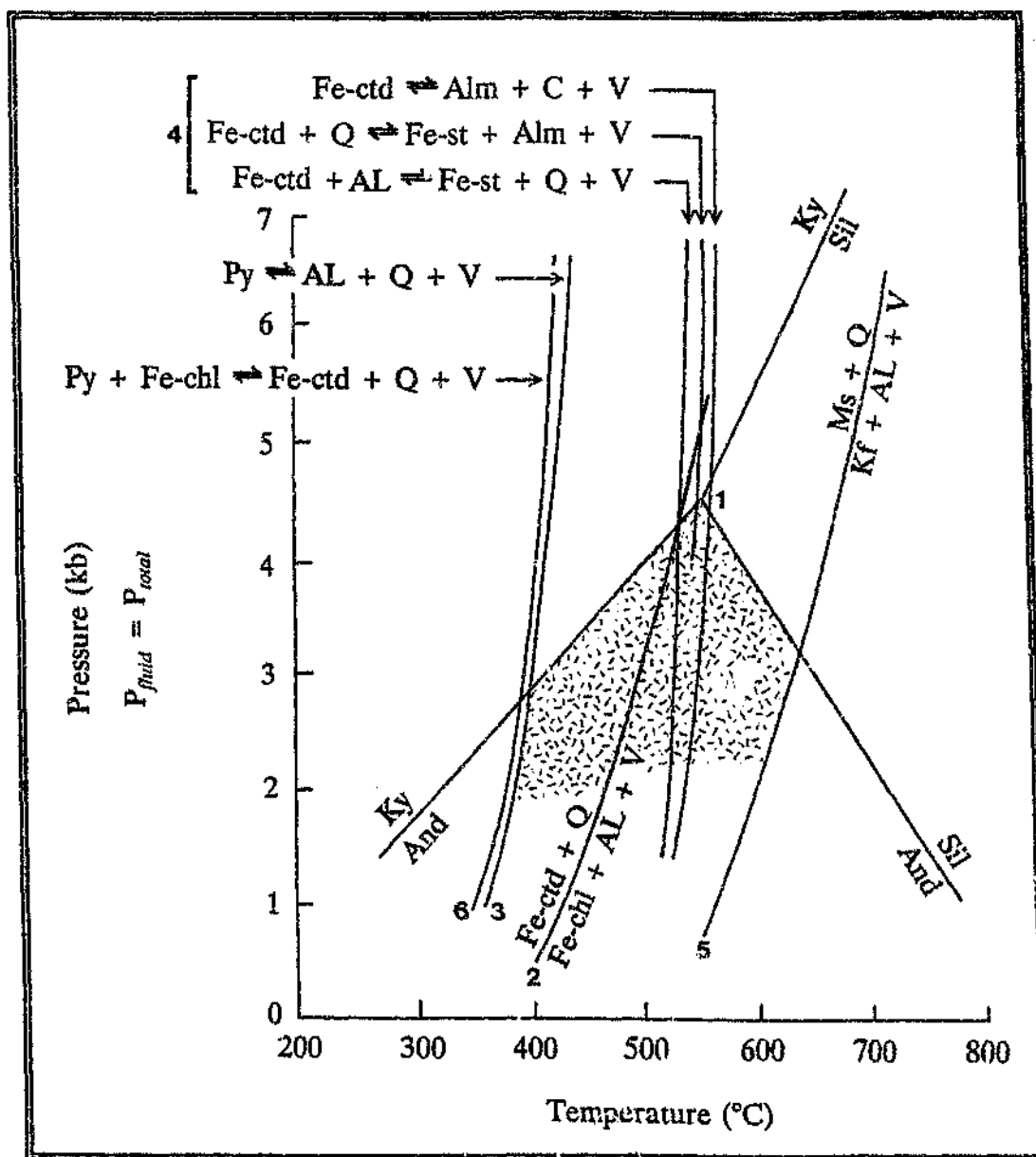


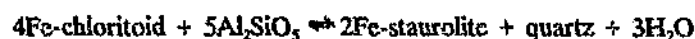
Figure 5.5 P-T grid showing the various equilibria that have been used to constrain the conditions of prograde alteration of quartz-muscovite schists in the Three Sisters area (randomly oriented dashes). Phase abbreviations: AL - Al_2SiO_5 polymorph; Alm - almandine; And - andalusite; C - corundum; Fe-chl - Fe-chlorite; Fe-ctd - Fe-chloritoid; Kf - K-feldspar; Ky - kyanite; Ms - muscovite; Py - pyrophyllite; Q - quartz; Sil - sillimanite; Fe-st - Fe-staurolite; V - H_2O . Equilibria: 1 - Pattison (1992); 2 - Frimmel (1994); 3 - Hemley et al. (1980); 4 - Ganguly (1969); 5 - Chatterjee and Johannes (1974); 6 - Zhou et al. (1994).

work of Chatterjee and Johannes (1974), these two phases coexist to fairly high temperatures (~600°C at 2 kb and ~680°C at 4.5 kb) before reacting to form K-feldspar and andalusite / sillimanite (Figure 5.5):



[10]

Maximum temperatures away from the immediate granitoid contact may be estimated from the stability of chloritoid, but are subject to chemical (i.e. bulk-rock and mineral composition, f_{O_2}) provisos. As a first approximation, four equilibria based on the work of Ganguly (1969) and Frimmel (1994) have been considered (Figure 5.5):



(~525°C at 2 kb; ~540°C at 4.5 kb) [11]



(~555°C at 4.5 kb) [12]



(~540°C at 2 kb; ~565°C at 4.5 kb) [13]



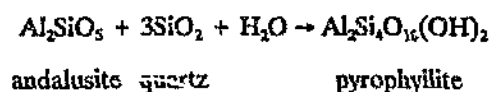
(~460°C at 2 kb; ~530°C at 4.5 kb) [14]

These equilibria were chosen because they involve the breakdown of chloritoid to form staurolite, almandine, corundum and kyanite which are reported to occur in siliceous rocks elsewhere in the BGB and surrounding greenschist zone remnants (e.g. Viljoen and Viljoen, 1969d; Anhaeusser, 1972, 1978; De Wit, 1983). Chloritoid stability indicates that temperatures away from the Stentor pluton contact did not exceed ~460 - 530°C depending on the pressure.

Minimum temperatures during prograde alteration are limited by the stability of biotite, which requires a minimum of ~400 °C (Aggarwal and Nesbitt, 1987; Winkler, 1979), and also the apparent absence of pyrophyllite within the paragenesis, which implies temperatures of greater than ~380 - 410°C (Hemley *et al.*, 1980; Frimmel, 1994, Zhou *et al.*, 1994)(Figure 5.5).

5.2.1.2 Retrograde effects

Retrograde effects, probably related to cooling during the waning stages of contact metamorphism, are mainly manifested by the partial replacement of the andalusite by pyrophyllite and the chloritization of biotite and chloritoid (Section 4.3.1). The breakdown of andalusite to pyrophyllite can be accounted for by the reaction (Hemley *et al.*, 1980; Frimmel, 1994):



[15]

which proceeds at temperatures of between ~380 - 410°C in the andalusite field (Figure 5.5).

The chloritization of biotite and chloritoid reflects a shift to the left of reactions [8] and [9] in Section 5.2.1.1.

5.2.2 Element distribution patterns

Evidence outlined in Sections 4.3.1 and 5.2.1.1 indicates that the alteration of the quartz-muscovite schists involved a change from a primary quartz + plagioclase + K-feldspar assemblage to a secondary quartz + muscovite dominated assemblage. These changes have produced complex and often seemingly erratic element distribution patterns which differ markedly from those characterising unaltered igneous suites. As will be shown, alteration led to the decoupling of LFSE and HFSE distribution patterns. The

LFSE's show coherent trends with K suggesting that they are primarily controlled by muscovite. The HFSE's, on the other hand, do not exhibit any systematic variations with K ; their present-day distribution appears to reflect complexities associated with the superposition of alteration-related chemical enrichment effects onto the primary compositional characteristics.

5.2.2.1 Low field-strength elements

One of the notable features of the chemistry of the quartz-muscovite schists is their low Na_2O and CaO contents (Section 5.2). As shown by reactions [2] and [3] in Section 5.2.1.1, this can be attributed to the hydrolysis of primary plagioclase which releases Na^+ and Ca^{2+} to the hydrothermal fluids. K^+ , on the other hand, appears to have been incorporated mainly into muscovite (reactions [1], [2] and [3] in Section 5.2.1.1). The marked depletion of Na and Ca relative to K during alteration is clearly evidenced by the remarkably high K_2O/Na_2O (5 - 21) and K_2O/CaO (11 - 210; BVR16 excluded) ratios recorded for the feldspar-free samples. By contrast, sample BVR15, which contains relic plagioclase (Section 5.2), is characterised by much lower K_2O/Na_2O (0.4) and K_2O/CaO (1.4) ratios. Unaltered dacitic-to-rhyodacitic volcanics have average K_2O/Na_2O and K_2O/CaO ratios of 0.5 - 0.8 (Le Maitre, 1976).

A plot of Na_2O versus K_2O for the feldspar-free specimens shows a positive linear trend, suggesting that the small concentrations of Na in the rocks can be attributed to the paragonite ($NaAl_3Si_3O_{10}(OH)_2$) component of muscovite (Figure 5.6). Ca probably occurs as the margarite ($CaAl_4Si_2O_{10}(OH)_2$) component of muscovite, but data points on a plot of CaO versus K_2O are widely scattered, reflecting poor XRF analytical precision at low absolute CaO abundances (Figure 5.6).

Presented in Figure 5.7A - C are a series of variation diagrams showing the extent to which K controls the distribution of the trace elements Rb, Cs, Ba and Sr in the schists. Plots of Rb and Cs against K yield well-defined positive trends attributed to

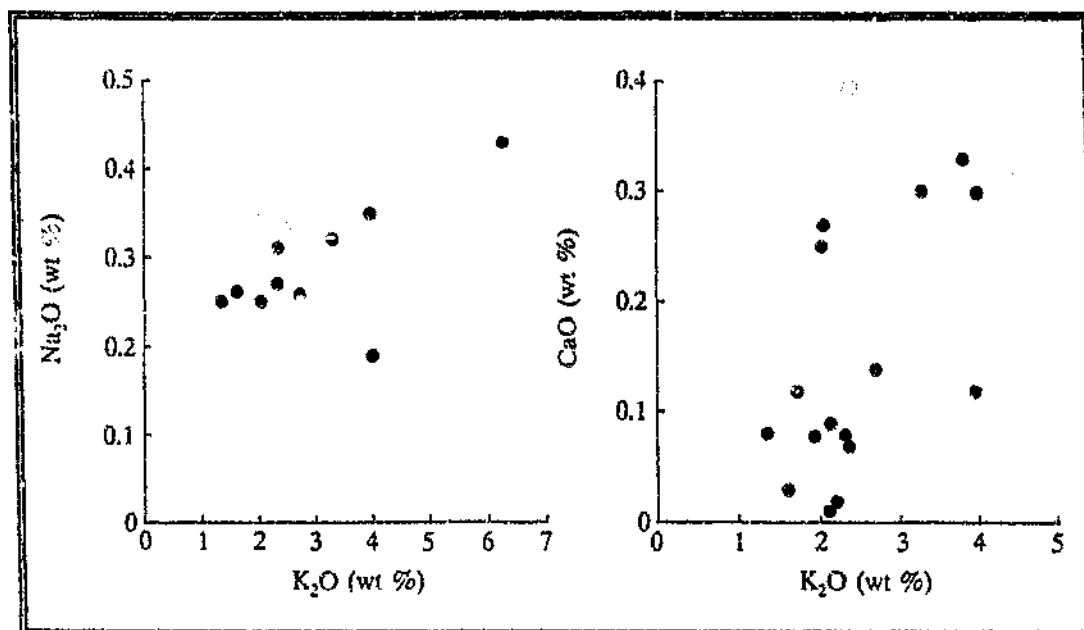


Figure 5.6 Plots of Na₂O and CaO versus K₂O for quartz-muscovite schists showing the extent to which muscovite controls Na and Ca distributions in the rocks. Note that data for samples BVR15 and BVR16 have been omitted in order to obviate the extraneous influence of relic plagioclase and secondary carbonate.

the replacement of K⁺ by Rb⁺ and Cs⁺ within the muscovite structure. K/Rb ratios vary by a factor of 5 from fairly low values of 130 to high values of 680, but mostly lie in the 300 - 400 range. K/Cs ratios also exhibit considerable variation, ranging from 3100 - 14300 with an average of 6000. A plot of Ba against K exhibits a similar, albeit less well-defined, sympathetic relationship reflecting the coupled substitution of Ba²⁺ for K⁺. K/Ba ratios vary in the range 74 - 320. The calculated average K/Rb (350) and K/Ba (150) ratios for the samples analysed are markedly higher than the average K/Rb (281) and K/Ba (46) ratios for unaltered Archaean silicic volcanic rocks as listed by Taylor and McLennan (1985).

K/Rb, K/Cs, K/Ba ratios generally increase with higher K concentrations, but appear to be largely independent of Rb, Cs and Ba values. These relationships conform with trends recorded in the alteration zones of some VHMS deposits, in which K/Rb and

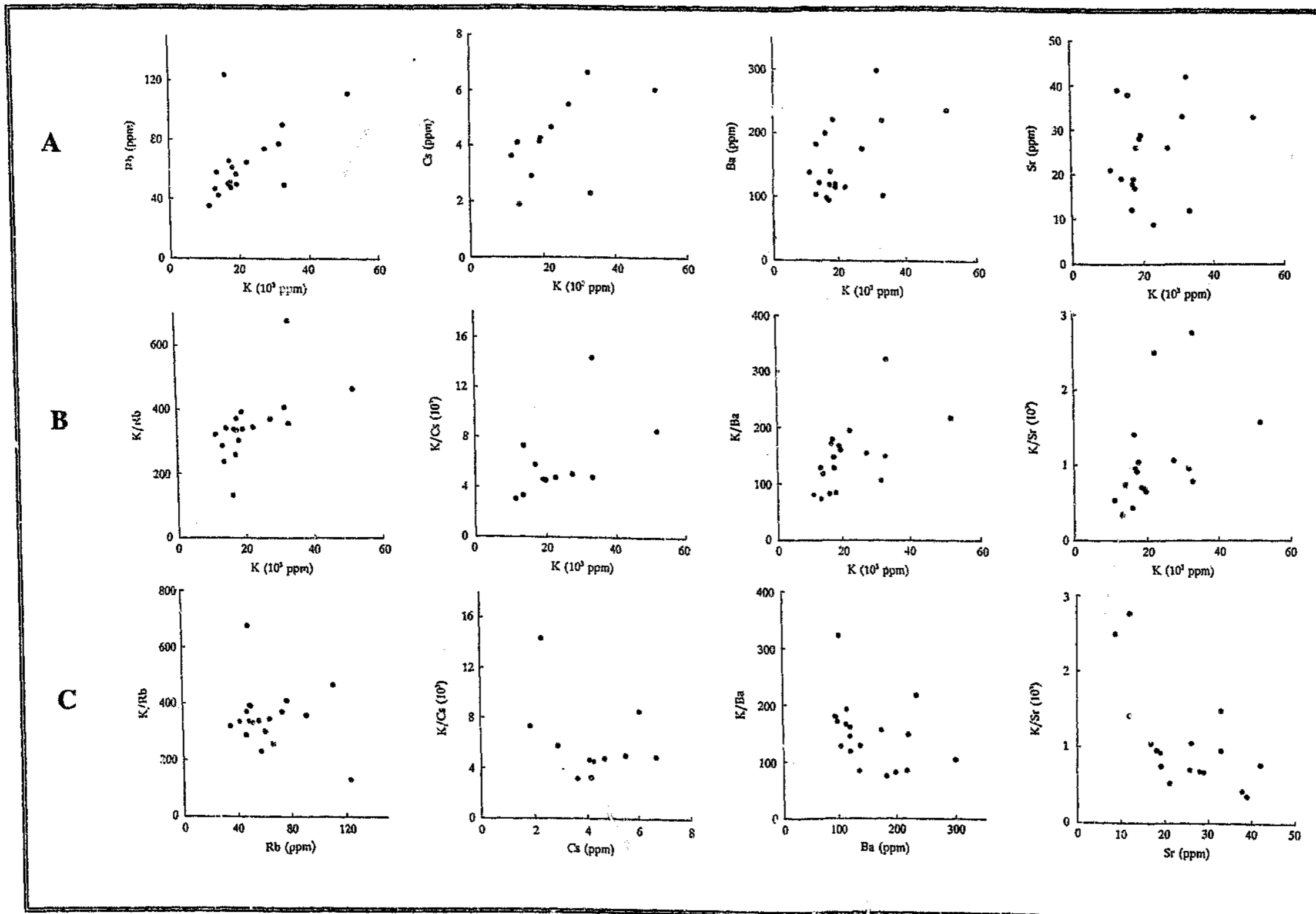


Figure 5.7 LFSE plots for the quartz-muscovite schists showing the extent to which muscovite controls Rb, Cs, Ba and Sr distributions: (A) Variation diagrams of Rb, Cs, Ba and Sr plotted against K; (B) Variation diagrams of K/Rb, K/Cs, K/Ba and K/Sr plotted against K; (C) Variation diagrams of K/Rb versus Rb, K/Cs versus Cs, K/Ba versus Ba and K/Sr versus Sr. Note that data for sample BVR15 has been omitted from the Sr versus K, K/Sr versus K and K/Sr versus Sr plots in order to obviate the extraneous influence of relic plagioclase.

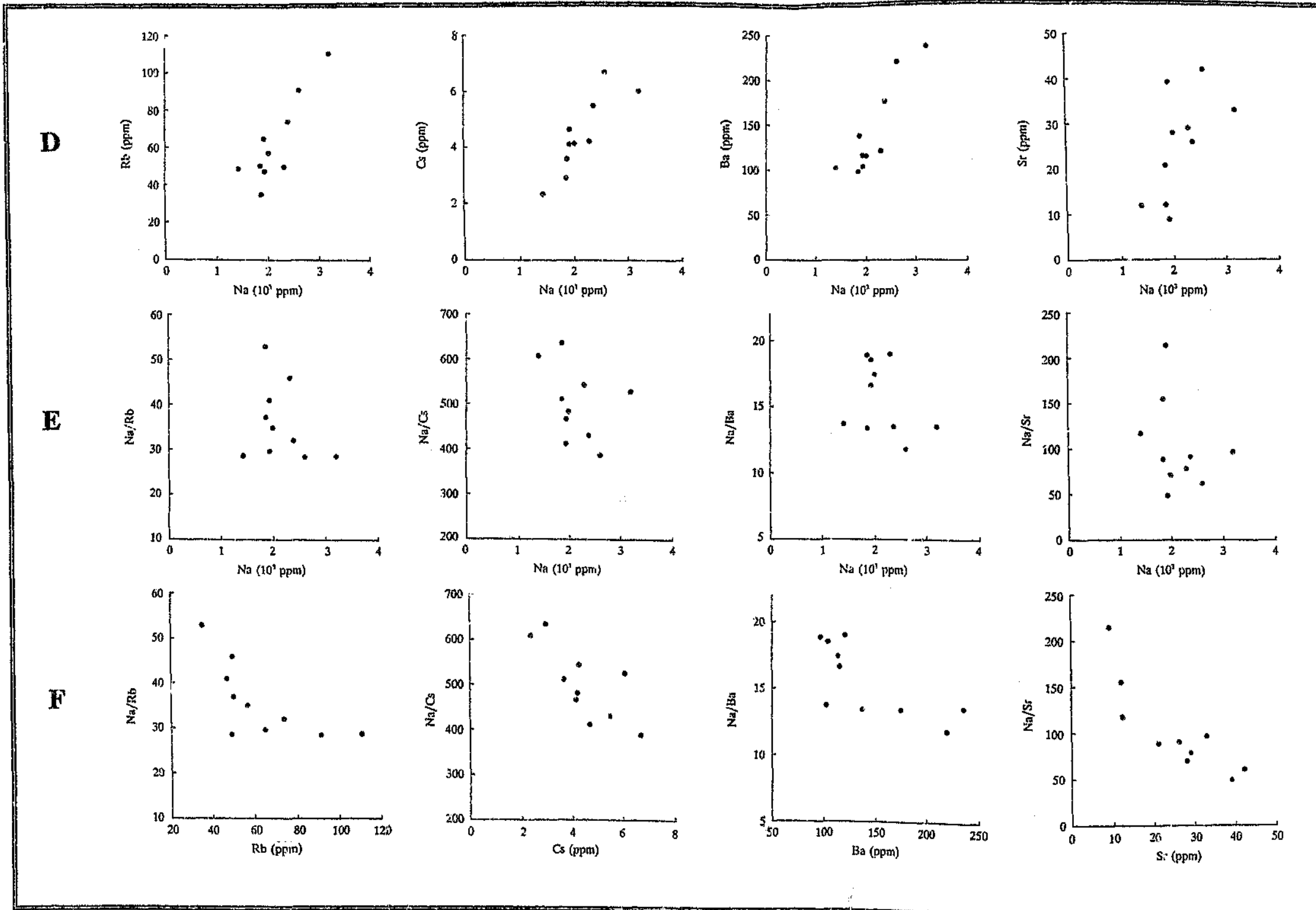


Figure 5.7 (continued): (D) Variation diagrams of Rb, Cs, Ba and Sr plotted against Na; (E) Variation diagrams of Na/Rb, Na/Cs, Na/Ba and Na/Sr plotted against Na; (F) Variation diagrams of Na/Rb versus Rb, Na/Cs versus Cs, Na/Ba versus Ba and Na/Sr versus Sr. Note that data for sample BVR15 has been omitted from all plots in order to obviate the extraneous influence of relic plagioclase.

K/Ba trend towards higher values with increasing degrees of sericitization, the latter manifested by higher K content (e.g. MacLean and Hoy, 1991).

Comparison of sample BVR15 (Table 5.1) with the remaining samples demonstrates that the breakdown of plagioclase to muscovite also resulted in a marked depletion of Sr, which displays geochemical similarities with Ca. Sr values are only weakly correlated with K, but K/Sr ratios vary sympathetically with K and antipathetically with Sr.

Given the covariance of K and Na (Figure 5.6), it follows that the Rb, Cs and Ba contents of the feldspar-free schists also vary systematically with Na (Figure 5.7D - F). A similar, although less well-defined, relationship holds for Sr. Na/Rb and Na/Ba ratios occupy fairly narrow ranges from 29 - 53 ($\bar{x} = 36$) and from 12 - 19 ($\bar{x} = 16$), respectively, and are significantly lower than the estimated average values in unaltered Archaean silicic volcanics for which Na/Rb = 491 and Na/Ba = 80 (Taylor and McLennan 1985). Na/Sr ratios are more variable, ranging from 49 - 210; the calculated average Na/Sr (100) ratio for the samples is, however, close to the estimated average Na/Sr (106) ratio recorded for unaltered silicic rocks (Taylor and McLennan, 1985). Na/Cs ratios range between 390 - 640, with an average of 500.

By contrast with the K/Rb, K/Cs, K/Ba and K/Sr ratios, which mainly vary as a function of K abundance, Na/Rb, Na/Cs, Na/Ba and Na/Sr ratios are independent or only weakly dependant of the Na content, but show pronounced trends to lower values at higher concentrations of Rb, Cs, Ba and Sr.

5.2.2.2 High field-strength elements

It is well known that binary plots of any two geochemically unrelated immobile elements in a heterogeneous assemblage of altered rocks that have been derived from the allochemical and/or allovolumetric alteration of a compositionally uniform precursor, characteristically yield well-defined linear alteration arrays (Figure 5.8A) (Finlow-Bates and Stumpfl, 1981; MacLean and Kranidiotis, 1987; MacLean, 1990). These alteration arrays pass through the precursor composition and project towards the origin. Altered rocks plotting between the origin and the precursor composition have experienced *in situ* dilution due to the addition of other, more soluble, components, and / or an increase in rock volume. On the other hand, rocks that have experienced *in situ* enrichment of their immobile components due to the removal of mobile species, and / or a decrease in volume, plot at higher values than the precursor composition. Thus, it is clear that alteration results in systematic changes in the abundances of the immobile elements. The presence of a linear alteration array that extrapolates through the origin in a binary plot of the concentrations of any two elements of contrasting geochemical affinity can be taken as evidence that these elements were essentially immobile (e.g. MacLean, 1988; Whitford *et al.*, 1989; Bernier and MacLean, 1989). Furthermore, the presence of such alteration arrays indicates that the altered rocks were derived from a precursor which was chemically homogeneous with respect to these components.

It is also evident that while certain elements may have behaved in an immobile fashion during alteration, their absolute abundance in any given altered rock need not necessarily reflect primary values. However, since any given alteration array passes through the precursor rock composition, it follows that ratios of immobile elements remain constant during alteration. Identification of the most likely primary characteristics of altered assemblages should therefore rely on immobile element ratios. Furthermore, geochemical comparison of altered assemblages for the purposes of correlation (e.g. Sections 5.2.3 and 5.3.1) should ideally only be carried out using ratios of immobile elements.

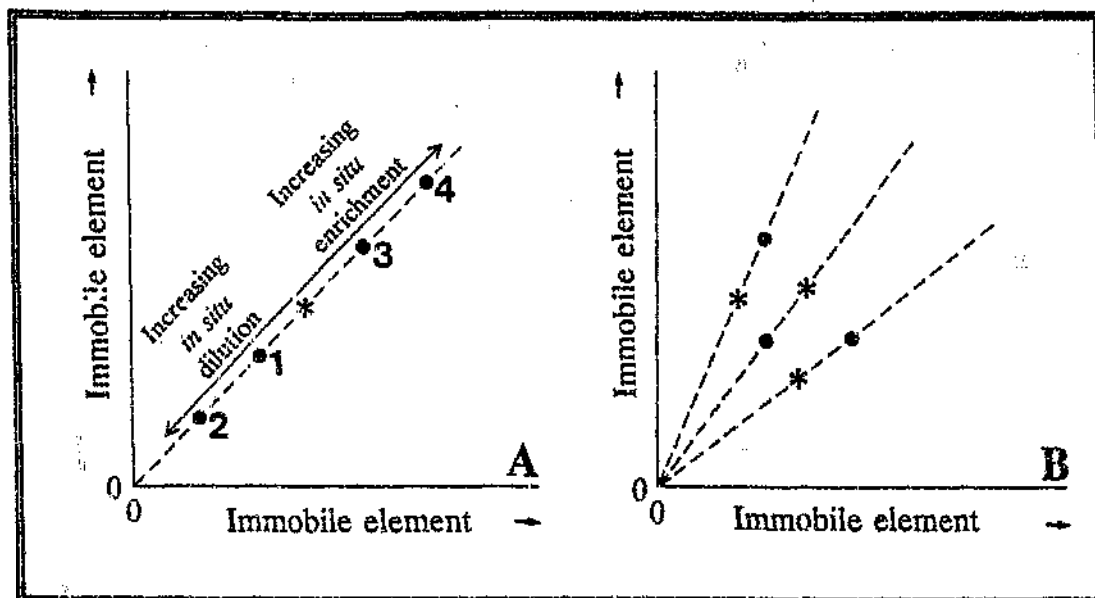


Figure 5.8 Schematic diagrams illustrating the effect of allochemical / allovolumetric alteration on immobile element abundances in chemically homogeneous and heterogeneous precursor systems (modified after Finlow-Bates and Stumpfl, 1981; MacLean and Kranidiotis, 1987). Symbols: asterisk - precursor composition; circle - altered sample composition.

(A) Chemically homogeneous (single) precursor system: alteration produces a linear alteration array that passes through the precursor composition and the origin. Slope of the alteration array is defined by the precursor composition. Samples plotting between the origin and the precursor composition (1) have experienced in situ dilution due to the net addition of other, more mobile, components, and/or an increase in volume; increasing degree of dilution results in a progressive shift of the data points closer to the origin (2). Samples plotting above the precursor composition (3), on the other hand, have suffered in situ enrichment due to a net depletion of other components, and/or a decrease in volume; increasing degree of enrichment is reflected in a shift of the data point to higher values (4).

(B) Chemically heterogeneous (multiple) precursor system: alteration path for each specimen is determined by its own unique precursor composition.

In many instances, however, binary plots of immobile element abundances in altered assemblages do not exhibit well-developed linear alteration arrays that project through the origin. As shown in Figure 5.9, this is the case for the quartz-muscovite schists of the Bien Venue Formation. The absence of a well-defined alteration array in, for example, the plots of TiO_2 versus Al_2O_3 and Zr versus TiO_2 may indicate that Ti, Al and Zr were mobile, contrary to the findings of other chemical studies indicating that these elements are in fact characterised by a high degree of immobility (Section 5.1). Alternatively, the lack of an alteration array reflects primary compositional variations within the protolith (Finlow-Bates and Stumpfl, 1981; MacLean, 1990). The influence of precursor heterogeneity on HFSE distributions during alteration is schematically illustrated in Figure 5.8B. Since the relative abundance of any two immobile elements in an altered rock is fixed by a line passing through that specific rock's pre-alteration composition and the origin, it follows that any sample in a compositionally heterogeneous sequence undergoing alteration will alter along its own unique alteration path. In effect, the position of any altered sample in a binary plot of immobile element concentrations depends firstly on the composition of its respective protolith, and secondly, on the influence of mass and volume changes. As was the case previously, it follows that ratios of immobile elements remain constant during alteration, and that a spread of such ratios in a compositionally diverse suite of altered rocks reflects original variations in the precursor.

From the foregoing, and taking into account the findings of previous geochemical studies indicating a high degree of immobility for the HFSE's (Section 5.1), it is considered likely that the quartz-muscovite schists were derived from a compositionally heterogeneous precursor suite - i.e. each sample analysed was derived from its own chemically unique precursor. These primary heterogeneities probably reflect differences in degree of fractionation. Evidence presented in Sections 4.3.1 and 4.3.9 also suggests that the silicic precursors were erupted in a subaqueous environment and that they exhibit features characteristic of epiclastic rocks. Hence, some of the chemical

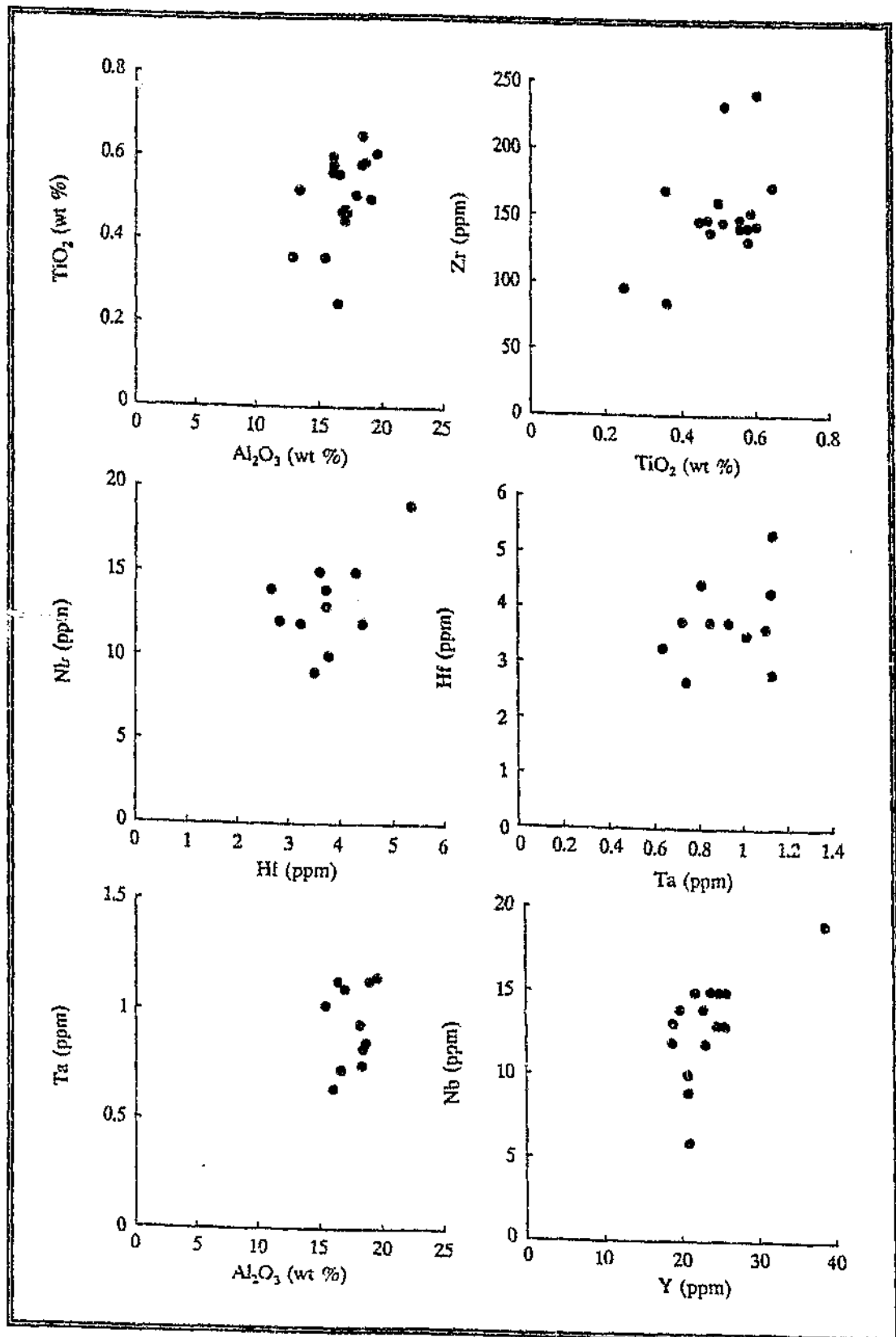
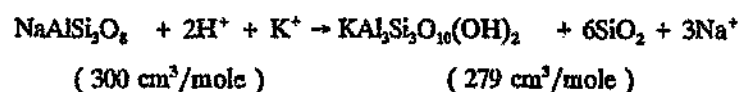
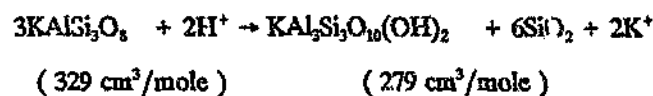


Figure 5.9 Selected HFSE variation diagrams for the quartz-muscovite schists.

heterogeneity may be due to submarine weathering and the reworking of the volcanic pile by epiclastic processes. The latter, in particular, results in the fractionation of some trace elements due to the preferential concentration of resistant minerals such as zircon (Czr and Wright, 1987).

It is also important to note that the transformation of the silicic volcanoclastic rocks to quartz-muscovite schists involved a change in volume. Calculations by the writer indicate that the breakdown of K-feldspar and albite to muscovite, as outlined by reactions [1] and [2] in Section 5.2.1.1, is accompanied by a volume loss of 7 - 15 %:



The presence of a well-developed schistosity in the rocks provides further evidence of a decrease in volume during alteration. Studies on fossils and reduction spots in slates indicate volume losses of up to ~50 % during cleavage development (Wright and Platt, 1982; Beutner and Charles, 1985). Microstructural observations of porphyroblast / matrix relationships in schists (Bell *et al.*, 1986; Bell and Cuff, 1989) also suggest that significant volume losses accompany alteration and deformation. This decrease in volume implies that the quartz-muscovite schist samples are enriched in the immobile elements relative to their respective protoliths - i.e. the observed HFSE and REE concentrations should be regarded as maxima. However, since the amount of enrichment of each immobile element in any given sample is the same, it follows that the shapes and slopes of chondrite- and primordial-mantle-normalized (see later) plots reflect those which would have characterised the precursor suite.

Owing to a lack of strain markers, precise determination of the volume changes during the alteration of the quartz-muscovite schists is not possible. However, studies have shown that changes in volume and mass during alteration can be determined from differences in the concentration of an immobile reference element between an altered rock and its precursor (e.g. Bernier and MacLean, 1989; MacLean and Hoy, 1991; Aque, 1991). These changes are most easily determined for altered assemblages that have been derived from a single, chemically homogeneous precursor, since differences in the relative values of the immobile reference element are exclusively attributable to alteration. The determination of volume and mass changes accompanying the alteration of rocks that have been derived from a chemically heterogeneous precursor suite, however, requires a more sophisticated approach because the calculations must take into account primary compositional variations. Finlow-Bates and Stuepfl (1981) and MacLean (1990) have shown that the intersection of primary fractionation or mixing trends, as deduced from least-altered specimens, with alteration paths can be used to determine primary characteristics of metasomatised rocks (Figure 5.10). Similarly, the intersection of alteration arrays with fractionation trends in modern igneous suites of appropriate petrochemical affinity provides the only feasible means of determining the pre-alteration composition of altered samples for which no unaltered precursor material remains (Whitford *et al.*, 1989). The following is an attempt to determine the volume change during the alteration of the Bien Venue schists using simple comparative procedures with modern volcanics. Note that the results clearly depend on how closely the inferred pre-alteration composition of the schists matches the actual composition.

Presented in Figure 5.11 is a binary plot of Al_2O_3 against Zr for the quartz-muscovite schists. Also shown is the averaged low pressure fractionation trend for unaltered Cenozoic calc-alkaline basaltic-to-rhyolitic volcanic and volcanoclastic rocks

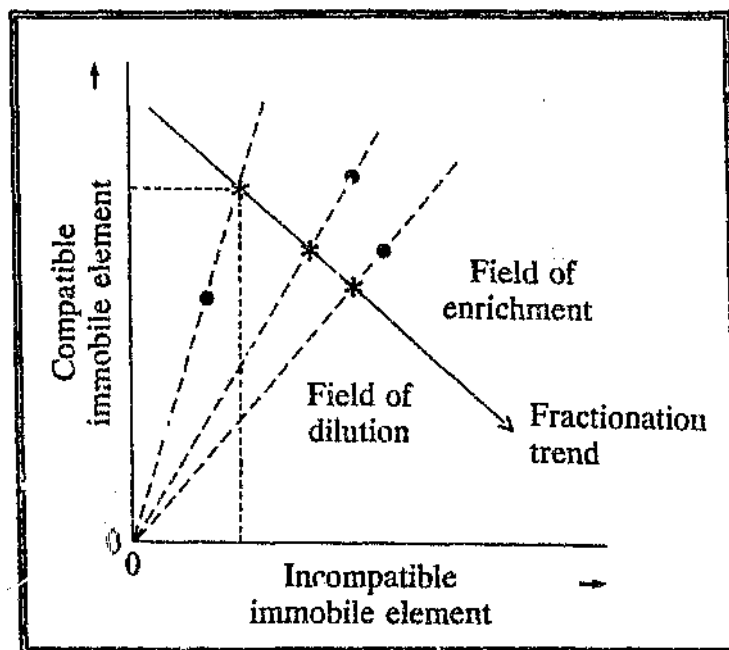


Figure 5.10 Schematic diagram showing the relationship between alteration arrays and primary igneous trends (modified after Finlow-Bates and Sturrock, 1981; MacLean, 1990). Symbols: asterisk - precursor composition; circle - altered sample composition. Note how each altered sample's precursor composition can be determined from the intersection of its alteration path and the primary fractionation trend.

from arcs in the southwestern Pacific (SWP) region⁶. This trend was specifically chosen because, as will be shown in Section 5.5.3, the schists chemically resemble rocks found in modern arcs. In Figure 5.11 it is evident that the majority of quartz-muscovite schist samples lie between two alteration paths that intersect the Cenozoic trend in the dacite / rhyodacite field, suggesting that they were derived from dacitic and rhyodacitic protoliths. This is compatible with the conclusions of Section 5.2. It is also apparent that the bulk of the schist samples plot to the right of the Cenozoic trend. This is consistent

⁶ Data were compiled by the writer from the averaged compositions of ~800 major element and ~400 trace element analyses as listed by Ewart (1979, 1982) for arc-related rocks in the Solomon Islands, Papua New Guinea, New Hebrides, Fiji, Tonga-Kermadec Islands and New Zealand.

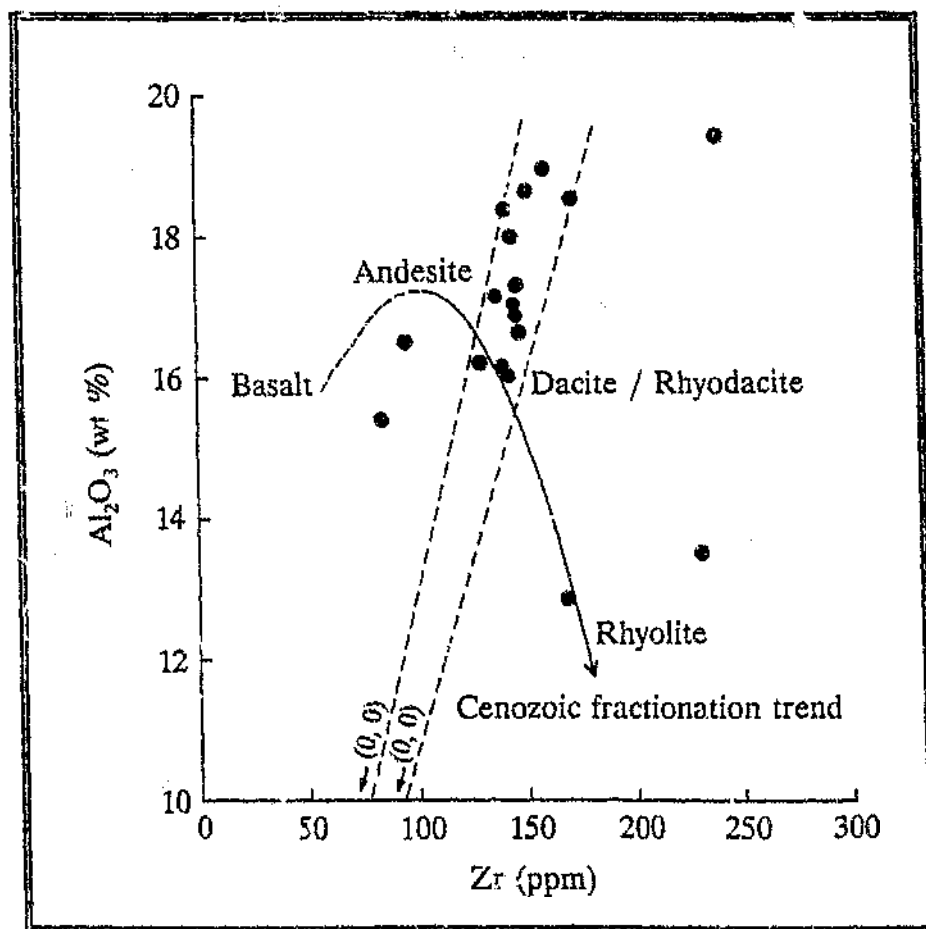


Figure 5.11 Plot of Al_2O_3 against Zr for the samples of quartz-muscovite schist (circles). Also shown is the igneous fractionation curve defined by Cenozoic calc-alkaline volcanic rocks from magmatic arcs in the southwestern Pacific region (data compiled from Ewart, 1979, 1982). Equation for the solid part of the fractionation trend is $y = -0.00088x^2 + 0.17942x + 8.12386$. Note how the majority of schist samples plot to the right of the fractionation trend, indicating that they are enriched in Al and Zr relative to the Cenozoic rocks.

with the aforementioned chemical and textural considerations indicating a decrease in volume during the dynamothermal alteration of the rocks.

Before proceeding with the mass and volume change calculations, the use of Zr as the incompatible immobile reference element must be justified. In Figure 5.11 it is evident that Zr behaved as an incompatible element during the fractionation of rocks in the SWP region - i.e. Zr concentrations increase from basalt through andesite and dacite to rhyolite. However, such incompatible behaviour may not necessarily have applied to the precursor suite of the Bien Venue Formation schists, since Zr often exhibits compatible behaviour in rocks of the calc-alkaline series (MacLean, 1990). Unfortunately, due to alteration, the behaviour of Zr in the precursor rocks of the Bien Venue Formation cannot be evaluated. However, comparison of the Zr contents of the quartz-muscovite schists (85 - 241 ppm; \bar{x} = 152 ppm) with concentrations in the biotite-oligoclase (79 - 126 ppm; \bar{x} = 106 ppm) and chlorite (70 - 130 ppm; \bar{x} = 103 ppm) schists, which were probably derived from less evolved protoliths (Sections 5.3 and 5.4), strongly suggests that Zr behaved incompatibly. Hence, the writer decided to utilize Zr instead of other incompatible elements such as Nb for which comparatively little data exists for the Cenozoic volcanics.

Concentrations of Zr in the inferred precursor for the quartz-muscovite schist samples have been visually determined from the intersection of each sample's alteration path with the SWP fractionation trend. Changes in mass for each sample have been calculated using the following formula (Bernier and MacLean, 1989; Aque, 1991):

$$\Delta M = [(C_{Zr}^i / C_{Zr}^f) - 1] \times 100$$

[1]

where ΔM is the change (in %) in total mass, and C_{Zr}^i and C_{Zr}^f are the concentrations of Zr in the inferred precursor and altered rock, respectively. Relative to the Cenozoic

rocks, the majority of samples appear to have experienced total mass losses of 1 - 30 % (Table 5.2). However, sample BVR2 shows an apparent mass gain of 33 %. The discrepancy between the calculated mass change for this sample and the remaining samples can probably be attributed to marked deviation of the former's actual precursor composition from its inferred composition, rather than any true mass gains. This highlights the difficulties in determining the most likely primary compositional characteristics of altered rocks.

Table 5.2 Calculated mass and volume changes for the quartz-muscovite schists

Sample	Zr ^f (ppm)	Zr ⁱ (ppm)	ΔM or ΔV (%)
BVR1	131	134	+2.3
BVR2	85	113	+33
BVR3	169	173	+2.4
BVR4	141	113	-20
BVR5	147	134	-8.8
BVR6	152	122	-20
BVR7	147	131	-11
BVR8	145	123	-15
BVR9	140	138	-1.4
BVR10	142	138	-2.8
BVR11	138	128	-7.3
BVR12	145	132	-9.0
BVR13	148	136	-8.1
BVR14	171	131	-23
BVR15	241	168	-30
BVR16	96	99	+3.1
BVR17	160	123	-23
BVR18	232	174	-25

Zr^f - Zr concentration in altered rock (data are from Table 5.1)

Zrⁱ - inferred Zr concentration in precursor rock

ΔM - total mass change

ΔV - total volume change (note that if $\rho^i = \rho^f$ then $\Delta M = \Delta V$)

+ΔM or ΔV - mass or volume gain

-ΔM or ΔV - mass or volume loss

Volume changes during alteration may be computed using the equation (Bernier and MacLean, 1989):

$$\Delta V = [(V'/V) - 1] \times 100 \quad [2]$$

where ΔV is the change in total volume (in %), and V' and V are the volumes of the precursor and altered equivalent, respectively.

Volume and mass are related as follows:

$$\rho = M/V \quad [3]$$

where ρ is density.

Measurements carried out by the writer on 10 samples of quartz-muscovite schist indicate that these rocks range in density from 2.76 - 2.82 g/cm³. These values fall within the range of densities for Cenozoic dacitic and rhyodacitic rocks (2.76 - 2.85 g/cm³)⁷, suggesting that density did not significantly change during the alteration process. If this is correct, then the volume changes correspond to mass changes and ΔV can be calculated directly from Zr concentrations in the altered rock and its inferred precursor using the equation:

$$\Delta V = [(C_{Zr}'/C_{Zr}) - 1] \times 100 \quad [4]$$

Hence, it would appear that the schist samples experienced volume losses of up to 30% (Table 5.2).

⁷ Densities of the modern volcanic rocks were determined from their CIPW norms using appropriate mineral densities.

5.2.3 Comparison with rocks of the Theespruit Formation.

Rocks of the Bien Venue Formation have, as mentioned in Sections 1.4 and 4.1, previously been considered to constitute part of the Theespruit Formation (Viljoen and Viljoen, 1970). With this in mind, the writer undertook several field trips to examine the latter unit where it is best preserved and exposed in the southwestern parts of the BGB and in the Weergevonden greenstone remnant (see the location map in Figure 1.4). Comprehensive descriptions of the geology of these areas are provided by Viljoen and Viljoen (1969d), Viljoen *et al.* (1969) and Anhaeusser (1980).

Although similar in some respects, the two formations show distinct differences in the relative proportions of their respective constituent lithologies. Whereas the Theespruit Formation is composed principally of basic and ultrabasic metavolcanics with minor intercalated silicic rocks (Viljoen and Viljoen, 1969d; Viljoen *et al.*, 1969), the Bien Venue Formation consists almost entirely of quartz-muscovite schists (Section 4.3.1). In addition, biotite-oligoclase schists such as those found within the Bien Venue Formation (Section 4.3.2) have not been reported from the Theespruit Formation.

Despite these differences, broad similarities are apparent when the textural and mineralogical properties of quartz-muscovite schists within the Bien Venue Formation are compared with the silicic rocks of the Theespruit Formation. Hence, the writer decided to compare the rocks on the basis of geochemistry. Due to the paucity of good quality geochemical data for the Theespruit Formation, the writer collected and analysed five samples of silicic schist to supplement the two analyses given by Glikson (1976). These data, together with the analyses from Glikson (1976), are listed in Table 5.3. The sample sites are shown on the location map in Figure 1.4. Sample TJ1 (30°50'03"E and 25°59'52"S), collected to the east of Tjakastad Township, consists mainly of quartz and muscovite with lesser amounts of relic plagioclase, chlorite, biotite, calcite, tourmaline and opaque phases, and appears to have only been metamorphosed to the greenschist facies. Sample VER1 (30°39'07"E and 25°58'05"S), collected in the vicinity

Table 5.3 Chemical data for silicic metavolcanic-volcaniclastic rocks from the Theespruit Formation

Sample	329 ¹	G34 ¹	TJ1	VER1	W1	W2	W3
SiO ₂ (wt %)	74.34	79.28	76.13	79.02	74.83	76.41	75.52
TiO ₂	0.12	0.20	0.17	0.13	0.13	0.13	0.19
Al ₂ O ₃	11.73	12.60	12.69	12.25	12.49	12.74	12.99
Fe ₂ O ₃ <i>total</i>	3.64	0.39	1.98	1.02	1.90	1.83	1.94
MnO	0.03	-	0.04	0.01	0.03	0.04	0.02
MgO	3.06	0.85	0.60	0.30	0.23	0.16	0.58
CaO	0.13	0.21	1.05	0.47	0.69	0.66	1.05
Na ₂ O	3.27	0.11	4.08	3.45	1.91	1.92	2.36
K ₂ O	0.55	4.01	2.22	4.00	5.96	5.89	3.32
P ₂ O ₅	0.06	0.03	0.04	0.01	0.02	0.02	0.03
L.O.I.	2.81	1.98	1.47	0.42	0.38	0.50	0.73
Total	99.74	99.56	100.47	101.08	98.57	100.30	98.73
Ba (ppm)	170	1300	752	666	847	733	1014
Rb	24	141	83	70	125	124	79
Sr	22	12	93	57	62	61	11
Cs	0.19	0.46	0.74	0.35	-	-	0.53
Pb	-	-	15	7	14	13	15
U	3.2	1.5	4.83	3.49	-	-	3.16
Th	14	18	21.7	23.1	-	-	22.8
Y	27	11	26	16	26	18	21
Nb	23	26	26	22	19	19	30
Zr	280	170	183	144	164	169	173
Hf	5.3	4.4	5.32	4.91	-	-	5.53
Ta	-	-	1.87	1.87	-	-	1.57
Ga	-	-	20	18	20	20	20
V	14	13	15	12	11	11	19
Cr	11	14	27	27	31	26	26
Sc	7	6	1.37	0.80	-	-	1.55
Zn	62	13	41	16	25	32	25
Cu	108	3	8	14	11	14	9
Ni	39	4	11	10	10	10	9
Co	13	3	2.26	1.27	-	-	2.41
As	-	-	0.12	0.18	-	-	0.21
La	88	12	72.5	22.1	-	-	62.0
Ce	97	29	128	46.4	-	-	122
Nd	44	7	43.5	11.9	-	-	33.7
Sm	6.4	1.7	6.83	2.19	-	-	5.24
Eu	0.84	0.49	0.99	0.43	-	-	0.87
Tb	0.55	0.27	0.77	0.44	-	-	0.66
Yb	1.9	1.2	2.59	2.12	-	-	2.68
Lu	-	-	0.40	0.27	-	-	0.31
Au (ppb)	-	-	3.9	4.7	-	-	6.3

§ - data from Glikson (1976); L.O.I. - loss on ignition

of the barite occurrence on the farm Vergelegen 728 JT, and samples W1 - W3 (30°41'47"E and 26°04'02"S), which come from the main silicic unit in the Weergevonden greenstone remnant, contain conspicuous amounts of coexisting secondary microcline and plagioclase in addition to quartz, muscovite, biotite, chlorite, epidote and opaque components. The close spatial association of the latter samples with hornblende amphibolites (Anhaeusser, 1980) suggests that they have been metamorphosed to the amphibolite facies.

Comparison of chemical data presented in Tables 5.1 and 5.3, indicates that the Theespruit samples generally compare well with those from the Bien Venue Formation, but tend to be enriched in Na_2O , Ba and Nb, and depleted in Al_2O_3 , TiO_2 and V. However, as discussed in Section 5.2.2.2, the comparison of altered rocks suites solely on the basis of element abundances may lead to spurious conclusions due to the effect of mass and/or volume changes during alteration. In order to overcome this problem, the writer compiled a series of ternary diagrams which contrast the compositions of the two sample suites. The effect of the ternary plots is to utilize interelement ratios rather than absolute abundances, the former remaining constant despite intense alteration provided elements were immobile (Section 5.2.2.2). Three of these plots, two of which are based on elements with assumed low mobility (Nb, Y, Zr, Ti, Cr and V; Section 5.1), are presented in Figure 5.12 and illustrate some geochemical differences between the rocks from the two formations. Discrimination on the basis of the Ba, Rb and Sr may be attributed to differences in the redistribution of these elements during alteration, but discrimination on the basis of the less mobile elements clearly reflects differences in the pre-alteration chemistry of the rocks.

A chondrite-normalised REE plot showing the envelopes of samples from both formations is presented in Figure 5.13. It is evident from this plot that while REE distributions are similar overall, rocks from the Theespruit Formation, with the exception of one specimen, are characterized by negative Eu anomalies ($\text{Eu}/\text{Eu}^* = 0.51 - 0.57$; sample G34 excluded), a feature not shown by the rocks of the Bien Venue Formation (Section 5.2).

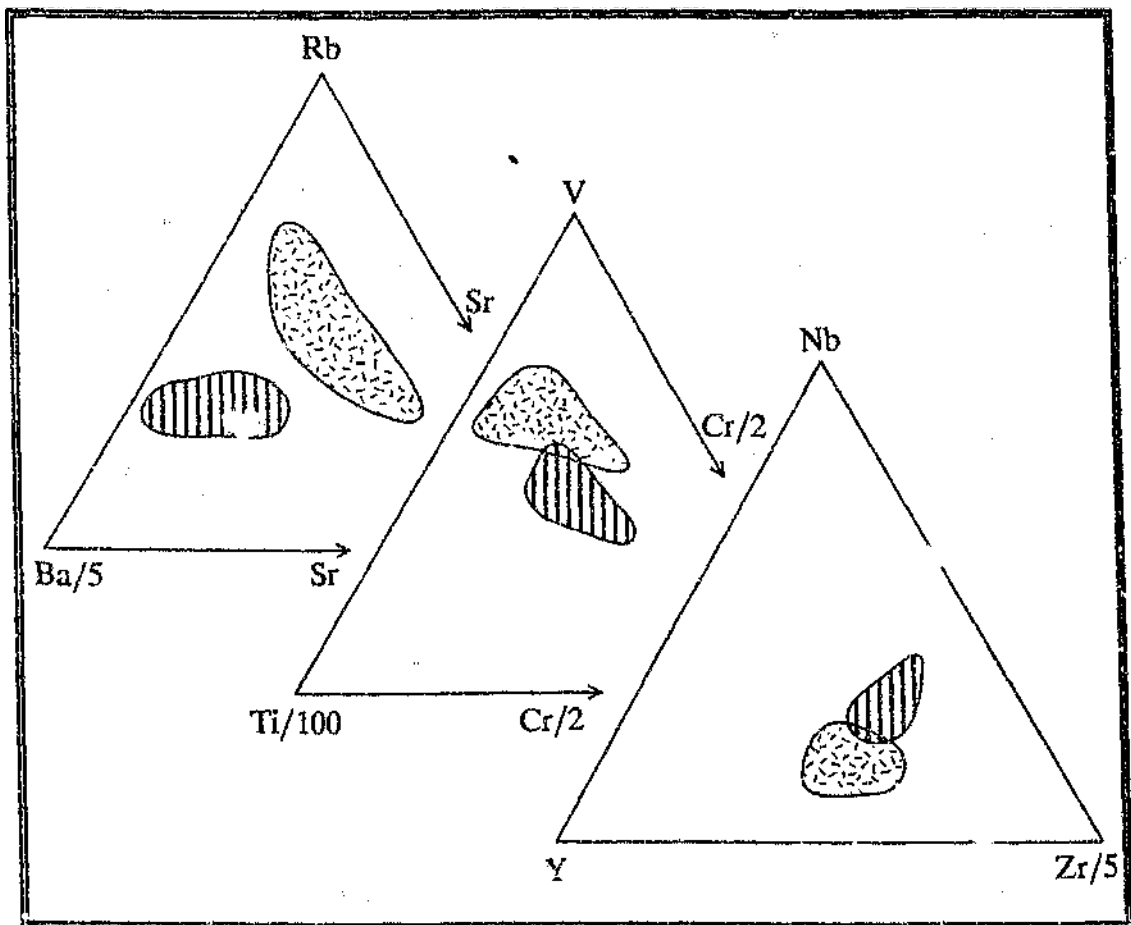


Figure 5.12 Ternary Ba - Rb - Sr, Ti - Cr - V and Y - Nb - Zr plots illustrating some compositional differences between quartz-muscovite schists from the Bien Venue Formation (randomly oriented dashes) and silicic metavolcanic-volcaniclastic rocks from the Theespruit Formation (horizontal hatch).

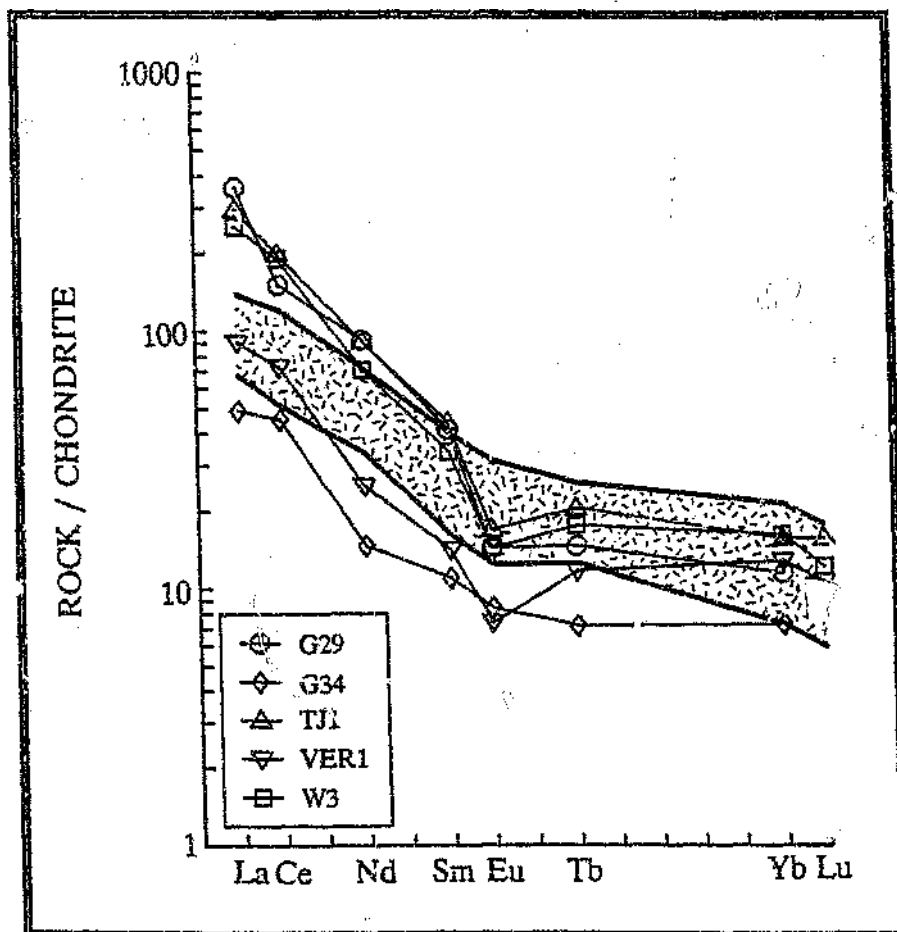


Figure 5.13 Chondrite-normalized REE patterns for silicic metavolcanic rocks from the Theespruit Formation (sample labels as in Table 5.3 and Figure 1.4) and comparison with the compositional envelope of quartz-muscovite schists from the Bien Venue Formation (randomly oriented dashes).

5.3 Biotite-oligoclase schists

Major and trace element data for seven samples of biotite-oligoclase schist, collected from both major occurrences of this rock type in the study area (Figure 1.4), are given in Table 5.4.

Initially it was thought, on the basis of the high ferromagnesian mineral content of the rocks, that the schists might have chemical affinities with bonninites. The latter are characterised by high MgO ($> 6 \text{ wt } \%$), SiO₂ ($\geq 55 \text{ wt } \%$), Ni ($> 70 \text{ ppm}$), and Cr ($> 200 \text{ ppm}$) concentrations, coupled with low TiO₂ ($\leq 0.3 \text{ wt } \%$) contents (Wilson, 1989), but examination of the data presented in Table 5.4 indicates that the schists bear no resemblance to bonninites. On the Zr/TiO₂ - Nb/Y classification diagram (Figure 5.1), the schists plot mainly in the andesite field, although overall, the major and trace element data suggest that they were probably derived from a dacitic precursor.

Compared with the quartz-muscovite schists (Section 5.2), the biotite-oligoclase schists are generally characterised by lower SiO₂ (66 - 70 wt %) and Zr (79 - 126 ppm) contents, coupled with higher abundances of MgO (1.5 - 4.3 wt %), CaO (0.9 - 2.8 wt %), Na₂O (3.6 - 5.4 wt %) and Sr (66 - 129 ppm). K/Ba (56 - 180), K/Rb (190 - 430), K/Cs (2300 - 8200) and K/Sr (82 - 400) ratios are generally lower, but Na/Ba (55 - 380), Na/Rb (270 - 940), Na/Cs (4500 - 16200) and Na/Sr (300 - 550) values are distinctly higher.

Chondrite-normalised REE profiles for the biotite-oligoclase schists (Figure 5.14) are similar to those characterising the quartz-muscovite schists, showing marked relative enrichment of the LREE relative with the HREE ($La_N/Yb_N = 6 - 21$) which, coupled with Nb/Y ratios generally < 0.65 (Figure 5.1), suggests a primary calc-alkaline affinity (e.g. Jakeš and Gill, 1970; Lesher *et al.*, 1986; Winchester and Floyd, 1977). Despite their high plagioclase content, the rocks exhibit no, or only weakly developed, positive Eu anomalies ($Eu/Eu^* = 0.88 - 1.39$).

Table 5.4 Chemical data for biotite-oligoclase schists from the Bien Venue Formation

Sample	BVD1	BVL2	BVD3	BVD4	BVD5	BVD6	BVD7
SiO ₂ (wt %)	67.23	68.83	67.75	69.63	70.33	69.77	65.67
TiO ₂	0.44	0.41	0.43	0.50	0.52	0.50	0.62
Al ₂ O ₃	15.42	13.08	15.38	12.94	13.53	12.94	14.85
Fe ₂ O ₃ ^{total}	3.97	4.00	4.32	2.95	3.55	3.75	4.49
MnO	0.05	0.07	0.04	0.07	0.06	0.07	0.06
MgO	3.33	2.81	4.33	1.49	2.48	2.34	4.13
CaO	1.01	2.53	0.99	2.71	1.86	2.81	0.88
Na ₂ O	5.42	3.70	4.20	5.19	3.64	4.56	4.42
K ₂ O	2.54	1.50	0.89	2.11	3.32	2.07	3.17
P ₂ O ₅	0.14	0.16	0.13	0.12	0.12	0.11	0.15
H ₂ O ⁻	0.01	0.02	0.02	0.12	0.02	0.03	0.05
H ₂ O ⁺	0.46	0.58	1.70	0.38	0.26	0.34	0.56
CO ₂	0.08	0.88	0.13	1.43	0.11	1.04	0.08
Total	100.10	98.57	100.31	99.64	99.80	100.33	90.13
Ba (ppm)	213	157	83	367	495	97	195
Rb	69	66	38	41	100	57	75
Sr	73	77	90	129	85	99	66
Cs	7.59	5.48	-	-	4.53	2.05	7.27
Pb	12	9	5	bdl	13	bdl	7
U	1.22	1.03	-	-	1.19	0.82	1.07
Th	3.96	3.49	-	-	4.78	4.63	4.09
Y	14	18	15	17	18	14	17
Nb	7	8	7	11	10	10	11
Zr	86	105	79	115	121	111	126
Hf	3.20	3.52	-	-	3.42	3.18	3.39
Ta	0.80	0.76	-	-	0.90	0.89	0.85
Ga	22	19	22	13	13	12	16
V	68	55	70	53	55	50	77
Cr	47	44	37	7	8	7	42
Sc	8.28	7.53	-	-	6.61	6.34	9.33
Zn	51	57	26	40	100	45	53
Cu	28	21	14	42	43	11	10
Ni	47	40	45	22	22	26	45
Co	14.5	14.4	-	-	12.9	11.7	15.7
As	0.46	0.78	-	-	0.18	0.15	0.25
La	30.4	26.8	-	-	57.6	23.0	18.9
Ce	42.1	48.8	-	-	86.9	43.7	42.2
Nd	18.7	21.7	-	-	40.9	19.6	17.9
Sm	4.04	3.81	-	-	6.04	2.72	2.87
Eu	1.08	1.18	-	-	1.56	0.90	1.33
Tb	0.50	0.58	-	-	0.69	0.49	0.54
Yb	1.80	1.92	-	-	1.83	1.74	2.06
Lu	0.26	0.28	-	-	0.26	0.28	0.23
Au (ppb)	4.0	5.5	-	-	0.7	1.6	-

bdl - below detection level

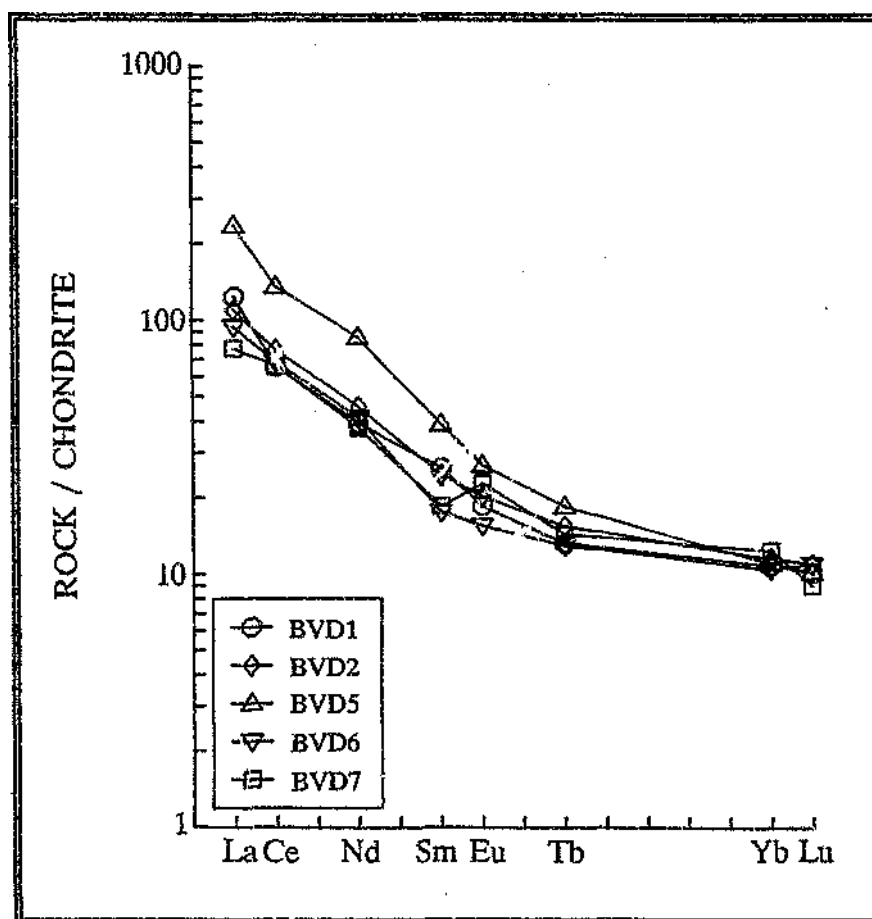


Figure 5.14 Chondrite-normalized REE profiles for biotite-oligoclase schists (sample labels as in Table 5.4 and Figure 1.4).

5.3.1 Comparison with rocks of the Schoongezicht Formation

In terms of mineralogy and texture, the biotite-oligoclase schists within the Bien Venue Formation resemble metavolcaniclastic rocks found within the Schoongezicht Formation, which forms the uppermost unit of the Fig Tree Group in the southwestern parts of the BGB (Section 2.3). Rocks from these two formations have accordingly been compared to establish any similarities in whole-rock geochemistry. Data for the Schoongezicht Formation were obtained from six specimens collected by the writer from road-cutting exposures in the type area in the closure of the Stolzberg Syncline

(SCH5 and SCH6 - 30°52'30"E and 25°53'52"S; SCH7 - 30°52'12"E and 25°54'15"S), as well as from exposures along the northern limb of the Eureka Syncline at Ezzey's Pass (EZ1 and EZ2 - 31°10'05"E and 25°41'01"S) and to the south-southeast of the New Consort Gold Mine (CON1 - 31°05'15"E and 25°39'31"S) (see the location map in Figure 1.4; Table 5.5). The samples contain abundant large (up to 4 mm across), euhedral-to-anhedral oligoclase, perthite and microcline phenocrysts in a fine grained, locally foliated, groundmass composed of biotite, actinolite, quartz, carbonate, chlorite, feldspar and muscovite. Epidote, sphene and zircon occur as accessory minerals.

Examination of the data presented in Tables 5.4 and 5.5 indicates that samples from both formations are broadly comparable in terms of major element composition. However, marked differences are evident in the concentrations of some trace elements, especially Ba, Sr and Zr, and to a lesser degree Rb and Th, which tend to be enriched in samples from the Schoongezicht Formation. Ratios of some trace elements which are assumed to have been essentially immobile during alteration (Section 5.1) are also distinctly higher in the Schoongezicht Formation rocks - e.g. Zr/Nb (Bien Venue = 11 - 13; Schoongezicht = 14 - 29), Nb/Ta (9 - 13; 16 - 21) and Hf/Ta (4 - 5; 7 - 11). Furthermore, the latter are also generally enriched in the LREE and the MREE relative to the Bien Venue Formation rocks, but have similar or lower HREE contents, consequently displaying steeper chondrite-normalized profiles with La_N/Yb_N between 19 - 32 (Figure 5.15).

5.4 Chlorite schists

Chemical analyses of five specimens of chlorite schist, collected from least-altered outcrops along the southern limb of the Strathmore Anticline (Figure 1.4), are listed in Table 5.6. No samples of talc schist or serpentinite were analysed as these rocks are highly weathered and not suitable for geochemical study.

Table 5.5 Chemical data for metavolcanic-volcaniclastic rocks from the Schongezicht Formation

Sample	EZ1	EZ2	CON1	SCH5	SCH6	SCH7
SiO ₂ (wt %)	63.21	61.67	64.88	62.85	62.15	68.67
TiO ₂	0.51	0.59	0.64	0.66	0.74	0.50
Al ₂ O ₃	14.16	14.33	14.89	12.85	14.10	15.40
Fe ₂ O ₃ total	5.24	5.97	4.18	5.09	5.98	1.78
MnO	0.12	0.09	0.04	0.08	0.09	0.05
MgO	3.28	3.67	3.52	3.12	1.82	0.71
CaO	3.23	3.71	2.09	2.86	2.33	0.88
Na ₂ O	4.65	4.32	3.91	3.89	2.66	2.23
K ₂ O	2.94	3.03	3.52	3.64	5.39	6.97
P ₂ O ₅	0.41	0.47	0.33	0.35	0.43	0.13
H ₂ O ⁻	0.02	0.04	0.04	0.15	0.07	0.06
H ₂ O ⁺	0.41	0.27	0.45	1.29	1.35	0.64
CO ₂	2.06	1.44	0.15	1.78	2.36	1.12
Total	100.18	99.60	98.64	98.61	99.47	99.14
Ba (ppm)	1057	1045	1243	923	946	893
Rb	94	89	88	113	113	125
Sr	676	578	936	749	302	389
Cs	3.34	-	3.26	2.18	-	3.84
Pb	19	30	10	13	bdl	12
U	2.92	-	2.72	2.15	-	1.83
Th	13.2	-	11.5	7.26	-	6.24
Y	29	37	27	24	28	15
Nb	8	11	11	10	10	7
Zr	229	240	231	223	226	101
Hf	5.49	-	5.25	3.56	-	2.55
Ta	0.51	-	0.54	0.54	-	0.34
Ga	25	22	19	17	19	17
V	92	145	84	106	109	46
Cr	70	99	58	115	122	189
Sc	9.34	-	8.91	2.88	-	5.76
Zn	88	101	57	92	39	20
Cu	50	41	37	bdl	21	bdl
Ni	43	31	25	41	104	67
Co	17.7	-	12.9	6.22	-	9.95
As	2.21	-	0.82	0.88	-	4.20
La	71.2	-	53.7	37.1	-	37.4
Ce	164	-	114	72.3	-	71.0
Nd	70.3	-	53.6	29.4	-	33.3
Sm	14.3	-	10.5	4.82	-	6.43
Eu	3.85	-	3.49	1.54	-	2.67
Tb	1.25	-	1.09	0.46	-	0.68
Yb	2.12	-	1.81	0.79	-	1.30
Lu	0.31	-	0.18	0.14	-	0.13
Au (ppb)	7.2	-	0.4	0.6	-	0.5

bdl - below detection level

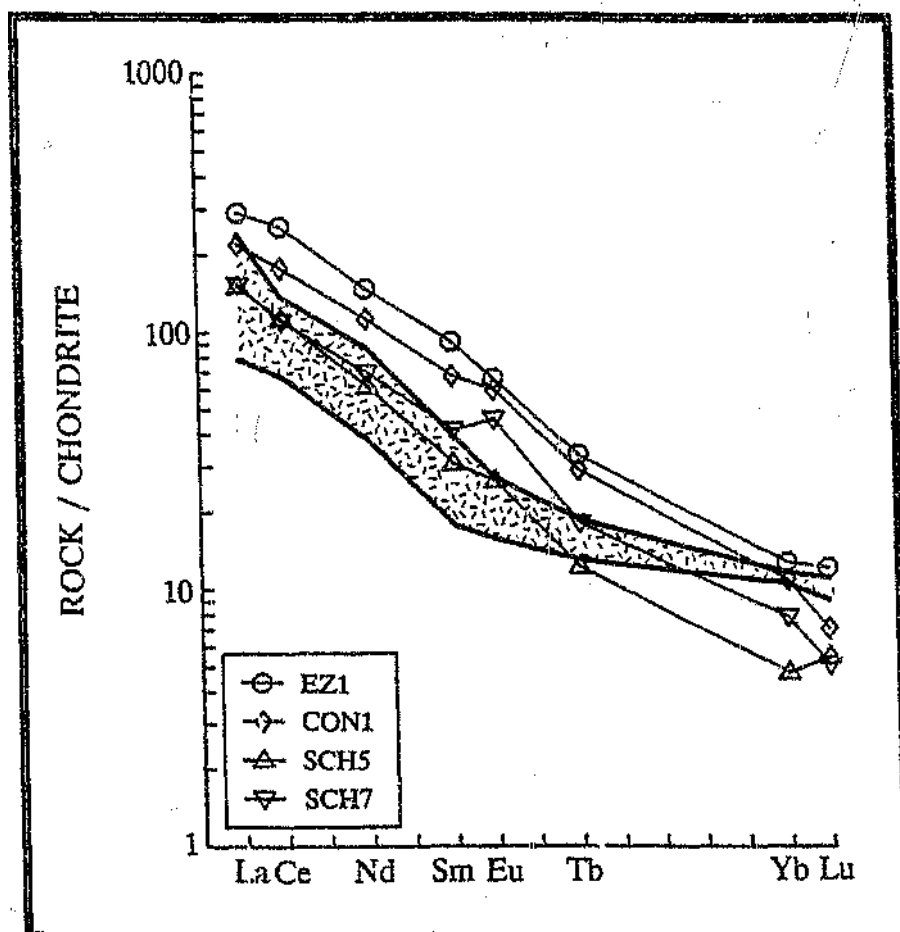


Figure 5.15 Chondrite-normalised REE abundance patterns of Schoongezicht Formation metavolcaniclastic rocks (sample labels as in Table 5.5 and Figure 1.4) and comparison with the compositional envelope of biotite-oligoclase schists from the Bien Venue Formation (randomly oriented dashes).

Table 5.6 Chemical data for chlorite schists from the Bien Venue Formation

Sample	BVM1	BVM2	BVM3	BVM4	BVM5
SiO ₂ (wt %)	47.01	53.00	55.35	50.59	56.17
TiO ₂	0.89	1.23	1.37	1.19	1.38
Al ₂ O ₃	7.88	10.75	12.07	10.96	12.99
Fe ₂ O ₃ total	13.06	16.45	17.49	16.32	15.20
MnO	0.24	0.24	0.19	0.20	0.09
MgO	5.49	3.15	2.85	3.55	4.53
CaO	8.67	5.10	2.00	4.45	1.84
Na ₂ O	1.58	2.91	2.85	2.97	1.89
K ₂ O	0.09	0.68	0.70	0.16	0.08
P ₂ O ₅	0.10	0.13	0.15	0.12	0.17
H ₂ O ⁻	0.07	0.14	0.27	0.04	0.19
H ₂ O ⁺	1.91	1.64	2.47	1.94	3.45
CO ₂	12.85	3.60	1.49	6.39	1.45
Total	99.84	99.02	99.25	98.88	99.43
Ba (ppm)	192	188	223	215	67
Rb	11	38	27	12	13
Sr	224	178	140	98	44
Cs	0.46	5.99	-	6.85	0.72
Pb	bdl	5	bdl	bdl	5
U	0.44	0.63	-	0.55	0.89
Th	1.46	2.11	-	2.16	2.93
Y	16	22	26	21	23
Nb	6	7	10	9	9
Zr	70	100	119	95	130
Hf	1.97	2.73	-	2.72	3.70
Ta	0.36	0.47	-	0.48	0.62
Ga	13	18	19	20	18
V	177	181	204	230	160
Cr	66	17	bdl	7	bdl
Sc	19.6	17.0	-	16.3	16.7
Zn	84	135	160	131	135
Cu	169	100	269	321	314
Ni	78	31	25	36	15
Co	43	45	-	47	41
As	5.90	0.53	-	6.81	20.6
La	8.26	11.2	-	10.7	13.8
Ce	19.8	27.7	-	25.0	35.2
Nd	13.7	18.5	-	16.2	20.8
Sm	2.93	4.03	-	3.79	4.37
Eu	1.59	1.79	-	1.55	1.72
Tb	0.63	0.77	-	0.76	0.83
Yb	1.93	2.32	-	2.27	2.62
Lu	0.32	0.38	-	0.35	0.42
Au (ppb)	1.2	2.3	-	2.1	4.4

bdl - below detection level

In Figure 5.1, the chlorite schists plot in the field of sub-alkaline basalts suggesting that they were derived from a basaltic precursor. Major element abundances also point to a basaltic parent, although low K_2O and high CO_2 values clearly reflect the effects of metamorphism - metasomatism. In a chondrite-normalized plot (Figure 5.16), the rocks exhibit flat profiles with only slight enrichment of the LREE relative to the HREE ($La_N/Yb_N = 2.9 - 3.6$), a feature characteristic of tholeiitic basalts (see Jakeš and Gill, 1970; Barrett *et al.*, 1991), and weak positive Eu anomalies ($Eu/Eu^* = 1.17 - 1.52$). Low Nb/Y (0.32 - 0.43; Figure 5.1) ratios are consistent with a tholeiitic affinity, but high Th^{*8}/Yb (0.89 - 1.32), Ce/Yb (10 - 13) and Ta/Yb (0.19 - 0.24) ratios suggest some calc-alkaline tendencies (see Pearce, 1982). Compared to normal-type mid-ocean ridge basalt (N-MORB; Pearce, 1982), the schists are strongly enriched in Th^* (8 - 17 x N-MORB) and weakly enriched in Ta, Nb and Ce (1.7 - 3.5 x). Zr, Hf, Sm and Ti concentrations are generally comparable to N-MORB, but Y, Yb and Sc (0.4 - 0.9 x) are weakly depleted, and Cr (< 0.03 - 0.3 x) is strongly depleted.

5.5 Palaeotectonic setting

The purpose of this section is to propose a palaeotectonic setting for the Bien Venue Formation using simple trace element comparative procedures with Phanerozoic suites of known tectonic setting. However, in order to understand the relevance of these comparisons it is first necessary to consider the nature and role of the plate tectonic processes during the Archaean, and also the tectonic setting of modern silicic volcanism.

5.5.1 The role of plate tectonics in the evolution of the Earth's early crust

Structural, geochemical, palaeomagnetic and theoretical studies during the past 20 years have provided extensive evidence for the operation of a plate tectonic regime during the Archaean, although the exact nature of the mechanisms involved and the applicability of modern-style (Phanerozoic) processes has proved to be controversial

⁸ Decay corrected Th value.

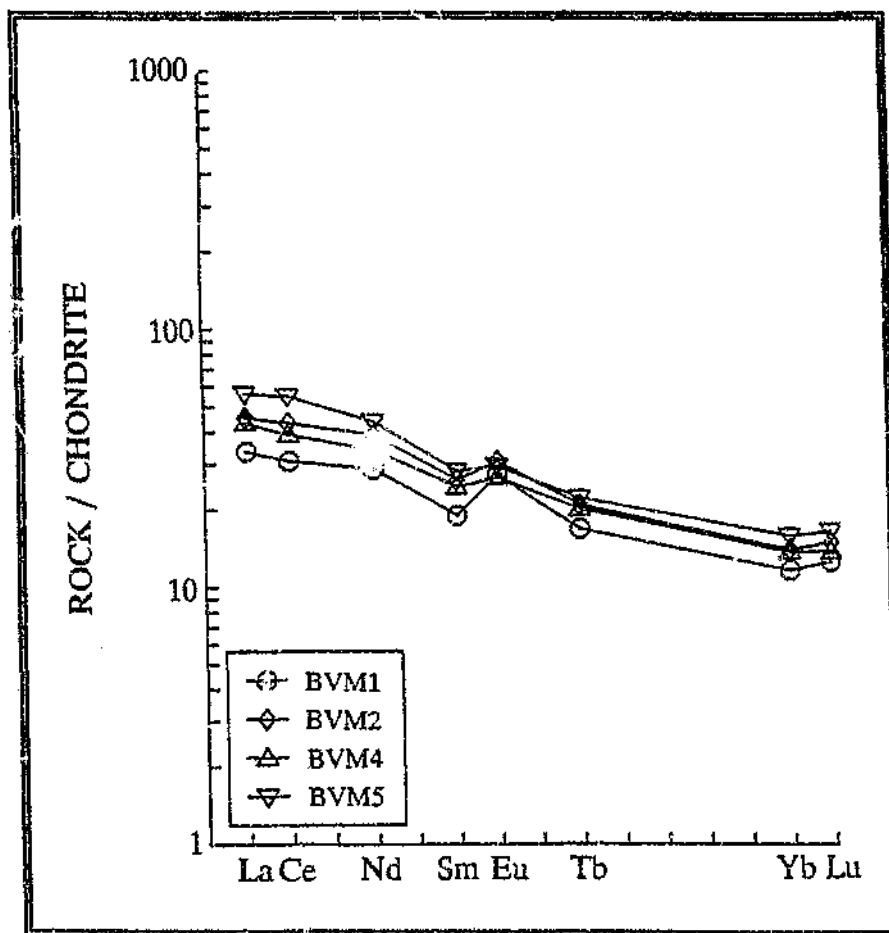


Figure 5.16 Chondrite-normalised REE patterns for chlorite schists (sample labels as in Table 5.6 and Figure 1.4).

(e.g. Condie and Harrison, 1976; Windley, 1977, 1981; Dewey and Windley, 1981; Nisbet and Fowler, 1983; Abbott and Hoffman, 1984; Kröner, 1985; Helmstaedt *et al.*, 1986; Nisbet, 1987; Layer *et al.*, 1989; Drummond and Defant, 1990; Nutman and Collerson, 1991; De Wit *et al.*, 1992; Kröner and Layer, 1992; Meyer *et al.*, 1992; Taira *et al.*, 1992; Davies, 1992). Nonetheless, there is a growing realization that Archaean plate tectonic processes were in all likelihood similar to those during the Phanerozoic (Cassidy *et al.*, 1991; Feng and Kerrich, 1992; Barley, 1993; Jackson *et al.*, 1994): early crustal evolution has been described in terms of oceanic arc (e.g. Vearncombe, 1991), continental arc

(e.g. Bickle *et al.*, 1983), combined oceanic / continental arc (e.g. Sylvester *et al.*, 1987), back-arc (e.g. Tarney *et al.*, 1976) and mid-ocean ridge (e.g. De Wit *et al.*, 1992) related magmatism and sedimentation. Tonalite - trondhjemite - granodiorite (TTG) suites surrounding and intruding greenstone belts are widely considered to have been derived from the anatexis of primordial oceanic crust in early subduction zones (e.g. Sleep and Windley, 1982; Martin, 1986, 1987, 1993; Drummond and Defant, 1990; Feng and Kerrich, 1992).

Apparent differences between Archaean and Phanerozoic successions may reflect the predominance of certain tectonomagmatic environments in response to higher radiogenic heat production in the early mantle (Wilks, 1988, and references therein). Hotter mantle temperatures would have resulted in smaller plates, faster spreading and increased plate convergence (Bickle, 1978, 1986; Nisbet and Fowler, 1983; Richter, 1985; Vlaar, 1986), but may, alternatively, also have resulted in greater total ocean ridge lengths and slower spreading rates (Hargraves, 1986). Preliminary studies of the palaeomagnetism of the rocks in the Barberton region, however, suggest that plate motion during the late-Archaean was not radically different from the present-day situation (Layer *et al.*, 1989; Kröner and Layer, 1992). Oceanic crustal thicknesses during the early Precambrian may also have been greater than present due to increased anatexis at constructive plate margins (Sleep and Windley, 1982; Nisbet and Fowler, 1983; Bickle, 1986; Davies, 1992). Crust which was thicker and warmer than modern analogues was probably also more buoyant and may have resisted subduction giving rise to ocean-ocean crustal collision (Wilks, 1988), or would have undergone shallow-angle subduction during ocean-continent convergence, leading to underplating (Molnar and Atwater, 1978; Sleep and Windley, 1982). On the other hand, Arndt (1983), Abbott and Hoffman (1984) and De Wit *et al.* (1987b, 1992) have argued that Archaean oceanic crustal thicknesses were similar or possibly even less than at present. However, whereas Abbott and Hoffman (1984) and Arndt (1983) favoured the operation of subduction-related tectonics dependant on the presence of dense komatiitic volcanics, De Wit *et al.* (1987b, 1992)

speculated that the Archaean oceanic crust was extensively hydrated and low in density and, hence, that earliest plate tectonic regimes were dominated by obduction processes.

Other workers (e.g. Gorman *et al.*, 1978; Anhaeusser, 1975, 1981a, b, 1984; Vlaar, 1986; Minnitt and Anhaeusser, 1992) suggested that crustal evolution during the Archaean differed markedly from that during the Phanerozoic, arguing that the former was dominated by gravity-driven tectonic processes involving diapirism. Models invoking diapirism generally envisage dense komatiite-dominated volcanic assemblages overlying lower density uppercrustal or uppermantle assemblages, with the resulting gravitational instabilities leading to pronounced vertical displacements. Anatexis of the volcanic successions to produce TTG diapirs is considered to have mainly occurred in the root-zones of the downsagging greenstone piles (Anhaeusser, 1984).

Interpretation of Archaean successions in terms of plate tectonic concepts is justified by the general stratigraphic and metallogenic similarities between greenstone successions and some Phanerozoic terranes (Abbott and Hoffman, 1984; Poulsen *et al.*, 1992; Barley *et al.*, 1992). Furthermore, the presence of komatiite and high-Al TTG assemblages of Cretaceous and Cenozoic age, suggests that some Archaean tectono-magmatic processes may have modern analogues (Drummond and Defant, 1990; Defant and Drummond, 1990; Storey *et al.*, 1991; Martin, 1993). While vertical tectonic processes involving diapirism clearly played an important role in the evolution of most, if not all, granitoid-greenstone terranes (e.g. Anhaeusser, 1981a, 1984; Jelsma *et al.*, 1993), they probably formed part of a larger-scale plate tectonic regime (Barker, 1979; Drummond and Defant, 1990; Cassidy *et al.*, 1991; Feng and Kerrich, 1992).

5.5.2 Geotectonic setting of modern silicic magmatism

Silicic magmatism has been recognised in a variety of modern volcano-tectonic settings. These include within-plate oceanic islands (e.g. Hawaiian Islands) and continental rifts (e.g. East African Rift), which are related to mantle plume activity and crustal extension, as well as magmatic arcs on oceanic (e.g. Indonesia, Marianas) and

continental (e.g. Japan, Andes) crust, both of which are linked to subduction zones at convergent plate boundaries. Silicic magmatism in intraplate settings characteristically has tholeiitic or alkalic affinities (Wilson, 1989). Magmatism in arc settings, on the other hand, ranges from tholeiitic through calc-alkalic to alkalic depending on subduction geometry and stage of evolution (e.g. Brown *et al.*, 1984). Nonetheless, rocks of the calc-alkaline series are typical of continental and evolved oceanic arcs / back-arc basins (Hamilton, 1988; Wilson, 1989), and the recognition of calc-alkaline affinities in ancient rocks, like those of the Bien Venue Formation (Sections 5.2 and 5.3), can be taken as evidence of a subduction-related origin at a convergent plate boundary (e.g. Bickle *et al.*, 1983; Cassidy *et al.*, 1991; Barley, 1993).

Rocks of mature arcs range in composition from basalt through basaltic andesite and andesite to dacite and rhyolite (or their respective intrusive equivalents), with andesites usually predominating (Hamilton, 1988; Wilson, 1989). Silicic volcanism is commonly far more voluminous in continental arcs (100's to 1000's of km³) than in oceanic arcs (generally less than a few km³), and in some continental regimes - e.g. the Taupo Volcanic Zone in New Zealand (Cole, 1981) and parts of the Sunda - Banda arc in Indonesia (Wheller *et al.*, 1987) - volcanism is predominantly silicic. The greater abundance of silicic rocks in continental settings is generally considered to reflect the hydrous fluxing of the over-riding continental crust in response to dehydration of the subducted slab and/or the influence of crustal contamination processes (see Wilson, 1989, for a review).

5.5.3 Discrimination and interpretation

Numerous geochemical studies have shown that magmatism in specific tectonic regimes is characterised by distinctive trace element distribution patterns (e.g. Pearce and Cann, 1973; Pearce and Norry, 1979; Thompson *et al.*, 1984; Pearce *et al.*, 1984; Meschede, 1986; Harris *et al.*, 1986), and the palaeotectonic discrimination of ancient (Phanerozoic and Proterozoic) sequences by empirical comparison with younger rocks

of known tectonic setting has gained widespread acceptance. Recognition of possible similarities between Archaean and Phanerozoic plate tectonic regimes (Section 5.5.1) has recently led to the application of such comparative procedures to granitoid-greenstone terranes (e.g. Sylvester *et al.*, 1987; Cassidy *et al.*, 1991; Feng and Kerrich, 1992). However, the significance of these comparisons is subject to two main provisos: (1) the effect of alteration on primary geochemistry; and (2) possible evolutionary changes in the nature of source regions and processes of magma generation between Archaean and post-Archaean times. While the influence of alteration-related compositional changes can be minimized by making use of the less-mobile elements (Section 5.1), the effect of possible changes in processes of magma generation are more difficult to assess. Martin (1986, 1987, 1993) and Condie (1989) have shown that some Archaean intermediate-to-silicic suites are strongly depleted in the HREE's and Y compared with Proterozoic and Phanerozoic analogues, and have suggested that this can be explained by higher geothermal gradients and, hence, different processes of magma production in early subduction zones. The deficiency in HREE's is interpreted to reflect the anatexis of primordial oceanic crust in the presence of a garnet + amphibole residue with a high bulk distribution coefficient for the HREE's (D_{HREE}), whereas melting of oceanic lithosphere during the Proterozoic and Phanerozoic is considered to have occurred in the presence of an olivine + pyroxene residuum with lower D_{HREE} values. Thus it is evident that the interpretation of Archaean successions solely on geochemical grounds is bedeviled by uncertainties (Bickle *et al.*, 1993; Collins, 1993). Nonetheless, comparison with Phanerozoic sequences may provide useful constraints concerning the most likely tectonomagmatic setting of Archaean rocks (e.g. Cassidy *et al.*, 1991; Feng and Kerrich, 1992; McDonough and Ireland, 1993). Indeed, it can be argued that uniformitarianism, *with appropriate caution*, offers the only realistic approach to interpreting Archaean geology.

Shown in Figure 5.17 are a series of geotectonic discriminant diagrams for schists of the Bien Venue Formation. On the Hf - Zr, Ta - Nb and Ta - Yb diagrams of Condie

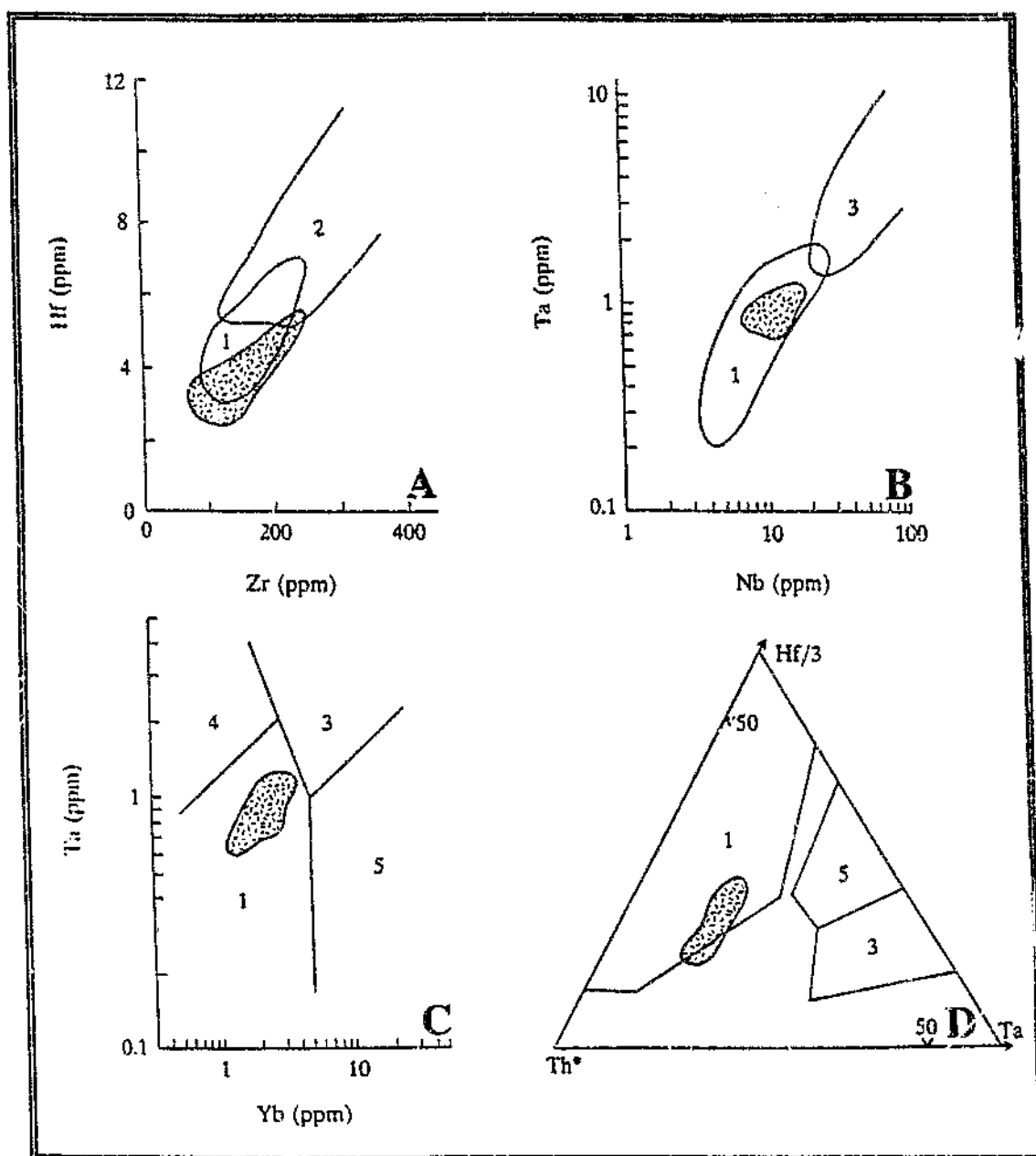


Figure 5.17 Chemical discriminant diagrams showing the geotectonic affinities of rocks from the Bien Venue Formation (randomly oriented dashes): (A) Hf - Zr plot (after Condie, 1986); (B) Ta - Nb plot (after Harris et al., 1986); (C) Ta - Yb plot (after Pearce et al., 1984); (D) Th* - Hf - Ta plot (after Wood et al., 1979; Th* is decay corrected value). Fields: 1 - magmatic arc; 2 - extensional basin; 3 - within-plate; 4 - syn-collision; 5 - ocean ridge. Note that (A), (B) and (C) only show data for the quartz-muscovite and biotite-oligoclase schists, whereas (D) shows data for all schist varieties.

(1986), Harris *et al.* (1986) and Pearce *et al.* (1984), the schists are seen to have relatively low Hf, Zr, Ta, Nb and Yb contents, a feature characteristic of rocks from Phanerozoic magmatic arcs. As was pointed out in Section 5.2.2.2, absolute abundances of these elements in the schists probably exceed concentrations in their protoliths, a conclusion which emphasises, when one considers the distribution of fields in the diagrams, their arc-like characteristics. On the Th - Hf - Ta diagram, which is usually used to determine the petrotectonic environment of basalts, but which may also be used to discriminate intermediate and silicic rocks (Wood *et al.*, 1979), the schists, once again, plot within, or close to, the arc domain.

Primordial-mantle-normalized trace element plots provide an alternative method of evaluating the most likely palaeotectonic affinity of the Bien Venue rocks (Figure 5.18). Noteworthy in all of the spiderdiagrams are troughs at Ta - Nb and Ti. The relative depletion of these so-called TNT elements is a typical feature of Phanerozoic subduction-related assemblages, irrespective of magmatic affinity; volcanic rocks erupted in intraplate settings rarely⁹ show such anomalies (e.g. Wood *et al.*, 1979; Brown *et al.*, 1984; Thompson *et al.*, 1984; Arculus, 1987; Briggs and McDonough, 1990; Rock, 1991; Van Bergen *et al.*, 1992; Peccerillo, 1992; Mitropoulos and Tarney, 1992). The deficiency of the TNT elements is generally considered to reflect their retention by refractory residual phases such as sphene, ilmenite, rutile, amphibole and garnet during partial anatexis of the subducted slab, the overlying mantle wedge or the deep arc crust (e.g. Saunders *et al.*, 1980; Briquieu *et al.*, 1984; Arculus and Powell, 1986; Hildreth and Moorbath, 1988; Drummond and Defant, 1990; Stolz *et al.*, 1990).

The arc-like affinities of the quartz-muscovite and biotite-oligoclase schists is further emphasized by their high LREE/HFSE ratios, particularly La/Nb (1.2 - 2.7) and La/Ta (22 - 32), which are similar to values found in silicic volcanic and intrusive rocks from modern arcs (e.g. Ewart, 1979; Pearce *et al.*, 1984). The low abundances of

⁹ Recent work by Foley and Wheller (1990) and Müller *et al.* (1992) indicated that some potassic and ultrapotassic suites in within-plate settings also exhibit TNT anomalies.

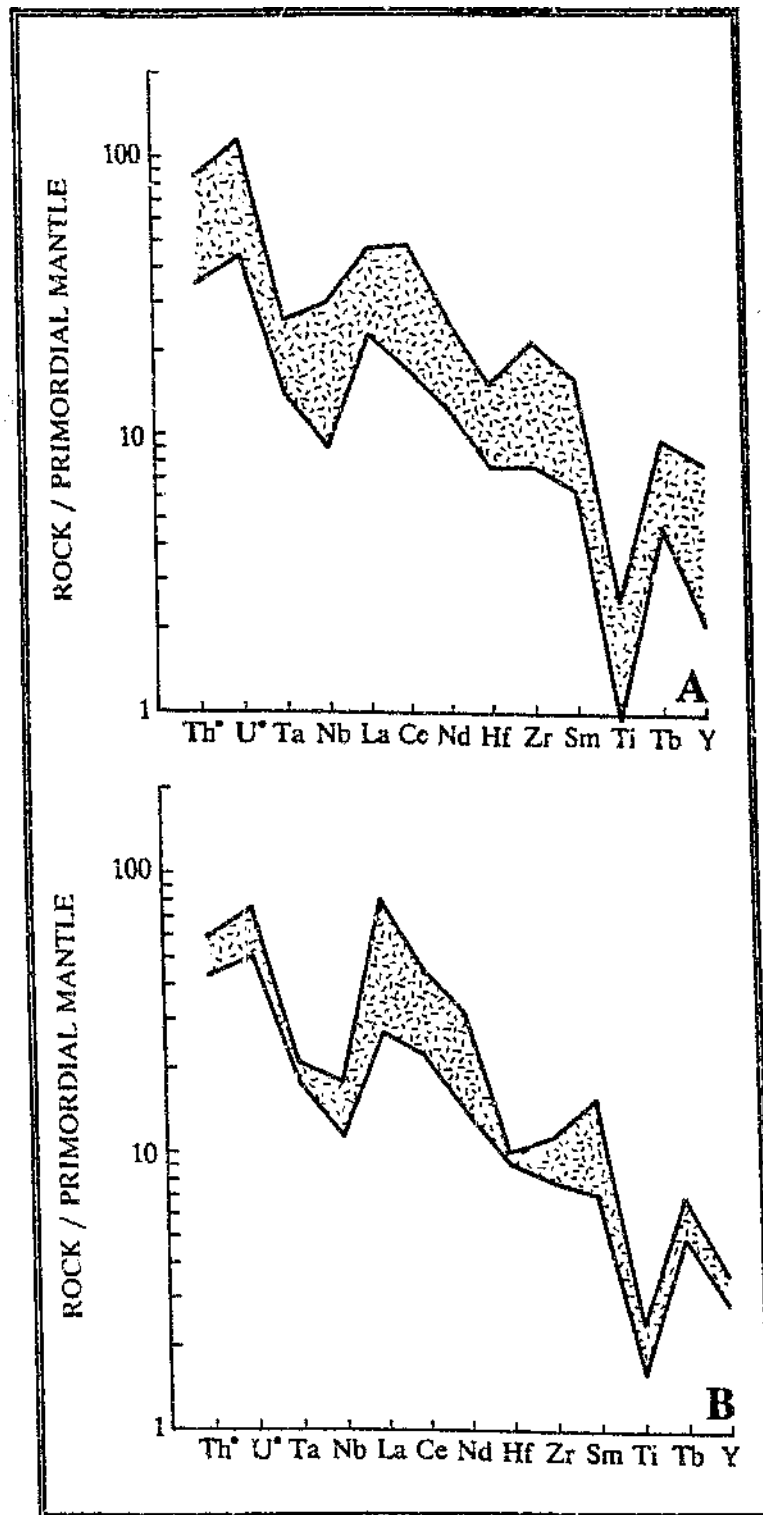


Figure 5.18 Primordial-mantle-normalized trace element diagrams for schists of the Bien Venue Formation: (A) quartz-muscovite schists; (B) biotite-oligoclase schists. Normalizing values and element order after Wood (1979). Th^* and U^* are decay corrected values.

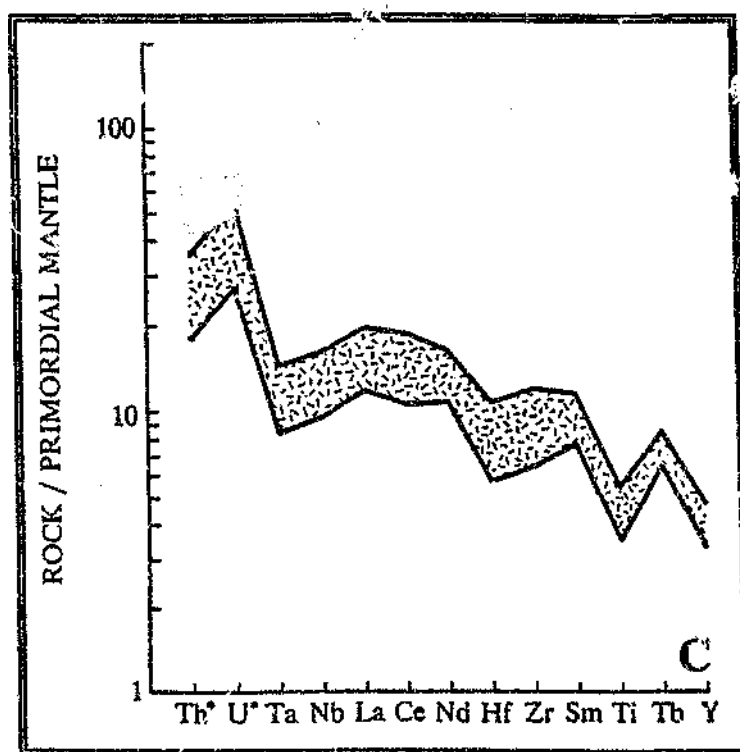


Figure 5.18 (continued): (C) chiorite schists. Th^* and U^* are decay corrected values.

Ni (15 - 78 ppm), Cr (< detection level - 66 ppm) and Y (16 - 26 ppm) recorded for the chlorite schists (Table 5.6) are comparable with abundances in some modern arc tholeiitic basalts (e.g. Ewart, 1982; Pearce, 1982), but elevated Ti/V values (30 - 52) are distinctly higher than those characterising arc tholeiites, and are more typical of calc-alkaline basalts (e.g. Shervais, 1982).

From the foregoing it is clear that the compositional characteristics of schists from the Bien Venue Formation are similar to Phanerozoic subduction-related assemblages at modern convergent plate boundaries. An arc-like setting is also indicated by the Bien Venue massive sulphide deposit (Section 4.3.7); research has shown that Kuroko-type mineralization is characteristically associated with subduction-related magmatism in arc or transitional arc / back-arc settings (e.g. Hutchinson, 1990; Urabe and Marumo, 1991; Sawkins, 1990; Swinden, 1991).

Although showing a distinctive arc-like geochemical signature, the Bien Venue Formation differs from most Phanerozoic subduction-related suites in terms of its compositional homogeneity. Whereas modern calc-alkaline sequences typically show a spectrum of compositions from basalt through to rhyolite, with andesites predominating (Section 5.5.2), the Bien Venue Formation consists almost entirely of silicic metavolcanics. Of course it can be argued that this reflects the preservation of only portion of a single, dominantly silicic, volcanic edifice. Nonetheless, the great abundance of silicic metavolcanics (Figure 1.4) suggests that the formation records a period of continental arc volcanism (see Section 5.5.2). Volcanic rocks of modern continental arcs are typically enriched in large-ion lithophile elements compared to suites in arcs built on oceanic crust (e.g. Wilson, 1989), but alteration renders suspect any geochemical discrimination based on these elements. Martin (1986, 1993), Drummond and Defant (1990) and Defant and Drummond (1990) have argued that the preponderance of silicic rocks in some Archaean calc-alkaline arc-like suites is due to faster spreading rates during early plate tectonic regimes. According to these workers, rapid spreading results in the subduction of young, hot oceanic crust, favouring the production of HREE-depleted TTG melts via direct fusion of the slab. Slower spreading, on the other hand, results in the hydration anatexis of the overlying mantle wedge in response to the pre-fusion dehydration of older and cooler oceanic crust, resulting in the production of relatively HREE-enriched melts of basaltic, andesitic, dacitic and rhyolitic composition. Comparison of the REE distribution patterns for the quartz-muscovite and biotite-oligoclase schists with data published by Martin (1993), however, indicates that the preponderance of silicic metavolcanics in the Bien Venue Formation cannot be attributed to a different subduction thermal regime, since the rocks do not exhibit marked depletion of the HREE indicative of derivation by direct melting of young subducted lithosphere.

Thus to summarise, the chemical data indicate that schists from the Bien Venue Formation have strong chemical affinities with Phanerozoic calc-alkaline subduction-related assemblages, suggesting that their protoliths were erupted in a mature volcanic

arc. This conclusion is supported by the presence of a Kuroko-type VHMS deposit within the succession. The predominance of silicic metavolcaniclastic rocks suggests that the arc was a continental arc.

5.6 Geochronology

Owing to structural complications, the stratigraphic position of the silicic metavolcanic-volcaniclastic rocks to the north of Three Sisters could not be unequivocally determined. A geochronological study was therefore undertaken to resolve their chronostratigraphic position.

5.6.1 Analytical method

A 27 kg sample (BVR4) of low-grade quartz-muscovite schist was collected from an outcrop in the western part of Stentor 219 JU (see Figure 1.4 for locality). The sample was crushed and sieved in the laboratories of the Council for Science and Industrial Research in Pretoria using equipment which had been thoroughly pre-cleaned using brushes and compressed air. The $< 150 \mu\text{m}$ crushed fraction was subsequently enriched over a WilfleyTM table. Zircons were extracted from the heavy mineral concentrate using standard magnetic (Franz Isodynamic SeparatorTM) and densimetric (bromoform and methylene iodide) methods. Following a detailed morphologic study under a binocular microscope, the writer decided to remove the $< 63 \mu\text{m}$ zircon fraction with the aid of a microsieve as these grains appear to be identical to the $> 63 \mu\text{m}$ fraction, but are more likely to have experienced isotopic disturbance. A selection of hand-picked zircons was sent to Prof. S.A. Bowring and Dr. C. Isachsen of the Department of Earth, Atmospheric, and Planetary Sciences, MIT, for isotopic analysis. Results of these analyses are given in Table 5.7. A summary of the analytical procedures employed at MIT is presented below.

Table 5.7 U-Pb isotope data for sample BVR4

Fraction	Zircon type [‡]	Sample weight (mg)	Total Pb (ppm)	U (ppm)	²⁰⁶ Pb/ ²³⁸ U			²⁰⁷ Pb/ ²³⁵ U			²⁰⁷ Pb/ ²⁰⁶ Pb		
					Ratio [¶]	% error	Age [*]	Ratio [¶]	% error	Age [*]	Ratio [¶]	% error	Age [*]
1	A, m	0.0260	148.8	233.0	0.512392	0.398	2666.8	17.6761	0.402	2972.3	0.250197	0.0474	3186.0 ± 0.8
2	A, m	0.0383	266.9	298.0	0.527509	0.568	2730.9	18.1356	0.812	2997.0	0.249345	0.487	3180.6 ± 7.7
3	B, m	0.0105	94.3	119.6	0.597491	1.33	3019.7	21.4057	1.33	3157.1	0.259834	0.0916	3245.7 ± 1.4
4	B, m	0.0675	138.9	201.3	0.556460	0.339	2852.0	19.6594	0.343	3074.8	0.256233	0.0449	3223.7 ± 0.7
5	B, m	0.0038	9.84	14.38	0.514574	2.96	2676.1	18.2483	2.96	3002.9	0.257201	0.0794	3229.6 ± 1.3
6	B, m	0.0125	132.5	170.7	0.573582	0.834	2922.5	20.4186	0.839	3111.4	0.258184	0.0791	3235.7 ± 1.2
7	B, s	0.0025	102.1	121.7	0.659888	0.802	3266.7	23.9084	0.804	3264.7	0.262772	0.0721	3263.4 ± 1.1
8	B, s	0.0025	161.1	201.9	0.656628	0.525	3254.0	23.6834	0.526	3255.5	0.261591	0.0421	3256.3 ± 0.7
9	B, s	0.0025	86.2	110.2	0.621428	0.964	3115.6	22.2930	0.964	3196.6	0.260381	0.046	3247.8 ± 0.7
10	B, m	0.0032	156.7	199.6	0.630694	0.407	3152.3	22.5666	0.409	3208.4	0.259506	0.0446	3243.7 ± 0.7

‡ - m = multigrain, s = single-grain; ¶ - corrected for common Pb, spike, fractionation and blank; * - age and 2σ error in Ma

Following air-abrasion and prior to dissolution, the zircons were leached in warm dilute HNO_3 for 10 minutes in order to remove any surficial contamination and then weighed into TFE teflon™ micro-capsules. Dissolution was accomplished using an HF/HNO_3 mixture at a temperature of 230°C in pressure sealed vessels using the method of Parrish (1987). Analyses 1 - 6, consisting of 3 - 4 grains each, were aliquoted and spiked with a mixed $^{206}\text{Pb}/^{235}\text{U}$ tracer. After examination of the data from these analyses, it was decided to analyse a further 4 fractions (7 - 10) with a mixed $^{205}\text{Pb}/^{235}\text{U}/^{233}\text{U}$ spike. Analyses 7 - 9 were of single crystals, while analysis 10 consisted of 5 small grains. The solutions were dried to fluoride salts and converted to chlorides in 6 N HCl at a temperature of 180°C . Lead and uranium were isolated using standard anion column separation employing Hcl chemistry. Lead was loaded onto Re filaments using a silica gel-phosphoric acid technique, and the uranium was loaded onto Re filaments with graphite. Pb blanks for all analyses averaged 10 ± 5 pg total Pb. Most isotopic measurements were performed in static multicollector mode using a Daly electron multiplier for ^{204}Pb data on a VG SECTOR 54 mass spectrometer housed in the Mass Spectrometry Laboratory at MIT. For analysis 9, however, a single collector peak-switching mode was used employing the Daly electron multiplier. Mass fractionation factors determined by replicate analyses of NBS standards SRM 981 (common Pb) and SRM 983 (radiogenic Pb) were applied to all data. Data were corrected by 0.14% and 0% per atomic mass unit for Pb and U, respectively. Radiogenic Pb concentrations and Pb/U values were calculated from raw fractionation corrected mass spectrometer data following Ludwig (1980) and using the computer program PBDAT, version 1.03 (Ludwig, 1988). Initial Pb compositions were estimated according to the two-stage evolutionary model of Stacey and Kramers (1975). Ages were calculated using decay constants recommended by Steiger and Jäger (1977) ($\lambda^{238}\text{U} \approx 1.55125 \times 10^{-10} \text{ year}^{-1}$; $\lambda^{235}\text{U} = 9.8485 \times 10^{-10} \text{ year}^{-1}$). Linear regression and calculation of intercepts and uncertainties was carried out with the computer program GEODATE, version 2.2 (Eglington and Harmer, 1991). All ages are reported at the 2σ confidence level.

5.6.2 Zircon description

Zircons from sample BVR4 range from $\sim 20 - 250 \mu\text{m}$ across and are of two morphologic types (Figure 5.19):

(1) Type A zircons account for an estimated 65 % of the total zircon content of BVR4, and comprise euhedral-to-subhedral, generally stubby crystals having length-to-width ratios of between 1.5 - 3. They are light- to dark-brown in colour, exhibit prominent multiple growth zoning, and are invariably characterized by a high degree of alteration / metamictization, particularly in their core zones. Most grains contain clear, globular, ovoidal or vermicular inclusions, 1 - 20 μm in diameter, which are haphazardly distributed.

(2) Type B zircons are pale pink or light-brown, euhedral or subhedral crystals with high elongation ratios (usually > 3). They rarely exhibit radiation damage and carry clear tubular inclusions, 5 - 100 μm in length, which are subparallel to the c-axis of the host. Some grains exhibit faint multiple growth zoning, but others show no obvious zonation when viewed under a binocular microscope. The Type B phase is occasionally found as partial to complete overgrowths on Type A grains; the interface between the two phases is typically well-defined.

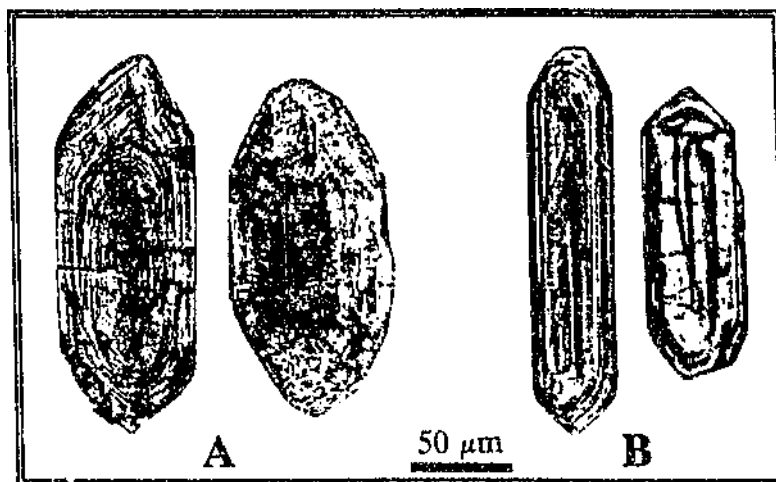


Figure 5.19 Photomicrographs of zircons from sample BVR4: (A) Type A zircons; (B) Type B zircons.

Both zircon varieties have features typical of magmatically formed zircons (see Speer, 1982; Pupin, 1980), and are thus interpreted to be of magmatic origin. Nonetheless, it is clear that some, if not all, Type B zircon growth post-dated formation of the Type A crystals; the latter variety could therefore represent xenocrysts. This interpretation is, however, not favoured by the writer since the Type A zircons constitute more than half of the total zircon content of sample BVR4 and do not exhibit any marked intrapopulation heterogeneity. According to Speer (1982), rapid magma crystallization favours the growth of elongate zircons, whereas slower crystallization rates favour stubby crystals. Hence, the observed differences in morphology may indicate a discontinuous zircon growth history. It is possible that the Type A zircons crystallized in a slower cooling environment, whereas the Type B zircons crystallized in a faster cooling environment (E.A. Retief, pers. comm., 1991). The presence of two morphologically distinct magmatic zircon varieties in sample BVR4 may thus reflect the entrainment of slightly younger microphenocrysts prior to the eruption and solidification of the magma.

Due to the high degree of alteration / metamictization of the Type A zircons and financial constraints, it was decided to focus on the Type B crystals for purposes of the isotopic age determination.

5.6.3 Results and interpretation

In Figure 5.20 it is evident that most data points plot below concordia to define a Pb-loss discordia. However, fractions 7 and 8, which represent single zircon analyses, are concordant within error. Fraction 7 displays Pb-inheritance and its Pb-Pb age of 3263 ± 1 Ma provides an upper limit for the volcanism. The Pb-Pb age of 3256 ± 1 Ma obtained for fraction 8 is thus considered to be the best age estimate of the Bien Venue Formation (Table 5.7). Regression of fractions 3 - 10 (uncertainties augmented according to errorchron option 4 of Eglington and Harmer, 1991) also gives an upper intercept age

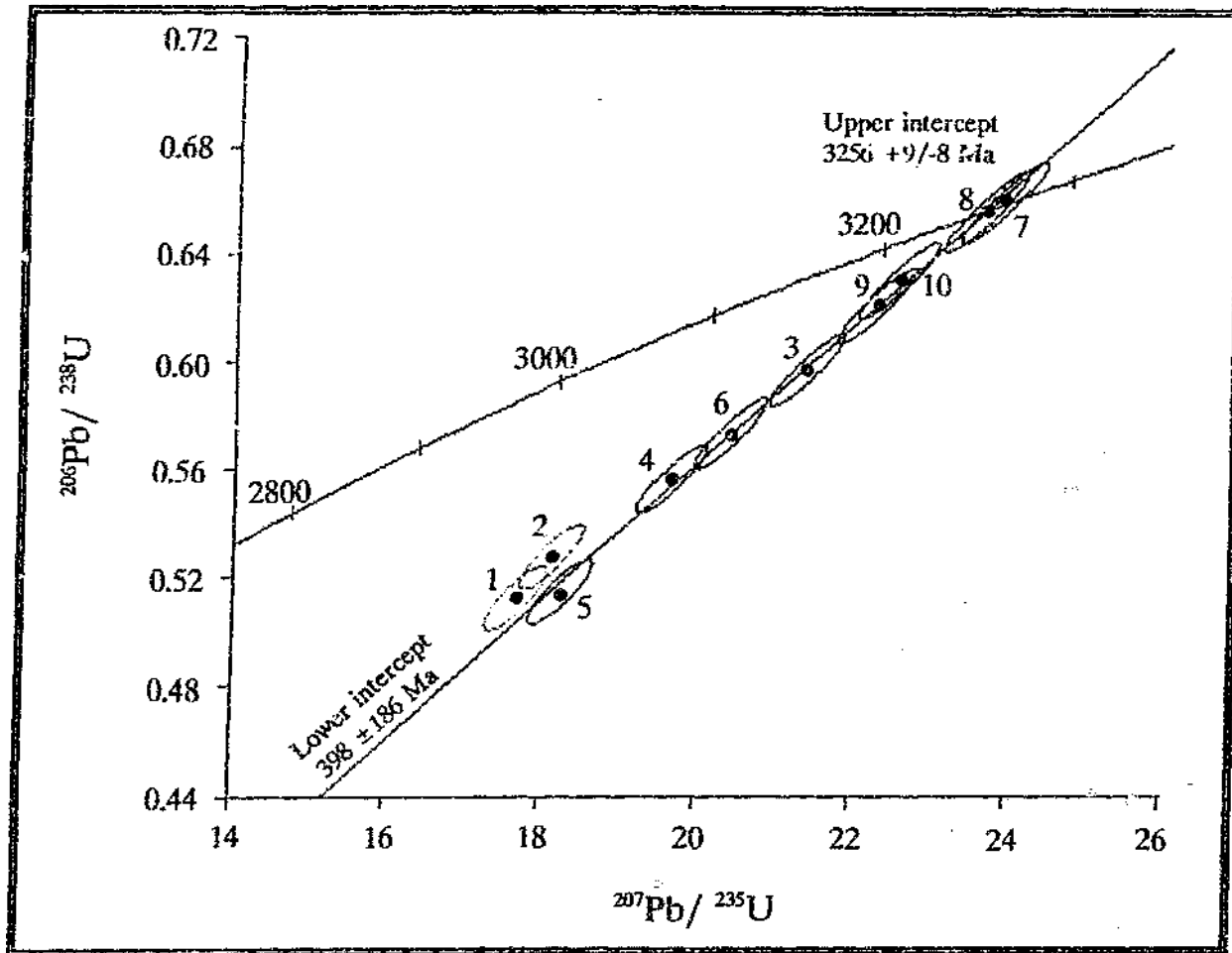


Figure 5.20 Concordia diagram showing U-Pb data for all zircon fractions analysed (numbers refer to fractions listed in Table 5.7). Also shown is the best fit line for fractions 3 - 10. Age errors and error ellipses are at the 2 σ level.

of $3256 \pm 9/-8$ Ma. These ages are identical, within error, to the Pb-Pb evaporation age of 3259 ± 5 Ma reported recently by Kröner *et al.* (1991a) for a sample collected at the Bien Venue massive sulphide deposit.

The following conclusions may be drawn from the isotopic study:

(1) The age of 3256 Ma obtained for the silicic schists is ~200 Ma younger than recent age estimates for the lower portions of the Onverwacht Group (Armstrong *et al.*, 1990). Hence, it is clear that the silicic metavolcanic-volcaniclastic succession in the study area cannot be correlated with the Theespruit Formation as previously proposed by Viljoen and Viljoen (1970), but forms part of the Fig Tree Group (< 3453 - 3222 Ma; Kröner and Compston, 1988; Kröner *et al.*, 1991a; Kamo and Davis, 1994). Further, the age obtained is ~30 Ma older than recent high precision age determinations carried out on the silicic metavolcanic rocks of the Schoongezicht Formation (3226 - 3222 Ma; Kröner *et al.*, 1991a; Kamo and Davis, 1994), precluding correlation with this unit. Accordingly, the writer concludes that the Bien Venue Formation constitutes a separate chronostratigraphic unit at the top of the Fig Tree Group in the northeastern sector of the BGB.

(2) The age data also indicates that the Bien Venue Formation is 30 - 44 Ma older than the Kaap Valley (3229 - 3226 Ma; Tegtmeier and Kröner, 1987; Armstrong *et al.*, 1990; Kamo and Davis, 1994) and Nelshoogte (3212 Ma; York *et al.*, 1989) plutons. Hence, the metavolcanics do not represent the coeval effusive equivalents of tonalite-trondhjemite plutonism along the northern flank of the BGB, as has been proposed for silicic metavolcanic rocks of the upper Fig Tree Group elsewhere in the BGB (Kröner *et al.*, 1991a; Kamo and Davis, 1994). Instead, the Bien Venue Formation records a period of silicic volcanism for which no plutonic equivalents have yet been identified (Section 2.5.2).

(3) The age of the Bien Venue Formation provides a minimum constraint on the age of the sedimentation within the underlying Belvue Road Formation (Section 4.1), and a maximum age constraint on sedimentation within the overlying Moodies Group (Section 7.1). U-Pb and Pb-Pb age determinations by Heubeck *et al.* (1993) and Kamo and Davis (1994) on the Salisbury Kop pluton, which truncates Moodies Group strata, indicated that this intrusion has an age of 3109 - 3079 Ma. These data, together with the date obtained during the present study, bracket Moodies sedimentation in the northeastern sector of the BGB to between 3256 - 3079 Ma (see also Heubeck *et al.*, 1993).

6. ASSESSMENT OF THE BASE-METAL ORE POTENTIAL OF THE BIEN VENUE FORMATION AND OTHER SILICIC UNITS OF THE BARBERTON SUPERGROUP

6.1 Introduction

One of the more perplexing enigmas of the metallogeny of the BGB is the paucity of Cu - Zn and Cu - Zn - Pb VHMS ore deposits such as are extensively developed in Archaean greenstone terranes in the Superior Province of Canada (Viljoen and Viljoen, 1969g; Anhaeusser, 1976a, 1981b; Anhaeusser and Viljoen, 1986; Lowe, 1985). Despite considerable exploration, only one noteworthy, albeit subeconomic, deposit of this type has been discovered to date. This deposit, which is hosted by silicic metavolcaniclastic rocks of the Bien Venue Formation, is described in Section 4.3.7.

Anhaeusser (1976a, 1981b) suggested that the scarcity of VHMS deposits in the BGB, and indeed most other southern African greenstone belts, can be attributed mainly to the low lithologic abundance of silicic volcanics within these sequences. Lowe (1985) argued that the absence of noteworthy deposits in the Onverwacht Group is due to the predominance of shallow-water and subaerial conditions during silicic volcanism, leading to the erosion of the high-relief volcanic edifices, along with any base-metal ores which may have formed.

Research in the Superior Province by Campbell *et al.* (1982), Lesher *et al.* (1986) and Lesher and Campbell (1987), the results of which have been extended to include greenstone successions in the Slave Province (Goodwin, 1988, quoted in Padgham, 1992) and the Late Proterozoic rocks of Nova Scotia (Dostal *et al.*, 1992), has demonstrated that most *economic* VHMS deposits are associated with submarine silicic volcanic rocks that have distinctive trace element characteristics. From these observations it is reasonable to conclude that the mineral potential of silicic volcanic successions can be evaluated using a combination of geochemistry (Lesher *et al.*, 1986) and

palaeovolcanology (Lowe, 1985; Cas, 1992; Barley, 1992). The following is an attempt to assess the base-metal ore potential of the Bien Venue Formation and other silicic units of the Barberton Supergroup in light of this research. Note that the conclusions are subject to assumptions of element immobility as discussed in Section 5.1.

6.2 Classification and interpretation

According to Lesher *et al.* (1986) and Lesher and Campbell (1987), it is possible to subdivide the silicic metavolcanic-volcaniclastic rocks of the Superior Province into three main groups, F-I, F-II and F-III, the last of which is preferentially associated with economic VHMS mineralization. The classification is based mainly on the distribution of the REE's, specifically the La_N/Yb_N and Eu/Eu^* ratios. In the absence of REE data, the Zr (which displays geochemical similarities with the LREE's) to Y (which exhibits affinities with the HREE's) ratio can be used to approximate the La_N/Yb_N value (Lesher *et al.*, 1986). The pertinent characteristics of the three groups are summarised in Table 6.1 and briefly described below.

F-I silicic metavolcanics, which do not host economic VHMS mineralization, are characterised by steep, LREE-enriched chondrite-normalized REE profiles ($La_N/Yb_N \geq 6$), high Zr/Y (9 - 31) ratios, insignificant to moderate positive Eu anomalies ($Eu/Eu^* = 0.9 - 2$), and low abundances of the HFSE's.

F-II metavolcanics, which occasionally host major VHMS deposits, have moderate La_N/Yb_N (2 - 7) and Zr/Y (6 - 11) values, moderate concentrations of the HFSE's, and variable Eu anomalies ($Eu/Eu^* = 0.4 - 1.4$); REE profiles of mineralised F-II sequences are characterised by negative Eu anomalies, whereas unmineralized successions exhibit insignificant or small positive Eu anomalies.

Table 6.1 Comparison of the geochemistry of silicic metavolcanic rocks of the Barberton and Murchison greenstone belts with mineralized and barren successions in the Superior Province, Canada

Column	1	2	3	4	5	6	7	8	9	10
Classification	F-I	F-II	F-IIIa	F-IIIb	F-I	F-I	F-I	F-I	F-I	F-IIIb
Y (ppm)	3 - 31	17 - 55	25 - 70	72 - 238	10 - 35 (18)	14 - 18 (7)	15 - 37 (6)	5 - 7 (5)	11 - 27 (7)	49 - 437 (64)
Zr	86 - 273	96 - 451	170 - 370	194 - 732	96 - 241 (18)	79 - 126 (7)	101 - 240 (6)	45 - 191 (5)	144 - 280 (7)	444 - 985 (64)
Hf	2.2 - 6.0	2.3 - 11	3.9 - 8.6	5.8 - 24	2.7 - 5.3 (11)	3.2 - 3.5 (5)	2.6 - 5.5 (4)	-	4.4 - 5.5 (5)	-
Sc	1.6 - 21	4.4 - 25	7 - 20	1.4 - 11	4.5 - 13 (11)	6.3 - 9.3 (5)	2.9 - 9.3 (4)	-	0.8 - 7 (5)	-
La	9.2 - 46	9.1 - 43	9.8 - 37	2.6 - 163	16 - 34 (11)	30 - 58 (5)	37 - 71 (4)	12 - 53 (3)	12 - 88 (5)	3.1 - 6.7 (2)
Yb	0.4 - 3.8	1.7 - 6.0	3.4 - 9.3	7.3 - 32	1.2 - 3.5 (11)	1.7 - 2.1 (5)	0.8 - 2.1 (4)	0.6 - 3.0 (3)	1.2 - 2.7 (5)	6.2 - 19 (2)
Zr/Y	9 - 31	6 - 11	4 - 7	2 - 6	4 - 9 (18)	5 - 8 (7)	7 - 9 (6)	9 - 29 (5)	6 - 16 (7)	2 - 8 (64)
La _N /Yb _N	6 - 39	2 - 7	1 - 4	1 - 4	6 - 11 (11)	6 - 21 (5)	19 - 32 (4)	13 - 19 (3)	6 - 31 (5)	0.1 - 0.7 (2)
Eu/Eu*	0.9 - 2.0	0.4 - 1.4	0.4 - 0.9	0.2 - 0.6	0.8 - 1.0 (11)	0.9 - 1.4 (5)	1.1 - 1.9 (4)	0.8 - 1.8 (3)	0.5 - 0.9 (5)	0.2 - 0.3 (2)

Numbers in brackets indicate the number of samples used to determine the range of values

- Columns:
- 1 - 4. Barren and massive base-metal sulphide ore-associated rocks, Superior Province, Canada (Lesher *et al.*, 1986) - see text for explanation
 5. Bien Venue Formation, quartz-muscovite schists (this study)
 6. Bien Venue Formation, biotite-oligoclase schists (this study)
 7. Schoongezicht Formation (this study)
 8. Hooggenoeg Formation (this study; Glikson and Jahn, 1985; De Wit *et al.*, 1987a)
 9. Theespruit Formation (this study; Glikson, 1976)
 10. Rubbervale Formation, Murchison Supergroup, Murchison greenstone belt (Taylor, 1981; Vearncombe *et al.*, 1987)

F-III metavolcanics exhibit unfractionated or only weakly fractionated REE patterns ($La_N/Yb_N = 1 - 4$) and low Zr/Y (4 - 7) values, and are usually characterised by pronounced negative Eu anomalies ($Eu/Eu^* = 0.4 - 0.9$). They may be further subdivided, on the basis of HFSE and Sc concentrations, into F-III-A and F-III-B-type metavolcanics (Table 6.1), both of which host major VHMS deposits, including those of the Rouyn - Noranda, Kidd Creek and Matagami districts (Sangster and Scott, 1976).

Leshner *et al.* (1986) and Leshner and Campbell (1987) have argued that variations in geochemistry and mineral potential between the three main groups of silicic metavolcanic rock reflect differences in their respective modes of formation. Petrogenetic considerations indicate that prior to eruption, ore-associated F-III and F-II magmas underwent plagioclase fractionation in shallow-level magma reservoirs, leading to the marked depletion of Eu relative to the other REE in the residual magma, and the resultant formation of negative Eu anomalies in eruptive products. These subvolcanic intrusions are considered to have acted as the heat source for the hydrothermal fluids which gave rise to the VHMS mineralization. Magmas of barren F-I and F-II successions, on the other hand, are considered by Leshner *et al.* (1986) and Leshner and Campbell (1987) to have escaped extensive fractionation in shallow magma chambers, thus accounting for the lack of negative Eu anomalies and economic VHMS mineralization.

Included in Table 6.1 are chemical data for silicic metavolcanic-volcaniclastic rocks of the Bien Venue, Schoongezicht, Hooggeroeg and Theespruit Formations, encompassing the four principal periods of silicic volcanism in the Barberton Supergroup. The former are characterised by steep chondrite normalised REE profiles with no significant negative Eu anomalies (Sections 5.2 and 5.3) and, in terms of both absolute and relative REE distributions, closely resemble the group F-I metavolcanic rocks of Leshner *et al.* (1986) (Table 6.1). Low abundances of Y, Zr and Hf support this classification, but moderate Zr/Y values (usually between 6 - 8) are similar to those of

F-II metavolcanics in Canada. Trace element characteristics of rocks of the Schoongezicht and Hooggenoeg Formations are also comparable with group F-I rocks in the Superior Province (Table 6.1).

The available chemical data thus indicates that silicic lithologies of the Bien Venue, Schoongezicht and Hooggenoeg Formations are of a type not usually associated with economic VHMS mineralization in Canada. The rocks do not appear to have evolved in a shallow subvolcanic magma reservoir and, hence, their prospectivity for economic VHMS mineralization is assessed as poor.

Further mention should be made at this point of the Bien Venue massive sulphide deposit (Section 4.3.7). If the importance of subvolcanic intrusions in the genesis of VHMS ores as advocated by Lesher *et al.* (1986) is accepted, then it is reasonable to assume that the ore-forming process at Bien Venue also required a shallow magma chamber. Indeed, the presence of crystal-rich metavolcaniclastic rocks to the north of Three Sisters provides some evidence that the magmas of the Bien Venue Formation crystallized in shallow-level reservoirs prior to eruption (Section 4.3.9), although this is not apparent in their REE profiles. Schists in the immediate vicinity of the Bien Venue deposit have not been analysed chemically during the present study because they are highly altered. Trace element analyses of 25 samples presented by Murphy (1990) generally indicate moderate concentrations of Y (21 - 57 ppm; \bar{x} = 41 ppm) and Zr (142 - 332 ppm; \bar{x} = 235 ppm); Zr/Y ratios are highly variable, but ~40 % of the specimens analysed have values of less than 6. These data suggest that some of the rocks hosting the mineralization may have group F-IIIa characteristics, but further studies are needed to see if they exhibit Eu deficiencies indicative of feldspar crystal fractionation. Nevertheless, the subeconomic nature of the ores at Bien Venue suggests that if a subvolcanic intrusion provided the heat necessary for the mineralization process, that it

was either too small or too deep-seated to have formed an economic deposit. It is, of course, also possible that the ore-forming process at Bien Venue was driven by a heat source not directly linked to the volcanism.

Silicic lithologies of the Theespruit Formation exhibit chemical similarities with both F-I- and F-II-type rocks in the Superior Province, but, unlike rocks of the Bien Venue, Schoongezicht and Hooggenoeg Formations, are usually characterised by negative Eu anomalies (Section 5.2.3), suggesting that they have undergone feldspar fractionation (Table 6.1). Thus, on the basis of chemical data alone, the Theespruit Formation rocks may be regarded as being prospective for VHMS mineralization, even though they show LREE-enriched REE distribution patterns. However, as has been pointed out by Lowe (1982, 1985), silicic volcanism in the Theespruit Formation probably took place in a subaerial to shallow-water environment which was not conducive to the formation and preservation of VHMS-type ores (see also Section 4.3.9). Thus, even though their chemistry suggests that they may host VHMS deposits, the lack of a suitable ore-forming environment indicates that the Theespruit rocks are unlikely to contain any economic mineralization.

In order to contrast the geochemistry of the essentially barren units of the BGB with mineralized silicic successions in the central part of the Murchison greenstone belt, the writer has also included in Table 6.1 data for the low-grade rhyodacitic-to-rhyolitic schists of the Rubbervale Formation, Murchison Supergroup. The latter rocks have an age of $> 2950 \pm 38$ Ma (Vearncombe *et al.*, 1987) and host the ore bodies of the "Letaba Cu-Zn line" (Viljoen *et al.*, 1978; Taylor, 1981; Maiden, 1984). These deposits represent the only economic VHMS ores known in the Archaean of South Africa.

HFSE distributions in schists of the Rubbervale Formation indicate that they are chemically similar to the group F-IIIB metavolcanics of Leshner *et al.* (1986), having remarkably high Zr (444 - 985 ppm; \bar{x} = 670 ppm) and Y (49 - 437 ppm; \bar{x} = 186 ppm) concentrations, but low Zr/Y (2 - 8; \bar{x} = 3.9) values. REE analyses published by

Vearncombe *et al.* (1987) show peculiar LREE-depleted patterns ($La_N/Yb_N < 1$) which, in terms of their overall distribution, more closely resemble the FIII-type metavolcanics of the Canadian Archaean. Leshner *et al.* (1986) recognised similar REE distributions in silicic rocks associated with the Skorovass and Stekenjokk VHMS deposits in Sweden and the Snow Lake deposit in Canada, and speculated that they might be characteristic of a fourth type of silicic metavolcanic rock which is also associated with economic mineralization. More important to the present discussion, however, is the fact that the schists exhibit pronounced negative Eu anomalies ($Eu/Eu^* = 0.2 - 0.3$), possibly indicating that their precursors underwent plagioclase fractionation (Vearncombe *et al.*, 1987).

It is noteworthy that Vearncombe *et al.* (1987) recently proposed that the Rubbervale Formation volcanics are in part comagmatic with the Novengilla gabbro-anorthosite series of the Rooiwater Complex (see also Vearncombe, 1991). This intrusive body, which has an age of > 2650 Ma (Vearncombe *et al.*, 1987), crops out over a strike length of ~ 65 km along the northern margin of the Murchison greenstone belt, and has been interpreted by these workers as a shallow-level subvolcanic sill. Rocks of the Novengilla series show positive Eu anomalies ($Eu/Eu^* = 1.3 - 2.6$), suggesting that they represent the cumulate equivalents of the Rubbervale Formation metavolcanics (Vearncombe *et al.*, 1987). If this interpretation is correct, then it seems likely, taking into account the findings of Leshner *et al.* (1986), that the Rooiwater intrusion provided the heat necessary for the fumarolic activity which gave rise to the Letaba VHMS deposits. It is, however, also possible, given the lack of precise age data, that the Rooiwater cumulates and the Rubbervale metavolcanics are not coeval. In this case, the writer speculates that the Rubbervale rocks and associated deposits of the Letaba area are related to a subvolcanic intrusive body which is either not preserved or not presently exposed.

6.3 Discussion

Silicic schists of the Bien Venue Formation are chemically similar to group F-I metavolcanics in the Superior Province and, given the findings of Leshner *et al.* (1986), are unlikely to host economic VHMS mineralization, even though they were apparently erupted in a deep-water environment (Section 4.3.9). Available chemical data suggests that the Schoongezicht and Hooggenoeg Formation rocks are also of the F-I-type, and they are likewise considered to have little base-metal ore potential. Although the silicic metavolcanics of the Theespruit Formation often show negative Eu anomalies, possibly indicating that they evolved in a shallow-level magma reservoir, they were apparently mainly erupted in a subaerial to shallow-water setting (Lowe, 1982, 1985), and as such, are also considered unlikely to contain significant ore deposits.

In contrast to the essentially barren rocks of the BGB, silicic metavolcanics of the Rubbervale Formation resemble the group F-III rocks of Leshner *et al.* (1986) which are preferentially associated with major VHMS deposits in the Superior Province. The Rubbervale volcanics host the economic VHMS ores of the Letaba Cu-Zn line, and overlie what has been interpreted by Vearncombe *et al.* (1987) as a penecontemporaneous shallow-level intrusive body, the Rooiwater Complex. This intrusion may have been the heat source of the hydrothermal fluids which formed the Letaba deposits.

From the foregoing, it may be concluded that the absence of economic VHMS ores in the silicic successions of the BGB is due mainly to a combination of two factors. The first of these is the apparent scarcity of F-II- and F-III-type rocks such as are extensively developed in the mineralized greenstone successions of the Canadian Archaean. In making this statement, the writer does not preclude the possibility that F-III-type metavolcanic rocks are locally developed in the BGB. The conclusions presented above are based on a restricted number of chemical analyses which may not be representative of all silicic units in the Barberton Supergroup, since variations in the

petrochemical affinity of rocks within volcanic successions are known to occur (e.g. Gèlinas *et al.*, 1984; Ujike and Goodwin, 1987). The second factor which appears to have to have adversely affected the formation of economic base-metal ores in the BGB is the palaeoenvironment of the volcanism. Economic VHMS deposits form in deep-water settings (Section 4.3.9) and are thus unlikely to have developed in the mainly shallow-water to subaerially erupted silicic successions of the basal portions of the Onverwacht Group (Lowe, 1985).

The above mentioned factors have important implications for silicic-hosted volcanogenic Cu-Zn-(\pm Pb \pm Au \pm Ag) exploration in the BGB as well as other greenstone terranes in southern Africa. Prospective units for economic VHMS mineralization may be identified using a combination of whole-rock geochemistry and a knowledge of the palaeoenvironment of the volcanism. Geochemistry can be used to determine whether or not the rocks have undergone fractionation in a high-level magma chamber (Campbell *et al.*, 1982; Leshner *et al.*, 1986; Leshner and Campbell, 1987). Favourable deep-water successions may be indicated by the presence of hemipelagic muds and turbidites, or the absence of *in situ* pyroclastic (*sensu stricto*) deposits (Cas, 1992; McPhie and Allen, 1992). It is the writers opinion that any further base-metal exploration in the BGB should focus on a detailed chemical and volcanological evaluation of Fig Tree Group volcanics in the northeastern sector of the belt which were probably deposited in a deep-water environment (Sections 4.2.5 and 4.3.9).

7. MOODIES GROUP

7.1 Introduction

The Moodies Group constitutes the uppermost stratigraphic unit in the study area, coring all major F_m synclines (Section 9.2.1.1). It attains an estimated maximum preserved thickness of ~2200 m in the Big Buffalo Syncline (Section 9.2.1.1.1), and consists of variably metamorphosed and deformed rudaceous and arenaceous rocks, the relative proportions of which vary markedly along strike, as well as from one syncline to the next. Stratigraphic considerations over the study area as a whole, however, indicate that the basal part of the sequence is composed mainly of interbedded conglomerate and quartzite, while the upper portion is dominated by quartzite, with subordinate conglomerate, pebbly quartzite and, in places, siltstone and shale. Nevertheless, substantial quartzite sequences locally constitute the base of the succession. Due to a lack of suitable marker horizons, correlation of the succession from syncline to syncline, or with the Clutna, Joe's Luck and Baviaanskop Formations as outlined in Section 2.3, is generally equivocal.

The nature of the contact between the Moodies Group rocks and the underlying strata cannot readily be ascertained in the field owing to limited exposures and structural complexities. However, inspection of Figure 1.4 indicates that the rocks stratigraphically overlie a wide variety of metavolcanic and metasedimentary lithologies belonging to the Fig Tree, as well as the Onverwacht Groups. In the Three Sisters and American Synclines (Sections 9.2.1.1.6 and 9.2.1.1.7), the Moodies rocks rest on silicic schists of the Bien Venue Formation which, as previously described (Section 4.1), constitutes the uppermost formation of the Fig Tree Group in the northeastern sector of the BGB. In the Big Buffalo, Amo, Igwalagwala and Lily East Synclines (Sections 9.2.1.1.1, 9.2.1.1.3, 9.2.1.1.4 and 9.2.1.1.5), however, the Moodies strata overlie shale-greywacke assemblages of the lower Fig Tree Group (Section 4.1), while in the Lily West Syncline (Section 9.2.1.1.5), they overlie basic and ultrabasic schists assigned to the Theespruit Formation

(Section 3.1). This disparity in the nature and stratigraphic position of the underlying lithologies, coupled with the common presence of conglomeratic rocks near the base of the succession, suggests that the Moodies Group rests on a marked paraconformity or unconformity over much of the study area (see also Visser *et al.*, 1956; Heubeck and Lowe, 1994). This is contrary to the suggestions of Eriksson (1979, 1980b) and Jackson *et al.* (1987) that contacts between the Fig Tree and Moodies Groups in the northern part of the BGB are mostly conformable and gradational.

7.2 Conglomerates

Conglomerates occur in all regional F_2 synclinal structures identified in the mapped area, but are best developed in the Big Buffalo, Lily East, Three Sisters and American Synclines where they form laterally continuous zones, with intercalated quartzite, up to several hundred metres thick. The core zones of the Three Sisters and Lily East Synclines, in particular, consist largely of conglomerate. Conglomerates are also prominently developed in two southward-younging Moodies successions that straddle the southern boundary of Stentor 219 JU, extending eastwards onto Koedoe 218 JU and the eastern margin of Figure 1.4 (Section 9.2.1.1.11). Elsewhere, the rocks typically only form thin (a few centimetres or metres wide), inconsistent lenses sporadically interbedded with the quartzites (Figure 7.1A).

The conglomerates are mainly poorly sorted, range from matrix- to clast-supported, and usually contain a variety of chert and quartzite (quartz arenite, sublitharenite, subarkose; classification after Pettijohn *et al.*, 1972) clasts, 0.5 - 15 cm in size. Clast diameters seldom exceed 25 cm, except in the western parts of the Three Sisters Syncline where clasts 25 - 35 cm in diameter are not uncommon, and occasional quartzite boulders exceeding 70 cm across were recorded. The clasts occur in a grey-beige, recrystallized, fine- to medium-grained matrix that characteristically contains

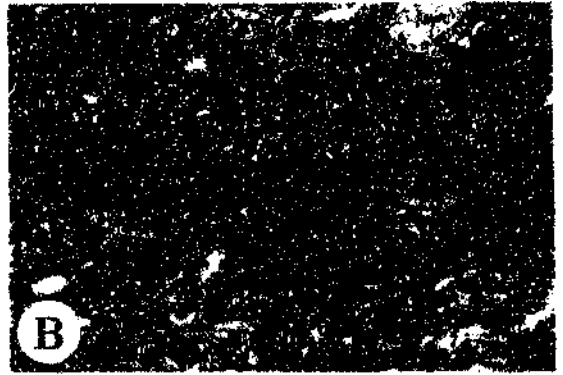


Figure 7.1 Features preserved in rocks of the Moodies Group:

(A) Thin conglomerate bands containing subangular chert clasts in cross-stratified quartzite (Singerton 260 JU). Coin (circled) is 2.4 cm in diameter.

(B) Well-rounded quartz arenite cobbles and pebbles in poorly sorted, oligomict conglomerate (Bien Venue 255 JU). Lens cap is 4.9 cm across.

(C) Subrounded BIF boulder 38 cm long and 24 cm wide in polymict conglomerate (Singerton 260 JU).

(D) Large-scale planar cross-bedding in coarse-grained quartzite (Kaalrug 465 JU).

(E) Sinuous, bifurcating, symmetrical ripples in medium-grained quartzite (Laughing Waters 454 JU).

(F) Desiccation cracks in siliceous siltstone (Rusoord 261 JU).

abundant angular, grit-sized, grey chert fragments. Those conglomerates that directly overlie ferruginous shales of the Fig Tree Group often display a rusty brown discoloration due to narrow veinlets and disseminations of secondary hematite - goethite within the matrix. These oxides were presumably derived from the underlying shales during diagenesis / metamorphism. The majority of conglomerate beds are internally structureless, although crude bedding, clast imbrication, as well as normal and inverse grading were recorded at a few localities. Some of thicker units are also split by lenticular beds of medium- to coarse-grained, often gritty, cross-stratified quartzite ranging up to several metres in thickness. These beds frequently contain scattered, granule- or pebble-sized clasts of chert and quartzite, or less commonly, discontinuous pebble lags.

Clasts of grey or grey and white banded chert dominate most of the conglomerates studied. They are generally angular to subrounded and have low sphericities. Quartzite clasts are often, but not invariably, present. In some conglomerates, however, particularly those in the western parts of the Three Sisters Syncline, quartzite clasts locally predominate over the cherty varieties (Figure 7.1B). The quartzite clasts are typically rounded or well-rounded, have moderate sphericities, and are present even in conglomerates at the base of the succession. They typically consist of moderately sorted, subangular-to-rounded, monocrystalline quartz grains with lesser chert, feldspar, muscovite, chlorite and opaques, and are on average 2 - 10 times larger than associated chert clasts. Subordinate clast varieties include BIF, jaspilite and green, often fuchsitic, chert, the latter likely representing silicified basic-to-ultrabasic volcanics (see Paris *et al.*, 1985; Duchač and Hanor, 1987; Hanor and Duchač, 1990)(Figure 7.1C). Clasts of granitoid, quartz-feldspar porphyry, greywacke, dolomite and chert-clast conglomerate were also recorded in some outcrops. Rarely, the larger chert, BIF and quartzite clasts exhibit structures such as small-scale folds and quartz-infilled tension fractures which, on the basis of clast / matrix relationships, clearly formed prior to their incorporation into the gravel beds. More commonly, however, the clasts, particularly the cherty varieties, are discoidal due to post-depositional tectonic flattening (Section 9.2.2.3). The matrix of

these deformed conglomerates characteristically exhibits a well-developed grain-shape foliation which is oriented perpendicular to the short axes of the flattened clasts.

7.3 Quartzites and siltstones

The quartzites characteristically weather buff or light-grey, range in texture from fine- to very coarse-grained, and are structured predominantly by planar-bedding. The bed thicknesses typically range from ~1 - 100 cm, with an average of between 5 - 20 cm. Internal planar and trough cross-beds were recognised at several localities. Set thicknesses generally vary from ~5 - 20 cm, although large-scale planar cross-sets with set thicknesses of over 40 cm were recorded in the Big Buffalo Syncline on Kaalrug 465 JU (Figure 7.1D). The cross-beds are often vertically stacked, forming cosets up to 50 cm or more in thickness. The forsets typically display upward-fining grain-size trends. Herringbone cross-beds, flaser beds, as well as symmetrical and asymmetrical ripples, were also noted in some areas (Figure 7.1E). The coarser-grained quartzites in places contain thin (a few millimetres or centimetres wide) gritty lenses composed of angular grey chert fragments, or more rarely, scattered angular-to-rounded clasts of chert and quartzite up to ~5 cm in diameter.

Thin sections of the quartzites show that they are predominantly quartz arenites, sublitharenites and subarkoses (classification after Pettijohn *et al.*, 1972), consisting of well-sorted, equidimensional, subangular-to-rounded, monocrystalline quartz grains, with lesser plagioclase, microcline and rock fragments. The latter include, in approximate order of decreasing abundance, polycrystalline quartz (chert), granitoid, chlorite schist, shale - greywacke, quartz-muscovite schist and hornblende amphibolite. Monomineralic allogenic grains composed of chlorite, chloritoid, tourmaline, rutile, zircon, mica and amphibole were also recorded in a few specimens. Deformed quartzites are characterised by a preferred alignment of lensoid quartz grains exhibiting pronounced undulose extinction (post-depositional) and evidence of pressure solution along their boundaries.

Partial overgrowths of secondary quartz and quartz-filled pressure shadows were also recorded in some specimens. Authigenic muscovite occurs either as ragged flakes aligned subparallel to the grain-shape foliation, or in fine aggregates rimming, and replacing, quartz and feldspar grains. Secondary chlorite forms fine, radial clusters that overgrow the margins of adjacent quartz grains.

Bedding in the quartzites is accentuated in places by thin (usually < 1 cm wide), impersistent partings of dark-grey, well-laminated, often siliceous siltstone, composed of subangular quartz grains contained in a matrix of chlorite and muscovite. Desiccation cracks (Figure 6.1F) and fine ripple marks are evident on the surfaces of some these partings, while scattered angular siltstone rip-up clasts frequently characterise the basal portions of overlying quartzite beds.

Thicker units of laminated, light- to dark-brown siltstone and shale up to ~70 m wide occur intercalated with quartzites in the Amo and Hlambanyathi Synclines. These units, which in places contain narrow (typically < 2 - 3 m wide) lenses of fine- to medium-grained, massive or cross-bedded sandstone, do not outcrop well and cannot generally be traced along strike for more than ~500 m. However, in the Hlambanyathi Syncline, a persistent band of argillite, traceable for over 7 km, occupies the core of the fold (Section 9.2.1.1.2). In most areas, this unit directly overlies gritty quartzites constituting the limbs of the fold, but along the western boundary of Singerton 260 JU, the argillites are separated from the latter by a sporadically developed BIF, consisting of interlayered reddish jaspilite and hematite beds 1 - 5 cm wide (Figure 1.4, H10 and H11). Thickness of the BIF, which rests directly on the quartzites and, in places, even conglomerate, could not be determined owing to inadequate exposures, but is almost certainly less than ~5 m.

7.4 Depositional setting

Preserved sedimentary structures are similar to those found in Moodies rocks elsewhere in the BGB (e.g. Anhaeusser, 1976b; Eriksson, 1977, 1979; Lamb and Paris, 1988) and point to a shallow-subaqueous to subaerial depositional environment characterised by a wide range of energy conditions. Clasts, cross-beds and ripple marks give evidence of high-energy, tractive bed-load transport. Symmetrical and asymmetrical ripples suggest the influence of oscillatory and current waves, respectively, while herringbone cross-beds indicate reversing current directions. The laminated nature of the shales and siltstones suggests that they represent suspended load material deposited via settling under low-energy conditions. The BIF is likely the product of chemical sedimentation below storm wave base. Desiccation cracks and siltstone rip-up clasts provide evidence of periodic subaerial exposure and reworking of pre-existing sediments.

Detrital constituents indicate sediment derivation from a heterogeneous provenance area dominated by volcanic and sedimentary rocks comparable to those found within the underlying Fig Tree and Onverwacht Groups. Some of the volcanic fragments display evidence of pre-incorporation silicification and low- to medium-grade dynamic alteration, pointing to fairly high metamorphic conditions in the source area(s). The granitoid clasts provide direct evidence of deep denudation of early continental crust, possibly as a consequence of vertical tectonic processes (Anhaeusser, 1973), while the quartzite clasts indicate concomitant erosion of pre-existing, mature indurated arenaceous rocks. The widespread occurrence of the latter clasts, even in the basal parts of the sequence, is problematical as no mature siliciclastic successions pre-dating the Moodies Group are known to be preserved on the Kaapvaal Craton (Tankard *et al.*, 1982). The quartzite clasts could not have been derived from the erosion of coarse sedimentary accumulations analogous to those which occur in the Fig Tree Group in the southern parts of the BGB, since these predominantly comprise immature, lithic-rich rocks (e.g. Eriksson, 1980b; Jackson *et al.*, 1987; Lamb and Paris, 1988; Nocita and Lowe, 1990).

Sedimentological studies by Eriksson (1977, 1979, 1980b) and Jackson *et al.* (1987) suggested that the Moodies Group strata accumulated in a north-facing braided alluvial plain - delta - shallow continental shelf system in response to denudation of a southerly provenance area. If correct, this interpretation implies a general decrease in maximum clast size and thickness of conglomerates towards the supposedly more distal parts of the basin in the north. This is clearly at variance with the presence of unusually thick and coarse conglomerate units at the base of the sequence in the northern part of the BGB, particularly within the Three Sisters Syncline. In this context, it is interesting to note that Heubeck and Lowe (1993, 1994) recently suggested that at least part of the Moodies sediments may have been derived from a source terrane to the north of the BGB.

8. GRANITOID ROCKS AND LATE-STAGE INTRUSIVES

8.1 Introduction

Preliminary reconnaissance mapping and geochemical studies of the granitoid terrane north of the BGB, previously undertaken by Robb *et al.* (1983), led these authors to define a large (~60 km long and ~6 km wide) plutonic body known as the Stentor pluton. This body separates the Nelspruit batholith to the north from the main mass of the BGB to the south (Figure 8.1). Robb *et al.* (1983) also suggested that the Stentor pluton was tonalitic-to-trondhjemitic in composition and, in the absence of any reliable isotopic age studies at the time, correlated the body with the tonalite-trondhjemite gneiss plutons that intrude the southwestern portions of the BGB (Section 2.4). Detailed mapping and geochemical work by the writer indicates, however, that the pluton has a much smaller areal extent, and that it consists of equigranular-textured granodiorite-adamellite, totally unlike any of the gneissic rocks encountered in the tonalite-trondhjemite plutons. The new field and chemical data suggest that the Stentor pluton forms part of the Nelspruit batholith (Kohler *et al.*, 1992). A heterogeneous suite of gneisses and migmatites, also forming part of the Nelspruit batholith, is exposed north and west of the pluton. The purpose of this chapter is to describe the geology and geochemistry of the Stentor pluton and adjacent gneisses, and to suggest possible correlatives of the former.

8.2 Description of the Nelspruit batholith

The Nelspruit batholith underlies vast tracts of country north of the BGB and consists of three main cogenetic textural phases (Robb, 1978; Robb *et al.*, 1983) (Figure 8.1):

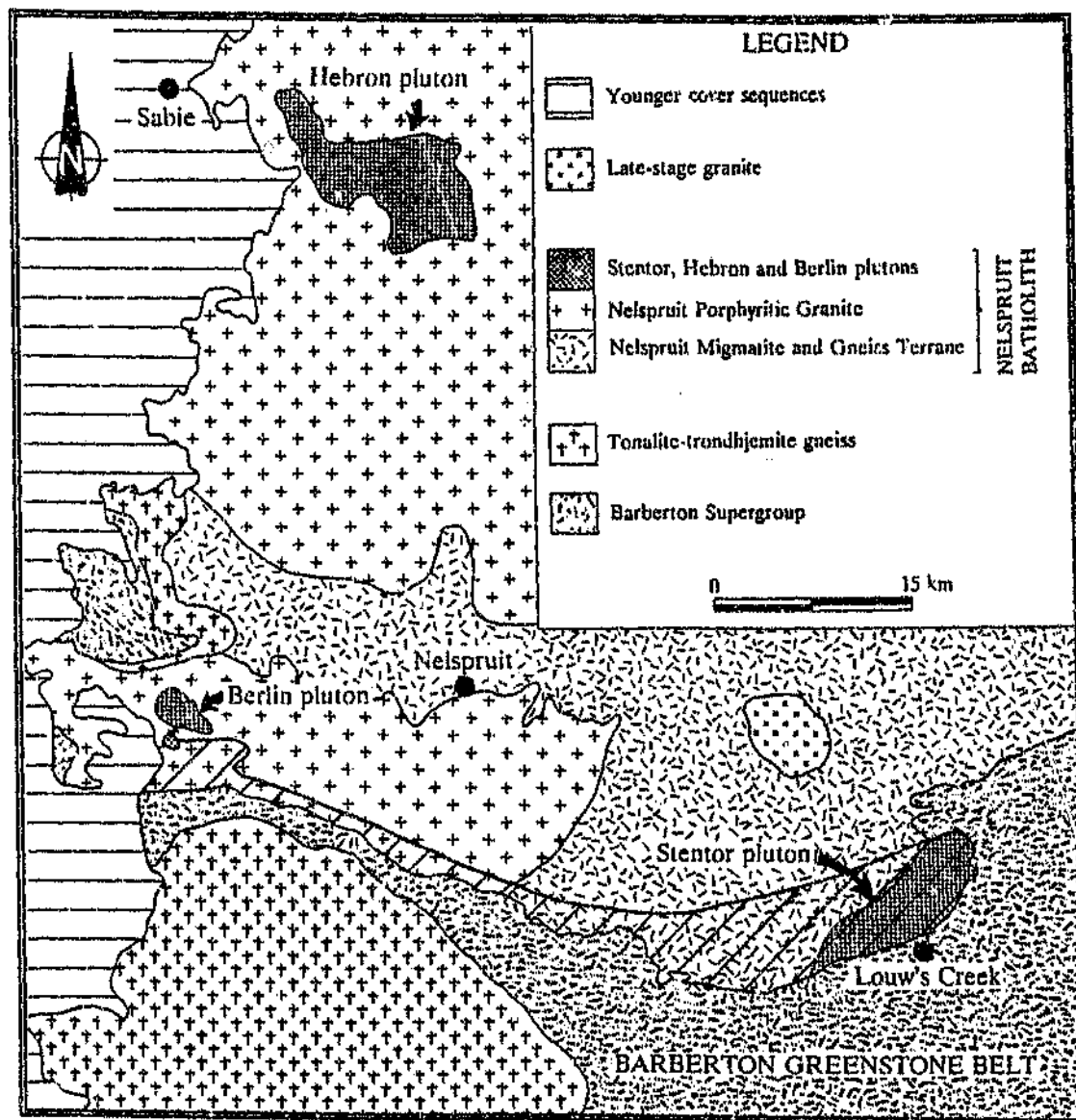


Figure 8.1 Simplified revised map of the northwestern sector of the BML showing the distribution of the three main phases of the Nelspruit batholith (modified after Robb et al., 1983). Distribution of the Stentor pluton as defined by Robb et al. (1983) is shown by the diagonal hatch.

- (1) a complex suite of strongly foliated, tonalitic-to-granitic (*sensu stricto*) gneisses and migmatites, known as the Nelspruit Migmatite and Gneiss Terrane, which is confined to the low-lying and marginal portions of the batholith;
- (2) a massive, coarse- to very coarse-grained, typically K-feldspar megacrystic granodiorite-adamellite phase known as the Nelspruit Porphyritic Granite, which dominates the topographically elevated central and western parts of the batholith, forming a sheet-like unit overlying the migmatites and gneisses; and
- (3) a medium- to coarse-grained, equigranular-textured granodiorite-adamellite phase which occurs in two discrete pluton-like bodies, intrusive into the Nelspruit Porphyritic Granite, known locally as the Hebron and Berlin plutons.

Robb *et al.* (1983) proposed a four stage evolutionary model for the Nelspruit batholith. The first stage involved the derivation of a K-rich granitoid magma from the anatexis of tonalite-trondhjemite gneiss precursors, possibly in response to a widespread mantle / lower crust degassing event. During their ascent to higher crustal levels the potassic melts are considered to have interacted with pre-existing granitoid and greenstone lithologies, forming the migmatites and gneisses. On cooling, the magmas underwent *in situ* fractional crystallization giving rise to the porphyritic granitoids. The initial stages of solidification appear to have been governed by the crystallization of a quartz + plagioclase + biotite cumulus assemblage, whereas the later stages involved the fractionation of an assemblage containing K-feldspar as an additional phase (McCarthy and Robb, 1978). The Hebron and Berlin plutons are considered by Robb *et al.* (1983) to have formed by a process of magma filter pressing shortly after crystallization of parts of the porphyritic phase.

8.3 Stentor pluton

8.3.1 Field characteristics

The Stentor pluton occurs as a small (~14 km long and ~4 km wide) northeast-trending ovoid body situated immediately north of Louw's Creek, and consists of homogeneous, medium- to coarse-grained, pinkish-grey, equigranular-textured granodiorite-adamellite (Figures 8.2 and 8.3A). Exposure over the pluton is generally fairly good, except in the north-central parts bordering the Kaap River and a narrow strip along the pluton's southern margin. Thick veneers of regolith and alluvium in these areas obscure relationships between the pluton and the adjacent gneissic and supracrustal assemblages. Granitoid rocks along the southern margin of the pluton have, however, been subjected to considerable shearing, and form the footwall of a major fault, referred to as the Revolver Fault, which extends along the northern boundary of the BGB as far east as Louw's Creek (Section 9.2.1.2.11) (Fripp *et al.*, 1980). The granitoids in this area are juxtaposed against amphibolites of the Theespruit Formation (Section 3.3), and display a pervasive mylonitic foliation (S_m - Section 9.2.1) that dips at 40 - 70° to the south. In places, the mylonites exhibit a semicontinuous compositional banding, defined by biotite enrichments, which also typically dips at moderate to steep angles to the south. A second, northeast-trending ductile fault, referred to as the Overton Fault, extends along the pluton's northern margin, but is only well-exposed in the vicinity of the defunct Overton Gold Mine (Section 9.2.1.2.9). Mylonites in this area are characterised by a northeast-striking, shallowly (~20 - 30°) southeastward-dipping S_m foliation.

In its eastern portion, the Stentor pluton intrudes quartz-muscovite schists of the Bien Venue Formation within the Stentor Antiform (Sections 4.3 and 9.2.2.1). The precise contact between the granitoids and the schists is rarely exposed, but unequivocal intrusive relationships were recorded on Driehoek 221 JU (Figure 8.3B). Numerous elongate granitoid apophyses, some of which are fringed by zones of variably hybridized

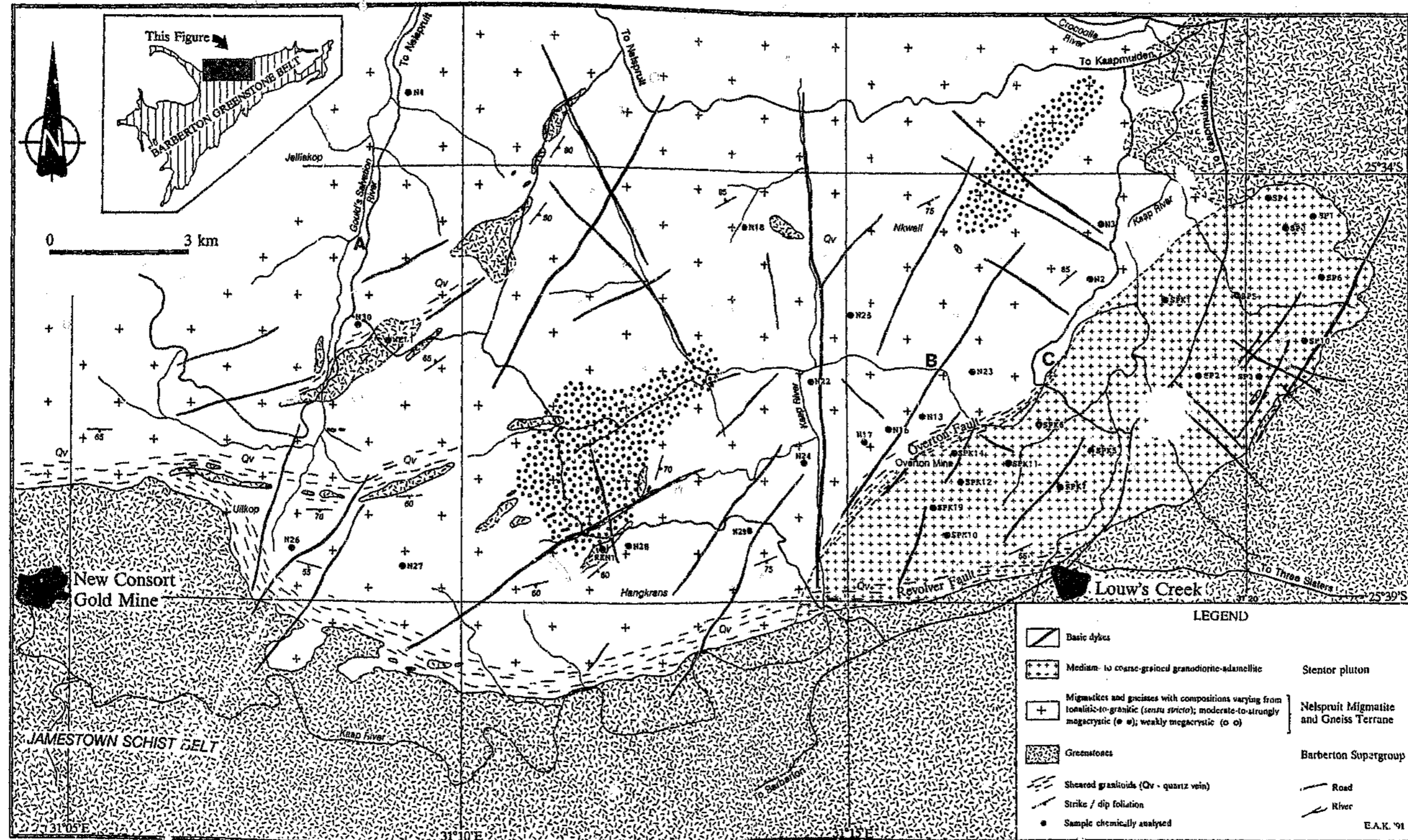


Figure 8.2 Geological map of the granitoid terrane north of the BGB. The letters A - C refer to localities mentioned in the text.

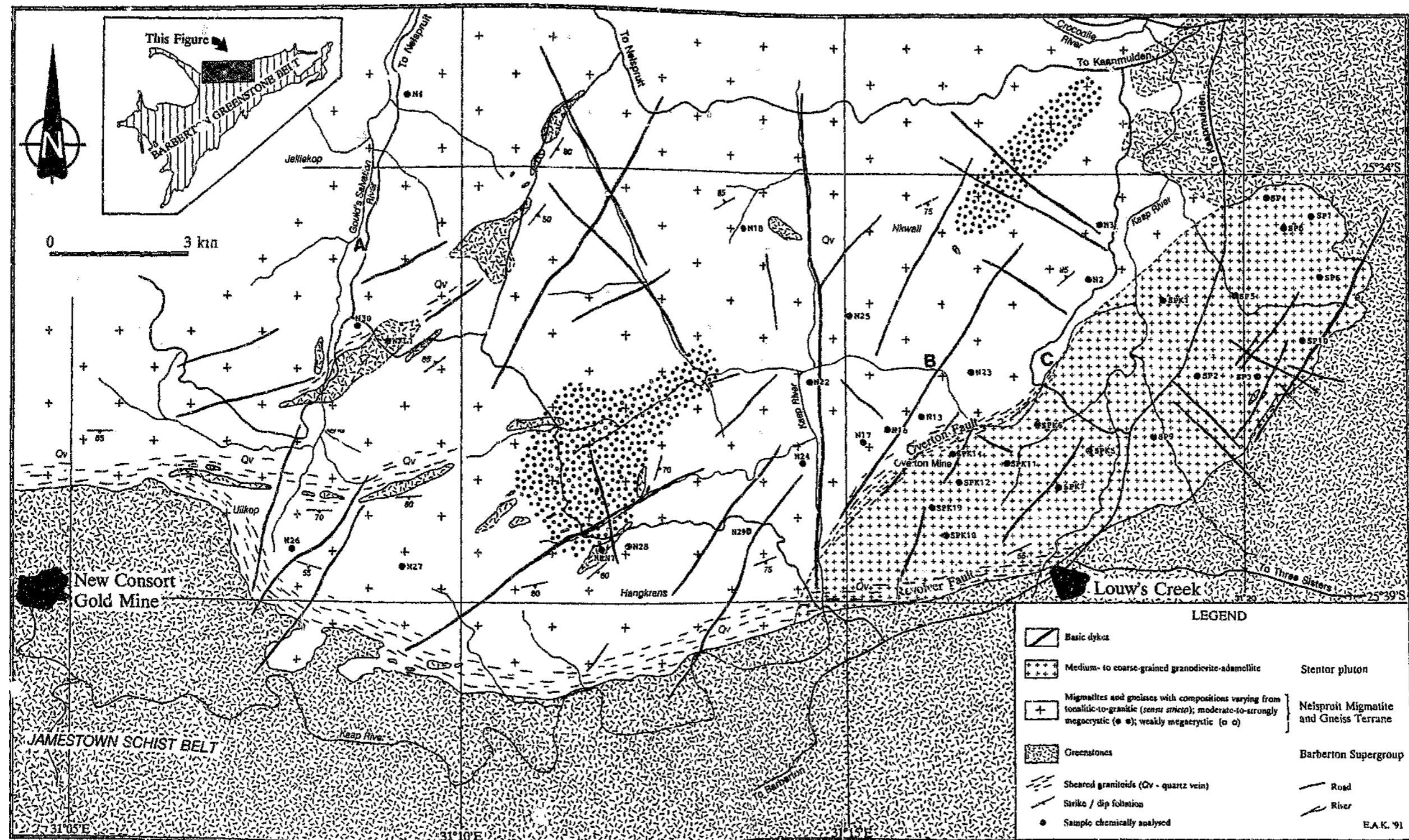


Figure 8.2 Geological map of the granitoid terrane north of the BGB. The letters A - C refer to localities mentioned in the text.

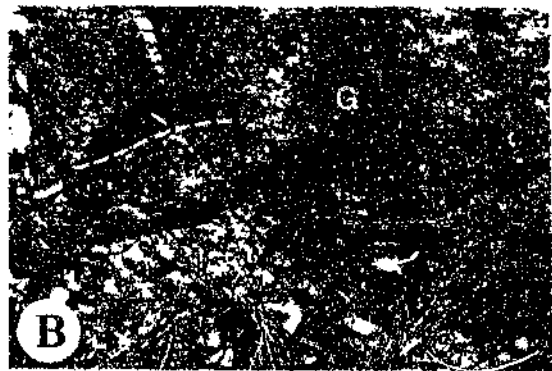
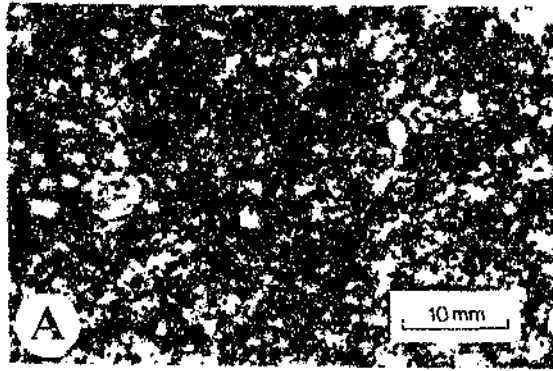


Figure 8.3 Mesoscopic features observed in rocks of the Stentor pluton:

(A) Polished slab showing the typical texture of granodioritic-to-adamellitic rocks from the Stentor pluton.

(B) Sharp intrusive contact between granodiorite (G) of the Stentor pluton and quartz-muscovite schist (S) of the Bien Venue Formation (Driehoek 221 JU). Note how the contact locally transgresses the schistosity (dashed line) in the country rocks on outcrop scale. Lens cap is 4.9 cm in diameter.

(C) Foliated (S_d ; dashed lines) granodiorite (G1) cross-cut by dyke of massive granodiorite (G2) (Esperado 253 JU).

(D) Aligned biotite inclusions and schlieren in strongly foliated (S_d) granodiorite (Esperado 253 JU). Hammer is 30 cm long.

(E) Fine-grained enclaves composed of biotite, quartz and feldspar enclosed by homogeneous, unfoliated granodiorite and cross-cut by pegmatite dyke (Naudes Rust 272 JU).

and assimilated quartz-muscovite schist, locally occur along the schist - granitoid interface. The apophyses have generally intruded subparallel to the schistosity in the country rocks.

Granitoid rocks in the southeastern quadrant of the pluton, as well as in some of the above-mentioned apophyses, also display a pervasive foliation (S_d - Section 9.2.2.1), defined mainly by the preferred dimensional alignment of lenticular biotite and / or muscovite aggregates. Field and petrographic evidence (see later) suggest that unlike the mylonitic S_m foliations along the pluton's northern and southern margins, which are clearly of post-emplacement origin, the S_d fabric formed contemporaneously with the diapiric intrusion of the pluton (Section 9.3.2). In some exposures, the S_d foliated rocks are seen to be cross-cut by thin dykes of massive, medium-grained granodiorite, providing further evidence of the syn-emplacement origin of S_d (Figure 8.3C).

S_d foliation planes in granitoids along the southeastern margin of the pluton strike parallel to the granitoid - schist contact, as well as the S_d schistosity in the country rocks (Section 9.2.2.1; Figure 8.4). They dip at 40 - 70° away from the pluton. A weak down-dip lineation, defined by the alignment of recrystallized quartz or biotite aggregates, is evident on some S_d surfaces.

The S_d fabric is heterogeneously developed in the central portions of the pluton. Dips in this area vary from steep (i.e. 60 - 75°) to subhorizontal, often over a distance of a few tens to few hundreds of meters; the subhorizontal foliations are not well represented in Figure 8.4 because of difficulties in reliably measuring their orientations on the flat outcrop surfaces. Granitoids in the northeastern quadrant of the pluton are typically devoid of S_d fabrics.

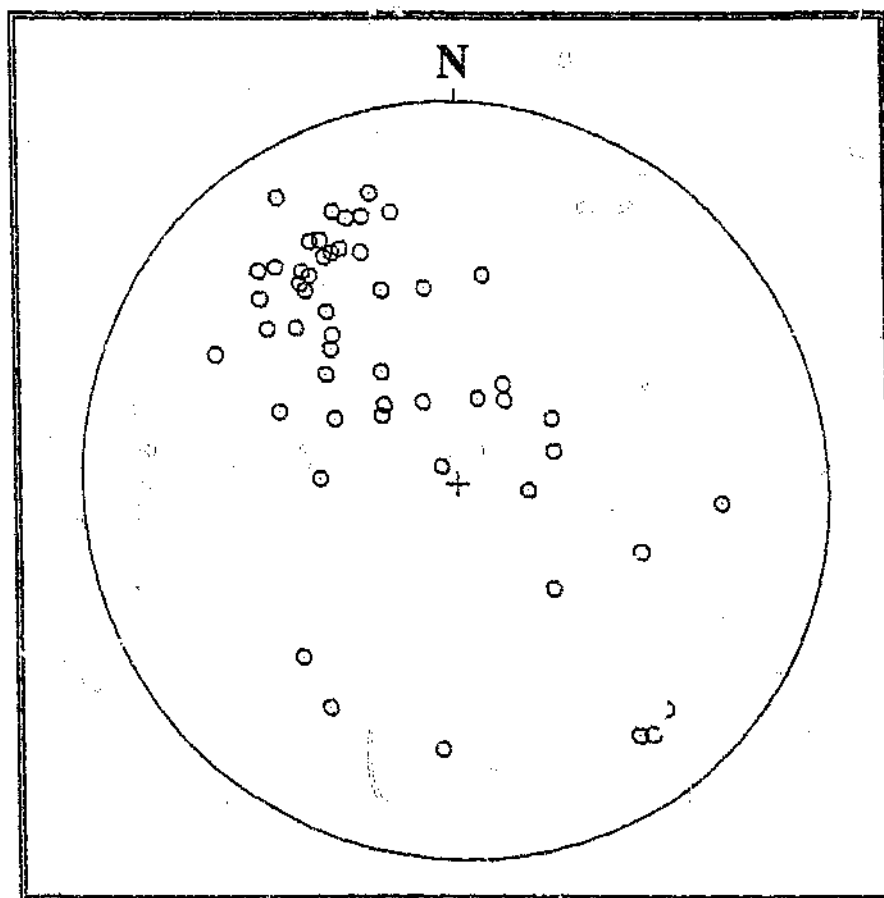


Figure 8.4 Lower hemisphere equal area projection of poles to S_4 foliation in the Stentor pluton ($n = 52$).

The dip of the granitoid - schist contact cannot readily be measured in most areas due to a lack of suitable outcrops. Exposures in river gullies along the southern boundary of Driehoek 221 JU indicate, however, that the contact dips away from the pluton at $\sim 45^\circ$, and that it parallels the S_4 fabric in the quartz-muscovite schists. Hence, it appears that the present level of exposure lies fairly close to the roof of the dike, and that schists in the western part of Stentor Antiform are underlain by granitoids of the Stentor pluton.

Dykes and irregularly shaped bodies of pegmatite, varying in thickness from a few centimetres to over 3 m, occur throughout the pluton. The dykes are undeformed, generally dip subvertically, and consist of microcline, plagioclase and quartz, together with lesser amounts of muscovite and Fe-oxides. Rarely, the pegmatites also contain traces of garnet and tourmaline. Contacts with the host granitoids vary from sharp to gradational. Some of the thicker pegmatite bodies exhibit a crude textural zonation manifested as a coarsening of the crystals towards the centre, and locally quartz and feldspar crystals up to ~10 cm in the maximum dimension were noted in the core zones. Outcrops containing abundant pegmatitic material often show a crude preferential alignment of the dykes; no preferred orientation or systematic variation could, however, be established regionally.

Thin dykelets of massive, white-to-pinkish, sugary-textured aplite, seldom wider than ~10 cm and showing variable dip and strike orientations, were recorded at a few localities. These consist dominantly of quartz, feldspar and mica, with muscovite predominating over biotite. Contacts between the dykes and the surrounding host rocks are invariably knife sharp. The aplites are locally seen to cross-cut the S_1 foliation in the granitoids, indicating that they post-date this fabric.

Steeply inclined extension fractures, filled with hydrothermal quartz or, more rarely, epidote, occur sporadically. The quartz veins vary in width from a few millimetres to ~20 cm and extend up to ~5 m along strike, whereas the epidote varieties seldom exceed 2-3 mm in width and 10 cm in length. The former often occur in subparallel sets and cross-cut pegmatite and aplitic dykes, indicating that they post-date the latter. In some outcrops, quartz veins are also seen to cross-cut other quartz veins, suggesting that several generations are present.

A variety of enclaves occur in the pluton. Most common are medium-grained, dark-grey to black inclusions composed of biotite or hornblende amphibolite. These seldom exceed a few tens of centimetres in length and show a variety of shapes ranging

from irregular to crudely ovoid. Inclusions in the unfoliated granitoids show no preferential orientation and tend to be more angular than inclusions in the foliated granitoids, which are often flattened and aligned with their long axes subparallel to the foliation. Lens-like aggregates of biotite also locally form schlieren in the foliated granitoids (Figure 8.3D). In terms of mineralogy, the amphibolite enclaves are comparable with medium-grade basic metavolcanics within the Onverwacht Group (Section 3.3), suggesting that they represent xenoliths.

Much larger elongate xenoliths composed of variably silicified quartz-muscovite \pm biotite schist occur along the eastern margin of the pluton, and appear to have been prised off the adjacent silicic metavolcanic assemblage. The largest of these xenoliths, traceable over a strike distance of ~300 m, crops out in the northern corner of Three Sisters 254 JU (Figure 1.4, F4). Centimetre- to decimetre-scale muscovite schlieren also locally occur in this area.

Small (generally < 1 m long), dark-grey, variably foliated, subangular- to irregularly shaped enclaves composed of quartz, biotite and feldspar were noted in some outcrops, but are not common (Figure 8.3E). The origin and significance of these inclusions could not be ascertained.

8.3.2 Petrography

The Stentor pluton consists of plagioclase, microcline, quartz and biotite, with accessory magnetite, chlorite, muscovite, epidote, allanite, sphene, apatite, zircon and rutile. A Streckeisen diagram showing the mineralogical compositions of samples from the pluton is presented in Figure 8.5.

Plagioclase is dominantly oligoclase and occurs as weakly zoned, euhedral-to-subhedral grains averaging 1 - 3 mm across. The crystals are often partially sericitized and saussuritized, and in some instances the core zones have been preferentially altered.

Most samples studied also contain minor amounts of myrmekite, most of which occurs as irregular-shaped grains at plagioclase - microcline interfaces.

Microcline typically forms anhedral grains ranging in size from ~0.5 - 1.5 mm, but also occurs as subhedral crystals up to ~3 mm long. The feldspar is usually perthitic and is seen to enclose small inclusions of quartz, plagioclase, biotite, apatite and sphene.

Quartz forms anhedral isolated grains or sutured aggregates between the feldspars. Inclusions commonly found in quartz include plagioclase, microcline, biotite and muscovite.

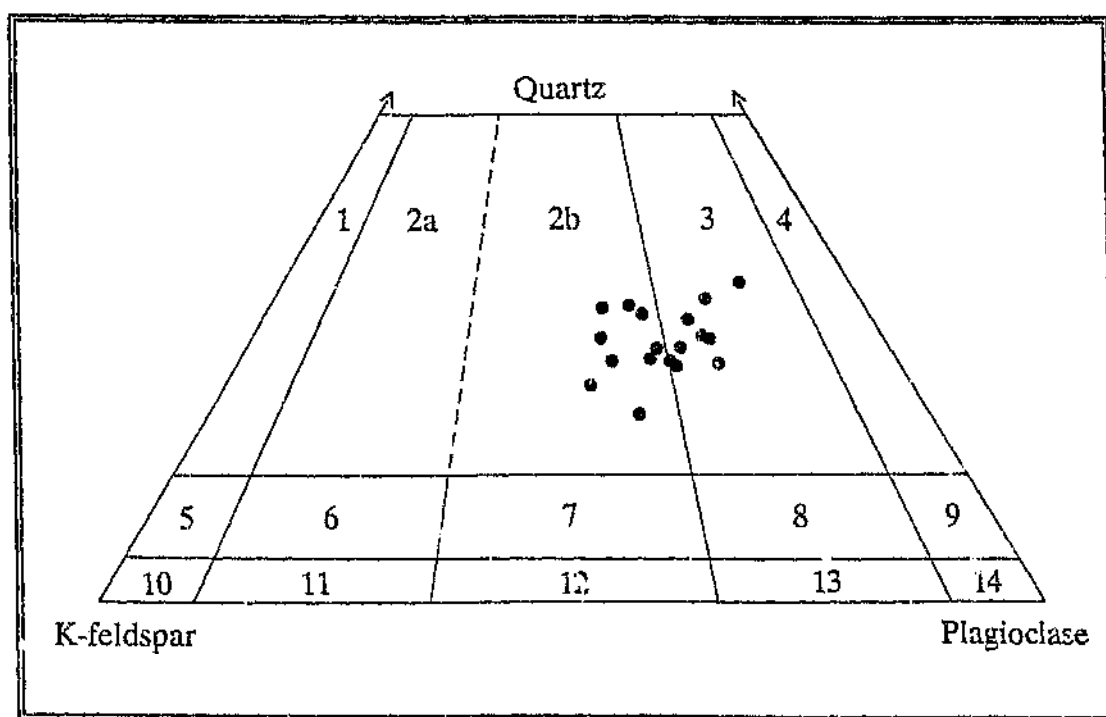


Figure 8.5 K-feldspar - quartz - plagioclase classification plot for samples from the Stentor pluton (diagram after Streckeisen, 1976). Fields: 1 - alkali-granite; 2a - syenogranite; 2b - monzogranite; 3 - monzotonalite / granodiorite; 4 - tonalite; 5 - quartz alkali-granite; 6 - quartz syenite; 7 - quartz monzonite (adamellite); 8 - quartz monzodiorite; 9 - quartz diorite / quartz gabbro; 10 - alkali syenite; 11 - syenite; 12 - monzonite; 13 - monzodiorite / monzogabbro; 14 - diorite / gabbro.

Biotite exhibits pleochroism from olive green to yellowish brown and occurs as discrete ragged flakes that are homogeneously distributed throughout the rock.

The S_4 foliated granitoids show evidence of having been deformed in the solid state: quartz exhibits pronounced undulose extinction and subgrain formation; plagioclase and microcline have sericitized fractures, weak undulose extinction and, in some cases, marginal recrystallization; and biotite and muscovite are often bent and kinked. Albite exsolution lamellae were recorded in some recrystallized microcline grains, indicating that at least part of the deformation took place at high temperatures near the granite solidus (see Paterson *et al.*, 1989).

Sheared granodiorites along the Revolver Fault are distinguished by a protomylonitic texture. Commonly occurring quartz ribbon structures exhibit a preferred orientation and, together with aligned laths and bundles of secondary muscovite and biotite, define the mylonitic foliation. Rocks at the Overton Mine are characterised by augen mylonitic and ultramylonitic textures. The augen mylonites contain angular and lenticular feldspar porphyroclasts set in a strongly foliated, quartz- and mica-rich microcrystalline matrix.

Magnetite forms minute granules which are often intimately associated with biotite. Weakly pleochroic, pale-green chlorite is locally found as an alteration product of biotite along the latter's grain boundaries and cleavage traces. Muscovite occurs as small anhedral flakes which are often intergrown with biotite. Epidote typically forms granular aggregates which are closely associated with altered plagioclase crystals. Some epidote is also found as subhedral or euhedral, occasionally zoned grains up to ~0.5 mm

across which appear to have a primary magmatic origin (see also Naney and Swanson, 1980; Zen and Hammarstrom, 1984). Allanite occurs as reddish-brown, partly metamict, subhedral crystals, some of which are rimmed by thin overgrowths of magmatic epidote. Sphene is sparsely present in most thin sections examined and occurs in two textural varieties: the bulk is present as greyish-brown, diamond-shaped euhedra which are clearly of magmatic origin; the remainder occurs in fine-grained granular clusters which probably formed during post-magmatic alteration. Apatite forms subhedral tabular or prismatic crystals. Zircon occurs as stubby pink euhedra exhibiting prominent growth zoning, and is most readily identifiable in thin section as minute inclusions in biotite. Rutile was recorded in specimens that have suffered substantial alteration.

8.3.3 Chemistry

Eighteen samples from the Stentor pluton have been analysed for major and trace element content by XRF. A list of the samples, their respective compositions and CIPW norms is given in Table 8.1. Five samples have also been analysed by INAA (Table 8.2).

Poor exposure and severe weathering in some areas precluded sampling on a grid basis. The sample localities are, however, widely dispersed over the plutons entire outcrop area so as to achieve as fair a representation as possible. Considerable care was taken to ensure that none of the outcrops sampled had been subjected to extraneous influences such as the nearby presence of basic dykes, quartz veining, or unusually intense pegmatite development. No samples of the mylonites, pegmatites or aplites were analysed chemically. Samples collected along the immediate contact with the quartz-muscovite schists of the Bien Venue Formation have also been omitted from the chemical study in order to obviate any contamination-related chemical effects.

Table 8.1 Major and trace element data obtained from XRF analysis of samples from the Stentor pluton. Fe_2O_3/FeO ratios were fixed at 0.45 in CIPW normative calculations, following Middlemost (1989)

Sample	SP1	SP2	SP3	SP4	SP5	SP6	SP8	SP9	SP10
SiO ₂ (wt %)	71.15	72.59	71.64	71.96	74.05	74.35	71.60	74.10	74.79
TiO ₂	0.48	0.30	0.31	0.28	0.17	0.39	0.31	0.18	0.16
Al ₂ O ₃	14.73	14.06	14.00	14.11	13.34	14.38	14.11	13.61	13.32
Fe ₂ O ₃ ^{total}	2.69	2.46	2.93	2.83	1.81	2.87	2.76	2.20	1.81
MnO	0.04	0.03	0.03	0.05	0.03	0.08	0.05	0.04	0.03
MgO	0.28	0.46	0.21	0.20	bdl	0.32	0.23	0.01	bdl
CaO	1.01	1.46	1.57	1.45	1.18	1.72	1.52	0.97	0.73
Na ₂ O	4.56	3.58	4.16	4.28	4.12	4.23	4.35	4.00	3.80
K ₂ O	3.20	4.69	3.41	4.41	3.41	2.51	3.48	4.07	4.03
P ₂ O ₅	0.17	0.09	0.10	0.14	0.06	0.17	0.16	0.06	0.05
H ₂ O	0.03	0.04	0.05	0.04	0.03	0.01	0.01	0.02	0.01
H ₂ O ⁺	0.27	0.19	0.31	0.28	0.22	0.07	0.14	0.24	0.19
CO ₂	0.20	0.27	0.40	0.03	0.18	0.29	0.05	0.29	0.24
Total	98.81	100.22	99.12	100.06	98.60	101.39	98.77	99.79	99.16
Ba (ppm)	1509	1374	1723	1317	757	1026	1071	1196	765
Rb	126	104	74	116	113	97	116	126	147
Sr	751	393	571	513	386	486	564	282	210
Pb	19	18	20	24	27	22	24	27	21
Y	20	10	14	32	13	25	27	26	22
Nb	11	9	5	16	9	13	15	18	17
Zr	344	277	338	239	125	269	218	195	138
Ga	25	19	24	25	24	26	26	25	25
Zn	74	61	65	77	47	68	66	56	39
Cu	31	bdl	15	19	16	18	23	17	21
Ni	14	5	14	14	13	15	15	14	13
CIPW norm									
Q (wt %)	30.04	30.18	31.09	26.27	34.53	36.30	29.03	33.33	35.85
C	2.80	1.28	1.78	0.07	1.29	2.66	0.92	1.68	2.06
Z	0.07	0.06	0.07	0.05	0.03	0.05	0.04	0.04	0.03
Or	18.91	27.72	20.15	26.07	20.15	14.84	20.57	24.06	23.82
Ab	38.58	30.29	35.20	36.21	34.86	35.79	36.80	33.84	32.15
An	2.64	4.95	4.61	6.09	4.32	5.59	6.18	2.59	1.78
Hy	2.36	2.88	2.66	2.63	1.37	2.84	2.59	1.75	1.39
Mt	1.21	1.11	1.32	1.27	0.81	1.29	1.24	0.99	0.81
Il	0.91	0.57	0.59	0.53	0.32	0.74	0.59	0.34	0.30
Ap	0.40	0.21	0.24	0.33	0.14	0.40	0.38	0.14	0.12
Cc	0.45	0.61	0.91	0.07	0.41	0.66	0.11	0.65	0.55
D.I.	88	88	86	89	90	87	86	91	92

bdl - below detection level; Q - quartz; C - corundum; Z - zircon; Or - orthoclase; Ab - albite; An - anorthite; Hy - hypersthene; Mt - magnetite; Il - ilmenite; Ap - apatite; Cc - calcite; D.I. - Differentiation Index (Thompson and Tuttle, 1960)

Table 8.1 (continued)

Sample	SPK1	SPK5	SPK6	SPK7	SPK10	SPK11	SPK12	SPK14	SPK19
SiO ₂ (wt %)	72.61	71.20	70.66	75.15	75.41	78	70.20	70.07	70.07
TiO ₂	0.27	0.29	0.37	0.11	0.14	0.14	0.50	0.45	0.38
Al ₂ O ₃	14.23	14.98	14.76	14.30	13.88	15.11	14.77	14.25	15.19
Fe ₂ O ₃ total	1.89	2.67	3.37	1.05	1.63	1.27	2.72	3.03	2.85
MnO	0.02	0.04	0.05	0.03	0.04	0.03	0.03	0.07	0.05
MgO	0.16	0.32	0.40	0.02	0.02	0.19	0.37	0.29	0.38
CaO	0.76	1.49	1.92	0.95	0.89	1.03	1.46	1.38	1.25
Na ₂ O	3.79	4.32	3.77	3.60	3.95	4.58	3.71	3.37	4.26
K ₂ O	4.32	29	3.13	4.05	3.61	4.70	4.29	5.43	4.09
P ₂ O ₅	0.08	0.07	0.16	0.03	0.04	0.06	0.15	0.20	0.19
H ₂ O ⁻	0.04	0.02	0.01	0.01	0.02	0.10	0.03	0.01	0.02
H ₂ O ⁺	0.30	0.26	0.24	0.17	0.17	0.32	0.27	0.21	0.26
CO ₂	0.14	0.20	0.25	0.09	0.16	0.13	0.37	0.14	0.19
Total	98.61	99.15	99.09	99.56	99.96	99.54	98.81	98.90	99.18
Ba (ppm)	844	718	1461	307	332	366	1388	1301	1190
Rb	144	107	92	154	134	117	102	134	129
Sr	298	374	601	159	245	307	695	628	620
Pb	23	18	21	20	20	17	16	24	27
Y	25	31	28	14	22	10	21	50	20
Nb	12	17	15	10	13	5	10	25	13
Zr	221	185	337	65	133	87	396	305	294
Ga	25	25	26	22	23	22	25	34	25
Zn	45	60	62	39	53	42	61	73	42
Cu	15	19	18	16	29	22	20	35	45
Ni	15	13	14	12	12	13	15	15	15
CIPW norm									
O (wt %)	32.18	29.65	32.03	36.60	36.64	24.85	29.18	26.28	26.52
C	2.45	2.24	2.64	2.55	2.32	1.06	2.59	1.12	2.38
Z	0.04	0.04	0.07	0.01	0.03	0.02	0.08	0.06	0.06
Or	25.53	19.45	18.50	23.94	21.34	27.78	25.36	32.09	24.17
Ab	32.07	36.55	31.90	30.46	33.42	38.75	31.39	28.51	36.04
An	2.36	5.67	6.90	3.95	3.14	3.90	3.92	4.65	3.76
Hy	1.66	2.75	3.46	0.85	1.33	1.42	2.56	2.79	2.93
Mt	0.85	1.20	1.51	0.47	0.73	0.57	1.22	1.36	1.28
Il	0.51	0.55	0.70	0.21	0.27	0.27	0.95	0.85	0.72
Ap	0.19	0.17	0.38	0.07	0.09	0.16	0.36	0.47	0.45
Cc	0.32	0.45	0.57	0.20	0.36	0.30	0.84	0.32	0.43
D.I.	90	86	82	91	91	91	86	87	87

C - quartz; C - corundum; Z - zircon; Or - orthoclase; Ab - albite; An - anorthite; Hy - hypersthene; Mt - magnetite; Il - ilmenite; Ap - apatite; Cc - calcite; D.I. - Differentiation Index (Thornson and Tuttle, 1960)

Table 8.2 Trace element data obtained from INAA of selected samples from the Stentor pluton

Sample	SP1	SP6	SPK6	SPK7	SPK19
Cs (ppm)	6.21	2.84	3.47	5.57	3.22
U	1.42	1.97	2.93	2.81	2.27
Th	9.06	12.1	14.9	13.0	16.1
Hf	7.71	7.51	8.19	3.62	7.48
Ta	0.72	1.00	1.05	1.22	1.01
Sc	2.34	3.53	3.26	1.71	2.74
Co	5.93	5.28	29.6	23.6	4.50
As	0.54	0.71	0.14	0.28	0.28
La	105	81.7	94.6	28.8	91.3
Ce	205	171	211	58.7	200
Nd	68.3	61.1	79.6	19.5	69.8
Sm	11.1	9.86	14.6	3.59	12.9
Eu	2.64	2.19	2.75	0.79	2.72
Tb	0.86	0.87	1.20	0.49	1.01
Yb	1.05	1.87	2.20	1.37	1.68
Lu	0.19	0.20	0.33	0.27	0.18
Au (ppb)	9.8	8.0	7.2	6.5	6.6

8.3.3.1 Major elements

The major element analyses indicate that the Stentor pluton is mildly peraluminous with an average molar $Al_2O_3/(Na_2O + K_2O + CaO)$ value of 1.1 (Figure 8.6). The CIPW norms typically contain between 1.0 - 2.5 wt % corundum (Table 8.1); Na_2O contents range from 3.4 - 4.6 wt %, while K_2O concentrations vary in the range 2.5 - 5.4 wt %. On the K_2O versus Na_2O classification diagram of Harpum (1963), the samples plot mainly in the fields of granodiorites and adamellites (Figure 8.7). SiO_2 contents are, however, unusually high for granodioritic-to-adamellitic rocks, averaging at ~72 wt %. The calculated average $Fe_2O_3^{total} + MgO$ (2.6 wt %) and CaO (1.3 wt %) contents of the pluton are also low compared to the average compositions of other

granodioritic-to-adamellitic rocks, which have average $\text{Fe}_2\text{O}_3^{\text{total}} + \text{MgO}$ and CaO values of 6.0 wt % and 3.6 wt %, respectively (Le Maitre, 1976). On the normative albite - anorthite - orthoclase classification plot of O'Connor (1965), as well as the multicationic R_1R_2 -diagram of De La Roche *et al.* (1980), the samples fall mainly into the field of granites (*sensu stricto*) (Figures 8.8 and 8.9). High Differentiation Index values (82 - 92) are also comparable with granites (*sensu stricto*) (Table 8.1). When projected onto the anhydrous base of the albite - quartz - orthoclase - H_2O tetrahedron, the samples cluster around minimum compositions for pressures of between 1 - 3 kb (Figure 8.10).

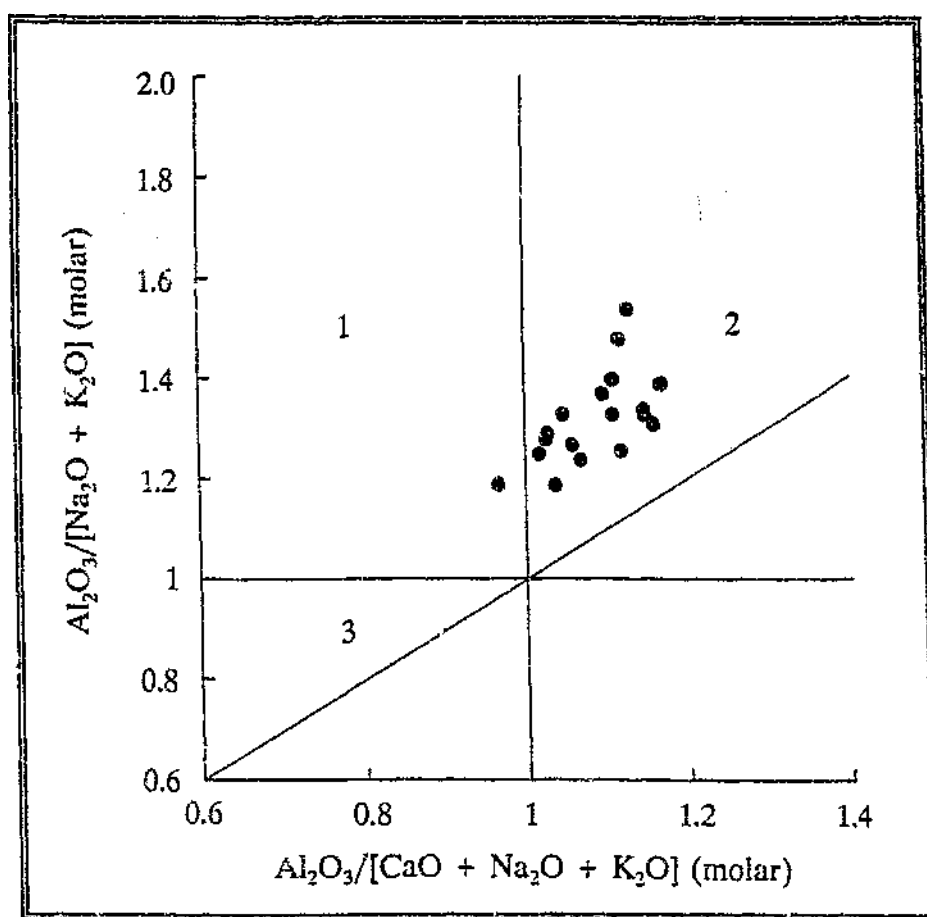


Figure 8.6 Plot of mol fraction $\text{Al}_2\text{O}_3 / (\text{Na}_2\text{O} + \text{K}_2\text{O})$ against $\text{Al}_2\text{O}_3 / (\text{CaO} + \text{Na}_2\text{O} + \text{K}_2\text{O})$ for samples from the Stentor pluton (diagram after Maniar and Piccoli, 1989). All abundances expressed as molecular proportions of the oxides. Fields: 1 - metaluminous; 2 - peraluminous; 3 - peralkaline.

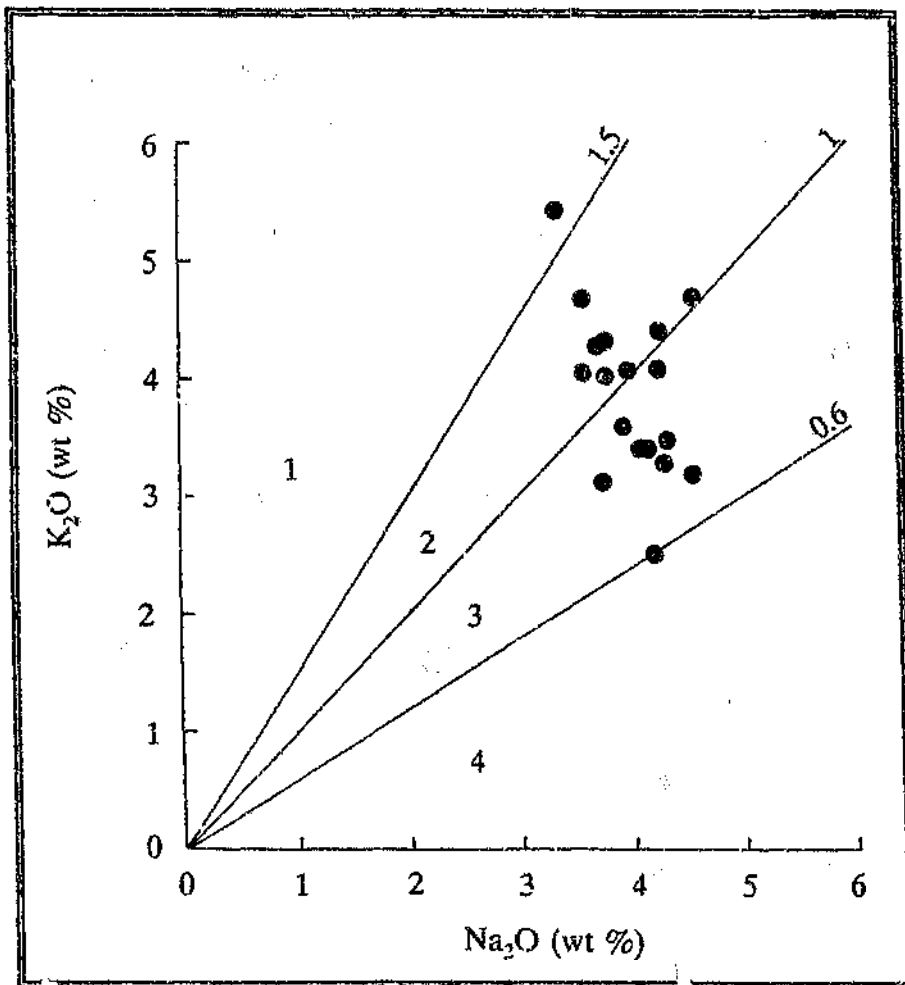


Figure 8.7 K_2O - Na_2O plot for samples from the Stentor pluton (diagram after Harpum, 1963). Fields: 1 - granite; 2 - adamellite; 3 - granodiorite; 4 - tonalite.

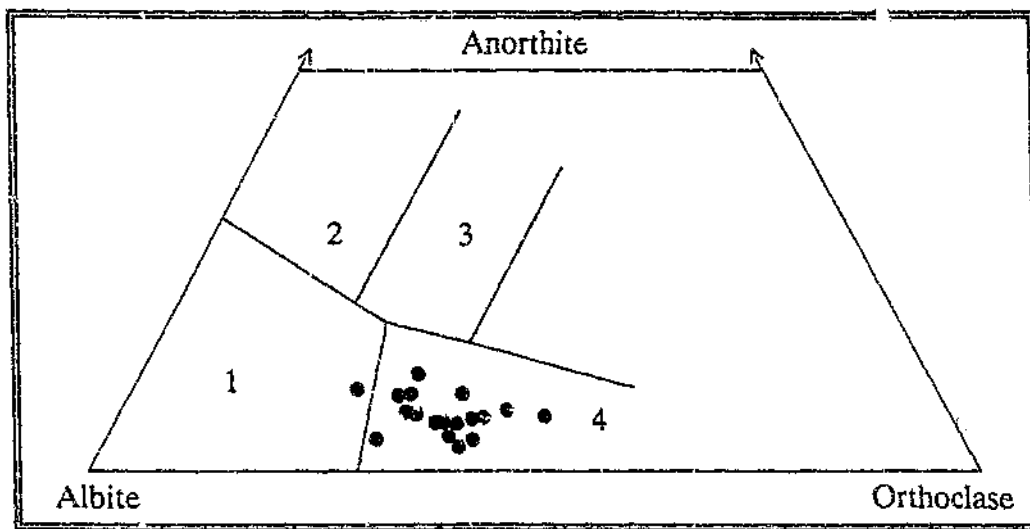


Figure 8.8 CIPW normative albite - anorthite - orthoclase plot for samples from the Stentor pluton (diagram after O'Connor, 1965; modified field boundaries after Barker, 1979). Fields: 1 - trondhjemite; 2 - tonalite; 3 - granodiorite; 4 - granite.

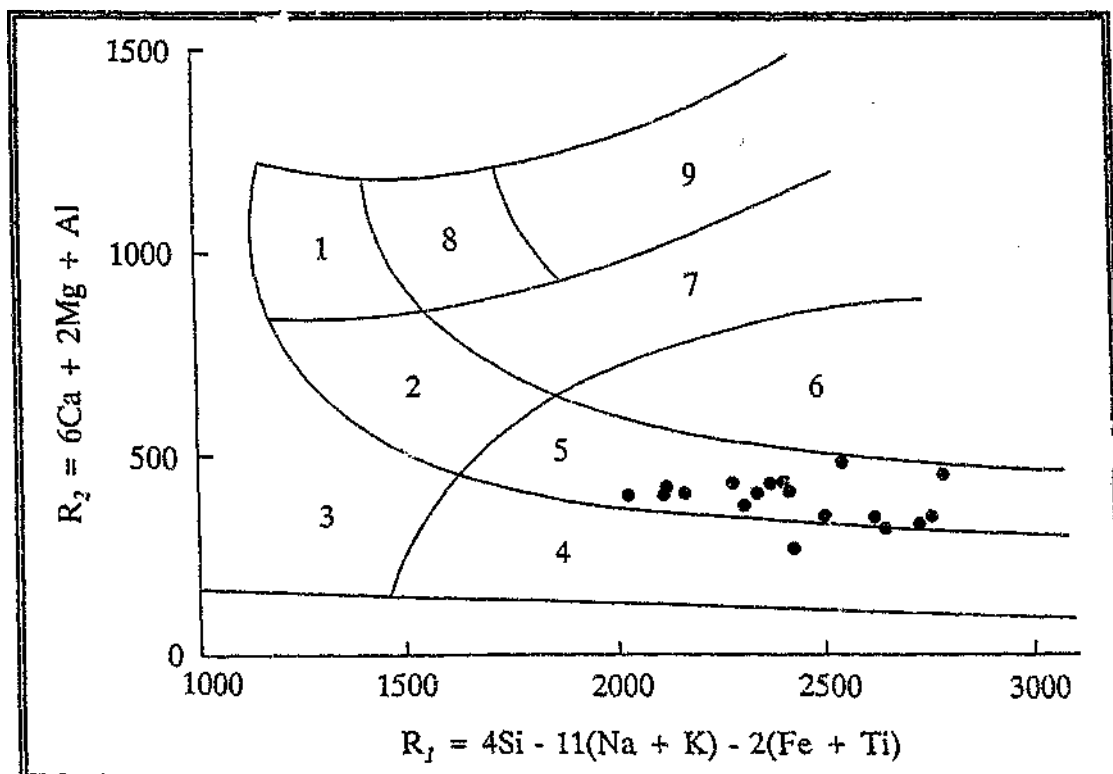


Figure 8.9 Classification of samples from the Stentor pluton based on the R_1R_2 plot of De La Roche et al. (1980). Fields: 1 - monzonite; 2 - quartz monzonite; 3 - quartz syenite; 4 - alkali-granite; 5 - granite; 6 - granodiorite; 7 - tonalite; 8 - monzodiorite; 9 - diorite.

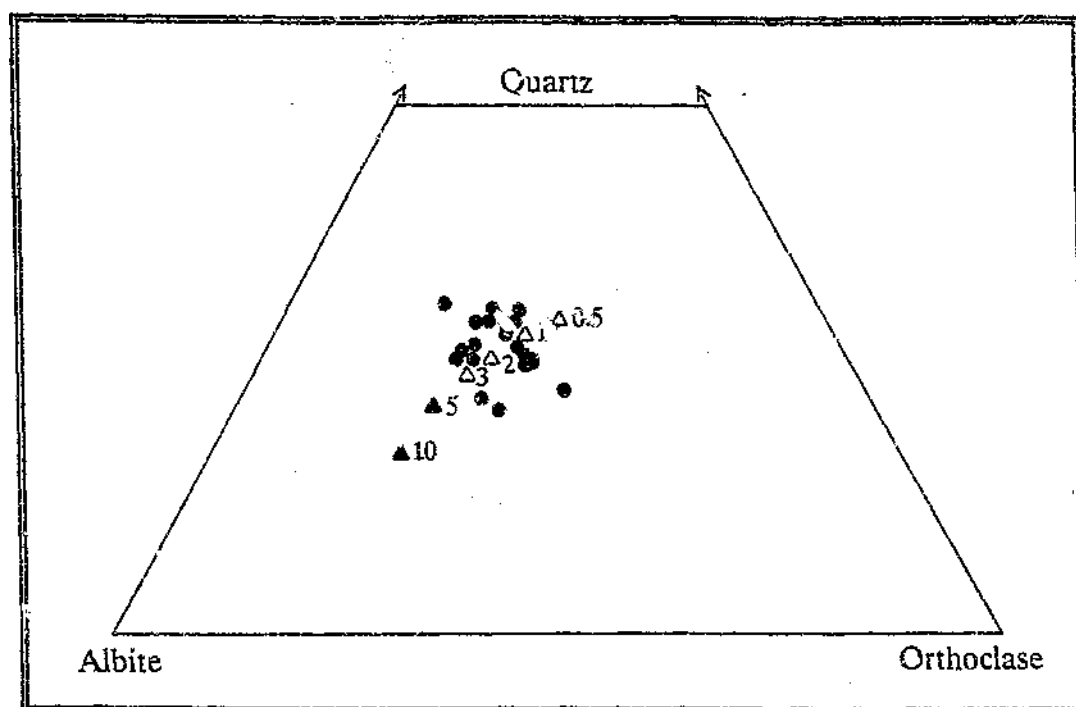


Figure 8.10 CIPW normative compositions of samples from the Stentor pluton (circles) projected onto the anhydrous base of the albite - quartz - orthoclase - H_2O tetrahedron. Also shown are isobaric minima (open triangles) and isobaric eutectic (closed triangles) points for pressures of 0.5 - 10 kb (after Tuttle and Bowen, 1958; Luth et al., 1964).

Selected major element Harker variation diagrams are presented in Figure 8.11. TiO_2 , $Fe_2O_3^{total}$, MgO and P_2O_5 display negative trends with SiO_2 despite the latter's restricted range. The variation diagrams for Al_2O_3 , CaO and K_2O show a fair degree of scatter of the data, suggesting some modification by the late- to post-solidification alteration noted in this section (Section 8.3.2). However, negative correlations, albeit poorly defined, are still discernable in the plots of Al_2O_3 and CaO . Scatter of the data points in the plot of Al_2O_3 against SiO_2 suggests limited mobility of Si rather than Al, since the latter element is generally insensitive to alteration (Section 5.1). This may also account for the scatter in the plot of TiO_2 against SiO_2 . The plots of Na_2O and K_2O show no systematic variation with SiO_2 .

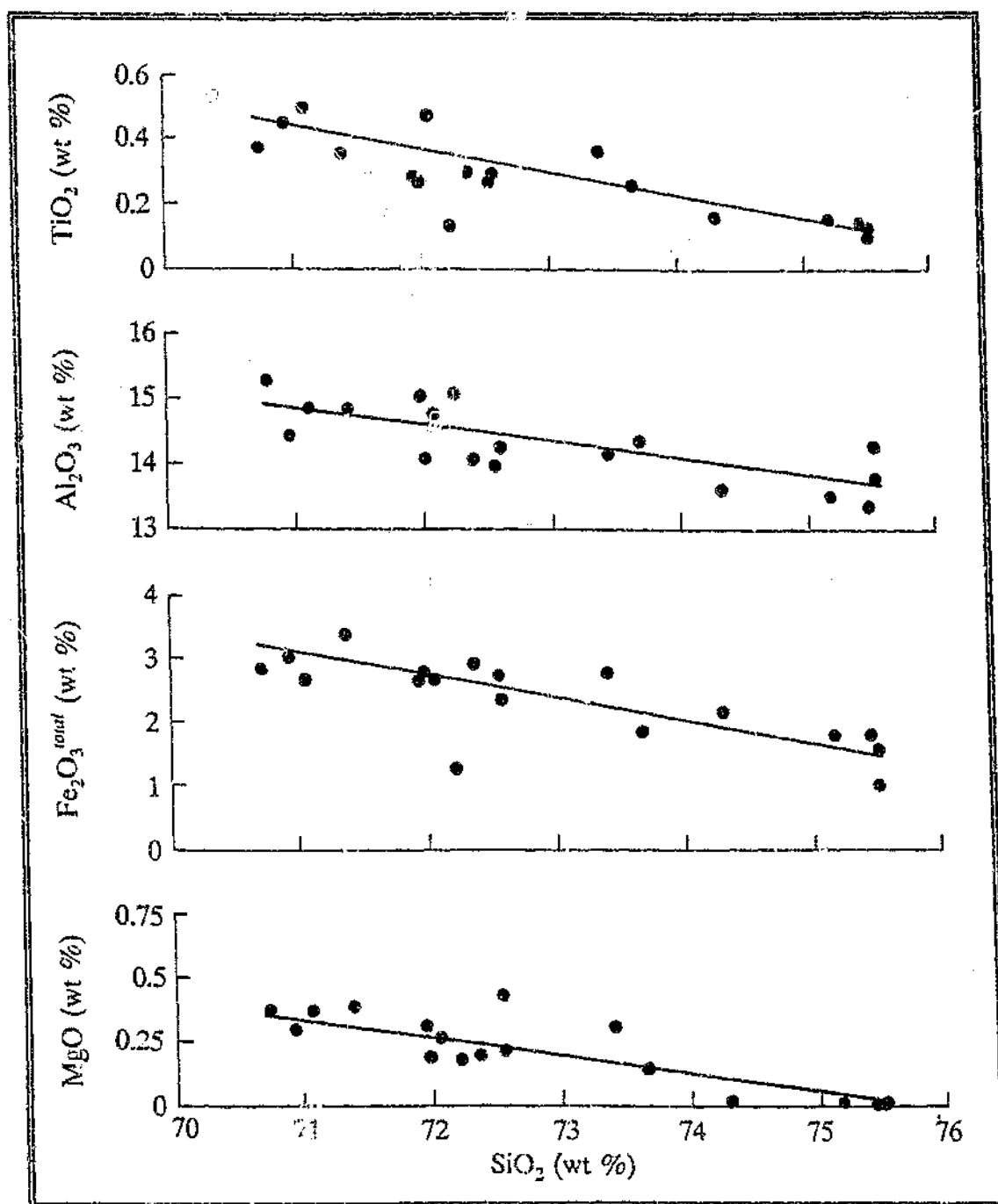


Figure 8.11 Harker variation diagrams for selected major elements in samples from the Stentor pluton. All values have been normalized to 100 wt % totals. Trend lines are visual estimates.

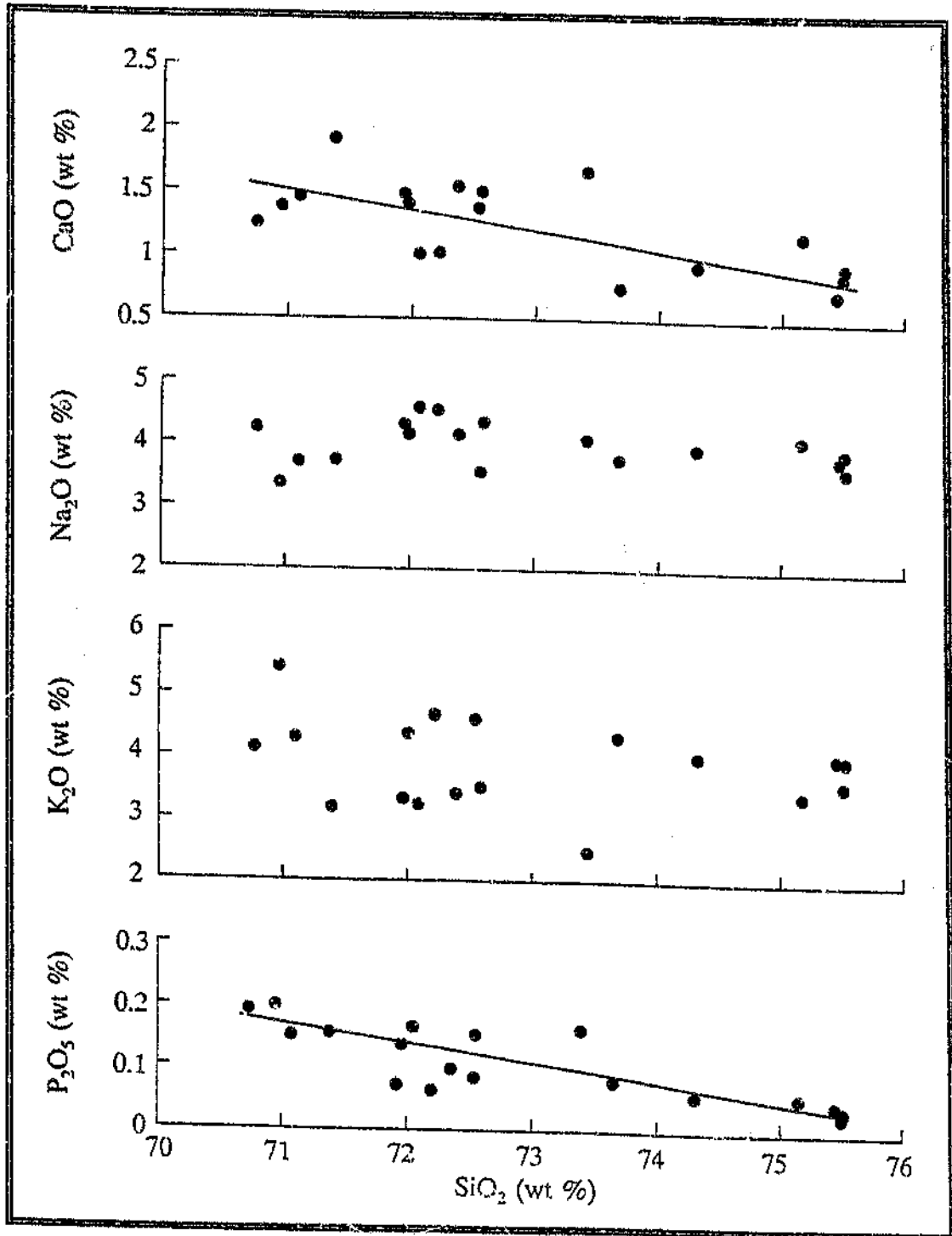


Figure 8.11 (continued).

8.3.3.2 Trace elements

Rb concentrations are moderate and occupy a narrow range from 74 - 154 ppm ($\bar{x} = 118$ ppm). Ba and Sr contents, on the other hand, vary by a factor of 5 from 307 - 1723 ppm ($\bar{x} = 1063$ ppm) and 159 - 751 ppm ($\bar{x} = 449$ ppm), respectively. Sr/Rb (1 - 8; $\bar{x} = 4$) and Ba/Rb (2 - 24; $\bar{x} = 10$) values consequently also display considerable variation. Ba/Sr and K/Rb ratios vary in the range 1 - 4 ($\bar{x} = 2$) and 210 - 380 ($\bar{x} = 280$), respectively. On the ternary Ba - Rb - Sr plot of El Bouseily and El Sokkary (1975), the samples plot within, or close to, the field of granodiorites and quartz diorites (Figure 8.12). Zr concentrations range from 65 - 396 ppm ($\bar{x} = 231$ ppm)

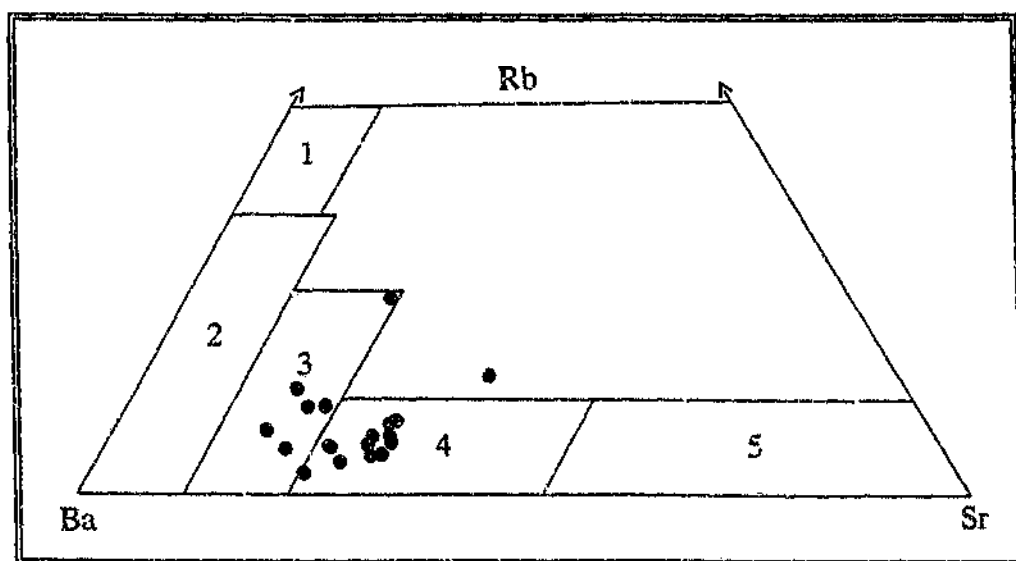


Figure 8.12 Ternary Ba - Rb - Sr plot for samples from the Stentor pluton (diagram after El Bouseily and El Sokkary, 1975). Fields: 1 - strongly differentiated granites; 2 - normal granites; 3 - anomalous granites; 4 - granodiorites and quartz diorites; 5 - diorites.

Harker diagrams for Ba, Rb, Sr and Zr are presented in Figure 8.13. Despite a fair degree of scatter of the data points, Ba, Sr and Zr concentrations decrease as SiO_2 content increases, while Rb concentrations show a slight increase. Deviation of some of the data points away from the general trend in the plot of Zr against SiO_2 may, once again, be attributed to the limited mobility of Si rather than Zr which is insensitive to alteration (Section 5.1).

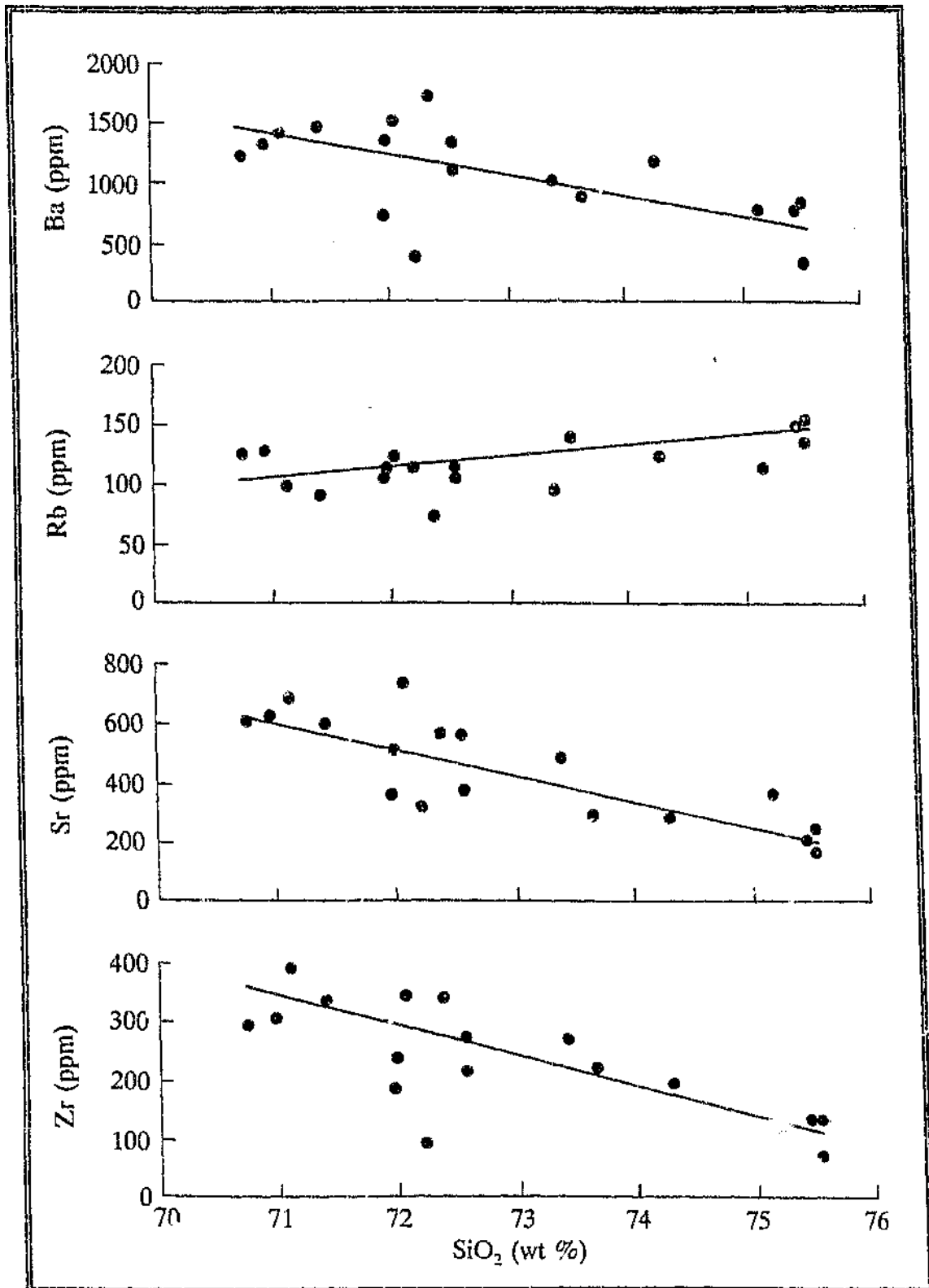


Figure 8.13 Harker variation diagrams for Ba, Rb, Sr and Zr in samples from the Stentor pluton. SiO₂ values have been normalized to 100 wt % totals. Trend lines are visual estimates.

Chondrite-normalized REE profiles for the samples analysed by INAA are shown in Figure 8.14. Samples SP1, SP6, SPK6 and SPK19 are characterized by fractionated patterns with La ~330 - 430 times enriched over chondrite, steep LREE traces ($La_N/Sm_N = 4.1 - 5.9$) and comparatively flatter HREE trends ($Tb_N/Yb_N = 2.1 - 3.6$). Sample SPK7, which is the most differentiated of the samples analysed by INAA having $SiO_2 = 75$ wt % and $Zr = 65$ ppm, is distinguished by much lower abundances of all the REE's except Yb and Lu. This specimen displays a LREE trend ($La_N/Sm_N = 5.1$) which is comparable to that shown by the other 4 samples, but is characterized by a less fractionated HREE trace ($Tb_N/Yb_N = 1.6$). All samples analysed are characterised by negligible or only weakly developed negative Eu anomalies ($Eu/Eu^* = 0.74 - 0.95$).

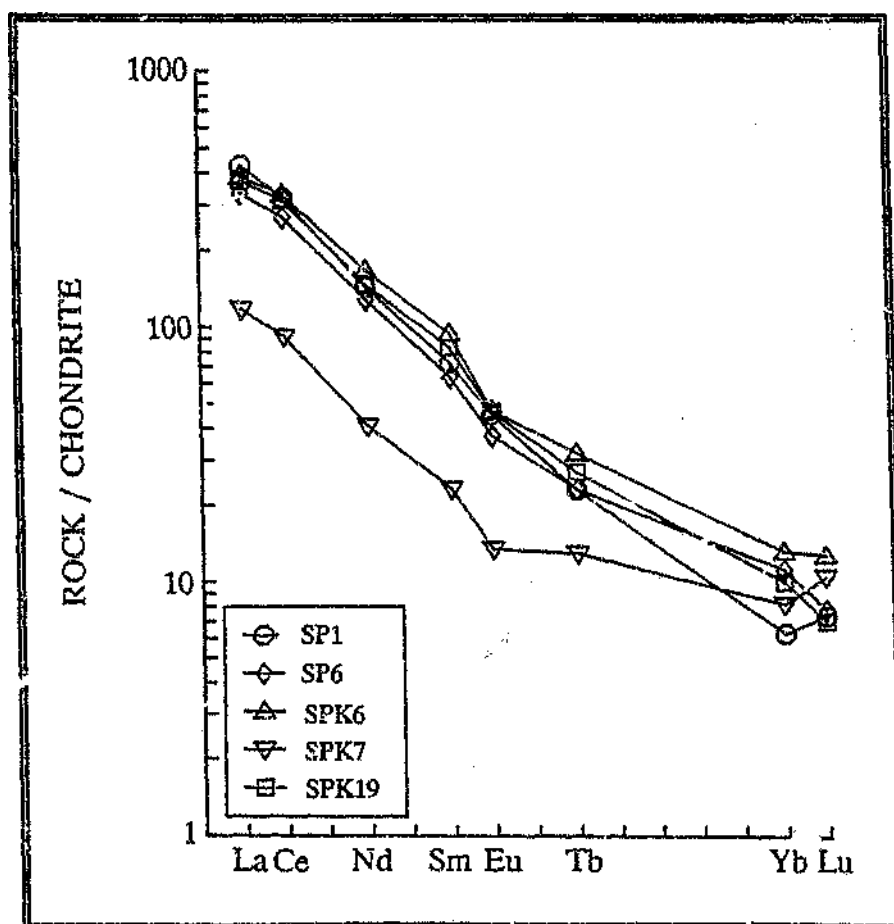


Figure 8.14 Chondrite-normalized distribution of the REE's in samples from the Stentor pluton (sample numbers as in Table 8.2 and Figure 8.2).

8.3.3.3 Modelling

Numerous publications have emphasized the usefulness of trace elements in elucidating the origin and evolution of igneous rocks (e.g. Hanson, 1978; Robb, 1983). Of particular interest in studying granitoids are the elements Ba, Rb and Sr which are controlled by major phases, specifically feldspar and mica (Harris and Inger, 1992). Far less useful are the REE's and HFSE's which reside predominantly in accessory minerals such as sphene, zircon and apatite, whose stability and behaviour during fractionation and anatexis are difficult to evaluate (McCarthy and Kable, 1978; Fourcade and Allégre, 1981; Gromet and Silver, 1983).

Robb (1983) demonstrated that Ba, Rb and Sr distributions can be used to distinguish between granitoids that have been derived via processes of crystal fractionation and liquid fractionation. According to Robb (1983), granitoids which have undergone crystal fractionation are typically characterised by marked variations in the abundances of compatible trace elements - i.e. those elements with bulk partition coefficients (D) of greater than unity - but comparatively small variations in the abundances of incompatible trace elements (i.e. those with D values < 1), whereas the opposite is true for granitoids which have been influenced by low-to-moderate degrees of partial anatexis. Calculated D values for Ba, Rb and Sr in rocks of the Stentor pluton indicate compatible behaviour for Ba and Sr, but incompatible behaviour for Rb (see later); this is also supported by trends of decreasing Ba and Sr, but increasing Rb, with SiO_2 in Figure 8.13. These observations, together with compositional data indicating a wide range of Ba and Sr concentrations, but a comparatively narrow range of Rb contents (Section 8.3.3.2), suggest that the magma which gave rise to the Stentor pluton underwent crystal fractionation. The aim of this section is to model the solidification of the pluton using simple equations describing the behaviour of trace elements during differentiation.

Before embarking on the modelling exercise, it was necessary to confirm that Ba, Rb and Sr abundances and interelement ratios have not been significantly modified during the late- to post-solidification alteration noted in thin section, mainly evidenced by the partial sericitization and saussuritization of feldspar and chloritization of biotite (Section 8.3.2). Mobile behaviour of Ba, Rb and Sr is also suggested by the scatter of data points in the Harker plots shown in Figure 8.13. However, the presence of discernable trends in these graphs suggests that these effects are not great; as discussed previously, even Harker plots of elements with low mobility such as Al, Ti and Zr exhibit some scatter of the data, probably reflecting limited Si mobility.

The suitability of Ba, Rb and Sr for modelling is reinforced further in Figure 8.15 which shows plots of Ba/Rb and Sr/Rb versus Zr. Bulk partition coefficient values for Ba, Rb and Sr (see later) indicate that as fractionation proceeded, Ba and Sr concentrations diminished while Rb concentrations increased, resulting in a progressive decrease in Ba/Rb and Sr/Rb ratios. Hence, binary plots of Ba/Rb and Sr/Rb against any suitable index of igneous differentiation can be used to test if these ratios have been significantly modified by alteration or not. Zr was preferentially employed as the index of differentiation because of its low mobility during low-grade alteration (Section 5.1). Both plots in Figure 8.15 show a marked increase in Ba/Rb and Sr/Rb ratios with increasing Zr concentration (decreasing degree of differentiation). Accordingly, the writer is of the opinion that these ratios approximate primary values.

Two theoretical end member crystallization models have been considered: (1) perfect equilibrium crystallization during which the solids and residual melts continually re-equilibrate throughout the entire solidification process; and (2) perfect fractional crystallization during which no re-equilibration occurs between the solid phases and the liquids remaining after further increments of crystallization. The intermediate case, which involves partial equilibration between the solids and the residual liquids (incremental equilibrium crystallization; McCarthy and Hasty, 1976), has not been evaluated.

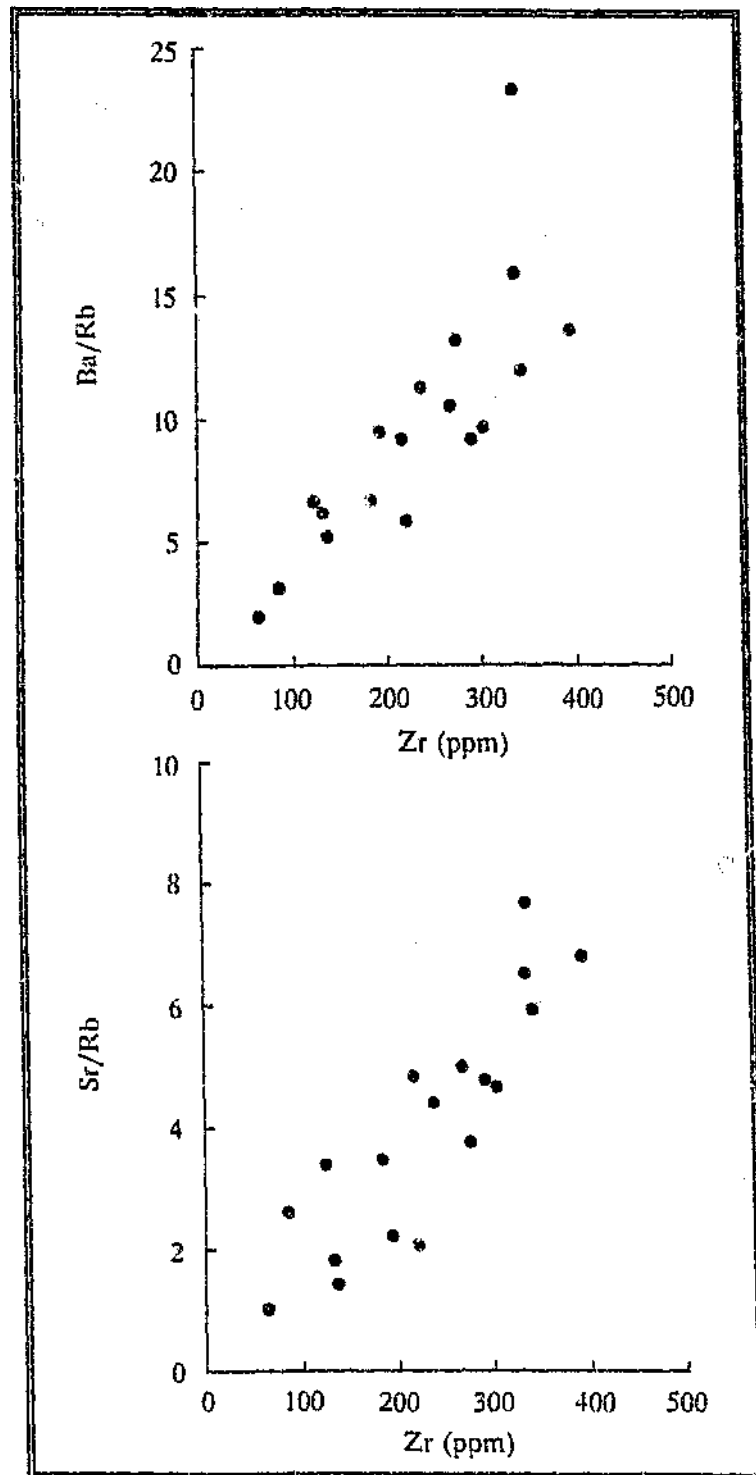


Figure 8.15 Plots of Ba/Rb and Sr/Rb against Zr for samples from the Stentor pluton.

The distribution of any given trace element between solid and liquid phases during crystallization can be calculated using equations derived by Albarede and Bottinga (1972) and Neumann *et al.* (1954):

equilibrium crystallization -

$$C_{Xs} = C_{Xo} D_X / (F + D_X - D_X F) \quad \text{and} \quad C_{Xl} = C_{Xo} / (F + D_X - D_X F)$$

fractional crystallization -

$$C_{Xs} = C_{Xo} D_X F^{(D_X - 1)} \quad \text{and} \quad C_{Xl} = C_{Xo} F^{(D_X - 1)}$$

where F is the mass fraction of liquid remaining; C_{Xo} , C_{Xs} , and C_{Xl} are the concentrations of trace element X in the initial melt, the solid, and the derived liquid; and D_X is the bulk partition coefficient of X for the crystallizing assemblage. D_X values may be calculated as follows:

$$D_X = \sum_{i=1}^n m_i K_{X_i}$$

where n is the number of phases present in the assemblage; m_i is the mass fraction of any given mineral i in the assemblage; and K_{X_i} is the mineral - liquid partition coefficient of X for i . Preferred mineral - liquid partition coefficients used in the calculations are listed in Table 8.3.

Table 8.3 Mineral - liquid partition coefficients used in model calculations

	Quartz	Plagioclase	K-feldspar	Biotite
Ba	0	0.36	6.12	6.36
Rb	0	0.05	0.56	3.26
Sr	0	2.84	3.87	0.12

Data from Hanson (1978)

Results of fractional and equilibrium crystallization modelling based on the approximate modal abundance of the main phases in the Stentor pluton (plagioclase = 40 %, quartz = 30 %, K-feldspar = 25 % and biotite = 5 %) are presented in Table 8.4. The initial magma is assumed to have contained 960 ppm Ba, 170 ppm Rb and 440 ppm Sr. Predicted trace element distributions for the solids and coexisting liquids are compared with data for samples from the Stentor pluton in Figure 8.16, where it is evident that Ba, Rb and Sr distributions in the latter more closely resemble the range of concentrations predicted by the fractional crystallization model than the equilibrium crystallization model. Thus, it appears that the compositional variations are compatible with ~10 - 75 % fractional crystallization of a quartz + plagioclase + K-feldspar + biotite assemblage. Nonetheless, it is also evident that most samples plot between the predicted pure solid and pure liquid compositions. This is consistent with suggestions by McCarthy and Hasty (1976) that complete segregation of the liquid and solid phases in natural systems is unlikely, and that most granitoid rocks actually represent cumulus - intercumulus mixtures. Some of the scatter observed may, however, also reflect: (1) the limited redistribution of Ba, Rb and Sr due to late- to post-solidification alteration; (2) partial re-equilibration between the cumulates and the melt; and/or (3) variations in magnitude of the bulk partition coefficients during solidification in response to subtle changes in pressure, temperature, melt composition and the relative proportions of the main crystallizing phases.

Table 8.4 Results of crystallization modelling for the Stearns pluton

Crystallizing assemblage: 40 % plagioclase, 30 % quartz, 25 % K-feldspar and 5 % biotite						
Bulk partition coefficients: Ba = 1.99, Rb = 0.35 and Sr = 2.11						
Assumed composition of initial melt: Ba = 960 ppm, Rb = 170 ppm and Sr = 440 ppm						
<u>Fractional crystallization model (Neumann <i>et al.</i>, 1954)</u>						
Degree of crystallization		1 %	25 %	50 %	75 %	90 %
Solid composition (ppm):	Ba	1893	1438	961	483	195
	Rb	59	71	93	146	265
	Sr	918	675	430	199	72
Liquid composition (ppm):	Ba	950	722	483	243	98
	Rb	171	205	267	420	765
	Sr	435	320	204	95	34
<u>Equilibrium crystallization model (Albarede and Bottinga, 1972)</u>						
Degree of crystallization		1 %	25 %	50 %	75 %	90 %
Solid composition (ppm):	Ba	1894	1532	1278	1097	1010
	Rb	59	70	88	116	143
	Sr	918	727	597	507	464
Liquid composition (ppm):	Ba	951	769	642	550	507
	Rb	171	203	252	333	412
	Sr	435	344	283	240	220

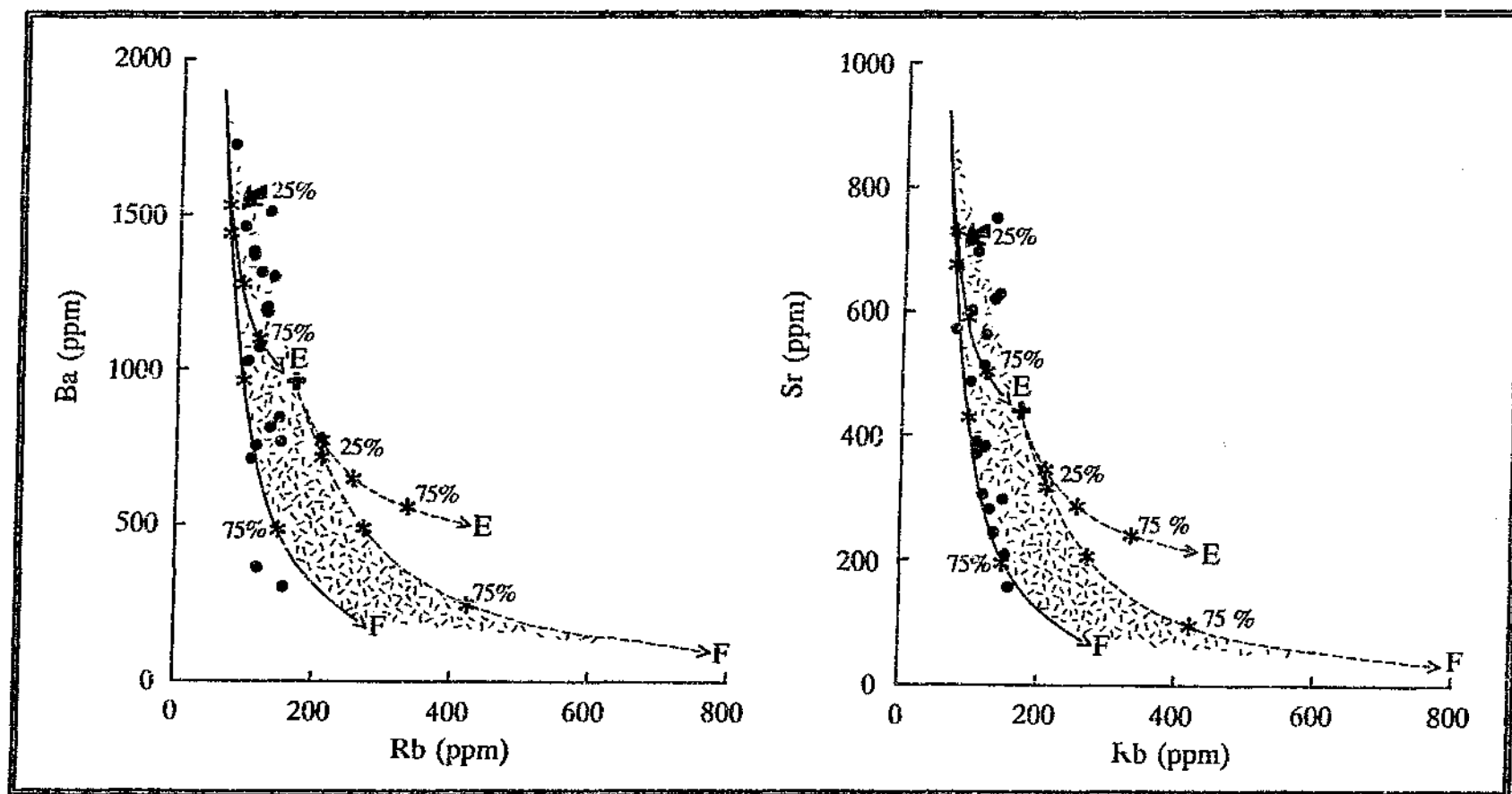


Figure 8.16 Distribution of Ba, Rb and Sr in samples from the Stentor pluton (circles) and comparison with the solid phase (solid lines) and residual liquid (dashed lines) compositions predicted by the fractional and equilibrium crystallization models for 1 - 90 % crystallization (data from Table 8.4). Abbreviations: F - fractional crystallization model; E - equilibrium crystallization model. The crosses represent the assumed initial melt composition. Asterisks mark increments of crystallization and have 25 % intervals. The randomly oriented dashes indicate the compositional field of cumulus - intercumulus mixtures between the predicted pure solid and pure liquid fractional crystallization curves.

8.3.4 Comparison with the Hebron and Berlin plutons

Textural, mineralogical and chemical evidence presented in the foregoing sections of this chapter indicates that the rocks of the Stentor pluton differ markedly from the tonalite-trondhjemite gneisses that intrude the southwestern parts of the BGB (Section 2.4), and more closely resemble granodiorites encountered within the Hebron and Berlin plutons. As previously mentioned, the latter bodies constitute a phase of the Nelspruit batholith (Section 8.2). Thus, the writer suggests that the Stentor pluton also forms an integral part of the Nelspruit batholith. This conclusion is corroborated by recent isotopic age studies carried out on a sample collected in the eastern part of the pluton. Conventional U-Pb isotopic studies on zircons extracted from this sample yielded an age of 3107 ± 5 Ma, which is identical, within error, to the ages of the Hebron pluton ($3104 \pm 3/-2$ Ma) and the Nelspruit Porphyritic Granite (3106 ± 3 Ma) (Kamo and Davis, 1994).

Despite the similarities between the three plutons, it is also apparent that they exhibit different spatial relationships with the BGB and the other phases of the Nelspruit batholith. Figure 8.1 illustrates that the Hebron and Berlin plutons intrude the Nelspruit Porphyritic Granite and are spatially removed from the rocks of the BGB. The Stentor pluton, on the other hand, was emplaced into the Nelspruit Migmatite and Gneiss Terrane, considered by Robb (1978) and Robb *et al.* (1983) to underlie the porphyritic phase (Section 8.2). More significantly, the Stentor pluton also intrudes and deforms the supracrustal assemblages of the BGB (Sections 4.3, 8.3.1 and 9.2.2.1), a feature usually only associated with the older tonalite-trondhjemite diapirs (Robb and Anhaeusser, 1983; Anhaeusser, 1984; Kisters and Anhaeusser, 1993).

Differences are also apparent when the chemical compositions of rocks from the three plutons are compared. Data presented in Table 8.5 indicates that while the plutons exhibit similar average K_2O/Na_2O values, samples from the Stentor pluton are

generally enriched in SiO_2 and depleted in TiO_2 , $\text{Fe}_2\text{O}_3^{\text{total}}$, MgO and CaO . Rocks of the Stentor pluton are also depleted in Ba, Rb, U, Th and Ta compared to those within the Berlin pluton, but compared with the granodiorites of the Hebron pluton, they are enriched in Cs and Th, and depleted in Ta (Figure 8.17A). In terms of REE geochemistry, samples from the Stentor pluton are depleted in the HREE relative to those from the Hebron and Berlin plutons, and also lack the negative Eu anomalies which characterize samples from the latter two bodies (Figure 8.17B).

Table 8.5 Averaged major element compositions and compositional ranges of the Stentor Hebron and Berlin plutons

	Stentor pluton n = 18		Hebron pluton [§] n = 3		Berlin pluton [§] n = 3	
	Range	Average	Range	Average	Range	Average
SiO_2 (wt %)	70.07 - 75.41	72.42	65.23 - 70.21	67.44	60.19 - 69.34	65.86
TiO_2	0.11 - 0.50	0.29	0.30 - 0.75	1.58	0.48 - 0.89	0.65
Al_2O_3	13.32 - 15.19	14.29	13.83 - 16.90	15.15	14.44 - 16.81	15.46
$\text{Fe}_2\text{O}_3^{\text{total}}$	1.53 - 3.37	2.38	2.11 - 4.75	3.59	3.41 - 5.98	4.42
MnO	0.02 - 0.08	0.04	0.06 - 0.07	0.05	0.04 - 0.08	0.06
MgO	bdl - 0.46	0.21	1.39 - 2.48	2.10	1.24 - 2.89	2.02
CaO	0.73 - 1.92	1.26	1.82 - 2.57	2.28	2.20 - 3.57	2.79
Na_2O	3.37 - 4.58	4.02	3.61 - 4.10	3.78	3.81 - 3.90	3.85
K_2O	2.51 - 5.43	3.89	3.48 - 3.68	3.61	3.83 - 4.43	3.89
P_2O_5	0.03 - 0.20	0.11	0.05 - 0.20	0.10	0.20 - 0.34	0.29
$\text{K}_2\text{O}/\text{Na}_2\text{O}$	0.59 - 1.61	0.98	0.90 - 1.01	0.96	0.87 - 1.15	1.01

[§] - data from Raeb *et al.* (1983) and D.A. Van Nierop (unpubl. data); bdl - below detection level

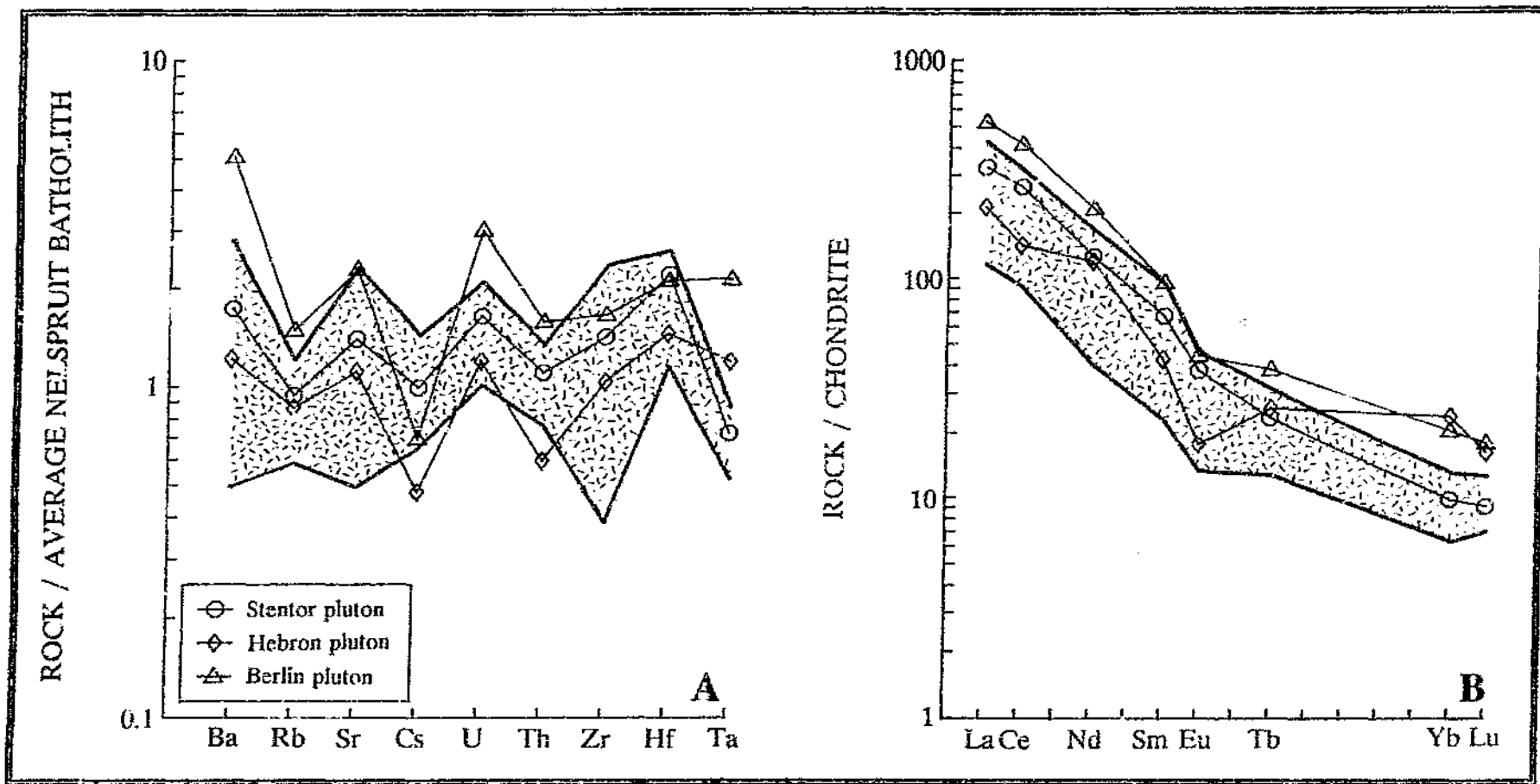


Figure 8.17 Comparison of the averaged trace element compositions of samples from the Stentor, Hebron ($n = 2$) and Berlin ($n = 2$) plutons, normalized against the average composition of the Nelspruit batholith (A) and chondrite (B). Also shown on both plots is the compositional envelope of the Stentor pluton (randomly oriented dashes). Data from Meyer (1983) and this study.

8.4 Nelspruit Migmatite and Gneiss Terrane

8.4.1 Field characteristics

Occupying the rugged terrane north and west of the Steunor pluton is a complex, exceedingly heterogeneous assemblage of strongly foliated, medium- to coarse-grained, locally migmatitic, dark-grey and pinkish gneisses forming part of the Nelspruit Migmatite and Gneiss Terrane (Figure 8.2). A detailed account of the rocks in this general area has previously been presented by Robb *et al.* (1983) so that only a brief description need be given here.

Rocks of the Nelspruit Migmatite and Gneiss Terrane range from homogeneous gneiss, to banded gneiss, to complex phlebitic-, stromatic-, schlieric- and nebulitic-textured migmatite (terminology after Mehnert, 1968) (Figure 8.18A and B). Spectacular pavement exposures occur along Gould's Salvation River on Mara 233 JU, and along the Kaap River on Oxo 224 JU, Klipriviersberg 225 JU and Esperado Annex 222 JU (locality sites A - C in Figure 8.2)¹⁰. Outcrops in these areas are extensively intruded by pods and veins of pinkish pegmatite (quartz + K-feldspar + plagioclase + muscovite) up to several metres wide, and typically contain several distinct gneiss / migmatite textural sub-types; contacts between the different phases are generally ill-defined. Feldspar augen, up to ~8 mm across, are locally developed, as are small, variably assimilated, lenticular- to irregularly shaped amphibolite and serpentinite enclaves, the latter being most common in outcrops fringing the larger greenstone remnants described in Section 3.1. Megacrystic gneisses containing large, randomly oriented to weakly aligned microcline crystals, 1 - 4 cm in length, occur in a northeast-

¹⁰ The reader is referred to the 1:50 000 topographic maps 2531CA SHEBA and 2531CB KAAPMUIDEN for the localities of the various farms mentioned in the text.

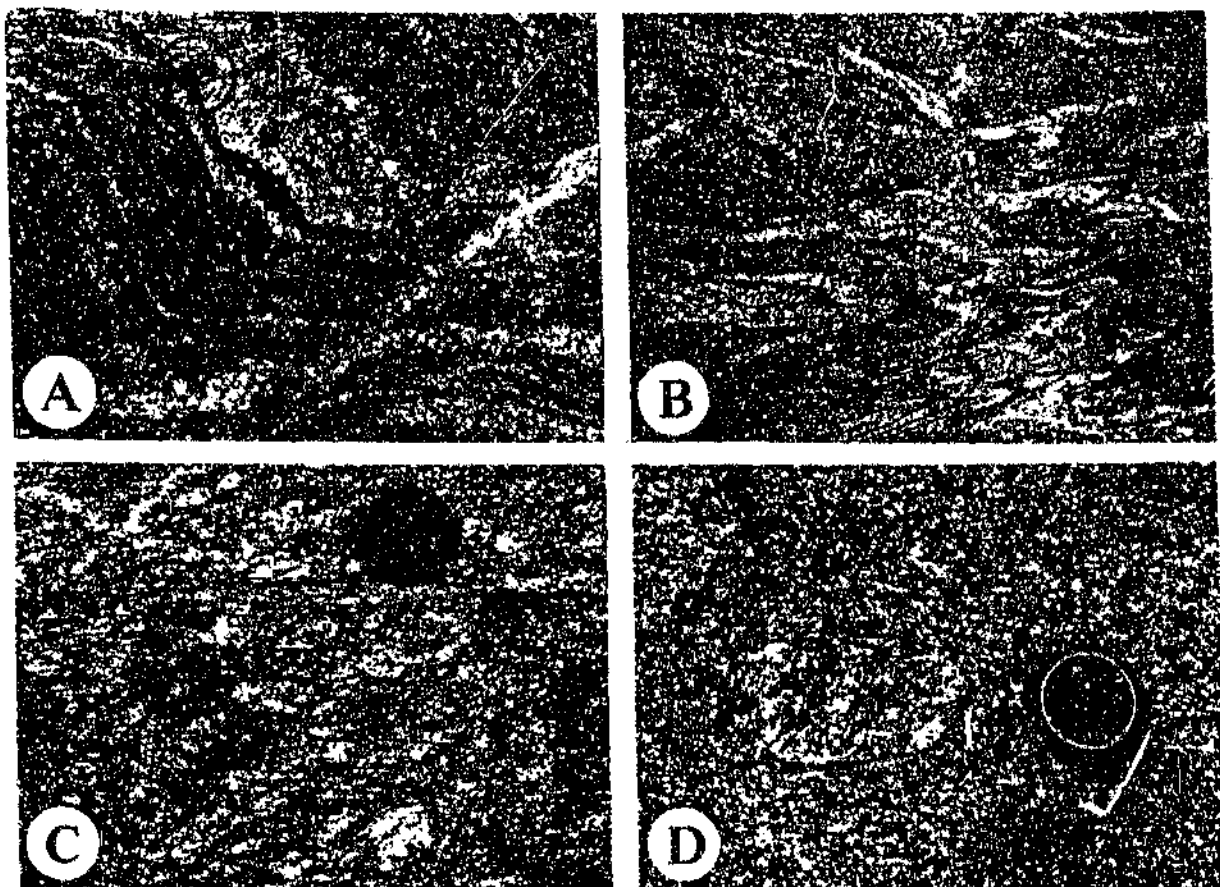


Figure 8.18 Features observed in rocks of the Nelspruit Migmatite and Gneiss Terrane:

(A) Weakly contorted, coarse-grained stromatic migmatite (Stonehaven 207 JU). Note that the thickest leucosome displays a distinct textural zonation, having a coarse-grained margin (arrows) and a finer-grained core. Lens cap (circled) has a diameter of 4.9 cm.

(B) Folding in banded migmatite (Mara 233 JU).

(C) Weakly aligned microcline crystals in megacrystic gneiss (Excelsior 211 JU).

(D) Isolated microcline megacryst in homogeneous, coarse-grained gneiss (Rensberg 273 JU).

trending zone near the confluence of the Crocodile and Kaap Rivers (Figures 8.2 and 8.18C). Isolated K-feldspar megacrysts are also sporadically encountered in outcrops on Rensberg 273 JU and Hillsowen 249 JU, west of the Stentor pluton (Figures 8.2 and 8.18D). Gneissic rocks in the higher-lying parts of the study area, particularly on Moederlief 209 JU, Stonehaven 226 JU, Weltevreden 229 JU and De Hoop 203 JU, are locally accompanied by a homogeneous, medium- to coarse-grained, pinkish granitoid phase which is generally devoid of any well-developed fabric.

8.4.2 Petrography

Petrographically, the gneisses and migmatites consist of plagioclase, quartz, microcline and biotite in varying proportions, with subordinate chlorite and muscovite. Plagioclase typically varies in composition from oligoclase to albite and occurs as irregular-to-ovoid, variably saussuritized grains exhibiting undulose extinction, kinked twin lamellae and quartz-filled peripheral pressure shadows. Minor amounts of myrmekite were recorded in some specimens. Quartz shows pronounced strain extinction and typically forms fine-grained, lenticular aggregates. Microcline is a major constituent of some gneisses, forming discrete, anhedral grains that contain albite exsolution lamellae, but is uncommon in others. The microcline megacrysts exhibit undulose extinction and are transected by sericitized microfractures. They commonly contain rectangular-to-rounded, occasionally embayed, inclusions of quartz, plagioclase, biotite and opaque phases. Biotite forms aligned aggregates which, in conjunction with the quartz aggregates, define the gneissic foliation wrapping around the feldspars. Partial replacement of biotite by chlorite is common. Muscovite is mainly restricted to the K-feldspar-rich gneisses, occurring as discrete, aligned, ragged flakes. Spinel, epidote, apatite, allanite, zircon and rutile occur as accessory minerals.

8.4.3 Chemistry

During the course of the fieldwork, the writer collected ~45 samples of gneiss and migmatite, most of which come from outcrops previously assigned by Robb *et al.* (1983) to the Stentor pluton. Sixteen representative samples of homogeneous gneiss were selected and analysed by XRF (Table 8.6). Five samples, encompassing the entire compositional spectrum, were also analysed by INAA (Table 8.7). The migmatitic and megacrystic gneisses have been excluded from the chemical study because they are exceedingly heterogeneous, necessitating the collection of unrealistically large samples.

8.4.3.1 Major elements

The major element analyses indicate a fair degree of compositional variability. K_2O and Na_2O concentrations vary, respectively, from 1.5 - 5.9 and 2.7 - 4.8 wt %. On the Harpum (1963) plot, the rocks range in composition from tonalite through to granite (*sensu stricto*) (Figure 8.19). This spread of compositions is similar to that noted by Robb (1978) for rocks of the Nelspruit Migmatite and Gneiss Terrane to the east and northeast of Nelspruit. Of the four samples plotting in the tonalite field in Figure 8.19, two (N3 and N17) may be classified as high-alumina trondhjemites according to the criteria of Barker (1979)¹¹. Molar $Al_2O_3/(Na_2O + K_2O + CaO)$ contents are generally high and indicate a dominantly peraluminous character with up to 4.7 wt % corundum in the norm (Figure 8.20 and Table 8.6). On the O'Connor (1965) and De La Roche *et al.* (1980) diagrams, the gneisses plot mainly in the field of granodiorites and granites (*sensu stricto*), with minor overlap into the trondhjemite field (Figures 8.21 and 8.22).

¹¹ According to Barker (1979), high-alumina trondhjemites have $SiO_2 > 68$ wt %, $Al_2O_3 > 15$ wt % @ $SiO_2 = 70$ wt %, $FeO^{total} + MgO < 3.4$ wt %, CaO between 1.5 - 3.0 wt %, Na_2O between 4.0 - 5.5 wt %, and $K_2O < 2.5$ wt %.

Table 8.6 Major and trace element data obtained from XRF analysis of gneisses from the Nelspruit Migmatite and Gneiss Terrane. Fe_2O_3/FeO ratios were fixed at 0.45 in CIPW normative calculations, following Middlemost (1989);

Sample	N2	N3	N4	N13	N16	N17	N18	N22
SiO ₂ (wt %)	72.24	71.28	66.65	71.68	70.52	73.52	71.87	71.97
TiO ₂	0.24	0.27	0.77	0.26	0.33	0.24	0.32	0.27
Al ₂ O ₃	14.58	15.22	16.34	15.48	14.51	15.23	14.67	14.68
Fe ₂ O ₃ ^{total}	2.25	2.09	4.57	2.15	3.10	1.62	2.43	2.31
MnO	0.04	0.03	0.09	0.04	0.06	0.03	0.05	0.04
MgO	0.20	0.50	1.10	0.38	0.79	0.91	0.65	0.23
CaO	1.48	2.21	2.81	2.04	2.69	2.21	2.78	1.28
Na ₂ O	4.08	4.48	4.80	3.92	3.94	4.69	3.78	3.48
K ₂ O	3.45	2.10	1.77	3.38	2.61	1.50	2.16	5.22
P ₂ O ₅	0.07	0.10	0.56	0.10	0.11	0.08	0.10	0.07
H ₂ O ⁻	0.01	0.02	0.05	0.01	0.01	0.02	0.03	0.02
H ₂ O ⁺	0.20	0.25	0.56	0.22	0.30	0.23	0.23	0.20
CO ₂	0.07	0.14	0.12	0.19	0.08	0.04	0.04	0.13
Total	98.91	98.69	100.19	99.85	99.05	100.32	99.12	99.90
Ba (ppm)	991	187	399	432	203	116	196	945
Rb	121	108	126	129	105	67	100	148
Sr	382	353	578	272	183	152	167	249
Pb	17	13	15	18	9	11	13	19
Y	13	12	45	12	22	19	24	15
Nb	11	5	29	18	11	10	14	12
Zr	217	135	301	148	93	72	94	168
Ga	24	24	28	24	22	20	22	23
Zn	52	46	86	55	48	30	46	45
Cu	30	11	27	15	39	13	71	15
Ni	14	17	21	14	22	15	20	13
CIPW norm								
Q (wt %)	31.46	31.70	24.85	31.10	30.14	34.24	34.28	28.43
C	1.77	2.12	3.04	2.34	0.76	2.16	1.39	1.45
Z	0.02	0.02	0.04	0.01	0.03	0.03	0.02	0.07
Or	20.39	12.41	10.46	19.98	15.43	8.87	12.77	30.85
Ab	34.52	37.90	40.61	33.17	33.34	39.68	31.98	29.44
An	6.44	9.43	9.52	8.27	12.12	10.19	12.89	5.07
Hy	2.16	2.70	5.67	2.49	4.27	3.36	3.36	2.24
Mt	1.01	0.94	2.05	0.97	1.39	0.73	1.09	1.04
Il	0.46	0.51	1.46	0.49	0.63	0.46	0.61	0.51
Ap	0.17	0.24	1.33	0.24	0.26	0.19	0.24	0.17
Cc	0.16	0.32	0.27	0.43	0.18	0.09	0.09	0.30

Q - quartz; C - corundum; Z - zircon; Or - orthoclase; Ab - albite; An - anorthite; Hy - hypersthene; Mt - magnetite; Il - ilmenite; Ap - apatite; Cc - calcite

Table 8.6 (continued)

Sample	N23	N24	N25	N26	N27	N28	N29	N30
SiO ₂ (wt %)	70.14	71.75	71.83	71.66	71.54	72.08	69.57	69.99
TiO ₂	0.33	0.29	0.31	0.15	0.27	0.25	0.32	0.28
Al ₂ O ₃	14.91	14.45	14.49	16.38	15.12	14.93	15.21	14.27
Fe ₂ O ₃ ^{total}	3.33	2.81	1.73	1.68	2.00	1.70	3.36	3.05
MnO	0.07	0.07	0.02	0.03	0.03	0.04	0.08	0.05
MgO	0.96	0.68	0.26	0.62	0.32	0.28	1.37	0.18
CaO	2.73	2.50	1.44	2.06	1.81	1.32	2.69	1.39
Na ₂ O	3.55	3.35	2.73	3.75	3.91	3.84	3.19	3.68
K ₂ O	2.34	3.00	5.94	2.28	3.82	3.92	3.13	5.11
P ₂ O ₅	0.11	0.09	0.08	0.09	0.11	0.07	0.11	0.10
H ₂ O	0.01	0.01	0.01	0.01	0.01	0.01	0.06	0.02
H ₂ O ⁺	0.20	0.14	0.37	0.14	0.38	0.24	0.29	0.41
CO ₂	0.09	0.04	0.10	0.21	0.13	0.14	0.03	0.17
Total	98.77	99.18	99.31	99.06	99.45	98.82	99.41	98.70
Ba (ppm)	188	197	782	526	492	956	289	1903
Rb	102	117	145	60	86	159	129	125
Sr	161	160	239	422	533	295	184	653
Pb	9	22	18	15	16	19	12	19
Y	25	22	11	6	11	17	22	28
Nb	14	12	6	3	2	6	13	14
Zr	108	75	209	73	146	146	89	370
Ga	22	21	21	20	24	23	21	25
Zn	46	62	37	34	45	39	56	61
Cu	12	21	12	16	14	12	38	94
Ni	22	19	14	17	13	13	24	14
CIPW norm								
Q (wt %)	32.64	33.79	29.74	36.01	29.85	31.54	30.43	25.45
C	2.05	1.46	1.38	4.70	1.83	2.46	2.02	0.79
Z	0.04	0.03	0.06	0.03	0.02	0.01	0.02	0.03
Or	13.83	17.73	35.11	13.48	22.58	23.17	18.50	30.20
Ab	30.04	28.34	23.10	31.73	33.08	32.49	26.99	31.14
An	12.26	11.56	5.99	8.30	7.44	5.21	12.44	5.17
Hy	4.92	3.83	1.70	2.84	2.17	1.86	6.00	2.77
Mt	1.50	1.26	0.78	0.76	0.90	0.76	1.51	1.37
Il	0.63	0.55	0.59	0.28	0.51	0.47	0.61	0.53
Ap	0.26	0.21	0.19	0.21	0.26	0.17	0.26	0.24
Cc	0.20	0.09	0.23	0.48	0.30	0.32	0.07	0.39

Q - quartz; C - corundum; Z - zircon; Or - orthoclase; Ab - albite; An - anorthite; Hy - hypersthene;
Mt - magnetite; Il - ilmenite; Ap - apatite; Cc - calcite

Table 8.7 Trace element data obtained from INAA of selected samples of gneiss from the Nelspruit Migmatite and Gneiss Terrane

Sample	N2	N17	N25	N28	N30
Cs (ppm)	8.11	9.47	1.95	7.52	6.07
U	1.20	1.30	0.70	2.43	1.60
Th	12.5	7.86	16.9	15.1	13.8
Hf	5.82	3.72	6.34	4.83	8.43
Ta	0.97	1.27	0.34	0.90	0.99
Sc	2.28	3.07	2.28	1.89	1.98
Co	29.3	3.49	3.74	3.35	4.13
As	0.93	0.27	0.13	0.63	0.73
La	83.2	35.2	80.0	70.3	136.8
Ce	172	72.0	161	134	269
Nd	59.6	24.6	53.1	38.8	90.8
Sm	9.47	3.84	6.27	6.31	6.30
Eu	1.85	0.95	1.17	1.31	3.38
Tb	0.66	0.54	0.48	0.59	1.18
Yb	1.03	2.26	0.97	1.58	1.99
Lu	0.18	0.24	0.16	0.26	0.19
Au (ppb)	5.0	3.2	3.4	4.7	4.7

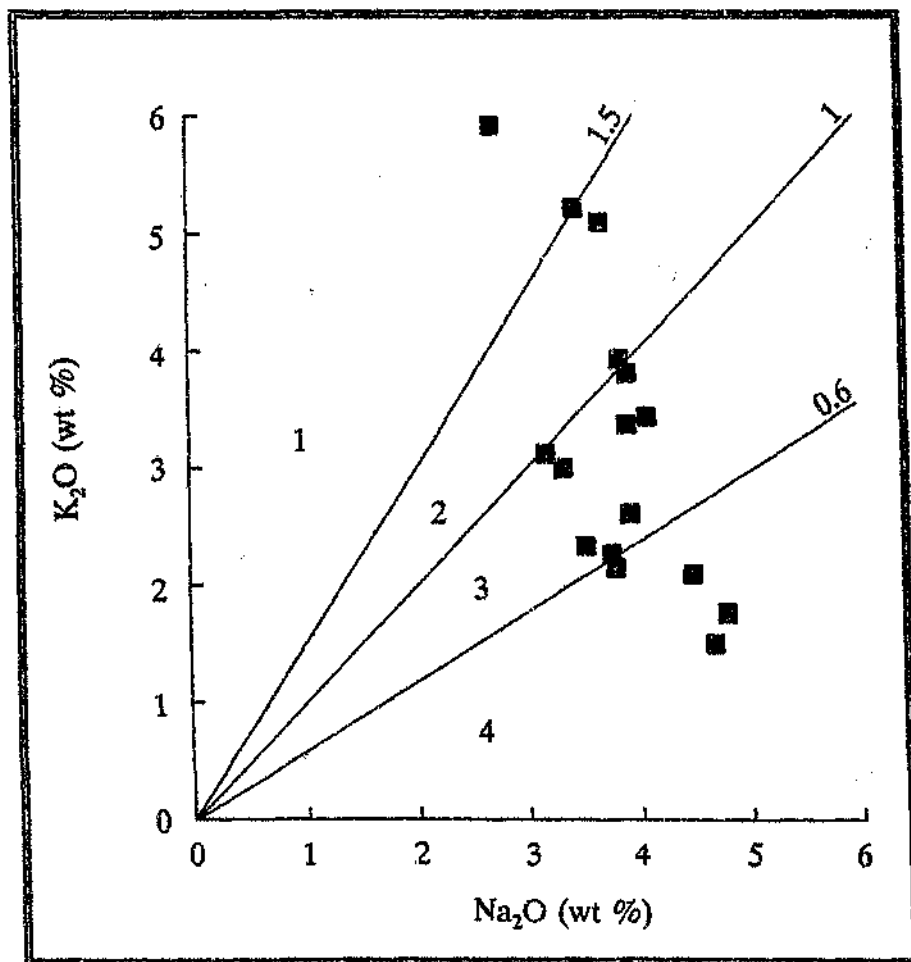


Figure 8.19 Plot of K_2O against Na_2O for gneissic samples from the Nelspruit Migmatite and Gneiss Terrane (diagram after Harpun, 1963). Fields: 1 - granite; 2 - adamellite; 3 - granodiorite; 4 - tonalite.

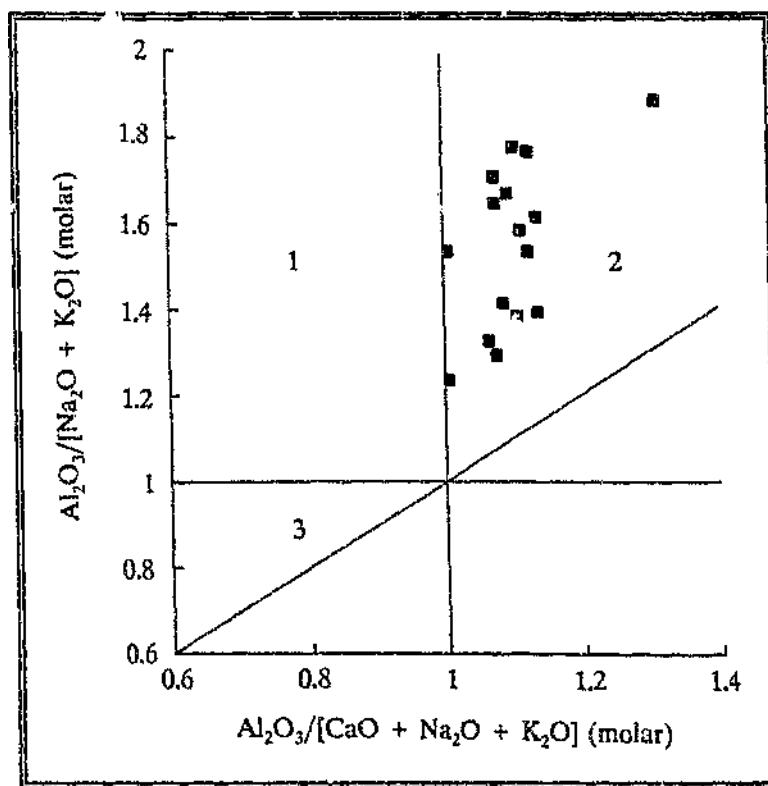


Figure 8.20 Plot of mol fraction $Al_2O_3 / (Na_2O + K_2O)$ versus $Al_2O_3 / (CaO + Na_2O + K_2O)$ for gneissic samples from the Nelspruit Migmatite and Gneiss Terrane (diagram after Maniar and Piccoli, 1989). Fields: 1 - metaluminous; 2 - peraluminous; 3 - peralkaline.

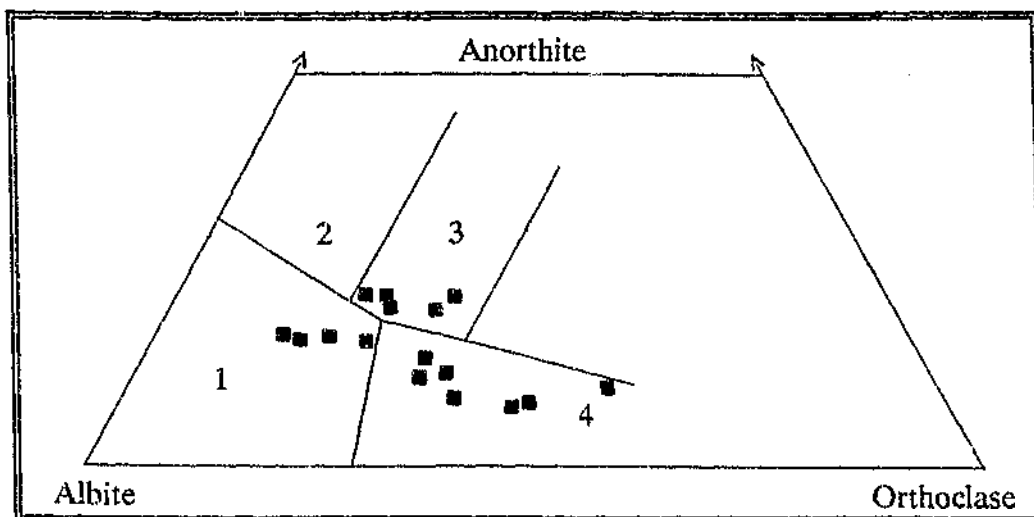


Figure 8.21 Normative albite - anorthite - orthoclase classification plot for samples from the Nelspruit Migmatite and Gneiss Terrane (diagram after O'Connor, 1965; modified field boundaries after Barker, 1979). Fields: 1 - trondhjemite; 2 - tonalite; 3 - granodiorite; 4 - granite.

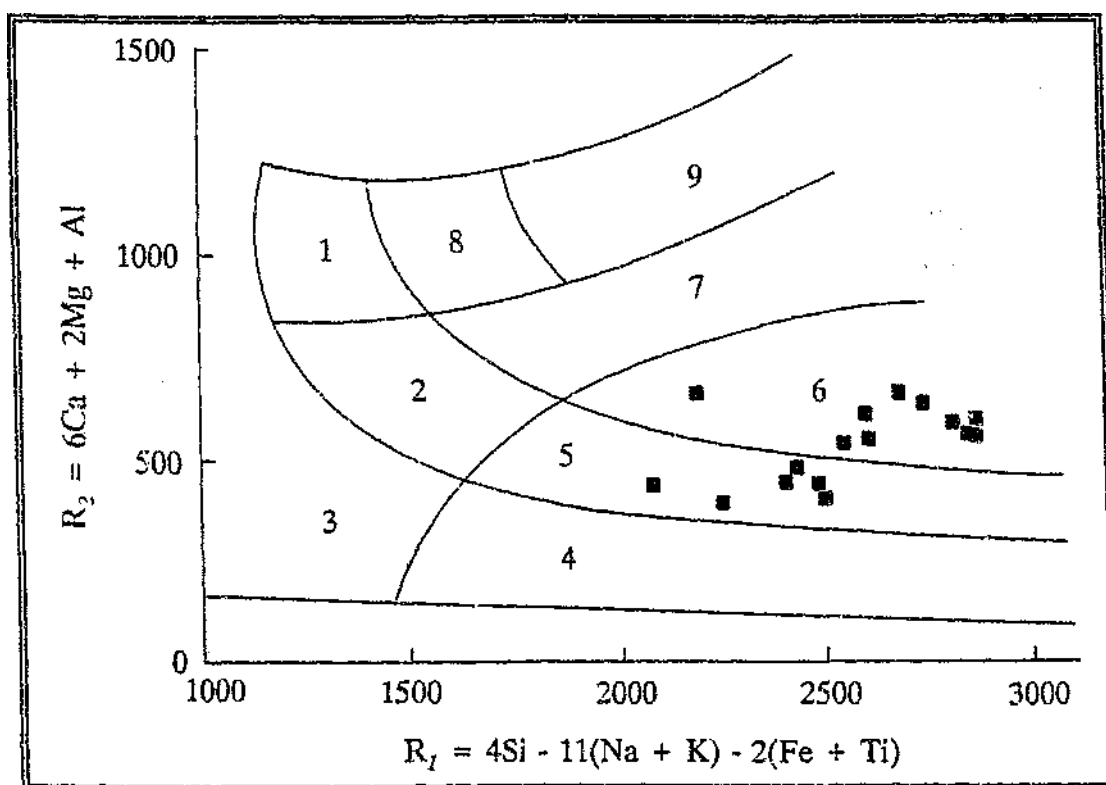


Figure 8.22 R_1R_2 plot for gneisses of the Nelspruit Migmatite and Gneiss Terrane (diagram after De La Roche et al., 1980). Fields: 1 - monzonite; 2 - quartz monzonite; 3 - quartz syenite; 4 - alkali-granite; 5 - granite; 6 - granodiorite; 7 - tonalite; 8 - monzodiorite; 9 - diorite.

8.4.3.2 Trace elements

The trace element abundances also show a fair degree of variation. Ba, Rb and Sr concentrations range, respectively, from 116 - 1903 ppm, 60 - 159 ppm and 160 - 653 ppm. Ba/Rb ratios vary from 2 - 15, Sr/Rb from 1 - 7, Ba/Sr from 0.5 - 4, and K/Rb from ~120 - 370.

Figure 8.23 shows chondrite-normalized REE profiles for those samples that have been analysed by INAA. Samples N2, N25, N28 and N30, which vary in composition from granodiorite-to-granite (*sensu stricto*), are characterised by highly fractionated profiles with La 300 - 550 times enriched over chondrite and La_N/Yb_N between 30 - 56.

Sample N17, a trondhjemite, displays distinctly lower abundances of the LREE's ($La_N = 140$) and a La_N/Yb_N ratio of 10. This sample is, however, markedly enriched in all of the REE's compared to the trondhjemitic gneisses intruding the southwestern parts of the BGB, which typically have $La_N < 70$ and $Yb_N < 3$ (Robb and Anhaeusser, 1983), and also does not show the steep L-shaped REE profile characteristic of the latter rocks. All samples analysed display small negative Eu anomalies with Eu/Eu^* between 0.75 - 0.85.

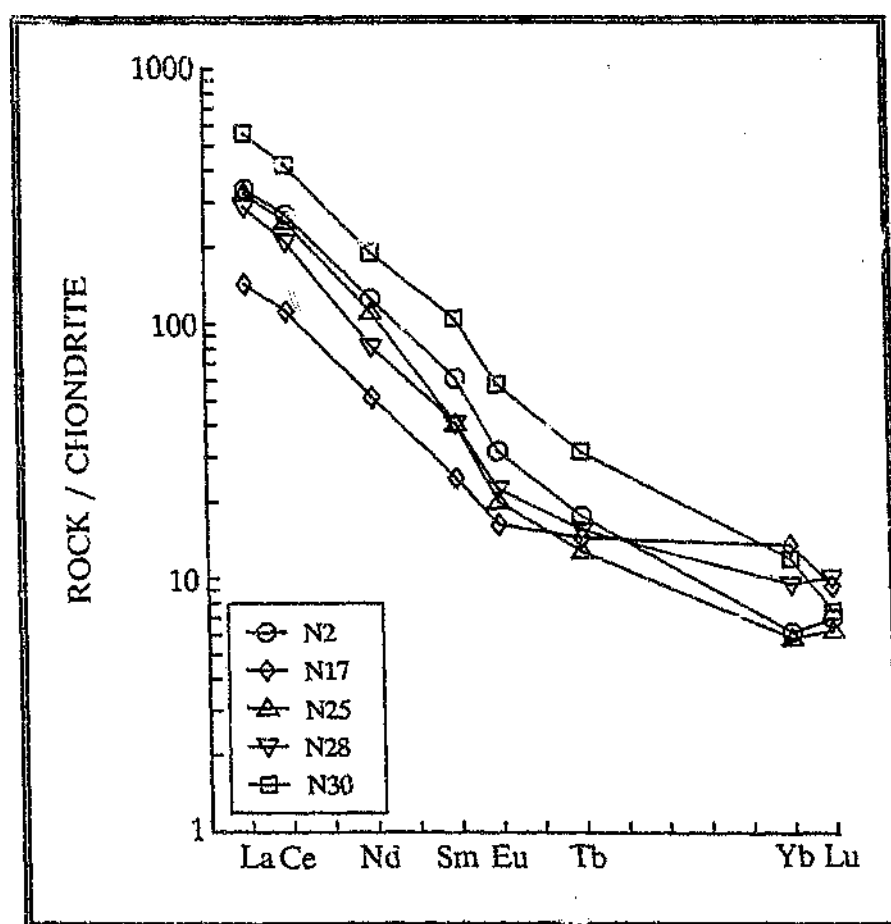


Figure 8.23 Chondrite-normalized REE distribution profiles for gneisses of the Nelspruit migmatite and Gneiss Terrane (sample numbers as in Table 8.7 and Figure 8.2).

8.5 Late-stage intrusive rocks

Basic dykes, consisting mainly of fine- to medium-grained diabase, occur throughout the study area, but are best developed in the granitoid terrane in the west, where they give rise to prominent, often densely vegetated, linear topographic depressions. The dykes are undeformed, dip subvertically, and typically either strike north-northeast or west-northwest (Figure 8.2). While individual intrusives can often be traced along strike for several kilometres, few exceed 10 m in width. In some exposures, the dykes are seen to cross-cut the gneissose and S_m mylonitic fabrics in the granitoids, but are themselves cut by narrow leuco pegmatite veins (Figure 8.24). Visser *et al.* (1986) and Hunter and Reid (1987) suggested that the dykes are mainly Early Proterozoic in age.

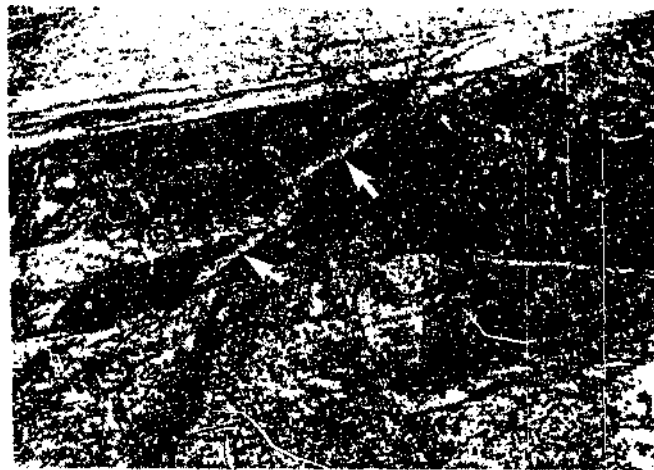


Figure 8.24 Diabase dyke intruding homogeneous gneiss of the Nelspruit Migmatite and Gneiss Terrane (Klipriviersberg 225 JU). Note how the dyke truncates the gneissose fabric in the host (dashed line), but is itself intruded by thin pegmatite veins (arrows). Lens cap is 4.9 cm in diameter.

Petrographically, the diabase dykes consist of subophitically intergrown augite and zoned plagioclase (labradorite - bytownite). Large, euhedral, but typically extensive¹⁴ saussuritized plagioclase phenocrysts up to ~6 cm across impart a porphyritic texture

some dykes. Minor amounts of olivine, orthopyroxene and uraltite were recorded in few specimens. Chlorite, biotite, quartz, epidote, calcite, magnetite, ilmenite, sphene and apatite are typical accessory phases.

A coarse-grained dyke of dioritic composition was recorded at a locality ~6 km east of the New Consort Mine on Dry Hoek 248 JU (near to sample site N26 in Figure 8.2). This dyke is characterized by a distinctive mottled appearance in outcrop due to the crude segregation of the light and dark coloured mineral constituents. Seen in thin section, the rock consists almost entirely of brownish-green pleochroic hornblende and zoned plagioclase, the latter often showing sericitic alteration patches. Accessory constituents include biotite, epidote - clinozoisite, quartz, chlorite and opaque phases.

Shales of the Fig Tree Group to the south of the Scotsman Fault on Three Sisters 256 JU are also intruded by a fairly large (~400 m long and ~150 m wide), ovoid body of dioritic composition (Figure 1.4, H4). This intrusion displays a massive, medium- to coarse-grained, equigranular-texture in outcrop, and is composed of twinned hornblende / actinolite and turbid plagioclase (andesine - labradorite), with accessory quartz, chlorite and ilmenite.

A small (~100 m long and ~70 m wide), very coarse-grained, leucocratic quartz-feldspar porphyry body intrudes argillaceous assemblages along the Igwalagwala Fault in the eastern part of the region (Figure 1.4, E11; Section 9.2.1.2.5). Seen in thin section, the quartz phenocrysts are characterised by deeply embayed crystal boundaries while the plagioclase phenocrysts exhibit more euhedral morphologies, but are often extensively saussuritized. The phenocrysts are set in a fine-grained matrix consisting of quartz, plagioclase, muscovite and epidote, with accessory calcite and magnetite.

9. STRUCTURAL GEOLOGY

9.1 Introduction

Analysis of the geometry, distribution and mutual relations of the structures and fabrics in the study area indicates that the rocks have been affected by three episodes of deformation. The main deformation event, here designated D_{main} or for brevity D_m , resulted in the formation of folds and faults. Early D_m structures (i.e. those which formed prior to the $D_{diapiric}$ event - see below) post-date strata of the Moodies Group, but pre-date the Stentor pluton. Late-phase D_m faults, however, deform granitoids of the Stentor pluton, indicating that the latter parts of D_m are younger than this intrusive body. Structures considered to have resulted from deformation accompanying the diapiric emplacement of the Stentor pluton during the $D_{diapiric}$ or D_d episode, are restricted to the area immediately north of Three Sisters. D_d deformation is believed to have occurred *during* the D_m event, and gave rise to folds that have refolded and reoriented early-formed D_m folds and faults. The final deformation event, D_{final} or D_f , led to the formation of cross-faults that typically have strike extents in the order of tens to hundreds of metres. These faults displace and truncate the earlier structures.

To facilitate documentation of the various features associated with each of the deformation events, folds (F), faults (B), foliations (S) and lineations (L) have been labelled by the appropriate suffix, so that F_m , B_m , S_m and L_m all represent structural elements that formed during D_m etc. Primary layering is designated S_p . A sketch map showing the distribution of folds and faults in the study area is presented in Figure 9.1. Table 9.1 summarizes the various structural elements encountered in the region.

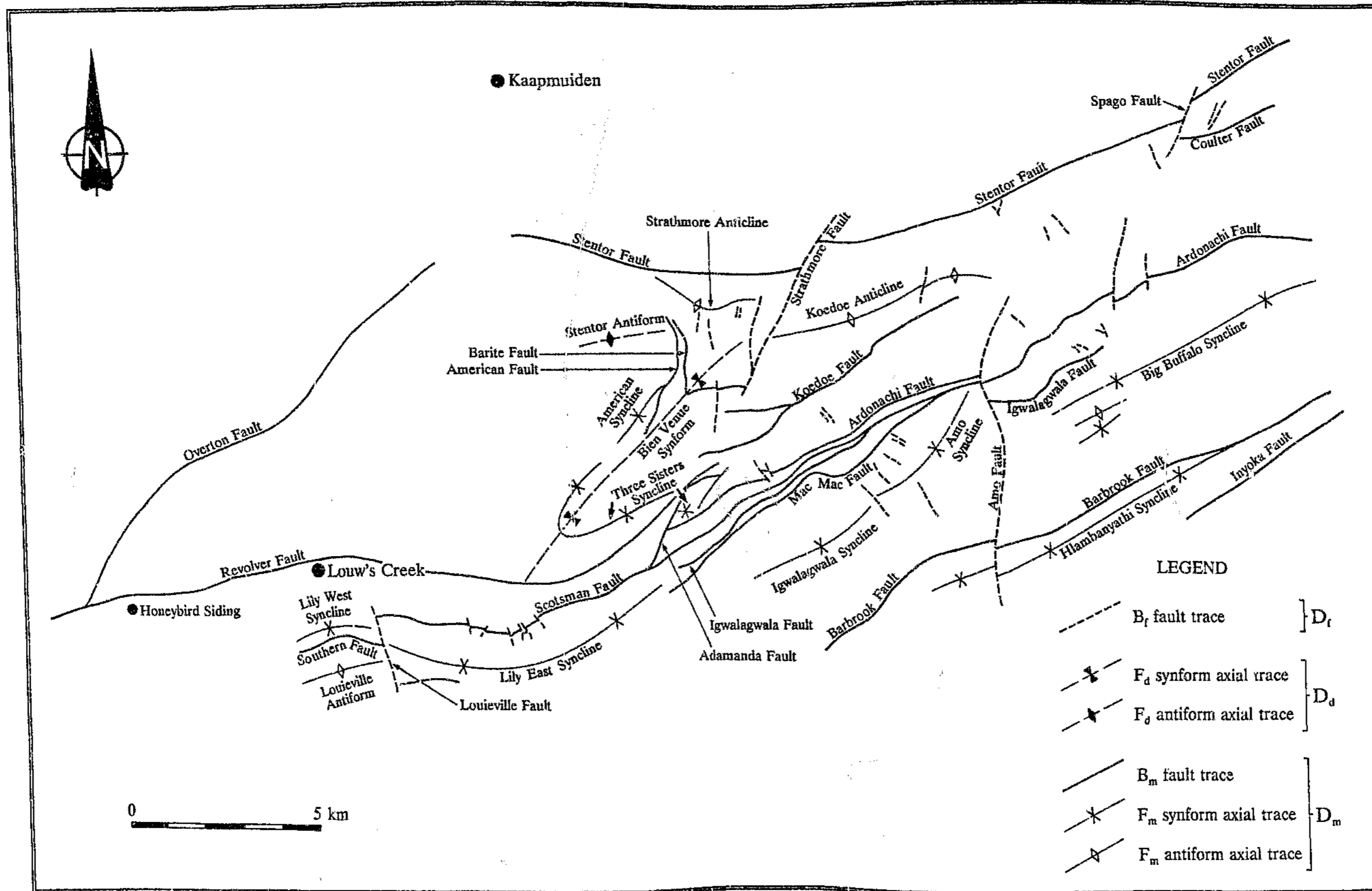


Figure 9.1 Sketch map showing the distribution of folds and faults in the study area.

Table 9.1 Summary of structural elements encountered in the study area

Deformation event	Folds	Faults	Foliations	Lineations
D_{final} (D_f)	-	B_f	S_f	-
$D_{diapiric}$ (D_d)	F_d	-	S_d	L_d
D_{main} (D_m)	F_m	B_m	S_m	L_m

9.2 Description of structural elements

9.2.1 D_{main} - D_m

D_m deformation affected all stratigraphic units and gave rise to northeasterly trending, subhorizontal- to steeply plunging F_m folds that are bounded by a series of subparallel, generally subvertical or steep southeasterly dipping B_m longitudinal strike faults. S_m foliations are heterogeneously developed within most F_m , and along all B_m structures and locally contain oblique or down-dip L_m mineral elongation lineations.

9.2.1.1 F_{main} - F_m

Eleven major F_m folds have been recognised in the study area. These include the Big Buffalo, Hlambanyathi, Amo, Igwalagwala, Lily West, Lily East, Three Sisters and American Synclines, as well as the Louieville Antiform and the Strathmore and Koedoe Anticlines (Figure 9.1). A summary of structural data for the F_m folds is presented in Figure 9.2.

9.2.1.1.1 Big Buffalo Syncline

Structure in the eastern part of the region is dominated by a large, close-to-tight, upright syncline which is clearly discernable on the SPOT image shown in Figure 1.2. Moodies Group quartzites and conglomerates coring the syncline are underlain by

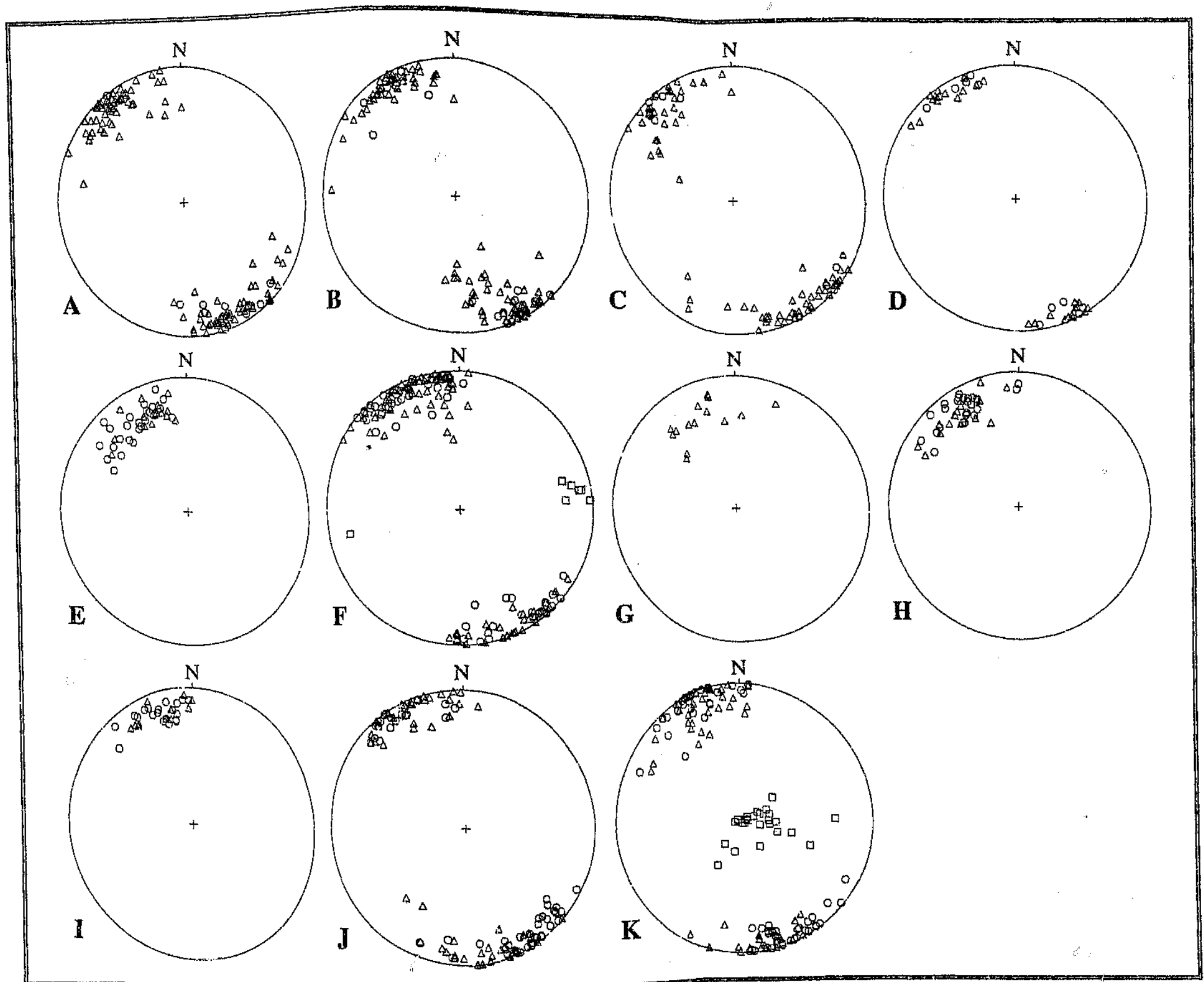


Figure 9.2 Lower hemisphere equal area projections summarizing structural data for F_m folds (poles to S_p - triangles; poles to S_m - circles; plunge of minor fold axes - squares):

- (A) *Big Buffalo Syncline ($S_p - n = 125$; $S_m - n = 11$).*
- (B) *Hlambanyathi Syncline ($S_p - n = 87$; $S_m - n = 22$).*
- (C) *Amo Syncline ($S_p - n = 75$; $S_m - n = 13$).*
- (D) *Igwagwala Syncline ($S_p - n = 27$; $S_m - n = 11$).*
- (E) *Lily West Syncline ($S_p - n = 15$; $S_m - n = 26$).*
- (F) *Lily East Syncline ($S_p - n = 82$; $S_m - n = 53$; axes of minor folds - $n = 7$).*
- (G) *Three Sisters Syncline ($S_p - n = 14$).*
- (H) *American Syncline ($S_p - n = 19$; $S_m - n = 24$).*
- (I) *Louieville Antiform ($S_p - n = 11$; $S_m - n = 21$).*
- (J) *Strathmore Anticline ($S_p - n = 57$; $S_m - n = 58$).*
- (K) *Koedoe Anticline ($S_p - n = 56$; $S_m - n = 68$; axes of minor folds - $n = 25$).*

poorly exposed argillites of the Sheba Formation (Figure 1.4). The latter rocks terminate in the north and south against the Ardonachi and Barbrook Faults (Sections 9.2.1.2.14 and 9.2.1.2.7). The nose of the fold is prominently outlined by cliffs at the western end of Kaalrug Ridge, on Amo 259 JU. In this area, the hingeline plunges east-northeasterly at 75° , but towards the east, plunge is less steep, attaining a minimum of 45° close to the eastern border of Sherlock 461 JU. The syncline also becomes progressively tighter from west to east. Rocks along the southern limb of the syncline, on Rusoord 261 JU and Kaalrug 465 JU, are deformed into a series of large, upright, tight, 'Z'-type parasitic folds that plunge at $50 - 65^\circ$ towards the east-northeast (Figure 1.4, F12 and E13). Bedding to the east of the Kaalrug trigonometrical beacon (Figure 1.4, E14) is overturned, dipping south-southeastward at $50 - 75^\circ$, and is locally accompanied by a heterogeneously developed S_m cleavage that generally dips steeply to the north-northwest (Figure 9.2A).

9.2.1.1.2 Hlambanyathi Syncline

This elongate, east-northeasterly trending structural basin, which is bounded on both sides by major longitudinal dislocations, deforms Moodies rocks building the Makhonjwa Range in the southeastern corner of Figure 1.4. Younging directions, as deduced from cross- and graded-bedding in the arenites, leave no doubt as to the synclinal nature of the fold. According to the 1:50 000 geological map of Visser *et al.* (1956), the syncline attains its greatest width of ~ 2.5 km in the eastern part of Fourieskraal 267 JU, and extends as far west as French Bob's Gold Mine, ~ 9 km due south of Louw's Creek. In the area presently under review, the position of the hinge zone is marked in the field by a 100 - 250 m wide band of soft, reddish-brown weathering siltstone, with minor quartzite and, in places, BIF (Section 7.3). This unit does not outcrop well and occupies a shallow topographic depression between quartzite ridges outlining the limbs of the syncline (Figure 9.3).

The Inyoka Fault, which bounds the syncline in the south (Section 9.2.1.2.8), strikes approximately parallel to the latter's axial trace and appears to have truncated



Figure 9.3 View of the Hlambanyathi Syncline looking west to east across the Amo Fault, the latter morphologically manifest as the steep-sided valley in the foreground. Width of field of view at the horizon is ~500 m; trees are ~4 m high. Plunge of syncline is at shallow angles away from the viewer. The topographic low (arrow) between the quartzite ridges marking the limbs of the fold is underlain by siltstones, with minor BIF and quartzite.

part of the southern limb. The Barbrook Fault, on the northern side (Section 9.2.1.2.7), trends oblique to the strike of the rocks and the axial trace. In the west, on Fourieskraal 267 JU, Singerton 260 JU and Rusoord 261 JU, this fault truncates part of the northern limb, but in the east, on Kaalrug 465 JU, the fault has eliminated the northern limb as well as portion of the southern limb.

Close to the western boundary of Singerton 260 JU, the Hlambanyathi Syncline is cross-cut by the north-striking Amo Fault, a major B_1 structure which in this area displays a right-lateral displacement of ~250 m (Figure 1.4, G10, H10 and H11). West of this fault, the syncline plunges east-northeast at 20° , has an interlimb angle of 55° with an axial surface that dips at 75° to the north-northwest. Geometry of the syncline immediately east of the Amo Fault is almost identical to that described above, except that the plunge is less steep at $\sim 10^\circ$ towards the east-northeast. Further east, however, the syncline is tight and upright, and plunges west-southwest at $5 - 30^\circ$. A steep- to subvertically dipping, east-northeasterly trending S_m grain- and clast-shape foliation is variably developed subparallel to S_p (Figure 9.2B).

9.2.1.1.3 Amo Syncline

Moodies rocks in the central part of Amo 259 JU occupy a broad, but tight, upright synformal structure that plunges at 60° towards the east-northeast (Figure 1.4). The quartzites and conglomerates are underlain in the south and northwest by shale and metapreywacke assemblages of the Sheba Formation, but terminate abruptly against the Igwalagwala and Mac Mac Faults in the north, and the Barbrook Fault in the south (Sections 9.2.1.2.5, 9.2.1.2.6 and 9.2.1.2.7). The S_m cleavage is most easily recognised in the argillites and is generally subparallel to S_p (Figure 9.2C). The rose of the syncline originally lay in the west, but has been removed by a north-striking fault which is correlated with the D_r deformation stage by virtue of its orientation (Figure 1.4, G9). This fault juxtaposes Moodies rocks within the Amo Syncline against Fig Tree assemblages within the Igwalagwala Syncline to the west (Section 9.2.1.1.4). Younging directions, preserved in cross-bedded arenites in both limbs of the Amo Syncline in this general area, confirm that the synform is upward-facing. Several other faults, also believed to have formed during the D_r deformation event, displace the northern and southern limbs by up to ~400 m (Figure 1.4, F9 and G10).

Poor exposures in the central parts of the syncline make it difficult to accurately position the axial trace. However, available younging data suggest that the latter is obliquely transected by the Igwalagwala Fault to the northeast of the Amo forestry station (Figure 1.4, E10). Further east, the Moodies strata young consistently to the north, indicating that only the southern limb, or portion thereof, is preserved.

9.2.1.1.4 Igwalagwala Syncline

This upright, isoclinal fold is defined by a northeast-trending, canoe-shaped outcrop of quartzite along the Scotsman 258 J / Fourieskraal 267 JU boundary, extending westwards onto Igwalagwala 263 JU (Figure 1.4). The orientation of the fold axis could not be established due to slumping of outcrops in the hinge areas. The writer

suspects, however, that it is near to horizontal. The S_m cleavage is best developed in the enclosing argillaceous rocks and is subparallel to bedding except in the hinges (Figure 9.2D).

9.2.1.1.5 Lily West and Lily East Synclines

Strata building the Lily Ridge are deformed by two prominent folds that are juxtaposed along the north-northwest-striking Louieville Fault to the southeast of Louw's Creek (Figure 1.4, H2 and I3). These folds are collectively referred to by Visser *et al.* (1956) as the "Lily Syncline". However, as shown in Figure 1.4, marked differences exist in the stratigraphy of the "Lily Syncline" on either side of the Louieville Fault. Moodies rocks to the east of the fault rest on shales and metagreywackes of the Sheba Formation, while those to the west are underlain in the north by basic and ultrabasic schists correlated with the Theespruit Formation. This distinction, which was overlooked by Visser *et al.* (1956), indicates that the "Lily Syncline" in fact comprises two separate folds. In order to emphasize this, but at the same time avoid confusing changes to the nomenclature used by previous workers, these folds will be referred to as the Lily West and Lily East Synclines.

Mapping by Anhaeusser (1963, 1969) and Viljoen (1963) indicated that the Lily West Syncline is traceable beyond the western boundary of the area shown in Figure 1.4 as far as the Jamestown Schist Belt (Figure 2.1), a distance of some 20 km. South of Louw's Creek, the syncline is near isoclinal and overturned with an axial surface that dips at 70° to the south-southeast. The hingeline plunges at 45° on a bearing of 105° . A pervasive, south-southeasterly dipping S_m foliation, produced by the preferential orientation of recrystallized quartz grains in the arenites, and chlorite laths in the underlying metavolcanic rocks, is developed subparallel to the axial surface of the syncline (Figure 9.2E). S_m generally overprints bedding in the metasediments. Rudaceous

and arenaceous rocks within the southern limb of the syncline tectonically abut against Onverwacht Group schists along the northern limb of the Louieville Antiform (Sections 9.2.1.1.8 and 9.2.1.2.3).

The Lily East Syncline extends as far east as the central part of Amo 259 JU and is also near-isoclinal in form, but unlike the Lily West Syncline, generally upright (Figure 9.4A). In map view, the syncline is characterised by a broad arcuate shape, concave to the north (Figure 1.4). Close to the Eldorado Gold Mine (Figure 1.4, I3), the hingeline plunges at 20° on a 090° bearing, but some 4 km to the east, at the Holnekt trigonometrical beacon (Figure 1.4, I5), plunge is at 40° on a bearing of 230° . The S_m cleavage in the Moodies conglomerates is mainly defined by strongly flattened clasts and is subparallel to S_p and the axial surface (Figures 9.2F and 9.4B). The fabric noticeably intensifies with proximity to the core of the fold.

Several small-scale, tight folds were recorded in road-cutting exposures along the Shannon Sawmill - Ka Ngwane Government Offices road on Holnekt 331 JU (Figure 9.4C). These folds, which occur in argillaceous rocks along the southern limb of the Lily East Syncline, have easterly-striking, upright axial planes and plunge mainly at shallow angles to the east (Figure 9.2F). They display a well-developed axial planar slaty cleavage.

On Ardonachi 257 JU, Igwalagwala 263 JU and Scotsman 258 JU, the position of the Lily East Syncline is marked by a comparatively narrow band of intensely sheared conglomerate, bounded on either side by major longitudinal faults (Sections 9.2.1.2.5 and 9.2.1.2.6). A marked increase in the width is, however, apparent further to the east on Amo 259 JU. The exact attitude of the fold in these areas is difficult to establish. However, cleavage and bedding are generally steeply inclined to the south-southeast, suggesting that the syncline is overfolded to the north.

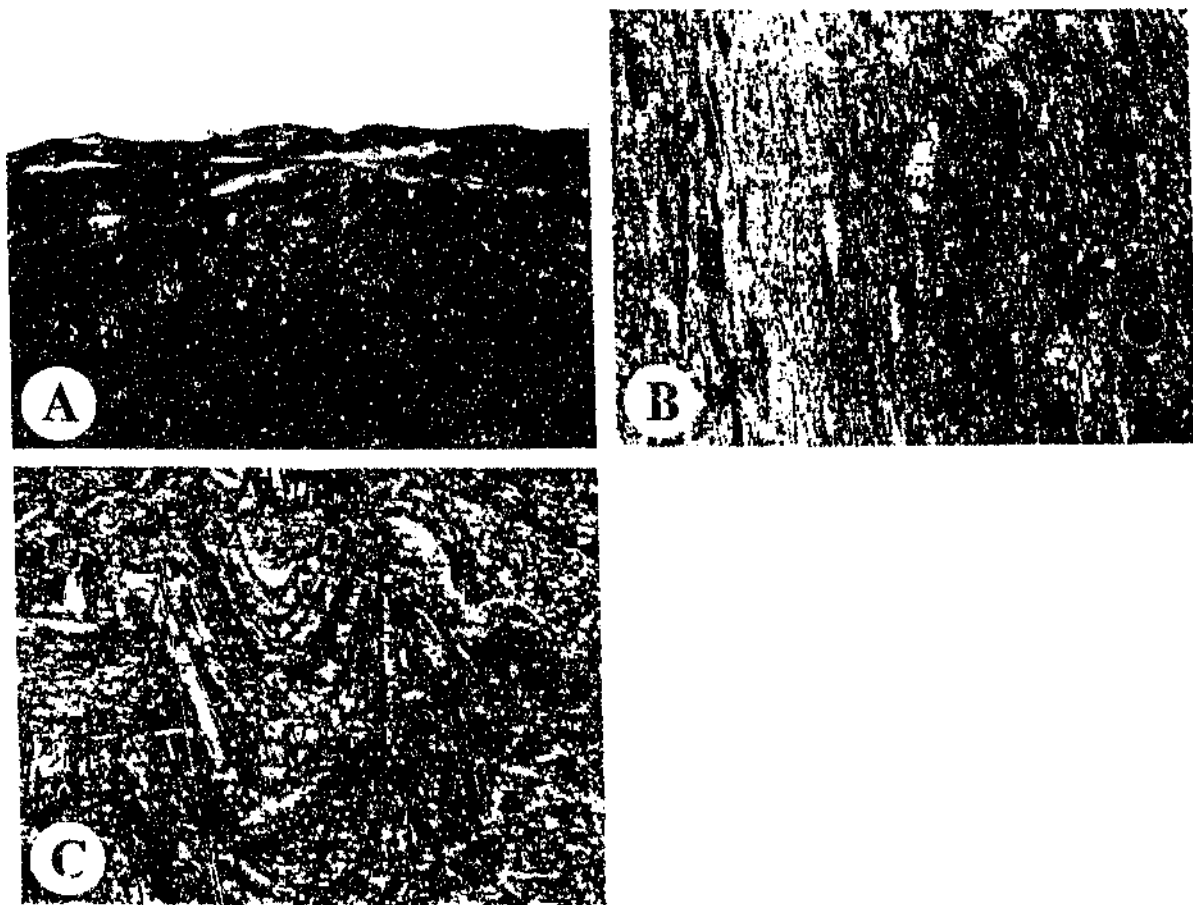


Figure 9.4 Structural features of the Lily East Syncline:

(A) The upright, near-isoclinal Lily East Syncline as seen looking south from the middle of the Three Sisters peaks.

(B) S_m cleavage (oriented perpendicular to the plane of the photograph) defined by strongly flattened chert clasts in conglomerate (Louieville 325 JU). Lens cap is 4.9 cm in diameter.

(C) Tight, upright synform - antiform pair in argillite (Holnekt 331 JU). Note the S_m axial planar slaty cleavage (dashed line). Hammer is 30 cm long.

9.2.1.1.6 Three Sisters Syncline

Rocks in the immediate vicinity of Three Sisters occupy a complex, mainly east-northeast-trending F_m structure that has been modified by faulting and refolding (Figure 1.4). Although this fold appears on the map of Visser *et al.* (1956), these workers were unable to verify its geometry or attitude; however, a regional cross-section shows it to be a synform. Subsequent investigations by geologists of Anglo American Prospecting Services (Pty) Ltd. led these workers to conclude that the fold is an antiformal anticline (C. Harrison, pers. comm., 1991). According to this interpretation, rudaceous rocks coring the fold constitute the oldest strata, stratigraphically underlying silicic metavolcanic rocks outcropping to the north and west. This is clearly at variance with the stratigraphy of the study area as outlined in the preceding chapters of this thesis, as well as the Barberton Supergroup as a whole (Section 2.3).

On the basis of the detailed lithostratigraphic and structural mapping carried out during the course of the present investigation, the writer is inclined to the view that the fold is an upward-facing synform. Conglomerates coring the synform have been correlated with the Moodies Group (Section 7.1) and rest on silicic metavolcanic rocks assigned to the Bien Venue Formation which, in turn, overlies lithologies of the Belvue Road Formation (Section 4.1). It should, however, be stated that the above interpretation is based solely on the regional distribution of lithostratigraphic units; the writer was not able to locate any unambiguous younging indicators based on primary structures. It is also clear from the above that the position of the axial trace of the syncline as shown in Figure 1.4 is largely interpretative.

Due to refolding during the D_4 episode, the western part of the Three Sisters Syncline trends at an angle to main mass of the fold. Penetrative S_4 cleavages associated with this refolding event have generally obliterated S_p in the metasedimentary and metavolcanic rocks, thus precluding determination of the geometry of the syncline in most areas. Stereographic analysis of bedding data collected in the relatively undeformed

parts of the fold north-northeast of the Three Sisters Mine (Figure 1.4, G6) indicates, however, that the syncline plunges at 60° towards the south-southeast, and that it is tight with an axial surface which is inclined at $\sim 70^\circ$ to the southeast. Hence, it appears that the southern limb is overturned. The presence of S_m cleavages such as those recorded in other F_m structures close to the northern flank of the BGB could not be verified due to pronounced overprinting by S_d .

In its western and central parts, the Three Sisters Syncline is bounded in the south by the Revolver Fault (Section 9.2.1.2.11) which, from west to east, progressively truncates and eventually eliminates silicic metavolcanic rocks along the southern limb. Another major fault, referred to as the Adamanda Fault (Section 9.2.1.2.13), displaces the eastern part of the fold in a dextral sense (Figure 1.4, G6). East of the latter, the Three Sisters Syncline is terminated on its southern side by the Ardonachi Fault (Section 9.2.1.2.14).

9.2.1.1.7 American Syncline

This syncline extends from a position just west of the Great American Gold Mine (Figure 1.4, F6) in a northeasterly direction for ~ 3 km. To the north and west of the mine, the position of the fold is marked in the field by a thin, southward tapering band of metamorphosed polymict conglomerate of the Moodies Group. The conglomerates rest on silicic schists of the Bien Venue Formation outcropping in the fold limbs. Younging directions preserved in sedimentary structures confirm the synclinal disposition of the strata. Bedding and cleavage in the sedimentary rocks are coincident and dip persistently south-southeastward at $65 - 80^\circ$, subparallel to foliations in the adjacent silicic schists (Figure 9.2H). Analysis of the structural data indicates that the fold has an interlimb angle of 15° and that the hingeline plunges at 70° to the east-southeast. The axial surface dips steeply at 70° to the south-southeast. At its northern end, where the Moodies strata attain their fullest outcrop width, the American Syncline is bounded on the eastern side by the American Fault (Section 9.2.1.2.1). This structure

cuts across the strike of the sedimentary rocks and the axial trace, progressively truncating the eastern and western limbs.

It is considered likely that the American Syncline represents a continuation of the Three Sisters Syncline (Section 9.2.1.1.6), although this could not be verified.

9.2.1.1.8 Louieville Antiform

Lithologies of the Theespruit Formation south of the Lily West Syncline have been deformed into an east-trending, near-isoclinal fold which is clearly outlined on aerial photographs by two converging ridges consisting of silicified quartz-muscovite schist with minor chert and argillite (Figure 1.4; Section 3.5). Mapping by Visser *et al.* (1956) and Anhaeusser (1963) indicated that while the ridges merge just beyond the western boundary of the region shown in Figure 1.4, the silicic marker unit is traceable sporadically as far as Eureka Siding, ~11 km due west of Louw's Creek. Towards the east, the ridges are truncated by the Louieville Fault (Figure 1.4, I3).

S_p in the silicic schists and associated argillaceous and cherty metasedimentary rocks dips at moderate-to-steep angles ($65 - 75^\circ$) south-southeastward (Figure 9.2I). The plunge of the fold is difficult to determine owing to the similar orientations of both limbs, but appears to be at shallow angles to the west, which, coupled with the presence of the fold hinge also in the west, indicates that the structure is an antiform. All rocks display a well-developed, steep south-southeasterly dipping S_m schistosity which is subparallel to the folds axial surface (Figure 9.2I). This fabric is locally accompanied by a down-dip L_m mineral elongation lineation.

9.2.1.1.9 Strathmore Anticline

Rock distributions in the southern sector of Strathmore 214 JU suggest the presence of a large, easterly trending anticline which is terminated in the east and west by faults, so that no fold closure can be identified on surface (Figure 1.4). The central

parts of this fold are underlain by basic schist and metagabbro of the Onverwacht Group, along with minor argillite and BIF correlated with the Belvue Road Formation. Schistose metavolcanic assemblages of the Bien Venue Formation crop out to the north and south of prominent grey and white banded chert marker units outlining the flanks of the fold. Primary layering in the argillaceous and cherty rocks is generally near-vertical or dips steeply towards the north (Figure 9.2J), and it is not possible to establish the direction and amount of plunge of the fold axis, or whether the fold is a synform or an antiform. The southern chert band outcrops discontinuously, and appears to be in tectonic contact with the adjacent metagabbroic rocks and BIF. This band is locally also displaced along small-scale B_f faults (Figure 1.4, D7 and E7). A variably developed, subvertical S_m foliation in the schists and argillites is generally subparallel to bedding and the axial surface (Figure 9.2J). Steep northeasterly to east-northeasterly plunging L_m mineral elongation lineations were recorded in places, but are most common in outcrops in the central and eastern parts of the fold.

9.2.1.1.10 Koedoe Anticline

The limbs of this large isoclinal fold, which straddles the boundary between Stentor 219 JU and Koedoe 218 JU, are defined by positively weathering argillaceous BIF of the Belvue Road Formation (Figure 1.4). The BIF is markedly thickened in the fold hinge, which lies in the east. Vertical limb attitudes (Figure 9.2K), combined with poor exposures and extensive slumping of outcrops in the hinge zone, however, make it impossible to conclusively establish the plunge of the fold and, hence, whether the structure is synformally or antiformally disposed. Furthermore, owing to the absence of sedimentary younging indicators, it could not be established with certainty whether the fold is upward or downward facing. Basic and silicic schists occupying the fold core have been correlated by the writer with the Onverwacht Group (Section 3.1), and if this is correct, then the fold appears to be an anticline. S_m foliations in the above-mentioned schists and adjacent argillites strike east-northeasterly and dip subvertically, subparallel

to the folds axial surface (Figure 9.2K). A subvertical L_m mineral lineation, defined by acicular actinolite crystals and chlorite aggregates, is locally developed on S_m . At its western end, in the north-central part of Stentor 219 JU, the fold is truncated by the north-trending B_f Strathmore Fault (Figure 1.4, E8).

Mesoscale, tight-to-isoclinal, upright folds with axes that typically plunge steeply towards the east, are sporadically developed within the BIF and adjacent argillites. These folds occasionally display 'Z'- (northern limb) or 'S' (southern limb) asymmetry when viewed in profile, and are characterised by a subvertical axial planar cleavage which is parallel to the S_m foliations recorded in the main fold. These observations suggest that the minor folds are related to the main structure. If this is correct, then according to Pumpelly's Rule (Pumpelly *et al.*, 1894), the plunge of the minor folds reflects that of the major structure, indicating the Koedoe Anticline is an antiform. A steeply plunging L_m intersection lineation (S_m / S_p) occurs parallel to the axes of the minor folds. Onverwacht Group silicic metavolcanic rocks outcropping in the central part of the anticline are deformed by symmetrical M-type folds (Figure 1.4, D9).

9.2.1.1.11 Koedoe and Scotsman Blocks

To the south of the Koedoe Anticline is a southward-younging block of Moodies rocks consisting of quartzite with lesser conglomerate (Figure 1.4). This block will be referred to hereafter as the Koedoe Block. The Moodies rocks are underlain in the north by shales and BIF, but terminate in the south against the east-striking Koedoe Fault (Section 9.2.1.2.4). Bedding in the quartzites strikes northeasterly and dips persistently towards the southeast at 65 - 80° (Figure 9.5A). S_m cleavages, which are well-developed throughout the succession, normally occur parallel to S_p , but locally transect the bedding at low angles (Figure 9.5A); on Koedoe 218 JU, S_m obliterates S_p . Chert clasts found in thin, inconsistent conglomerate lenses sporadically intercalated with the sheared quartzites in this area are strongly flattened and preferentially oriented with their short axes perpendicular to S_m .

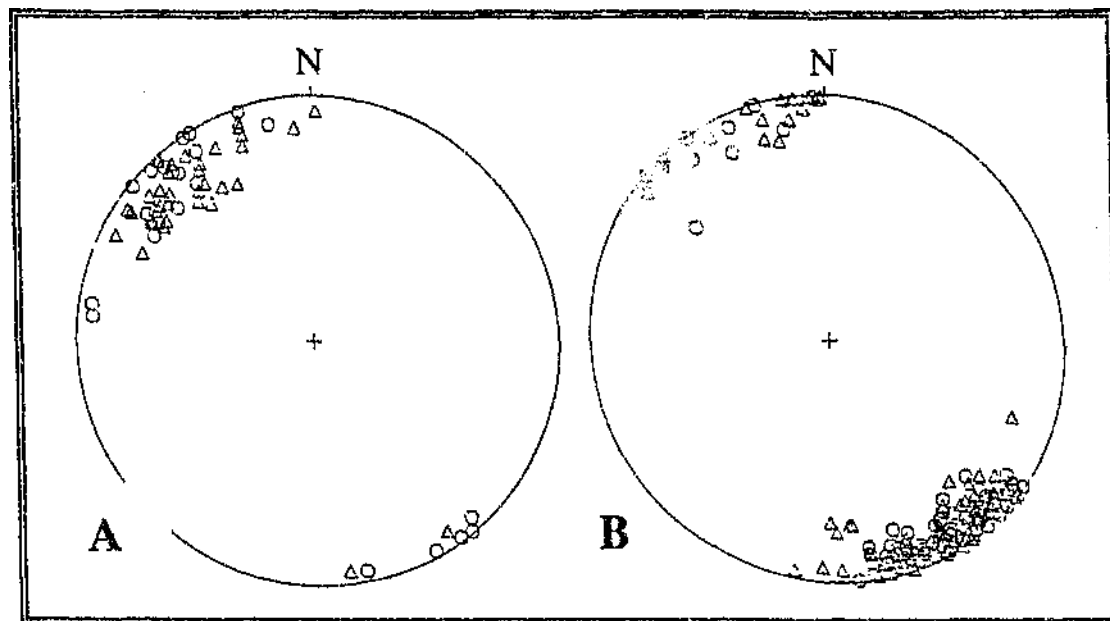


Figure 9.5 Lower hemisphere equal area projections summarizing structural data for the Koedoe and Scotsman Blocks (poles to S_p - triangles; poles to S_m - circles):

(A) Koedoe Block (S_p - $n = 35$; S_m - $n = 25$).

(B) Scotsman Block (S_p - $n = 69$; S_m - $n = 94$).

A second, east-northeast-trending and southward-younging package of quartzites and conglomerates, stratigraphically underlain in the north by argillite and BIF, occurs at the Scotsman trigonometrical beacon, situated at the junction of Scotsman 258 JU, Stentor 219 JU and Amo 259 JU (Figure 1.4, F8). This block, which will be referred to hereafter as the Scotsman Block, extends across and beyond the eastern part of the area shown in Figure 1.4, and is separated from rocks within the Three Sisters Syncline to the west by a poorly exposed, minor, northwest-striking fault (Figure 1.4, F7 and F8). To the north and south, the succession is bounded by the Koedoe and Ardonachi Faults (Sections 9.2.1.2.4 and 9.2.1.2.14). Rocks in the immediate vicinity of the Scotsman beacon are relatively undeformed, except where they abut against the Koedoe and Ardonachi Faults. S_p in this area strikes approximately east-northeast and generally dips steeply to the north - i.e. bedding is overturned (Figure 9.5B). Further

east, the rocks display a pervasive subvertical cleavage which mostly overprints S_1 (Figure 9.5B). Nonetheless, layering in BIF units to the north indicates that in this region, the sequence also dips steeply to the north.

Stratigraphic-structural relationships suggest that two southward-younging successions outlined above once formed the northern limbs of regional-scale synclines, the axes and southern limbs of which have been removed by faulting.

9.2.1.2 $B_{main} - B_m$

Field mapping has identified sixteen major B_m faults (Figure 9.1), two of which (Overton and Revolver Faults) affect and, hence, post-date the granitoid rocks of the Stentor pluton. The faults are mainly indicated in the field by: (1) the elimination, duplication or abrupt termination of strata; (2) younging inconsistencies at both the map and outcrop scale; (3) the presence of fault breccia, cataclasite and mylonite; and / or (4) the presence of abundant quartz veining and, in some cases, intense silicification-carbonatization of rocks adjacent to the fault.

9.2.1.2.1 American Fault

The American Fault marks the eastern boundary of the American Syncline, extending from the east-central part of Bien Venue 255 JU to the southern part of Strathmore 214 JU, a distance of some 3 km (Figure 1.4; Section 9.2.1.1.7). Slates and BIF's of the Belvue Road Formation crop out to the east of the fault. The workings of the Great American Mine (Figure 1.4, F6) are situated within this assemblage, and were apparently dug to exploit auriferous quartz veins found in subsidiary shears and fractures within the BIF or along the BIF/slate contact (Groeneveld, 1973). A road cutting across the fault in the mine area reveals a complex zone of imbrication which has resulted in

the duplication of banded cherty rocks at the base of the Bien Venue Formation exposed to the west. This zone has a width of ~50 m and consists of four main tectonic slices, composed either of sheared and brecciated chert or BIF / shale. Faults bounding these slices strike east-northeast and dip south-southeastward at 60 - 75°.

Immediately northeast of the mine, the American Fault has largely eliminated the chert marker horizon, so that the silicic schists of Bien Venue Formation abut directly against the argillites; however, fault-bounded lenses of recrystallized chert occur in places. One such chert lens, situated along the Bien Venue 255 JU / Stentor 219 JU boundary, displays numerous striae, manifest as prominent corrugations on moderately southeastward-dipping shear surfaces. These linear structures, some of which are up to 6 cm wide, plunge eastward at ~60°.

Proceeding northwards, the American Fault cuts across Moodies Group rocks coring the American Syncline (Section 9.2.1.1.7). Conglomerates and quartzites adjacent to the fault zone in this area display a prominent, northeasterly striking S_m shear cleavage that dips steeply southeastwards. Continuing to the north, the American Fault follows a north-northwesterly strike, truncating rocks along the western limb of the American Syncline, before finally running into area of poor exposure. Shear cleavages in exploration pit exposures of the fault plane close to its northern extremity consistently dip to the east-northeast at 50 - 65°, and are accompanied by down-dip striations.

The present-day northeasterly to north-northwesterly trend of the American Fault (and also the American Syncline) is due to reorientation by the F_4 Stentor Antiform - Bien Venue Synform pair (Sections 9.2.2.1 and 9.2.2.2). Restoration of the fault to its pre- D_4 position indicates that it originally had an east-northeasterly strike.

9.2.1.2.2 Barite Fault

Stratigraphic-structural relationships suggest the presence of another major B_m structure, referred to as the Barite Fault, immediately east of the American Fault (Figure 1.4). This fault is folded on a broad scale by the Bien Venue Synform (F_a ; Section 9.2.2.2) and separates lithologies of the Bien Venue Formation to the east and north from rocks of the Belvue Road Formation to the west and south. Evidence of shearing associated with the fault is scant owing to poor outcrop and pronounced overprinting by S_d . However, a prominent, ~20 - 40 m wide, but discontinuous band of variably sheared silicic metavolcaniclastic rocks, bounded on all sides by shales of the Belvue Road Formation, crops out along the western boundary of Stentor 219 JU (Figure 1.4, E6, E7 and F6). This unit, which has also been subjected to F_d folding, is believed to form part of the Bien Venue Formation, and is interpreted as a fault sliver associated with the Barite Fault. At its eastern end, the Barite Fault is truncated by the B_r Strathmore Fault (Figure 1.4, E7).

9.2.1.2.3 Southern Fault

This poorly exposed, steeply southward-dipping fault extends along the southern margin of the Lily West Syncline, placing arenites within the latter against basic schists along the northern limb of the Louieville Antiform (Figure 1.4; Sections 9.2.1.1.5 and 9.2.1.1.8). Although it is only traceable for a distance of ~2.5 km in the area presently under review, mapping by Anhaeusser (1963, 1969) and Viljoen (1963) indicated that this structure, referred to by these workers as the Main Southern and Kaap River Fault, can be traced for at least 20 km beyond the western limit of Figure 1.4. At its eastern extremity, it is cut off by the Louieville Fault (Figure 1.4, I3).

Quartzitic rocks adjacent to the Southern Fault show a well-developed S_m cleavage that dips south-southeasterly at ~70°. The cleavage is defined in thin section by parallel domains of flattened quartz grains alternating with fine-grained aggregates

and laths of white mica. The quartz grains exhibit undulose extinction, stress twinning, pressure solution and peripheral quartz-infilled pressure shadows. In some outcrops, thin (a few millimetres wide) quartz extension veinlets are seen to be parallel to the foliation planes. A thin (~1 - 3 m wide) unit of carbonaceous chert crops out sporadically along the fault near its eastern end.

9.2.1.2.4 Koedoe Fault

The Koedoe Fault extends in a east-northeasterly direction from the central part of Stentor 219 JU, across the northern part of Amo 259 JU, onto Koedoe 218 JU where exposures are lost under deep soil cover (Figure 1.4). At its western end, the fault separates Moodies Group quartzites and conglomerates within the Koedoe Block, which forms the footwall to the fault (Section 9.2.1.1.11), from silicic metavolcanic lithologies of the Bien Venue Formation (Figure 1.4, F7). Fault rocks in this general area are locally strongly silicified and display a pervasive S_m cleavage that dips southeasterly at 65 - 75°. Further east, the hangingwall is composed mainly of shale and greywacke of the Belvue Road Formation. Metre-scale fault-bounded pods of what has been interpreted as intensely deformed BIF occur in places along the fault zone. These pods consist of angular fragments of white chert set in a strongly sheared ferruginous matrix (Figure 9.6A), and presumably once formed part of a prominent BIF which is truncated along the southeastern boundary of Stentor 219 JU (Figure 1.4, E9). A road cutting across the fault zone in this area exposes this BIF unit where it is juxtaposed against strongly crushed, southward-younging quartzites. The fault plane is clearly visible and dips at 45° towards the southeast. Minor folds in the BIF tend to have subhorizontal axial surfaces, with axes that plunge at shallow angles (25 - 40°) to the east and northeast. The quartzites display a well-developed grain-shape S_m foliation that strikes northeasterly with steep northwesterly and southeasterly dips (Figure 9.6B). The cleavage is locally deformed by small, kink-like folds with moderate-to-steep southwesterly plunging axes

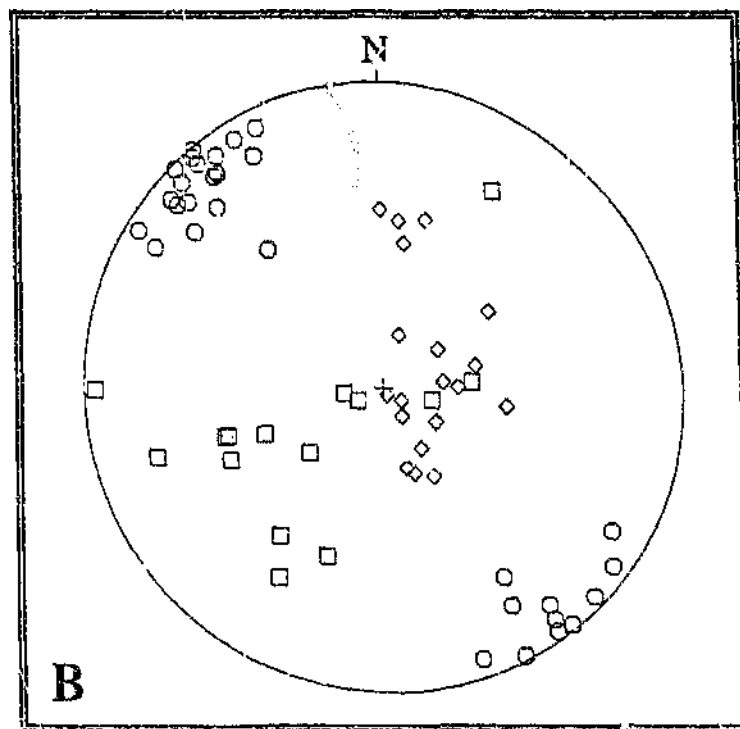


Figure 9.6 Structural features of rocks outcropping along the Koedoe Fault:

(A) Brecciated BIF pod (Amo 259 JU). Lens cap is 4.9 cm across.

(B) Lower hemisphere equal area projection of poles to S_m (circles; $n = 32$), L_m stretching lineations (diamonds; $n = 19$) and axes of minor folds deforming S_m (squares; $n = 15$).

(Figure 9.6B). Steeply dipping smoky quartz veins, some of which extend along strike for 2 - 3 m, transect the cleavage at low angles. The long axes of deformed pebbles in conglomerate beds sporadically interlayered with the quartzites define generally upright to steeply plunging stretching lineations (Figure 9.6B).

Immediately east of the road cutting, the fault trace bends to the north for a distance of ~300 m, cutting across strata within the Koedoe Block (Figure 1.4, E9). At its eastern mapped extremity, the fault once again trends east-northeasterly, subconcordant to bedding in the arenites and argillites. S_m cleavages measured along the fault in this area typically dip steeply ($70 - 80^\circ$) to the southeast or south-southeast.

9.2.1.2.5 Igwalagwala Fault

This poorly exposed, subvertical fault extends east-northeastwards from the border between Three Sisters 256 JU and Ardonachi 257 JU along the northern contact of Moodies strata within the Lily East Syncline (Figure 1.4; Section 9.2.1.1.5). The fault zone is best exposed in road cuttings between the Scotsman and Morning Mist Mines (Figure 1.4, G8 and E10). Cataclasites in this area are characterised by a prominent S_m cleavage that strikes northeasterly with steep ($75 - 90^\circ$) southeasterly and northwesterly dips. Subvertical striations are present in some outcrops. Smoky quartz veins are locally common.

In the area east of the Morning Mist mine, where it is dextrally displaced by about 600 m by the B_r Amo Fault (Figure 1.4, E10), the Igwalagwala Fault follows the contact between the northward-younging Moodies rocks making up the truncated southern limb of the Amo Syncline (Section 9.2.1.1.3), and argillaceous and talcose phyllites of the lower Fig Tree Group to the north. The latter rocks are intruded by a massive quartz-feldspar porphyry (Figure 1.4, E11; Section 8.5). The fault can be traced as far east as the boundary between Amo 259 JU and Sherlock 461 JU, where its position is delineated by outcrops of strongly sheared, fuchsitic chlorite-talc-carbonate

schist. These rocks contain veins and blebs of quartz and chert, as well as fine disseminations and patches of powdery limonite / stibiconite. The S_m foliation in the schists has a subvertical, northeasterly-striking attitude, and is locally accompanied by an oblique to down-dip L_m mineral lineation.

9.2.1.2.6 Mac Mac Fault

The Mac Mac Fault extends from Mac Mac 264 JU as far east as Amo 259 JU, following the southern contact of Moodie Group rocks coring the Lily East Syncline (Figure 1.4; Section 9.2.1.1.5). Along the western boundary of Scotsman 258 JU (at sample sites G1 - 3 in Figure 1.4, G7 and G8), the position of the fault is marked by a conspicuous, 2 - 20 m wide and ~700 m long, east-northeast-striking unit consisting of an enigmatic, extremely hard, chert-like lithology. These rocks are generally massive and weather to a light- to dark-brown colour; fresh surfaces are greenish-grey or pale yellow. Fine-grained crystals and crystalline masses of secondary sulphide (mainly pyrite) are sporadically developed within the rocks, particularly where they are traversed by thin (up to a few millimetres wide), irregular quartz veinlets. In some exposures, the rocks are characterised by a subvertical, east-northeast-striking banding consisting of alternating white and brown layers or lenticular domains (Figure 9.7). Brecciation is locally evident.



Figure 9.7 Strongly sheared and banded appearance of quartz-carbonate rock outcropping along the Mac Mac Fault (Scotsman 258 JU). Lens cap is 4.9 cm in diameter.

Thin section analysis of a sample collected near the eastern end of this unit (sample site G1 in Figure 1.4, G8) revealed fine-grained aggregates of recrystallized quartz (~80 % by volume) and a carbonate phase (~20 % by volume), the latter subsequently identified by a combination of XRD analysis and XRF scanning as gaspeite¹². Quantitative chemical analysis indicated that the sample (G1A) contains ~7700 ppm Ni (Table 9.2). This high value prompted the writer to collect a further 9 specimens along three traverses across the cherty unit in its eastern, central and extreme western parts. Additional samples from outcrops in the immediate vicinity of the original sample consist mainly of quartz with minor chlorite, chloritoid, mica and gaspeite, and contain between 1500 - 2200 ppm Ni. Ni concentrations in specimens from the remaining two traverses (sample sites G2 and G3 in Figure 1.4, G7 and G8) are, however, much lower, ranging from 100 - 1000 ppm with an average of 430 ppm (Table 9.2).

Table 9.2 Trace element analyses of samples of an enigmatic chert ± carbonate lithology outcropping along the Mac Mac Fault on Scotsman 258 JU

Sample	Ni (ppm)	Zn (ppm)	Cu (ppm)	Co (ppm)
G1A	7679	40	8	66
B	1464	42	18	139
C	1636	31	18	92
D	2249	48	24	147
G2A	1009	29	13	59
B	162	24	13	16
C	235	27	18	32
G3A	111	23	13	17
B	515	22	12	19
C	540	87	51	40

Continuing to the east, good exposures of the Mac Mac Fault occur along several forestry road cuttings on Amo 259 JU. S_m cleavages within the fault zone always dip steeply (~75 - 85°) to the south or southeast, subparallel to bedding where this is

¹² (Ni, Mg, Fe)CO₃

discernable in the adjacent pelitic and arenaceous rocks. No well-developed linear fabric was noted. In the central part of Amo 259 JU, the fault juxtaposes Moodies strata within the Lily East Syncline against argillites and arenites within the Amo Syncline to the south (Sections 9.2.1.1.5 and 9.2.1.1.3). The exact position of the fault east of the junction of these two synclines could not be determined owing to a lack of exposure, although it seems likely that it merges with the Igwalagwala Fault to the north, obliquely truncating the Lily East Syncline.

9.2.1.2.7 Barbrook Fault

The regionally traceable, southerly dipping Barbrook Fault enters the study area in the central part of Fourieskraal 267 JU, and continues in a east-northeasterly direction across Singerton 260 JU, Rusoord 261 JU and Kaalrug 465 JU (Figure 1.4). The extent of the fault east of Figure 1.4 could not be ascertained due to inadequate exposure. West of the map area, the fault extends as far as the town of Barberton (Visser *et al.*, 1956; Anhaeusser, 1976b), and hosts numerous gold deposits which have been described by Groeneveld (1973) and Houstoun (1987).

As previously mentioned, the Barbrook Fault marks the northern limit of the Hlambanyathi Syncline, separating Moodies Group rocks within the latter from ferruginous metagreywacke-shale assemblages of the Sheba Formation to the north (Sections 9.2.1.1.1, 9.2.1.1.2 and 9.2.1.1.3). Rocks on either side of the fault are strongly sheared and mylonitized, and exhibit a penetrative S_m foliation with steep north-northwesterly and south-southeasterly dips. Width of the zone of shearing locally exceeds 300 m. The intensity of fabric development decreases towards the east. Displacement of foliation planes by small-scale, shallowly southward-dipping curvi-planar fractures exposed in exploration trenches on Singerton 260 JU suggests a south-side-up movement sense.

Lenticular horizons of grey and white banded chert and BIF crop out in places along the fault zone (Figure 1.4, G11 and F13). These units lie subparallel to the regional trend of the fault, but are seldom traceable for more than ~1 km along strike. Only the main chert units are shown in Figure 1.4. Most of the cherts and BIF's have been subjected to varying degrees of shearing and tectonic brecciation. At one locality ~800 m east of the Amo Fault, which displaces the Barbrook Fault in a dextral sense on Singerton 260 JU (Figure 1.4, G10), thin (~1 - 10 m wide) fault-bounded slivers of BIF and argillite occur structurally interleaved with quartzite, forming a complex, ~200 m wide zone of fault imbrication. The slivers are aligned parallel to the fault foliation and are bounded by steep, southward-dipping faults. Impersistent bands of variably carbonatized quartz \pm talc \pm chlorite \pm muscovite-fuchsite schist also crop out sporadically, but are less common than the chert units. In some exposures, the schists are seen to enclose small lozenge-shaped pods of fuchsitic chert, BIF and brecciated quartzite.

9.2.1.2.8 Inyoka Fault

This subvertical, northeast-striking fault defines the southeastern boundary of Figure 1.4. In the field, the position of the fault is marked by a broad (> 200 m wide), but poorly exposed, zone of strongly sheared and brecciated micaceous quartzites fringing the southern margin of the Hlambanyathi Syncline (Section 9.2.1.1.2). The sheared quartzites are characterised by a well-developed S_m cleavage which dips steeply to both the south-southeast and to the north-northwest. In places, the S_m fabric anastomoses around laterally discontinuous, but concordant, pods of less deformed quartzite.

Cinnabar mineralization occurs at several localities along the Inyoka Fault on Rusoord 261 JU and Kaalrug 465 JU (Groeneveld, 1973). At the long-defunct Kaalrug Mine, situated in the extreme southeastern corner of the study area (Figure 1.4, F15), the fault rocks are extensively brecciated and cross-cut by numerous irregular-to-lenticular quartz veinlets. Pyrite and cinnabar occur within some of these veins, but are

more common as fine disseminations within the host rocks (Groeneveld, 1973). The breccias typically consist of angular fragments of quartzite in a crushed matrix, but locally the matrix is composed of quartz and even cinnabar.

9.2.1.2.9 Overton Fault

The southeasterly dipping Overton Fault separates the Stentor pluton from the Nelspruit Migmatite and Gneiss Terrane, and is best exposed over a strike length of ~2 km in the area of the Overton Gold Mine (Figure 8.2; Section 8.3.1). Here, the position of the fault is defined on surface by a broad (> 500 m wide), east-northeast-trending zone of very fine-grained, mica-rich protomylonite, mylonite and ultramylonite. These rocks are characterised by a well-developed S_m foliation dipping shallowly (20 - 35°) southeastward (Figure 9.8A and B). In some exposures, the mylonites exhibit a distinct millimetre-wide compositional banding, consisting of layers alternately rich and poor in biotite, which parallels the mylonitic foliation. Angular and ellipsoidal feldspar porphyroclasts are locally conspicuous. Accompanying the planar fabrics is a penetrative L_m mineral lineation, defined by the preferred orientation of quartz and biotite crystals / aggregates, which is consistently down-dip (Figure 9.8A). Fibrous quartz slickenside lineations, with identical attitudes to the above-mentioned mineral lineations, are common in some outcrops. Kinematic indicators (mainly rotated feldspar porphyroclasts) support south-over-north movement. Discrete mylonite zones of a few metres to tens of metres width occur sporadically within the gneissic rocks north of the fault. Orientations of planar and linear fabrics within these subsidiary shears are generally comparable to those within the Overton Fault.

Exploitation of the gold mineralization at the Overton Mine was carried out during the mid 1950's, when some 1160 tons of ore yielded ~7.7 kg of gold and 14.5 kg of silver (Groeneveld, 1973). Renewed interest in the mine was shown during 1989 - 1990, when the Phelps Dodge Mining Ltd. undertook detailed exploration work during

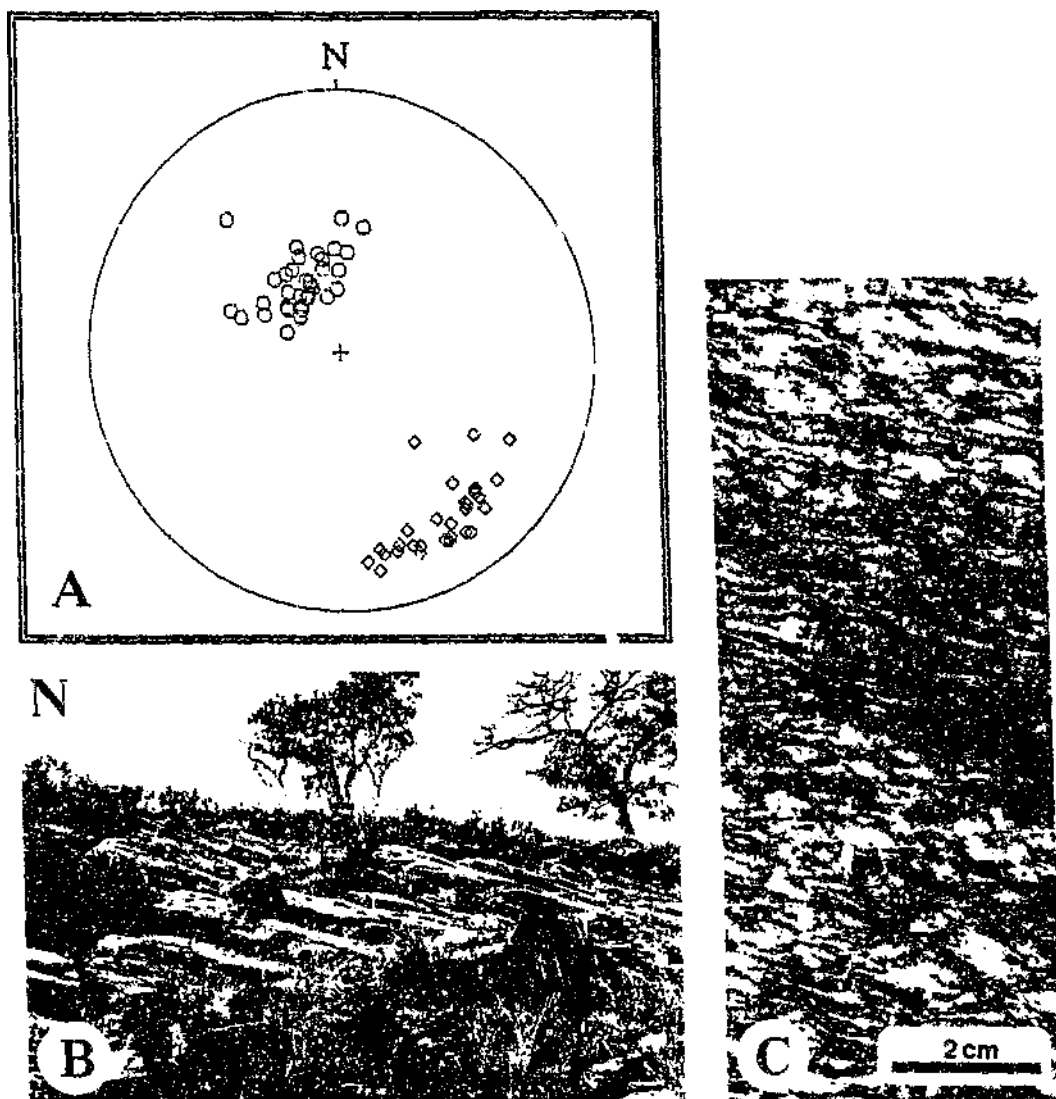


Figure 9.8 Structural features of rocks within the Overton Fault zone:

(A) Lower hemisphere equal area projections of poles to S_m (circles; $n = 36$) and L_m mineral lineations (diamonds; $n = 30$).

(B) Outcrop (~6 m wide) of mylonite (Mountain View Farm 250 JU).

(C) Augen blastomylonite showing large attenuated quartz and feldspar porphyroclasts (core courtesy of Phelps Dodge Mining Ltd.).

which four boreholes were drilled; no economic mineralization was, however, identified (C. Meyer, pers. comm., 1991). The borehole cores were made available to the writer to be incorporated in the present study.

The mineralization is localized along a single, northeast-striking band of strongly foliated, white-to-grey, often highly siliceous ultramylonite, gradationally bounded on either side by mylonite and augen blastomylonite (Figure 9.8C). This band dips southeasterly at shallow angles, and varies in thickness from ~5 - 12 m. Sulphides (mainly pyrite with minor chalcopyrite and, in places, pyrrhotite) occur throughout as fine disseminations. Much thinner (< 2 m wide) ultramylonite zones occur parallel to the main band, but do not appear to host any mineralization. On surface, the ultramylonites are weathered to highly friable rocks consisting of quartz, feldspar and kaolinite.

Abundant quartz \pm carbonate-filled tension gashes occur within the reef zone. These veinlets, which seldom exceed a few centimetres in thickness, often lie within the S_m foliation, but clearly cross-cut it in places. Thicker veins of clear white quartz infilling brittle fractures of variable orientation are exposed in the old mine workings and exploration trenches.

Breccia zones occur within or below the reef. These attain a maximum thickness of ~3 m and consist of angular fragments of mylonite-ultramylonite enclosed in a very fine-grained, quartzose matrix.

9.2.1.2.10 Stentor Fault

The Stentor Fault marks the northeastern boundary of the mapped area, juxtaposing metavolcanic and metasedimentary assemblages of the Fig Tree Group to the south against altered basic/ultrabasic effusive and intrusive rocks of the Komati Formation to the north (Figure 1.4). Reconnaissance mapping by the writer indicates that

the fault extends for at least 5 km beyond the eastern limit of Figure 1.4. In the west, the Stentor Fault is probably continuous with the Overton Fault (Section 9.2.1.2.9).

The Stentor Fault was previously described by Viljoen and Viljoen (1970) as a sinistral wrench fault based on deformation patterns within the doubly folded Koedoe Layered Ultrabasic Complex (Figure 2.1) which occurs on its northern side. It is the writers opinion, however, based on evidence presented below, that the fault is a high-angle reverse fault. A strike-slip component of displacement cannot, however, be ruled out, although evidence for such movement is, with the exception of deformation in the Koedoe Complex, lacking.

At its western end, the fault trace lies in a broad valley between the topographically prominent Budd Ultrabasic Intrusion (Figure 2.1) and hills along the northern margin of the Stentor pluton. Exposures in this area are extremely poor, and evidence of shearing associated with the fault is scant. A few outcrops of highly fissile actinolite-chlorite and quartz-muscovite schist were, however, recorded in river gulleys. Thin (1 - 2 m wide), laterally impersistent bands and pods of recrystallized grey chert lie along the fault in places. One such chert band, located near the western boundary of Driehoek 221 JU, displays a moderately north-northeastward dipping cleavage which carries a strong down-dip lineation defined by elongate chert rods.

Proceeding eastwards onto Strathmore 214 JU, the Stentor Fault cuts across the northern margin of the Strathmore Anticline, truncating the Basal Marker of the Bien Venue Formation (Figure 1.4, D6; Section 9.2.1.1.9). Further east, along the border between Strathmore 214 JU and Stentor 219 JU, the fault trace is displaced ~900 m northwards by the B₁ Strathmore Fault (Figure 1.4, C8 and D8)

On Koedoe 218 JU, The Buffalo 217 JU and Spago 460 JU, the position of the fault is delineated by series of east-northeast-trending ridges, formed by variably sheared and recrystallized chert of the Bien Venue Formation (Figure 1.4, C10 and C11). Strongly deformed, fuchsite- and talc-rich schists of the Komati Formation are exposed in exploration pits along the northern slopes of these ridges. S_m fabrics in the schists trend roughly east-northeast with steep ($70 - 85^\circ$) south-southeasterly and north-northwesterly dips.

Two main bands of chert, ranging in thickness from $\sim 10 - 60$ m, crop out on the ridges; these bands are locally accompanied by minor, laterally impersistent cherty units, most which are not shown in Figure 1.4. In the west, the rocks dip steeply to the north, but in the east, dips are subvertical or steep to the south. Several northwest- and northeast-trending cross-faults with varying displacements locally offset and brecciate the cherts. A single, relatively large (~ 4 m wide), upright, gentle antiform that plunges 45° on a 070° bearing occurs in the southern chert band on the westernmost ridge. Highly weathered silicic metavolcaniclastic rocks crop out between, and to the north and south of, the chert bands. S_m foliations in these rocks are heterogeneously developed such that relic feldspar crystals can still be observed in some outcrops. Thin lenses of basic and ultrabasic schist, and minor carbonaceous argillite, occur interlayered with the silicic schists in places. S_m foliations in the schists and argillites trend subparallel to the cherts and typically dip steeply ($75 - 85^\circ$) to the north or south. Highly fissile fuchsitic schists are locally exposed along some of the chert contacts; L_m mineral lineations, where developed, typically plunge steeply within the subvertical foliation. All lithologies are traversed by small quartz \pm carbonate veins. The chert bands are interpreted as a single unit which has been duplicated by subsidiary faulting in an imbricate structure associated with the Stentor Fault.

Eastwards of the imbricate, the fault trace is largely obscured by colluvium and soil. Near the eastern boundary of Malelane 389 JU, the Stentor Fault is sinistrally offset by a northeasterly-trending B_f fault that appears to die out under Spago Dam (Figure 1.4, B13).

9.2.1.2.11 Revolver Fault

The Revolver Fault extends along the northwestern margin of the BGB, but cuts into the greenstone succession immediately north of Louw's Creek (Figures 1.4 and 8.2). West of Louw's Creek, the fault manifests itself as a broad shear zone composed of heterogeneously foliated and mylonitized granitoids. This shear zone locally has an outcrop width of over 300 m and separates undeformed components of the Nelspruit batholith from medium-grade metabasite assemblages of the Theespruit Formation (Section 3.1). Augen-textured mylonites showing large, strongly attenuated K-feldspar porphyroclasts up to ~2 cm in diameter are best developed north of the New Consort Gold Mine (Viljoen, 1963). The mylonitic S_m fabric trends subparallel to the margin of the BGB and generally dips southward at 40 - 80°. In some outcrops, the foliation is seen to be deformed by small, tight-to-isoclinal folds that generally have inclined, east-trending axial surfaces, and either plunge southwest or southeast. A strong, down-dip to oblique L_m lineation defined by elongate mica aggregates, or less commonly, drawn-out feldspar porphyroclasts, accompanies the foliation in places. Amphibolites to the south of the fault are badly weathered, but display a well-developed S_m schistosity with moderate-to-steep southerly dips.

Quartz veinlets, ranging in thickness from ~1 - 100 cm, are fairly common throughout the shear zone and, in general, lie within the mylonitic foliation. Much larger quartz veins occur locally; the longest single vein structure encountered along the shear zone crops out on Lovedale 277 JU¹³ where it gives rise to a prominent, ~700 m long east-trending hill. Mapping by Anhaeusser (1963) indicated that this vein forms part of a much larger system of longitudinal veins that extend in a west-southwesterly direction for a distance of over 4 km onto Perl 278 JU.

¹³ The reader is referred to the 1:50 000 topographic map 2531CA SHEBA for the localities of the farms mentioned in the text.

The precise dip of the fault is difficult to determine in most areas due to inadequate exposure, although it is clear from the field evidence outlined above that the dip is to the south. Good outcrops in the Kaap River, which has incised a section perpendicular to the strike of the fault along the southern margin of the Stentor pluton to the northwest of Honeybird Siding (Figure 9.1), however, afford an excellent opportunity to study the fault zone in detail. This section has previously been investigated by Anhaeusser (1963) and Fripp *et al.* (1980), but was reinvestigated by the writer in order to determine relationships between the granitoids of the Stentor pluton and the adjacent supracrustal rocks.

Exposed at the Honeybird locality are several tectonically interleaved slices of granodiorite and retrogressed chlorite-epidote amphibolite. These slices collectively form a large imbricate or unroofed duplex structure. Part of this structure, extending for a distance of ~30 m upstream of the bridge crossing the Kaap River, is shown in Figure 9.9A. Four fault slices, each of which is bounded by east-northeast striking, moderately south-southeastward dipping faults (Figure 9.9B), are evident. Two of the horses (1 and 3) are composed of sheared granodiorite, in places containing abundant small, variably-shaped amphibolite schlieren and xenoliths, while the remaining two (2 and 4) consist of amphibolite. The amphibolites are intruded by strongly attenuated and boudinaged granitoid dykes. These dykes are up to ~0.5 m thick and are identical in mineralogy to granodiorites making up the Stentor pluton; they are thus considered to have been derived from the latter body. Exposures of two of the fault planes show that they contain abundant slickenside lineations that plunge at 45° on a 150° azimuth (Figure 9.9B).

S_m fabrics within the southernmost three horses (1 - 3) have the same general attitude as the faults along their margins. Foliation within block 2 is cross-cut by several of the granodiorite dykes, the thickest of which exhibits a prominent pinch-and-swell structure. These relationships indicate that the dykes and, hence, the Stentor pluton, post-date the foliation. Foliation patterns within the northernmost amphibolite horse (4)

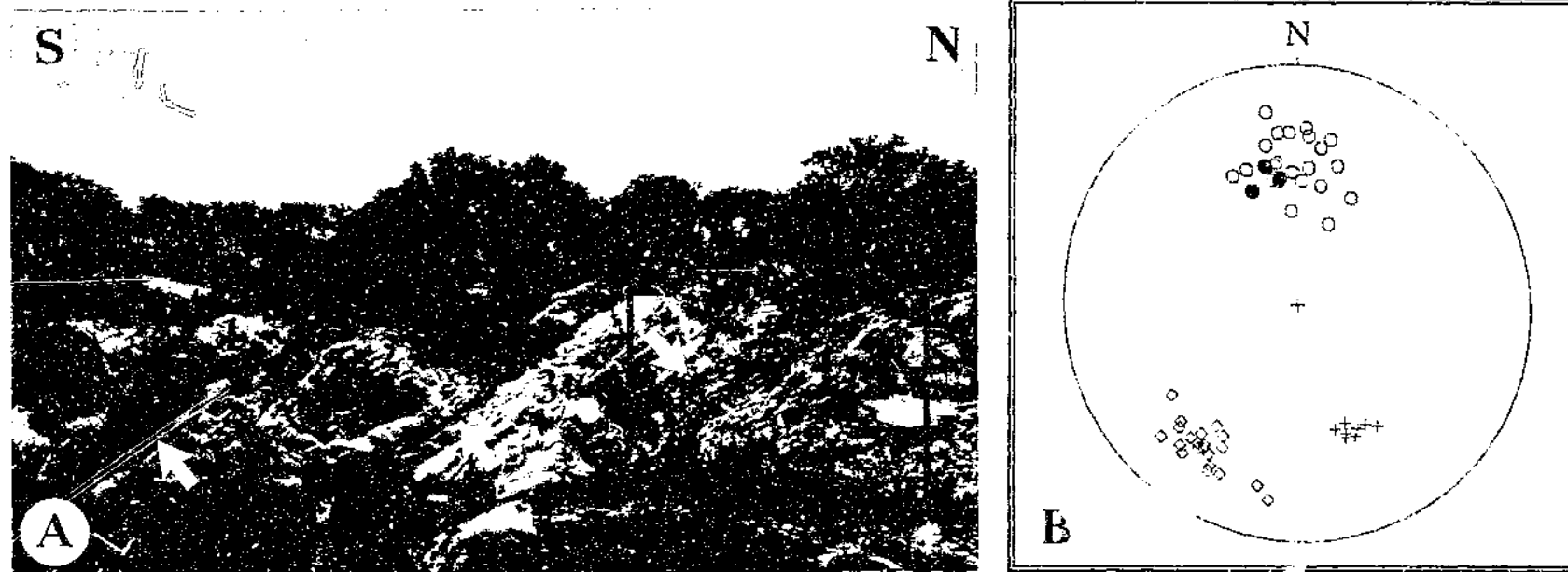


Figure 9.9 Structural features of rocks within the Revolver Fault zone:

(A) Wide-angle photograph of the imbricate structure exposed in the Kaap River near Honeybird Siding (Lovedale 277 JU). Width of the outcrop in view is ~30 m. The position of the faults is shown by the arrows. The numbers 1 - 4 refer to fault slices described in the text. The grey fault slices consist of foliated chlorite-epidote amphibolite of the Theespruit Formation, while the light coloured horses are composed of sheared granodiorite of the Stentor pluton. The outlined area is shown in greater detail in (C).

(B) Lower hemisphere equal area projections of poles to fault planes (closed circles; $n = 3$), poles to S_m (open circles; $n = 24$), L_m mineral lineations (diamonds; $n = 21$) and slickenside lineations (crosses; $n = 9$) at the Honeybird imbricate.

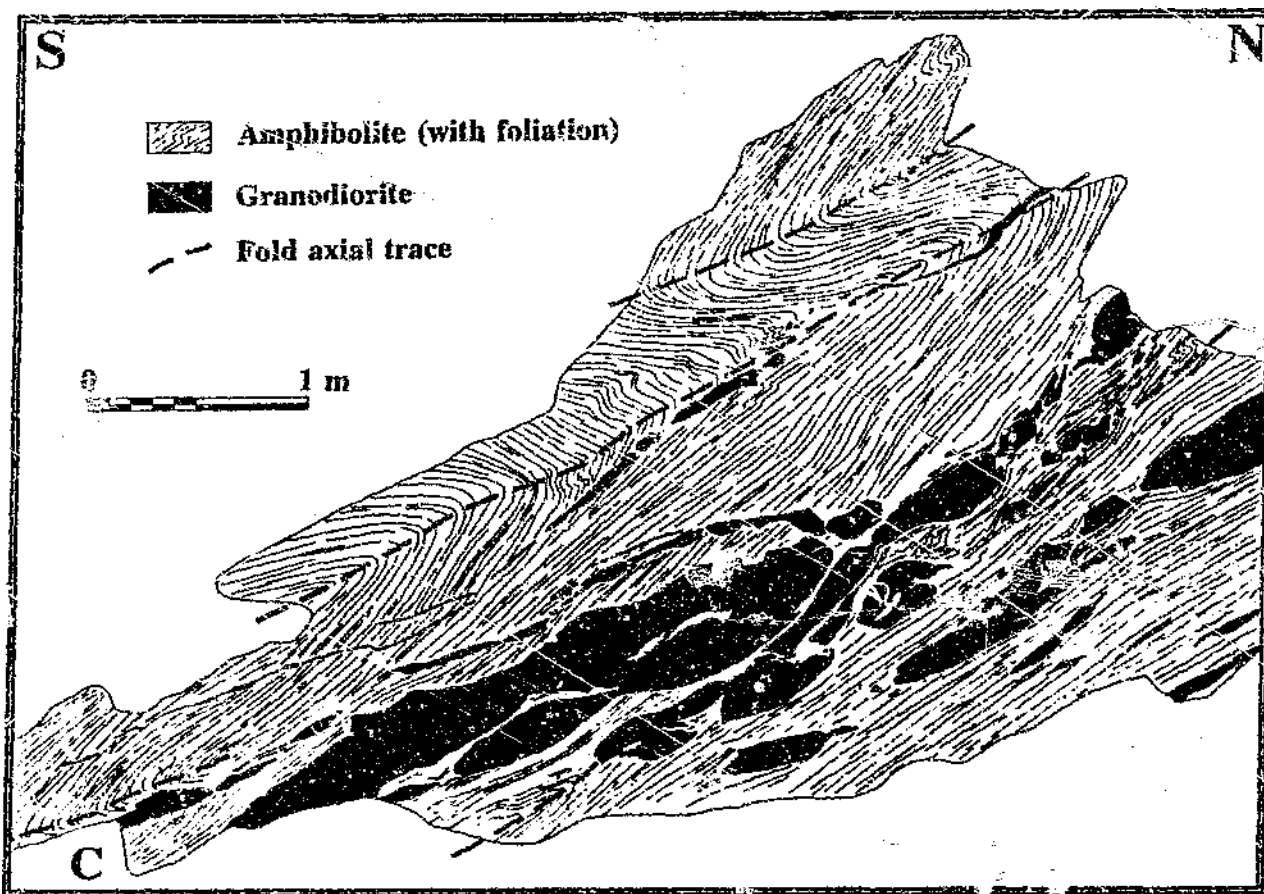


Figure 9.9 (continued): (C) Profile through the northernmost fault slice shown in (A). Note how the granodiorite dykes and boudins in the lower right hand portion of the section are generally aligned subparallel to the foliation, while those to the left in places cut across the fabric and, in the upper right hand part of the section, also the hinge zone and axial trace of the uppermost antiform.



Figure 9.9 (continued): (D) Mineral elongation lineation defined by quartz crystals in mylonitized granodiorites (Lovedale 277 JU). Coin is 2.4 cm across.

are more complex, having undergone similar folding about easterly trending, subhorizontal axes (Figure 9.9C). The folds are tight and have shallowly ($\sim 25^\circ$) southward-dipping axial surfaces. Parasitic 'Z', 'M' and 'S' folds, having amplitudes of less than a few centimetres, are evident on the limbs and in hinge zones of larger folds, and are often outlined by thin, tapering, quartz veinlets. Numerous irregularly shaped boudins and attenuated dykelets of granodiorite cross-cut the schistosity, and in one example, also the axial trace of the uppermost antiform (Figure 9.9C). Interpretation of the latter relationship indicates that the folding preceded the emplacement of the Stentor pluton, and is not related to the faulting which clearly post-dates the granitoids. Boudins elsewhere in the outcrop show a general alignment within the schistosity which is locally drawn into necked zones between the pods. No mesoscopic foliation is, however, evident in any of the boudins.

Sheared granodiorites to the north of the imbricate structure are dominated by a pervasive, but heterogeneously developed S_m foliation that strikes approximately east and dips $30 - 50^\circ$ to the south (Figure 9.9B). A strong mineral elongation lineation,

defined mainly by the parallel alignment of quartz crystals (Figure 9.9D) and biotite aggregates, accompanies the foliation and plunges south-southwesterly at 20 - 35° (Figure 9.9B). Shear lineations, manifest as prominent ridges on the foliation surfaces, also occur and exhibit identical orientations to adjacent mineral lineations.

Immediately east of Louw's Creek, the Revolver Fault separates silicic schists of the Bien Venue Formation to the north from basic/ultrabasic schists of the Theespruit Formation to the south, but is covered by soil so that its position as shown in Figure 1.4 must be regarded as approximate. It is possible that the fault is displaced southwards by the dextral Louieville Fault. Further to the east, the fault trace shows up as a prominent, densely wooded linear topographic depression along the southern margin of the Three Sisters Syncline which it truncates (Section 9.2.1.1.6; Figure 9.10). Near its eastern end, in the upper reaches of the Revolver Creek Valley, conglomerates in the footwall display a well-developed shear cleavage that dips southeasterly at 60°. It is considered likely that the Revolver Fault links up with the Koedoe Fault (Section 9.2.1.2.4) along the eastern border of Stentor 219 JU.

9.2.1.2.12 Scotsman Fault

The Scotsman Fault can be traced over a distance of ~14 km from the western border of Three Sisters 256 JU, where it is terminated by the Louieville Fault, across Ardonachi 257 JU and Scotsman 258 JU onto Amo 259 JU (Figure 1.4). Along its western extent, in the Revolver Creek Valley, the fault separates metasedimentary assemblages of the Sheba Formation in the Lily East Syncline (Section 9.2.1.1.5) from basic/ultrabasic metavolcanics of the Theespruit Formation to the north. Its position in this region is delineated by a thick (up to ~100 m wide), moderate- to steeply southward-dipping unit of grey and white chert which gives rise to a series of east-trending ridges (Figure 9.10). The cherts are locally characterised by a well-developed S_m shear cleavage which is subparallel to S_p . Fault striae, where developed, plunge steeply to the south or south-southeast. In some areas, shearing has eliminated the chert marker so that the argillites abut directly against the metavolcanics. S_e in the metavolcanics

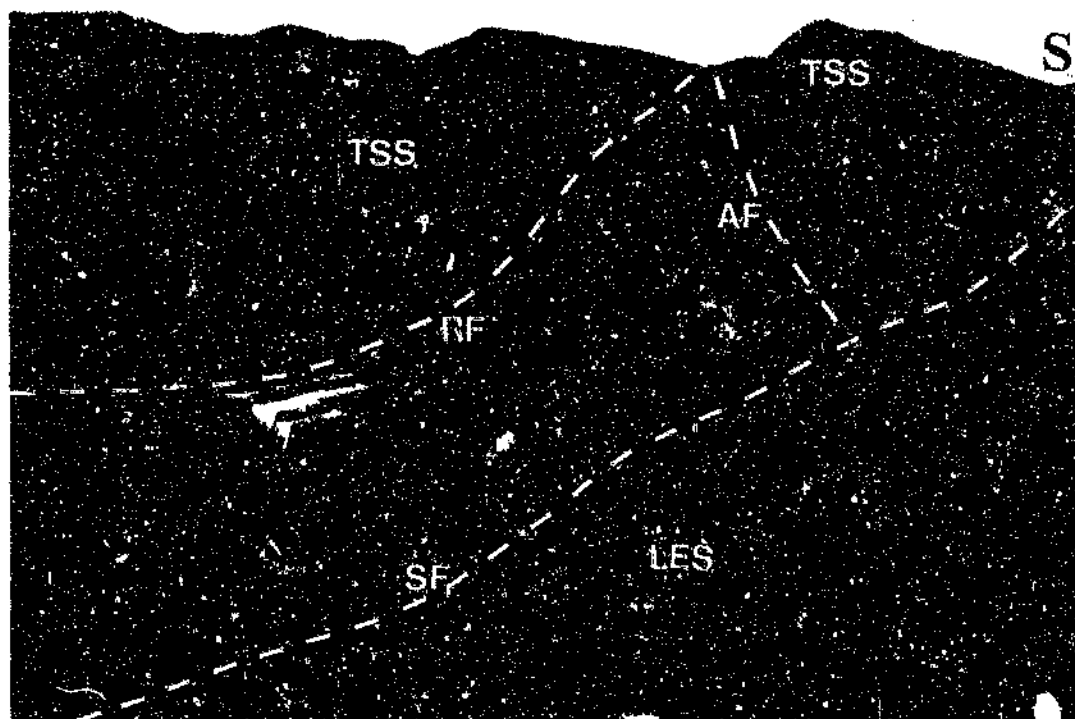


Figure 9.10 View, looking north-northeast from the Holnekt trigonometrical beacon (Figure 1.4, 15) showing the principal structures within the Revolver Creek Valley. The Three Sisters Mine, in the middle ground, is situated on basic and ultrabasic schists correlated with the Theespruit Formation. The Revolver (RF) and Adamanda (AF) Faults juxtapose these schists against rudaceous and arenaceous rocks of the Moodies Group coring the Three Sisters Syncline (TSS) to the north and east of the mine. The ridge to the south of the mine is formed by a prominent chert unit, and marks the position of the Scotsman Fault (SF). This fault separates the Onverwacht schists from argillaceous assemblages of the Sheba Formation along the northern limb of the Lily East Syncline (LES). Moodies conglomerates coring the Lily East Syncline are exposed in the lower right hand corner of the photograph.

strikes east-northeasterly and generally dips southward at 60 - 80° (Figure 9.11A). In some exposures, the schists contain a weak, steep- to moderately plunging L_m mineral elongation lineation (Figure 9.11A). Rare S-C structures in the schists support a reverse sense of movement. Several north-northwesterly trending B_f faults locally offset the Scotsman Fault by up to ~150 m (Figure 1.4, H4 and H5).

The workings of the defunct Weenan County Gold Mine (Figure 1.4, H5) are situated along two shear zones that trend subparallel to the trace of the Scotsman Fault and dip at 55 - 70° to the south. Also exposed in this general area are distinctive grey-to-green cherty rocks that are characterised by deep irregular gashes on weathered surfaces (Figure 9.11B). These rocks are rarely found *in situ*, typically occurring as large boulders strewn along northern slope of the prominent ridge south of the mine. Fresh surfaces show a well-developed planar fabric reminiscent of that encountered in schists and mylonites, as well as numerous close-spaced, foliation-parallel quartz veins. Thin section studies revealed a mineralogy dominated by microcrystalline quartz, amphibole and penninite, together with subordinate epidote, fuchsite, carbonate and opaque phases, suggesting that the cherts represent silicified basic schist.

East of the Adamanda Fault (Section 9.2.1.2.13), the Scotsman Fault lies mostly within argillaceous assemblages of the Fig Tree Group. However, a fairly large (~1 km long and ~200 m wide), east-trending block of talcose schist and sheared serpentinite is exposed at the junction of the two faults (Figure 1.4, G6). The exact relationship of this block to the surrounding rocks could not be determined due to inadequate outcrop and dense bush, although it seems likely that it is terminated on all sides by faults.

On Ardonachi 257 JU and Scotsman 258 JU, the chert marker is considerably reduced in thickness (typically ~0.5 - 2 m wide) and only crops out sporadically. In some exposures the marker is seen to consist of lenticular domains of less deformed chert set

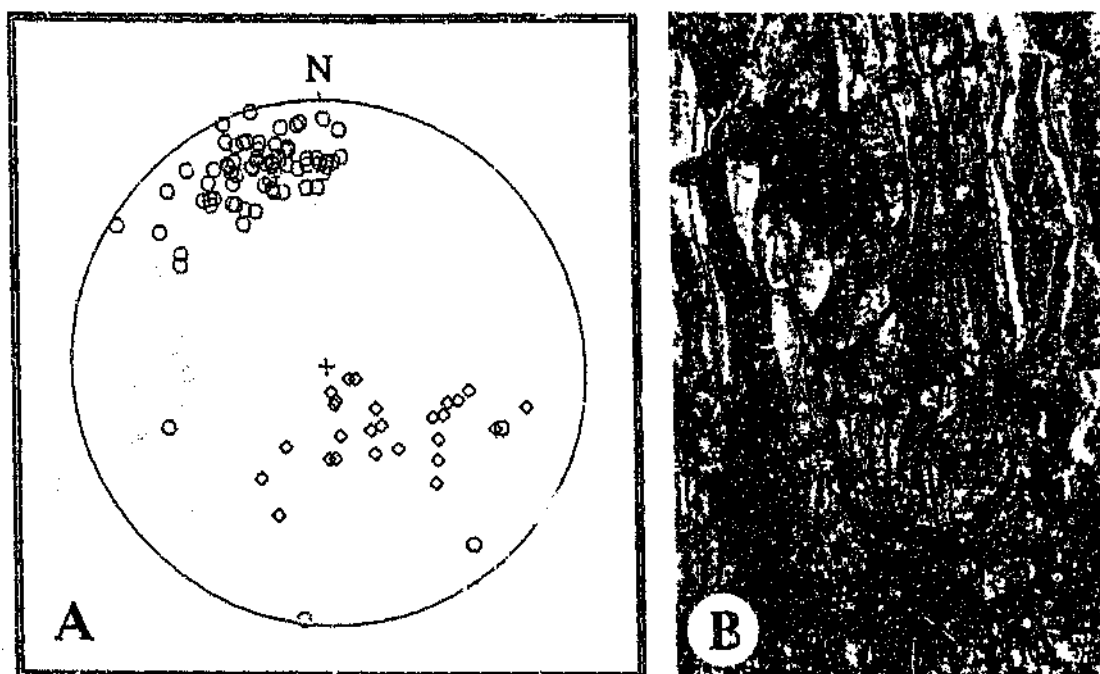


Figure 9.11 Structural features of rocks along the Scotsman Fault:

(A) Lower hemisphere equal area projections of poles to S_m (circles; $n = 74$) and L_m mineral elongation lineations (diamonds; $n = 31$) in basic schists within the Revolver Creek Valley.

(B) Chertified basic schist (Three Sisters 254 JU). Lens cap is 4.9 cm in diameter.

in a well-foliated, friable, cherty matrix. Intensely deformed micaceous and talcose schists are exposed in an 70 m wide and 900 m long east-trending zone along the cherts northern contact on Ardonachi 257 JU. S_m foliations in these rocks generally dip steeply ($75 - 90^\circ$) to the south.

In the area east of the Three Sisters Mine, the chert marker is accompanied by two northeast-trending, steep- to subvertically dipping horizons of argillaceous BIF (Figure 1.4, G7). These BIF's are separated by a 40 - 60 m wide zone of shale, with minor chert and fuchsitic schist. Several adits and prospecting pits occur in this area.

Most of these appear to be located along shear zones at or close to margins of the BIF's. Hence, it is possible that the two BIF's represent a single unit which has been duplicated by faulting. The western part of the southern BIF is tectonically juxtaposed against the chert marker (Figure 1.4, G6 and H6). The northern BIF, which can be followed eastwards onto Amo 259 JU, is separated from the chert marker, where this is developed, by a 10 - 30 m wide zone of mica schist and ferruginous phyllite. On Scotsman 258 JU, this BIF hosts the workings of the long-defunct Scotsman Gold Mine (Figure 1.4, G8). The eastern continuation of the Scotsman Fault is uncertain, although the writer suspects that the fault links up with the Igwalagwala Fault (Section 9.2.1.2.5) in a region of poor exposure ~3 km northeast of the Scotsman Mine.

9.2.1.2.13 Adamanda Fault

The Adamanda Fault is a poorly exposed, northeast-trending splay fault which connects the Revolver and Scotsman Faults in the upper reaches of the Revolver Creek Valley (Figures 1.4 and 9.10; Sections 9.2.1.2.11 and 9.2.1.2.12). The fault juxtaposes strata of the Moodies and Fig Tree Groups to the east against basic and ultrabasic rocks of the Theespruit Formation to the west. Exposures in exploration trenches in the vicinity of the Adamanda Gold Mine indicate that the fault dips steeply ($\sim 70^\circ$) to the southeast, while surface mapping shows that it has displaced the eastern part of the Three Sisters Syncline ~1 km southwest of the main mass of the fold (Figures 1.4, G6, and 9.12; Section 9.2.1.1.6).

Highly weathered ferruginous shales of the Fig Tree Group are exposed in road cuttings near the source of Revolver Creek (Figure 1.4, G6). In the east, these rocks tectonically abut against silicic schists and conglomerates along the northern limb of the Three Sisters Syncline. The western contact of the shale unit is not exposed, but is probably also faulted, suggesting that the shales represent a fault-bounded slice associated with, and forming the footwall to, the Adamanda Fault.



Figure 9.12 View, looking east from the middle of the Three Sisters peaks, showing the position of the Adamanda Fault along the northwestern slope of the easternmost of the Three Sisters peaks (dashed line). The fault has displaced the eastern part of the Three Sisters Syncline (TSS) to the southwest of the main mass of the fold, part of which occupies the foreground.

Gold mineralization at the now-defunct Three Sisters Gold Mine (Figure 1.4, G6) is localized along three main subparallel shear zones which strike northeasterly and generally dip southeasterly at $50 - 70^\circ$ (Groeneveld, 1973), roughly parallel to the Adamanda Fault. These shears are offset by a number of east-striking, generally moderately southward-dipping sinistral faults that post-date the mineralization. Auriferous quartz-carbonate \pm tourmaline veins showing evidence of post-emplacment shearing and boudinage pervade the ore bodies. These veins, which range in width up to a few tens of centimetres, are usually subparallel to the S_m schistosity in the basic and ultrabasic host rocks, but clearly cross-cut this fabric in places. Pervasive carbonatization, sericitization and silicification are the dominant alteration styles encountered in the ore bodies. Sulphides (mainly pyrite with minor chalcopyrite, stibnite, pyrrhotite and tetrahedrite - Schweigart and Liebenberg, 1966) occur as fine disseminations in khaki-coloured alteration haloes surrounding the veins. In the Adamanda section, the shear-zones are tightly folded about axes which plunge steeply to the northeast (Groeneveld,

1973; P. Harrison, pers. comm., 1991). The folding can be related to dextral shearing and increases in intensity towards the northeast (Groeneveld, 1973), suggesting that it resulted from movement along the Adamanda Fault.

9.2.1.2.14 Ardonachi Fault

The subvertically dipping Ardonachi Fault extends along the southern margin of the displaced eastern part of the Three Sisters Syncline (Figure 1.4; Section 9.2.1.1.6). At its western end it is obliquely truncated by the Adamanda Fault (Section 9.2.1.2.13). Road cuttings across and along the fault zone reveal strongly sheared conglomerate and quartzite to the north, and ferruginous shale and, at one locality, argillaceous BIF to the south. The conglomerates consist of flattened and brecciated chert and quartzite clasts in a cataclastic quartzose matrix that weathers brick-red (Figure 9.13). A north-northeasterly to east-northeasterly striking S_m cleavage that dips subvertically or steeply to the northwest is prominently developed in the rocks.



Figure 9.13 Polished slab showing strongly flattened and brecciated pebbles in sheared conglomerate along the Ardonachi Fault (sample collected on the farm Three Sisters 256 JU).

Further east, the Ardonachi Fault follows the southern contact of the southward-younging Moodies quartzites and subgreywackes making up the Scotsman Block (Section 9.2.1.1.11). Shearing has resulted in the development of a pervasive S_m foliation that dips steeply to the north-northwest. Numerous minor shear zones with northeasterly to easterly strikes and subvertical dips occur adjacent to the fault. Ferruginous argillites of the Fig Tree Group in the vicinity and to the east of the defunct Morning Mist Antimony Mine on Amo 259 JU (Figure 1.4, E10) contain lenses of fuchsitic quartz-sericite, quartz-chlorite and talc \pm chlorite schist / phyllite. Impersistent pods of highly weathered serpentinite and an enigmatic massive-to-schistose talc-carbonate lithology characterised by large (a few millimetres across) crystalline masses and rhombs of dolomite, also crop out in places. Stibnite mineralization occurs intimately associated with small, irregular quartz veins hosted within minor, but intensely carbonatized shear zones (Viljoen *et al.*, 1986). On surface the mineralization is manifest as fine powdery disseminations of stibiconite, limonite and goethite. In the western part of Amo 259 JU, where the trace of the Ardonachi Fault is dextrally offset by the Amo Fault (B_f), the argillites contain several subvertically dipping bands of sheared and brecciated chert, BIF and silicic metavolcaniclastic rock. The metavolcanics are heterogeneously deformed such that relic angular clasts can still be observed in some outcrops. Variably deformed quartzites and conglomerates of the Moodies Group also crop out in places as fault-bounded outliers within the shales. Continuing to the east onto Sherlock 461 JU, the fault is displaced \sim 350 m to the south by a north-northwesterly striking B_f fault.

Pale-grey, massive-to-schistose, talc-carbonate rocks of the Onverwacht Group are exposed in the quarry of the Buffelspruit Talc Mine (Figure 1.4, D13). The structural significance of these rocks could not be resolved owing to inadequate exposure; however, they either mark the core of a minor anticlinal structure or, more likely, form part of a fault block against the Ardonachi Fault. Several narrow lenses and veins of bright-green, generally massive talc occupy shear-zones within the quarry. The main shear-zone strikes east-northeasterly, dips subvertically, and attains a maximum width of \sim 1 m. Numerous

small, irregular carbonate veinlets and blebs intrude the rocks adjacent to the shear. These veins generally lie within or close to the steep north-northwesterly dipping S_m schistosity and locally exhibit boudinage.

North of the Big Buffalo trigonometrical beacon, the Ardonachi Fault places quartzites along the northern limb of the Big Buffalo Syncline against assemblages within the Scotsman Block (Figure 1.4, C14 and D14; Sections 9.2.1.1.1 and 9.2.1.1.11). The contact between the two synclines is marked by a broad (200 - 300 m wide), but generally poorly exposed zone of sheared quartzites, conglomerates, quartzose schists and siliceous cherty rocks. S_m strikes east-northeasterly and varies in dip about the vertical. Thin (-1 - 2 m wide) bands of a pinkish-brown, massive-to-foliated-to-brecciated quartzose lithology occur interlayered within the fault zone in places. Foliations in these rocks are locally seen to be deformed by small open-to-tight folds; the precise orientation of these folds is, however, difficult to establish because the rocks are no longer *in situ*.

9.2.1.3 Other D_{min} structures

9.2.1.3.1 Structure of the Eldorado Mine area

The defunct Eldorado Gold Mine (formerly the Kimberley Imperial Mine) lies due east of the Ka Ngwane Government Offices on Louieville 325 JU and is located in a subvertical- to steeply southward-dipping succession of Sheba Formation rocks along the southern limb of the Lily East Syncline (Figure 1.4, I3; Section 9.2.1.1.5). The old workings consist of several adits, shafts and trench-like opencast excavations which have been described in considerable detail by Groeneveld (1973). The surface geology of the mine area is dominated by a 30 - 75 m thick, easterly striking unit of argillaceous BIF that can be traced over a strike length of about 1.5 km (Figure 1.4, I3). Layering within this unit is locally deformed into small, close-to-tight folds displaying variable plunges and axial plane attitudes. In the south, the BIF is underlain by carbonaceous shale and

metagreywacke assemblages. A 20 - 35 m wide lens of carbonatized and silicified fuchsitic talc-chlorite schists and talcose serpentinites occurs north of the BIF. These rocks, which probably belong to the Onverwacht Group (Zwartkoppie Formation?), display a steeply (-80°) southward-dipping S_m foliation with associated down-dip L_m lineation. Along strike, the schists give way to argillites which are succeeded to the north by a second, much thinner (1 - 2 m wide) BIF unit and finally another succession of argillites.

Shearing, brecciation and striations are evident along all contacts, with the exception of the southern contact of the main BIF, suggesting that they have undergone displacement. The striae generally plunge steeply within east-striking, subvertically-dipping, fault-parallel foliation surfaces. It is likely that this fault-zone represents the strike extension of the east-trending Lily Fault which occurs immediately west of the mapped region (see the location map in Figure 1.4)(Anhaeusser, 1963, 1965, 1986b), although this could not be verified owing to a lack of exposure. Gold mineralization is mainly hosted by thin quartz \pm carbonate \pm sulphide infilled fractures along east-striking, subvertically dipping shear-zones within, or immediately adjacent to, the BIF's (Groeneveld, 1973).

9.2.1.3.2 Structure of the Spago and Sussex Mines areas

The extreme northeastern corner of the study area is a structurally complex zone. The most conspicuous lithologic unit in this region is a 100 - 300 m wide, vertically dipping horizon of BIF with intercalated cherty shale, referred to as the Spago BIF (Figure 1.4, C12). This unit is well-exposed in the quarry of the Spago Iron Mine (Figure 1.4, C12), and in the spillway and adjacent road cutting at Spago Dam (Figure 1.4, B13). The unusually large outcrop width of the Spago BIF is unlikely to reflect its primary thickness as it contains numerous small-scale, upright, open-to-isoclinal folds that generally plunge east-northeast (Figure 9.14A). Some of these folds are characterised by

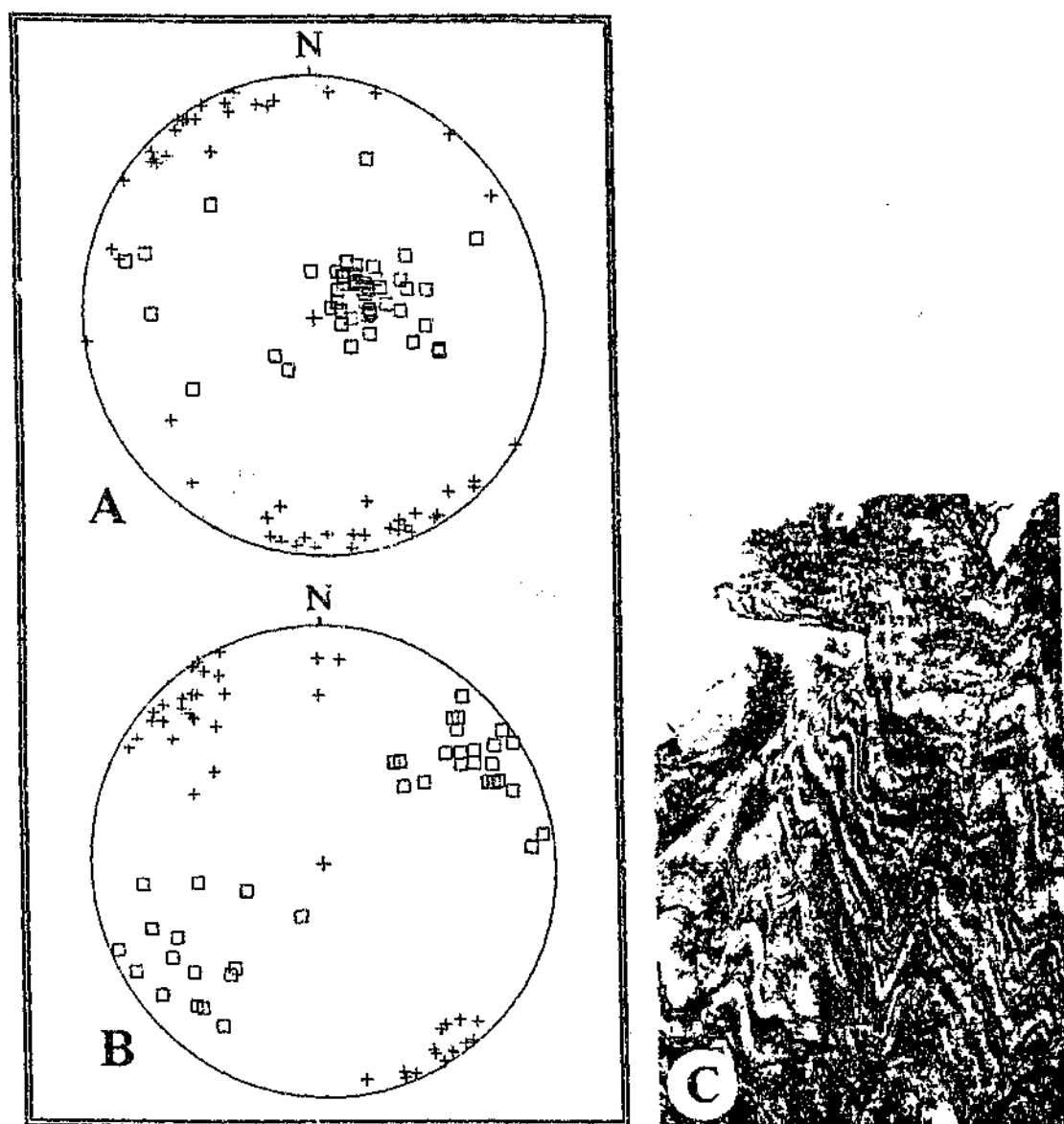


Figure 9.14 Structural features of rocks outcropping in the vicinity of the Spago and Sussex Mines:

(A) Lower hemisphere equal area projections of fold axes (squares; $n = 52$) and poles to axial surfaces (crosses; $n = 52$) of minor folds in the Spago BIF.

(B) Lower hemisphere equal area projections of fold axes (squares; $n = 41$) and poles to axial surfaces (crosses; $n = 41$) of minor F_m folds in the area of the Sussex Mine.

(C) Small-scale F_m folds in a chert unit northeast of the Sussex Gold Mine (Malelane Estate B 390 JU). Hammer is 30 cm long.

'Z'- and 'S'-shaped profiles, suggesting that they occur on the limbs of larger folds whose geometry is difficult to verify in the field owing to a lack of exposure, although plunge is probably also steep to the east-northeast. The BIF is abruptly truncated in the west by a northwesterly striking B_r fault (Figure 1.4, C11) and is separated from poorly exposed silicic metavolcaniclastic rocks of the Bien Venue Formation to the north by robust chert of the Basal Marker (Section 4.3). The latter attains a maximum thickness of ~350 m immediately north of Spago Dam, where it is offset by the B_r Spago Fault and associated splay fault (Figure 1.4, B13). In this general area, the cherty rocks are locally deformed into small-scale upright F_m folds which plunge steeply to the northeast or east-northeast. The stratigraphic relationships outlined above suggest that the succession youngs towards the north. The silicic metavolcaniclastic rocks are juxtaposed in the north against ultrabasic schists of the Komati Formation along the Stentor Fault (Section 9.2.1.2.10).

East of Spago Dam, the Basal Marker gives rise to a prominent east-northeast-trending ridge. Silicic rocks of the Bien Venue Formation along the northern slopes of this ridge are locally intensely deformed and are succeeded to the north by poorly exposed ferruginous shales which probably form part of the Belvue Road Formation (Section 4.1). The contact between the two successions is not exposed, but is interpreted as a B_m fault, referred to as the Coulter Fault, which is truncated in the west by the Spago Fault (Figure 1.4, B13). In the field, the position of the Coulter Fault is locally marked by subvertically dipping lenticular units of BIF and chert which are probably bounded on all sides by faults. At its eastern mapped extremity, the Coulter Fault obliquely truncates the Basal Marker (Figure 1.4, B14).

Further exposures of BIF and grey and white banded chert, the latter possibly representing the Basal Marker, occur north of the Coulter Fault, forming a second east-northeast-trending ridge which is locally offset by right-lateral B_r faults (Figure 1.4, B13). The BIF unit occurs along the southern slope of the ridge, but is usually only exposed in exploration trenches; elsewhere, its presence has been inferred from BIF scree. Developed between the Basal Marker and the Stentor Fault to the north is an

exceedingly heterogeneous, poorly exposed assemblage of rocks, including silicic metavolcaniclastic lithologies, ferruginous shales, argillaceous BIF's and cherts, all of which belong to the Fig Tree Group. It is possible that this succession represents a distal assemblage of the Bien Venue Formation. The silicic metavolcanics are best exposed along the western border of Malelane Estate B 390 JU where they are seen to be intensely, but heterogeneously, deformed to quartz-muscovite \pm fuchsite schists. These rocks are characterised by a pervasive, moderate-to-steeply ($60 - 80^\circ$) south-southeastward-dipping S_m foliation which is traversed by thin (a few millimetres or centimetres wide), randomly oriented blebs, veins and stockworks of quartz and chert. In some outcrops, the quartz-muscovite schists grade into small, irregularly shaped bodies of massive- to weakly laminated white, grey or green chert. Laterally discontinuous lenses of variably sheared grey and white banded chert also occur intercalated with schists in places. The contacts between these cherts and the enclosing rocks locally show evidence of intense shearing and are frequently marked by outcrops of fuchsitic schist showing a crude layering similar to that found in the grey-to-green cherty rocks along the Scotsman Fault (Section 9.2.1.2.12). Carbonate veining is generally uncommon and is mainly restricted to sporadic outcrops of basic and ultrabasic schist.

The silicic schists grade eastwards into a zone of deeply weathered shales and argillaceous phyllites. To the northeast of the Sussex Gold Mine (Figure 1.4, A14), these rocks contain numerous lenses of metagreywacke and silicic metavolcaniclastic rock up to several metres wide. Quartz-muscovite \pm fuchsite \pm carbonate schists, talc-carbonate schists, cherts and argillaceous BIF's also crop out sporadically. The former are best developed in a 30 - 100 m wide zone extending along the contact with the main chert unit at the Sussex Mine. The cherts and BIF's are locally sheared and contain numerous centimetre- and decimetre-scale tight-to-isoclinal, upright and northwestward-verging F_m folds that either plunge to the northeast or southwest (Figures 9.14B and C). S_m foliations in the adjacent pelitic rocks and schists are oriented parallel to the axial surfaces of these folds. Duplication of some of the chert and BIF / banded ferruginous shale units by metre-scale, upright- to northward-verging F_m folds that plunge at moderate angles to

the west, southwest and northeast is evident in places. Fault repetition is also likely, but could not be confirmed due to a lack of exposure. Gold mineralization at the Sussex Mine is largely confined to small, generally concordant smoky quartz veins within thin, easterly trending and generally subvertically dipping, sulphide and limonite impregnated shear zones deforming units of banded ferruginous shale / BIF (Groeneveld, 1973; this work).

9.2.2 $D_{\text{diapiric}} - D_4$

D_4 deformation resulted in the development of two major F_4 folds, namely the Stentor Antiform, which was originally identified by Viljoen and Viljoen (1970), and a previously unrecognised synform, herein referred to as the Bien Venue Synform (Figure 9.1). These structures are accompanied by several large-scale parasitic folds, as well as a pervasive planar (S_4), and associated linear (L_4) fabric, and are responsible for the complex structural patterns north of Three Sisters. However, despite their size, the F_4 structures only affect lithologies of the Fig Tree and Moodies Groups. The overall form of the Stentor Antiform - Bien Venue Synform pair is schematically illustrated in Figure 9.15.

9.2.2.1 Stentor Antiform

The Stentor Antiform occurs due east of the Stentor pluton and deforms silicic metavolcanic lithologies of the Bien Venue Formation (Figures 1.4 and 9.15). Primary structures and layering within this succession have, for the most part, been obliterated by a pervasive S_4 schistosity (Section 4.3), making it difficult to establish the geometry and orientation of the fold, or younging directions, or the position of the axial trace. However, orientation of phyllite/slate intercalations within the schists (Section 4.3.5) indicates that the fold is open in form and upright, and that the hingeline plunges at moderate angles ($\sim 50^\circ$) to the east-northeast.

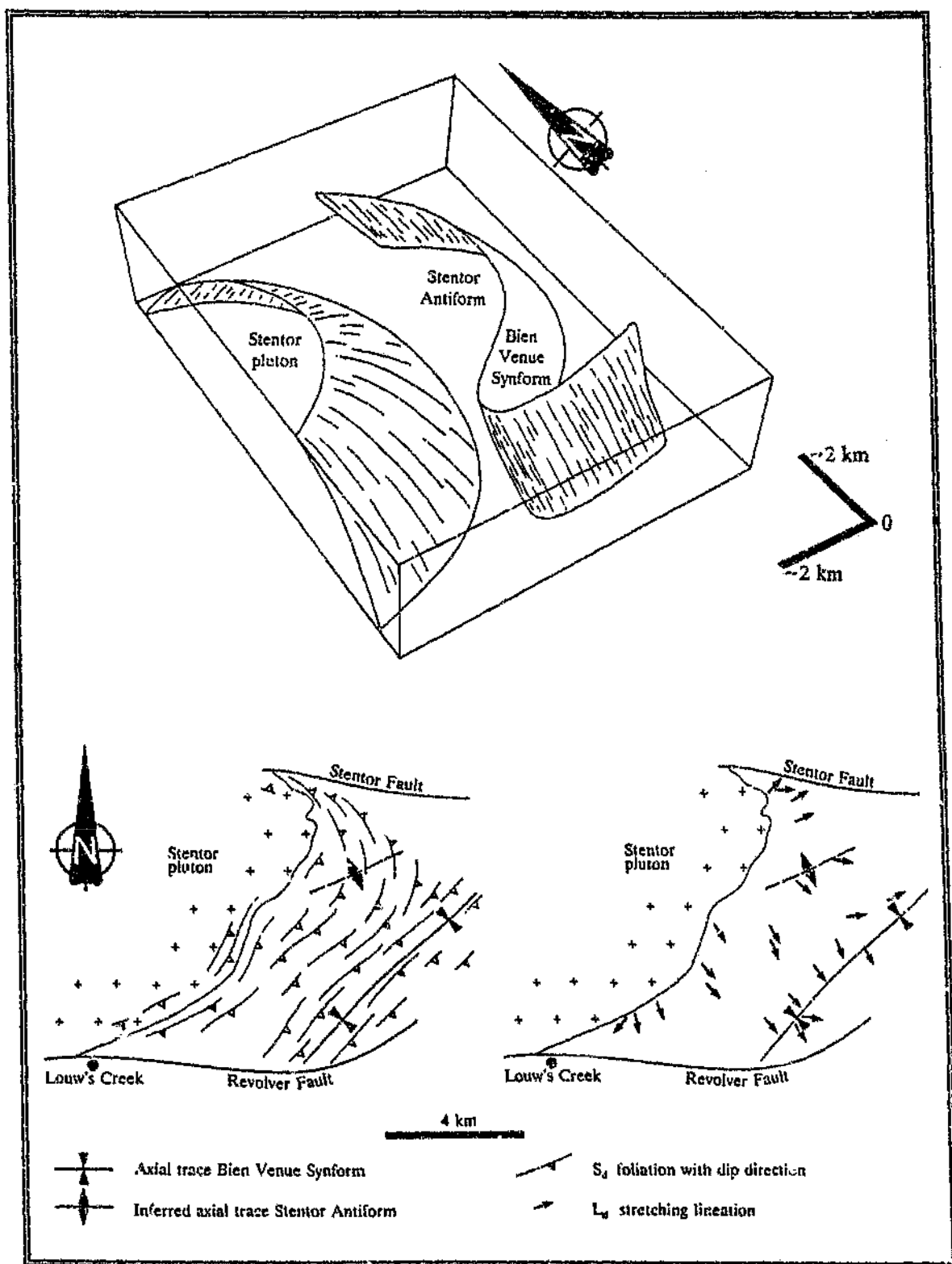


Figure 9.15 Schematic three-dimensional representation of the Stentor Antiform - Bien Venue Synform pair. Also shown are sketch maps of S_d foliation, and L_d stretching lineation trajectories.

The S_d foliation is concordant with the primary layering of the sequence where discernable, and has a pronounced arcuate trend parallel to the eastern margin of the Stentor pluton (Figure 9.15). The schistosity is conformable with the S_d foliation seen in the granodiorites (Sections 8.3.1 and 8.3.2), and dips at moderate-to-steep angles away from the granitoid contact; steepness of dip generally decreases with increasing strain, the latter reflecting greater proximity to the granitoids (Section 4.3). Poles to S_d fall on a great circle, the pole of which plunges at 45° on a bearing of 070° , roughly parallel to the trend and plunge of the hingeline (Figure 9.16). A weak-to-moderate L_d fabric, defined mainly by elongate biotite \pm muscovite aggregates is heterogeneously developed, and shows a broad subradial distribution pattern with respect to the granitoid contact (Figures 9.15 and 9.16). The mineral lineations are parallel to the long axes of deformed chert pebbles and quartz porphyroclasts, indicating that they represent stretching lineations. Rare kinematic criteria such as rotated porphyroclasts and porphyroblasts dominantly show a normal, "pluton-up" sense of movement along the foliation planes.

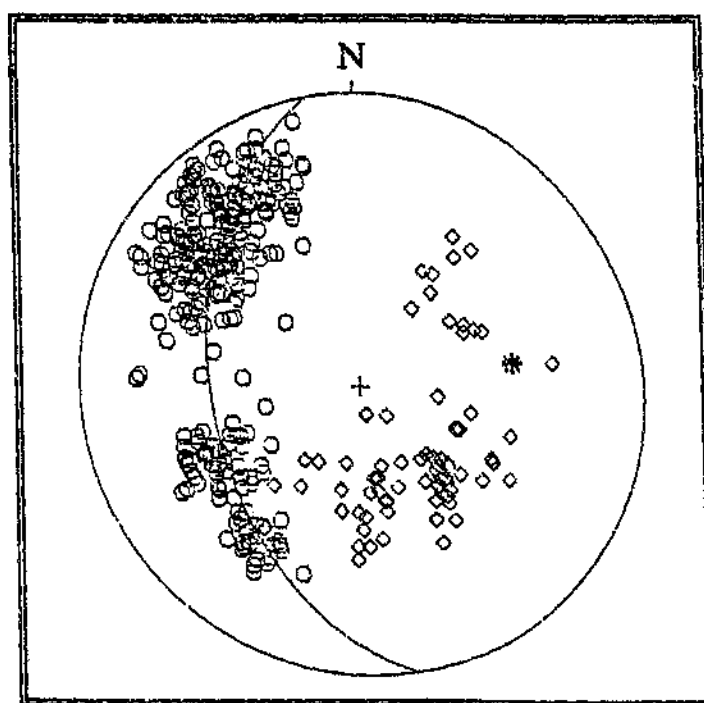


Figure 9.16 Lower hemisphere equal area projections of poles to S_d (circles; $n = 332$) and L_d stretching lineations (diamonds; $n = 74$) in the Stentor Antiform. Poles to the foliation define a great circle distribution, the pole of which (asterisk) plunges approximately parallel to the hingeline of the fold.

9.2.2.2 Bien Venue Synform

The axial trace of Bien Venue Synform can be followed from the area of the Weenan County Gold Mine (Figure 1.4, H5), where it is truncated by the Revolver Fault, for a distance of ~8 km to the Stentor Barite Mine (Figure 1.4, E7). This fold was responsible for the refolding of rocks in the western part of the Three Sisters Syncline (Section 9.2.1.1.6) to form a Type-3 interference structure (Ramsay and Huber, 1987).

Orientation data collected in the fold closure at the Great American Mine (Figure 1.4, F6) indicate that the synform is tight, with an axial surface dipping at 65° southeastwards and an axis plunging at 60° south-southeastwards, while stratigraphic relationships indicate that it is downward facing. Chert and BIF marker horizons in this area outline a series of northeasterly trending, overturned, tight-to-isoclinal, map-scale synformal and antiformal parasitic folds that plunge at moderate angles to the south-southeast (Figures 1.4, F6, and 9.17A). Large 'Z'- and 'S'-type asymmetric folds are also developed along the contact between the Moodies Group and the Bien Venue Formation at the Bien Venue massive sulphide deposit (Figure 1.4, G5), while W-shaped folds occur in the vicinity of the Stentor Mine (Figure 1.4, E7). Recognition of parasitic folding elsewhere is hampered by the lack of structural marker horizons, particularly in the silicic schists. However, the chert and BIF units described above contain numerous, steeply plunging, internal folds that show Z-, S- or M/W-shaped profiles depending on their position relative to the closures of the larger folds.

A strongly developed S_4 fabric, manifest as a slaty cleavage in the argillites, a schistosity in the silicic metavolcanic rocks, and a grain- and clast-shape fabric in the quartzites and conglomerates, occurs throughout the synform. This foliation generally dips southeastward at 45 - 75°, parallel to the synform's axial surface, and is continuous with the S_4 schistosity seen in the Stentor Antiform (Figures 9.15 and 9.17B). Microstructural and metamorphic investigations also suggest that the S_4 fabric in the

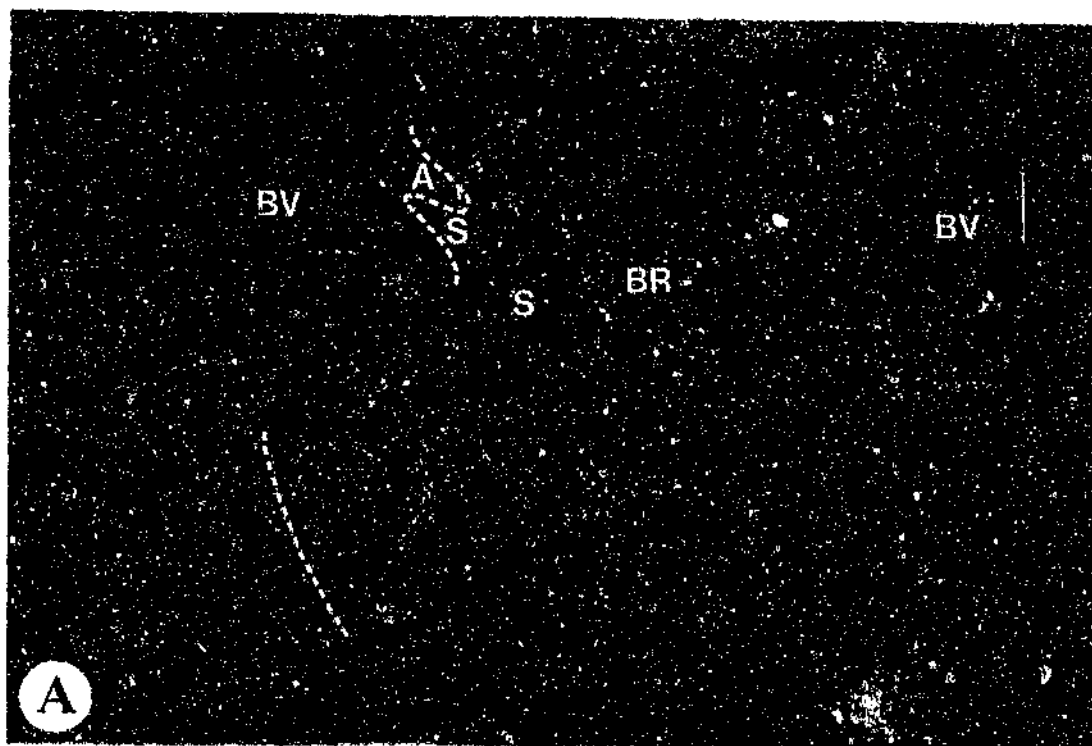


Figure 9.17 Structural features in rocks of the Bien Venue Synform:

(A) View of the eastern limb of the Synform showing large-scale Z-type parasitic folding. Bushes and trees are generally less than 4 m high. Silicic schists of the Bien Venue Formation (BV) along the eastern and western limbs of the synform are seen in the upper left and right hand corners of the photograph, respectively. The grass-covered slopes in the middleground are underlain by argillites correlated with the Belvue Road Formation (BR). The chert and BIF marker horizons described in the text are highlighted by the white and black dashed lines, respectively. The letters S and A mark the positions of synformal and antiformal parasitic folds. Plunge of the folds is towards the camera and steeper than the slope of the hill, so that the two synforms display apparent antiformal outcrop patterns while the antiform has an apparent synformal disposition.

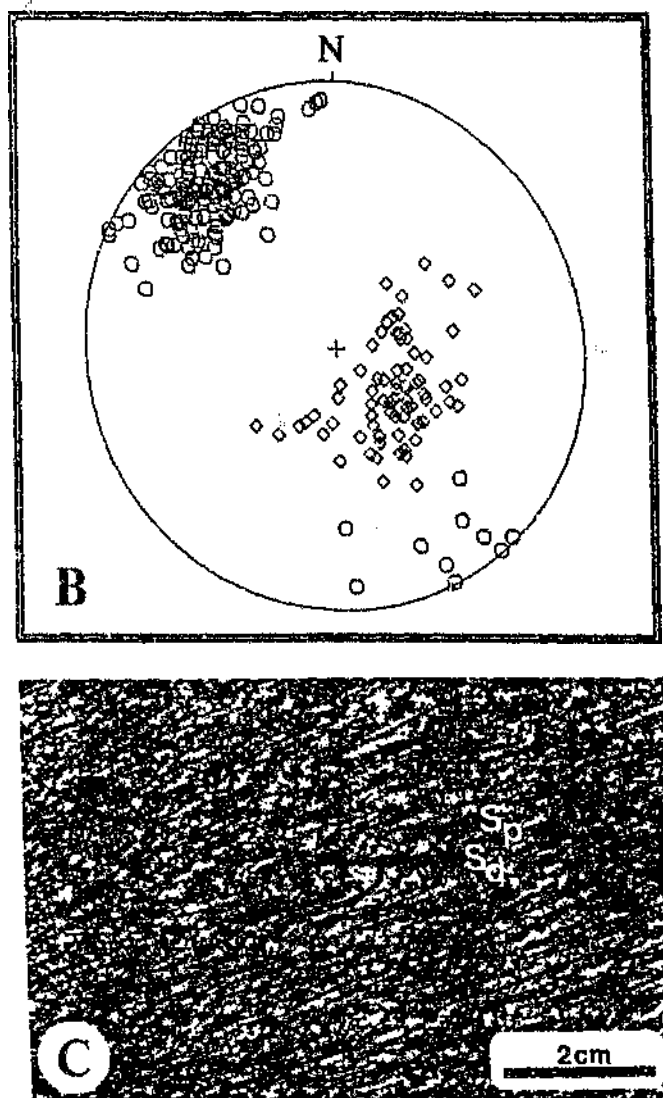


Figure 9.17 (continued):

(B) Lower hemisphere equal area projections of poles to S_d (circles; $n = 188$) and L_d stretching lineations (diamonds; $n = 78$).

(C) Crenulated silicic metavolcanic rock (Stentor 219 JU). The layering is defined by domains alternately rich and poor in ferromagnesian minerals, and may reflect original compositional variations in the rock - i.e. S_p .

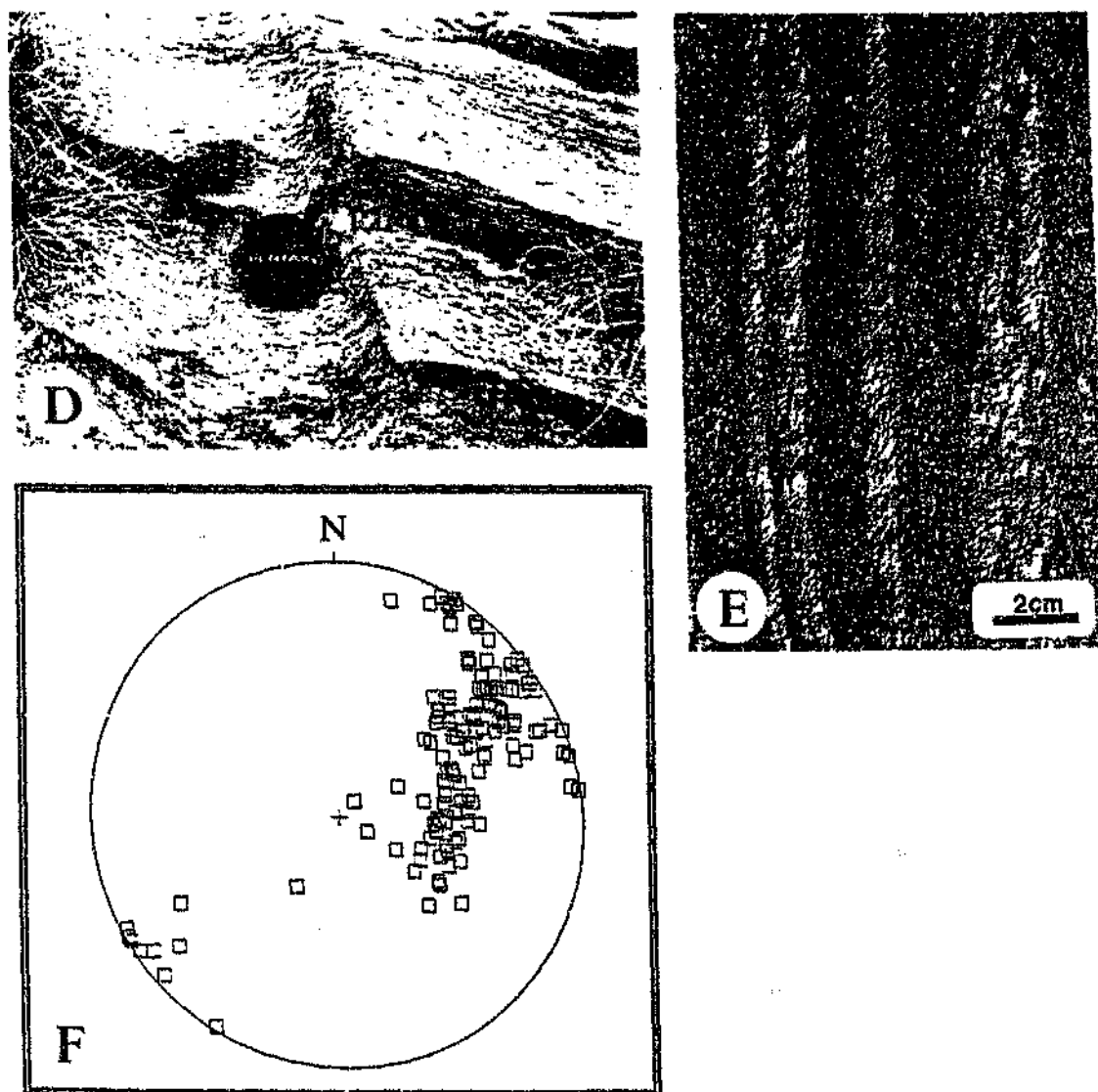


Figure 9.17 (continued):

(D) Steeply plunging monoclinial fold deforming S_d in quartz-muscovite schist (Bien Venue 255 JU). Lens cap is 4.9 cm across.

(E) Parallel kink bands in quartz-muscovite schist (Bien Venue 255 JU).

(F) Lower hemisphere equal area projections of fold axes of minor kink-like folds deforming S_d ($n = 143$).

synform is contemporaneous with S_4 in the antiform. S_4 generally strikes oblique to, and overprints, S_p , and is best developed in the southwestern parts of the synform where orientations in any given area show relatively little variation. Northeastwards, the intensity of the foliation progressively decreases and comparatively large variations in attitude occur locally; in some exposures, S_4 is seen to dip steeply to the north-northwest. S_4 crenulation cleavages that crenulate compositional banding (possibly S_p) in the silicic metavolcanic rocks were recorded at a single locality close to the western boundary of Stentor 219 JU (Figure 9.17C).

The S_4 fabric in the schists is often seen to be deformed by small-scale kink-like folds. These folds deflect the schistosity from its original orientation by $\sim 20 - 60^\circ$ and are best developed along the western limb, and in the closure, of the synform (Figure 9.17D). The smaller kink folds often occur in parallel arrays (Figure 9.17E). Orientation of the kink axes and axial planes varies considerably; some folds have near-horizontal attitudes while others plunge at moderate angles ($40 - 60^\circ$) to the northeast, east or east-southeast (Figure 9.17F).

L_4 stretching lineations, plunging at moderate angles to the southeast or east (Figures 9.15 and 9.17B), are defined mainly by the long axes of elongate quartz insets, and chert and quartzite clasts (see later). Crenulated rocks along the western boundary of Stentor 219 JU display a steeply plunging L_4 crenulation lineation.

9.2.2.3 Strain analysis

Deformed clasts have been investigated at two localities within the Stentor Antiform - Bien Venue Synform pair. The first of these localities is situated in the closure of the synform, immediately southwest of the Bien Venue massive sulphide deposit, where ellipsoidal quartzite clasts occur in conglomerate beds of the Moodies Group (strain analysis locality 1 in Figure 1.4, G5; Section 7.2). The second locality is situated along the southern limb of the antiform, on the ridge overlooking the homestead on Bien Venue 255 JU, where recrystallized chert clasts occur within quartz-muscovite

schists of the Bien Venue Formation (strain analysis locality 2 in Figure 1.4, F5; Section 4.3.1). Measurements taken at each locality included the orientation and length of the long (X), intermediate (Y) and short (Z) axes of the clasts, as well as the orientation of S_d in the enclosing matrix. The calculated average axial ratios and k -values of the clasts is summarised in Table 9.3. Figure 9.18 shows a Flinn diagram for the clasts and the orientations of the maximum, intermediate and minimum principal strains at each locality.

Table 9.3 Strain data for deformed clasts within the Stentor Antiform - Bien Venue Synform pair (localities are shown in Figure 1.4)

Locality	Clast Type	Matrix	n	\bar{X}	\bar{Y}	\bar{Z}	k^{\ddagger}	\bar{k}
1	Quartzite	Quartzite	28	4.5	2.5	1.0	0.16 - 2.33	0.69
2	Chert	Quartz-muscovite schist	37	10.2	5.1	1.0	0.05 - 1.57	0.35

$\ddagger - k = (R_{XY} - 1) / (R_{YZ} - 1)$ where R_{XY} and R_{YZ} are the strain ratios of the XY and YZ principal strain ellipses

The results in Table 9.3 and Figure 9.18A indicate that the clasts are mainly oblate and plot in the field of apparent flattening, suggesting that they have been subjected to a flattening-type deformation (see below). The average k -value for the chert clasts is lower than that for the quartzite clasts, suggesting that they have experienced greater flattening; this is also shown by the much higher R_{YZ} values of the former (Figure 9.18A). Unfortunately, owing to differences in the nature of the clasts and the enclosing matrix at each of the localities, direct comparison of these results is not practicable. In the absence of absolute strain data, the possible mechanisms of deformation as outlined by Ramsay and Huber (1983) are: (1) true flattening deformation with positive extension in two directions; (2) flattening deformation with volume loss; (3) deformation of a previously compacted sediment by flattening deformation with or without volume loss; (4) deformation under plane strain conditions with volume loss; and (5) deformation of a previously compacted sediment under conditions of plane strain with or without further volume loss.

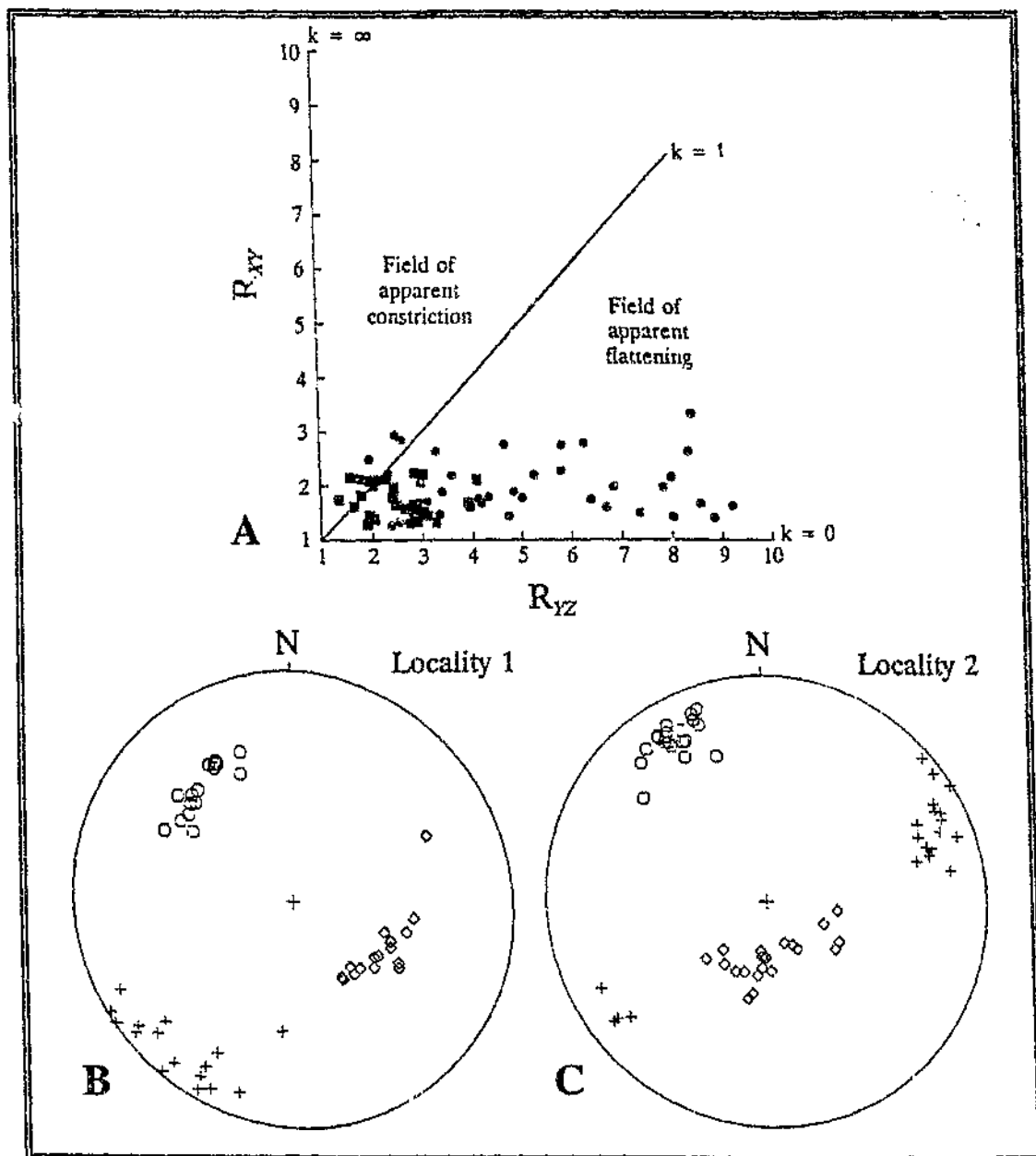


Figure 9.18 Results of strain analyses on deformed clasts within the Stentor Antiform - Bien Venue Synform pair:

(A) Flinn graph (after Flinn, 1962) showing data for quartzite (squares; $n = 28$) and chert (circles; $n = 37$) clasts.

(B) and (C) Lower hemisphere equal area projections showing the orientations of the maximum (X - diamonds), intermediate (Y - crosses) and minimum (Z - circles) principal axes of the finite strain ellipsoid as deduced from deformed clasts at strain analysis localities 1 ($n = 16$) and 2 ($n = 20$) in Figure 1.4.

Orientation data presented in Figure 9.18B indicates that the X axis of the finite strain ellipsoid is approximately parallel to the fold axis of the Bien Venue Synform (Section 9.2.2.2). The Y axis is subhorizontal, whilst the Z axis plunges at moderate angles northwestward, perpendicular to the S_4 axial planar foliation (Section 9.2.2.2). The overall similarity in the orientations of the strain ellipsoids at the two localities (Figures 9.18B and C) suggests that they formed under the same stress regime.

9.2.3 $D_{final} - D_f$

Structures attributed to the D_f event are present throughout the eastern sector of the study area, and comprise northwest- to northeast-striking, oblique- to dip-slip brittle faults (B_f) with varying displacements and strike lengths (Figures 9.1 and 1.4). These faults cut across the regional structural grain and appear to be steeply inclined. Horizontal offset is typically less than ~ 200 m, with both sinistral and dextral movement senses evident. Notable exceptions include the Strathmore and Spago Faults which exhibit strike displacements of 0.5 km or more (Figure 1.4, D8 and B13). The throw on these faults is difficult to ascertain, but is likely to be considerable since they truncate major F_m and B_m structures (e.g. Sections 9.2.1.1.10 and 9.2.1.3.2). Cherty units adjacent to some of the B_f faults show a nonpenetrative, subvertical, fault-parallel fracture cleavage (S_f) with associated moderately to steeply plunging striae.

9.3 Discussion and interpretation

9.3.1 D_{main}

D_m deformation gave rise to a series of folds and faults that are responsible for the overall east-northeasterly trending tectonic grain of the mapped area. F_m folds are tight-to-isoclinal, upright or north-verging structures with variable plunge. Some are

doubly plunging. Synclines predominate over anticlines. Although no complete first-order syncline - anticline pair is preserved, the scale of some F_m structures suggests fold wavelengths and amplitudes in the order of several kilometres. Parasitic folds that define several orders of subsidiary folding locally occur along the limbs and within the closures of the major folds. The latter are also bounded by B_m faults which strike subparallel to their east-northeasterly trending axial surfaces. In some places, however, the faults cut across the fold limbs and axial traces, indicating that they post-date the folds.

The faults are marked by zones of concentrated shear ranging from a few metres to several hundreds of metres in width, and commonly occur along the contact between lithologies of distinctly different competency. Faults within the supracrustal belt typically have subvertical or steep southerly dips, whereas those along the granitoid - greenstone interface, and within the granitoid terrane to the north, have shallow to moderate southerly dips. Biotite of metamorphic origin is widespread in mylonites along the latter faults, indicating that metamorphic grades of at least the upper-greenschist facies existed during late-stage shearing (see Winkler, 1979). Quartz \pm carbonate veining, as well as the localized occurrence of gold, stibnite and cinnabar mineralization, indicate that the B_m fault zones served as loci for hydrothermal fluid flow. The enhanced retrogression of basic and ultrabasic rocks due to the influx of CO_2 -bearing fluids is locally evident along some shear zones (Section 3.9).

Flaser-structured chert (\pm carbonate) lithologies similar to those along the Scotsman Fault have been documented in Onverwacht assemblages throughout the BGB (e.g. Viljoen and Viljoen, 1969f; De Wit, 1982; Lowe *et al.*, 1985; Houston, 1987). The origin and significance of these rocks has, however, been a subject of considerable debate. Field and petrographic observations led De Wit (1982), Paris (1984) and V.J. King (pers. comm., 1991) to conclude that the cherts represent silicified and carbonatized mylonites and cataclasites. On the other hand, Lowe *et al.* (1985), Lowe and Byerly (1986), Duchač and Hanor (1987) and Hanor and Duchač (1990) considered the cherts

as marking zones of early seafloor or subaerial alteration unrelated to deformation. It is the writer's opinion, based on observations within the present study area (Section 9.2.1.2.12), that the flaser cherts represent altered schistose or mylonitic rocks of basic or ultrabasic parentage.

The sense (and amount) of movement along most B_m faults is difficult to evaluate, although fault striae are consistent with major dip-slip movement, together with generally minor sinistral and dextral strike-slip deformational components. Some faults are characterised by older over younger rocks (e.g. Revolver and Koedoe Faults), suggesting that they represent reverse faults, while others have younger over older strata (e.g. Barbrook and Scotsman Faults), suggesting that they are normal faults. In rare cases however, small-scale kinematic features indicating a reverse sense of movement contradict the movement sense as deduced from stratigraphic relationships (Sections 9.2.1.2.7 and 9.2.1.2.12); clearly the latter cannot be used to determine the sense of movement because the faults cut previously folded strata.

In the absence of seismic-reflection data, the attitude and geometry of the B_m faults at depth remains speculative. It is possible that they are listric, with steep dips at surface and flatter dips at depth, and that they form part of an imbricate fan related to a southerly dipping décollement (see also Fripp *et al.*, 1980; De Beer *et al.*, 1988; Heubeck, 1990). The marked differences between the attitudes of the faults within the greenstones, and those along and to the north of the granitoid - greenstone interface, may reflect the exploitation of pre-existing, steeply dipping planes of weakness, such as lithological contacts and bedding surfaces, within the previously folded supracrustal assemblage. The subvertical attitude of some faults could also be due to steepening during shortening of the supracrustal succession as D_m continued.

The regional S_m foliation is represented by a schistosity in the metavolcanic rocks, a slaty cleavage in the argillites, and a grain- and clast-shape fabric in the arenaceous and rudaceous lithologies. The foliation strikes east-northeasterly and is

parallel to the axial surfaces of the F_m folds. S_m is heterogeneously developed, both on a local- as well as regional-scale: on a local scale, the foliation is seen to intensify as major B_m fault zones are approached; on a regional scale S_m becomes more intense towards the north. Where best developed, the fabric totally overprints S_p and other primary structures in the rocks. An oblique to down-dip L_m mineral lineation is locally developed on S_m surfaces.

The overall character of the D_m structures indicates that they formed within a north-northwestward-directed compressional tectonic regime.

There are few absolute constraints on the age of the D_m deformational episode. F_m folds deform, and hence post-date, strata of the Moodies Group which have an age of < 3256 Ma (Section 5.6.3). A minimum age for the formation of the major F_m structures may be inferred from the refolding of the Three Sisters Syncline during the D_a deformational episode, which is interpreted to have occurred contemporaneously with the emplacement of the Stenter pluton at 3107 Ma (Section 9.3.2). Early B_m structures, exemplified by the American and Barite Faults, probably also formed during this time interval, because they truncate F_m folds, but appear to have been reoriented and folded by the F_a folds (Sections 9.2.1.2.1, 9.2.1.2.2, 9.3.2). Thus, the deposition of the Moodies rocks and their subsequent deformation by the early D_m structures must have occurred between 3256 - 3107 Ma ago. Since the Stenter pluton constitutes an integral part of the Nelspruit batholith (Section 8.3.4), it is evident that early D_m deformation cannot be related to the emplacement of this body. Late-phase B_m faults, typified by the Revolver and Overton Faults, deform granitoids of the Stenter pluton, and therefore must be younger than 3107 Ma. No minimum age limit is available for D_m deformation. Barton *et al.* (1983) reported a Rb-Sr whole-rock isochron age of 2755 ± 51 Ma (2σ) for sheared samples from the Stenter pluton, and suggested that this age reflects homogenization of the Sr-isotope systematics during late-stage shearing (see also Robb *et al.*, 1983; Kamo

and Davis, 1994). The age may, however, also be interpreted to reflect isotopic disturbance associated with the intrusion of the Mpageni pluton (Figure 2.1) at 2740 Ma ago (Section 2.5.2).

D_m deformation can also be recognised outside the study area. Structural analysis of the region immediately northeast of Barberton led Ramsay (1963) and Anhaeusser (1969, 1976b) to conclude that the rocks along the northern margin of the BGB have undergone three major, post-Moodies aged, deformational episodes. The earliest of these resulted from a northerly oriented maximum principal stress, and produced upward-facing, easterly trending, upright and north-verging, tight-to-isoclinal folds, exemplified by the Eureka and Ulundi Synclines (see the location map in Figure 1.4). These folds are bounded by similarly trending, southward-dipping reverse faults, namely the Lily, Sheba and Barbrook Faults, which also formed during this event. Ramsay (1963) suggested that progressive deformation resulted in the development of a penetrative, easterly to northeasterly striking cleavage which was superimposed obliquely onto the folds. The final deformational episode is considered by Ramsay (1963) and Anhaeusser (1969, 1976b) to have resulted from an easterly directed compressive stress, possibly associated with the diapiric emplacement of the Kaap Valley pluton (Figure 2.1), and led to the refolding of the early structures.

More recently, Tomkinson and King (1991) proposed that the structural evolution of the northern flank of the BGB can best be explained in two deformational stages. The earliest event, D_1 , pre-dates the deposition of the Moodies strata. D_1 is represented by a series of easterly to northeasterly trending isoclinal antiforms, known locally as Swartkoppie Horizons, which only affect strata of the Onverwacht and Fig Tree Groups. Post-Moodies deformation, D_2 , is considered by Tomkinson and King (1991) to have produced the regional, upright to north-verging isoclinal folds and associated reverse faults, as well as a penetrative cleavage and lineation in suitable lithologies. The early parts of the D_2 event saw the development of easterly trending folds and faults, as well as the emplacement of the Kaap Valley pluton. The arcuation of the Eureka and

Ulundi Synclines was attributed by Tomkinson and King (1991) to a further period of D_2 thrusting during which the Kaap Valley pluton acted as a solid buttress, against which the synclines were deformed.

De Wit (1991), De Wit *et al.* (1992), De Wit and Hart (1993), De Ronde *et al.* (1992) and De Ronde and De Wit (in press) have suggested that the supracrustal rocks of the BGB have been affected by three main compressional episodes. The oldest recognizable event, D_1 , is believed to have occurred between 3445 - 3416 Ma ago, and involved the formation of low-angle thrusts and recumbent nappes that only affect rocks of the Onverwacht Group and lower Fig Tree Group in the extreme southwestern part of the belt (De Wit, 1982; De Wit *et al.*, 1983, 1987a). D_2 deformation is manifest in the west-central parts of the belt, and resulted from northwest-directed thrust faulting and tight-to-isoclinal, upright folding. Isotopic age studies on zircons from deformed and undeformed feldspar-quartz porphyries intrusive into Fig Tree sedimentary rocks that have been affected by the D_2 event, bracket this deformation to between 3229 - 3227 Ma (De Ronde *et al.*, 1991a; Kamo and Davis, 1994). This suggests that D_2 was approximately coeval with volcanism and sedimentation within the Schoongezicht Formation, as well as the emplacement of the Kaap Valley pluton (Sections 2.5.1 and 2.5.2) (De Wit, 1991; Kamo and Davis, 1994; De Ronde and De Wit, in press). The D_3 , post-Moodies, event produced the regionally extensive, east-striking faults and folds that dominate the structure of the BGB. D_3 folding has been constrained to between 3227 - 3216 Ma (Kamo and Davis, 1994). De Ronde *et al.* (1991a) reported an age of 3082 ± 18 Ma (2σ) for hydrothermal rutile grains in a sheared (D_3) and altered porphyry at the Fairview Gold Mine (Figure 2.1). This age may provide a minimum age constraint for the late-phase faulting (De Ronde and De Wit, in press). Although D_3 post-dated D_2 , both deformational events appear to have formed under the same stress regime as part of a progressive deformational episode that involved tectonic transport to the north and northwest (De Ronde and De Wit, in press). This implies that deposition of the Moodies Group was syndeformational (see also Lamb, 1984, 1987; Jackson *et al.*, 1987; Lamb and

Paris, 1988). Strike-slip reactivation of some D_3 faults has been inferred from the geometry of associated minor shear fractures, and the presence of late-stage subhorizontal fault striations (Anhaeusser, 1965; Houstoun, 1987; Robertson, 1989).

The orientation, age and movement sense of the D_m structures in the Three Sisters region indicate that they form part of the D_2 deformational phase defined by Tomkinson and King (1991), and the D_3 episode outlined by De Ronde and De Wit (in press). Pre-Moodies folding and faulting has not been recognised in the area under review. However, the presence of contorted, schistose and brecciated metavolcanic, chert and quartzite fragments in the rocks of the Fig Tree and Moodies Groups (Sections 4.2.2, 7.2 and 7.3) provides evidence of early deformation in the source terrane of these units (see also Visser *et al.*, 1956; Anhaeusser, 1976b; Daneel, 1986; Robertson, 1989). The recognition of a major unconformity at the base of the Moodies Group in the northern part of the BGB (Section 7.1) can also be taken as evidence of pre-Moodies deformation.

9.3.2 $D_{diapiric}$

D_d structures are of a restricted nature and are only developed close to the contact with the Stentor pluton. They consist of a large-scale synform - antiform pair, with associated planar and linear fabrics. The Stentor Antiform is upright and plunges in an east-northeasterly direction. The Bien Venue Synform, situated to the south of the antiform, has a southeasterly dipping axial surface and plunges south-southeasterly. The synform refolds rocks in the western extremity of the Three Sisters Syncline, indicating that D_d deformation occurred after the formation of the major F_m folds, but is truncated by the Revolver Fault, providing evidence that D_d pre-dated late-stage D_m faulting. Downward-facing parasitic folds that deform lithologies of the Bien Venue Formation occur within the central axial zone of the synform. The minor synformal and antiformal structures at the Bien Venue massive sulphide deposit are probably also parasitic on the Bien Venue Synform, but it should be noted that they could represent parasitic folds related to the Three Sisters Syncline.